Title
FW/CADIS-Ω: An Angle-Informed Hybrid Method for Neutron Transport

Author
Munk, Madicken

Publication Date
2017

Peer reviewed|Thesis/dissertation

FW/CADIS-Ω: An Angle-Informed Hybrid Method for Neutron Transport

by

Madicken Munk

A dissertation submitted in partial satisfaction of the

requirements for the degree of

Doctor of Philosophy

in

Engineering - Nuclear Engineering

in the

Graduate Division

of the

University of California, Berkeley

Committee in charge:

Assistant Professor Rachel N. Slaybaugh, Chair
Assistant Professor Massimiliano Fratoni
Professor John Harte
Dr. Tara Pandya

Summer 2017

FW/CADIS-Ω: An Angle-Informed Hybrid Method for Neutron Transport

Abstract

FW/CADIS-Ω: An Angle-Informed Hybrid Method for Neutron Transport

by

Madicken Munk

Doctor of Philosophy in Engineering - Nuclear Engineering

University of California, Berkeley

Assistant Professor Rachel N. Slaybaugh, Chair

The development of methods for deep-penetration radiation transport is of continued importance for radiation shielding, nonproliferation, nuclear threat reduction, and medical applications. As these applications become more ubiquitous, the need for transport methods that can accurately and reliably model the systems' behavior will persist. For these types of systems, hybrid methods are often the best choice to obtain a reliable answer in a short amount of time. Hybrid methods leverage the speed and uniform uncertainty distribution of a deterministic solution to bias Monte Carlo transport to reduce the variance in the solution. At present, the Consistent Adjoint-Driven Importance Sampling (CADIS) and Forward-Weighted CADIS (FW-CADIS) hybrid methods are the gold standard by which to model systems that have deeply-penetrating radiation. They use an adjoint scalar flux to generate variance reduction parameters for Monte Carlo. However, in problems where there exists strong anisotropy in the flux, CADIS and FW-CADIS are not as effective at reducing the problem variance as isotropic problems.

This dissertation covers the theoretical background, implementation of, and characterization of a set of angle-informed hybrid methods that can be applied to strongly anisotropic deep-penetration radiation transport problems. These methods use a forward-weighted adjoint angular flux to generate variance reduction parameters for Monte Carlo. As a result, they leverage both adjoint and contributon theory for variance reduction. They have been named CADIS-Ω and FW-CADIS-Ω.

To characterize CADIS-Ω, several characterization problems with flux anisotropies were devised. These problems contain different physical mechanisms by which flux anisotropy is induced. Additionally, a series of novel anisotropy metrics by which to quantify flux anisotropy are used to characterize the methods beyond standard Figure of Merit (FOM) and relative error metrics. As a result, a more thorough investigation into the effects of anisotropy and the degree of anisotropy on Monte Carlo convergence is possible.

The results from the characterization of CADIS-Ω show that it performs best in strongly anisotropic problems that have preferential particle flowpaths, but only if the flowpaths are not comprised of air. Further, the characterization of the method's sensitivity to determin-

istic angular discretization showed that CADIS-Ω has less sensitivity to discretization than CADIS for both quadrature order and P_N order. However, more variation in the results were observed in response to changing quadrature order than P_N order. Further, as a result of the forward-normalization in the Ω-methods, ray effect mitigation was observed in many of the characterization problems.

The characterization of the CADIS-Ω-method in this dissertation serves to outline a path forward for further hybrid methods development. In particular, the response that the Ω-method has with changes in quadrature order, P_N order, and on ray effect mitigation are strong indicators that the method is more resilient than its predecessors to strong anisotropies in the flux. With further method characterization, the full potential of the Ω-methods can be realized. The method can then be applied to geometrically complex, materially diverse problems and help to advance system modelling in deep-penetration radiation transport problems with strong anisotropies in the flux.

This dissertation is dedicated to the internet of cats: a series of interconnected paws, tails, fur, space, and autotune.

Thanks also to the human family, friends, and mentors for the support and assistance that, sometimes, only opposable thumbs can provide.

Contents

List of Figures

List of Tables

Acknowledgments

I have been profoundly lucky to have met and worked with some truly inspiring people throughout my studies in nuclear engineering. Before I begin, I must say that I would not be here without the contributions–whether large or small–from all of these wonderful people. I say this with the deepest sincereity: thank you to all of you.

First, I must thank my advisor, Prof. Rachel Slaybaugh. Rachel, you saw me through the highest peaks and deepest valleys of my journey in graduate school, and you provided nothing but support and encouragement. Thank you for sincerely caring about my well-being, facilitating my pursuit of knowledge, and enabling me to push my myself even when I thought it wasn't possible. Your mentorship has led to my foray into the world of hybrid methods, a field to which I never thought I could contribute. Your technical knowledge and sincere commitment to your students is unparalleled.

I am immensely grateful for my collaborators at Oak Ridge National Laboratory for their guidance and support. Without their help and mentorship, my methods development and software contributions would be far more paltry. Drs. Tara Pandya, Seth Johnson, Steven Hamilton, and Tom Evans have all been crucial in my professional transformation, each in their own way. Tara, the coolest sparkle-transport-developer in the world, thank you for taking the time to mentor me and help me to learn a topic which was intitially very overwhelming. Thank you also for your thorough weekly feedback on this project, which only made this work stronger. Seth, I aspire to have even a small fraction of the astronomical quantity of knowledge of Python, software devleopment, and software usability in your head. Thank you for helping me learn so much more about methods development than I thoguht possible. Steven, your cynicism beyond your years is truly astounding. Thank you for the math help and absurd humor to brighten my days.

I'd also like to thank my remaining committee members, Profs. Massimiliano Fratoni and John Harte for serving on my committee and providing feedback on the work contained in this dissertation.

I have been fortunate to have many great teachers throughout my young career in research thus far. Thank you Prof. Rick Norman for being a wonderful mentor and embodiment of a quality teacher. I also have deep gratitude for my undergraduate advisor, Dr. Todd Palmer, and mentor, Dr. Steve Reese, who gave me the opportunity to pursue research as a young and inexperienced undergraduate student. Their passion for research, wealth of knowledge, and kidness influenced my choice to go to graduate school.

My pursuits in graduate school would have been far more difficult had my friends not kindly supported, encouraged, and helped me in times of need. I am honored to have such an inspiring group of people that I am able to call my friends. First, to Denia Djokić, whose kindness knows no bounds and whose imagination is unparalleled. Denia, I can't believe that I met you on my first visit to Berkeley so many years ago, and we remain friends to this day. To Katy Huff, who always has helped me take pause and consider the deeper impact of my work and whose determination and achievements are a continuous source inspiration for me. To Alejandra Jolodosky, my cat-sister for life. To Ashley Reichardt, who helps me

to see a different perspective every time we talk and who allows me adventerous escapes from the day-to-day grind. To Patricia Schuster, my book club buddy and unwavering cheerleader. To Lakshana, for her ability to be kind to any person in any circumstance, even when they talk about her mom or change her background to animals kissing. And to Kelly Rowland, my commiserator in-chief. In no particular order, thank you to my other academic friends: Nathan Bailey, Sam Briggs, Sandra Bogetic, Tomi Akindele, Anagha Iynegar, Perry Chodash, James Bevins, Seth Cadell, and Micah Folsom. Thanks to my past collaborators on non-dissertation research, in particular Leah Morgan. Finally, thank you to the fellows and staff at the Berkeley Institute for Data Science for allowing me to write and work on this project in a stimulating, coffee-abundant, invigorating place.

Finally, I must thank my nuclear family for sowing and nurturing my desire for knowledge, my California family for ensuring I lived a life outside of graduate school, and my bay area friends for making the past several years in California so special. Last, I'd also like to thank Paul, for his unwavering support, patience, and kindness.

This material is based on work supported by the Department of Energy under award number DE-NE0008286. This report was prepared as an account of work sponsored by an agency of the United States Government. Neither the United States Government nor any agency thereof, nor any of their employees, makes any warranty, express or implied, or assumes any legal liability or responsibility for the accuracy, completeness, or usefulness of any information, apparatus, product, or process disclosed, or represents that its use would not infringe privately owned rights. Reference herein to any specific commercial product, process, or service by trade name, trademark, manufacturer, or otherwise does not necessarily constitute or imply its endorsement, recommendation, or favoring by the United States Government or any agency thereof. The views and opinions of the authors expressed herein do not necessarily state or reflect those of the United States Government or any agency thereof.

Chapter 1

Introduction

This dissertation covers the development, implementation, and characterization of a novel hybrid method for neutral particle, deep-penetration, steady-state, radiation transport in highly anisotropic problems. The method generates a forward-weighted adjoint scalar flux, which is then used to consistently generate variance reduction parameters for Monte Carlo radiation transport. Because of the incorporation of directionality into the adjoint scalar flux, the method has been named FW/CADIS-Ω. The name alludes to the lineage of the method, which builds on the Consistent Adjoint-Driven Importance Sampling (CADIS) [1, 3, 4, 2], and Forward-Weighted CADIS (FW-CADIS) [5, 6] methods. This research both develops a new method that can be used in problems with strong anisotropies and provides a novel analytical framework by which to characterize anisotropy characteristics of problems. This work advances the current state of hybrid methods and extends the availability of alternate hybrid methods in existing software.

1.1 Motivation

Radiation shielding is a realm of continued importance for nuclear engineering, nuclear security, and health physics applications. With the expansion of nuclear technology applications, the potential proliferation of nuclear materials, and the continued development of nuclear medicine, tools with which to predict the behavior of these systems are in ever-increasing demand. Over the course of many decades, radiation transport methods have been developed in two primary areas: stochastic (Monte Carlo) and deterministic.

These tools have the potential to be immensely powerful, but are not without their drawbacks. Monte Carlo methods have the benefit of modeling transport that is continuous in energy, space, and angle. A user can obtain results for any region in phase-space that one might desire. However, Monte Carlo methods also require adequate sampling in order to obtain a solution with sufficient precision. Adequate sampling depends on the number of particles transported to the tally region. The more particles that are run in a problem, the longer the computational time required. Depending on the complexity of the problem, this

may be difficult, computationally demanding, very time consuming, or impossible.

Deterministic transport methods discretize the problem phase-space in space, energy, and angle. They iteratively converge on a global problem solution that is equally valid across the entire problem space, rather than a potentially localized tally location. Deterministic solvers tend to be much faster than Monte Carlo methods, but also lose the continuity in phase-space that is offered by Monte Carlo. Depending on the coarseness of the problem discretization, features of interest in the particle flux may be incorrect, obfuscated, or missed entirely.

Hybrid methods leverage the speed and uniform solution validity of deterministically-obtained transport solutions to bias Monte Carlo transport to more effectively sample in regions of interest. Biasing Monte Carlo to move particles to regions of interest more effectively is called variance reduction. Many existing implementations of hybrid methods automate the variance reduction process to speed up the time to a desired solution or to achieve a more uniform uncertainty distribution in the problem.

Hybrid methods have been designed for an assortment of applications, and none are universally applicable to all problem types. In particular, hybrid methods are wanting for a method well-suited for highly anisotropic, deep-penetration radiation transport applications. The work presented herein endeavors to provide a potential solution for such applications.

1.2 Research Objectives

This dissertation addresses a number of research objectives. The primary research goal is to:

- develop a hybrid method capable of generating variance reduction parameters for highly anisotropic, deep-penetration radiation transport problems.

Several supporting objectives accompany this goal. They are:

1. Propose a hybrid method that capitalizes on a solid theoretical framework and lessons learned from existing hybrid methods.

2. Implement the method in a software package such that it is transparent and reproducible.

3. Devise a rigorous and consistent set of metrics with which to quantify method performance.

4. Develop a suite of problems that have anisotropic behavior induced by the problem physics with which to characterize the method.

5. Run the method and existing hybrid methods on the suite of problems. Using the results obtained from these runs, compare the method's performance to exiting hybrid methods.

6. Investigate the sensitivity of the method to other angular-flux perturbing parameters, such as the angular discretization of the deterministic transport.

By addressing each of these objectives, the new method will be proposed, developed, implemented, and characterized such that its behavior in different problems is well-understood and the method is usable by interested parties that do not have the expertise of a developer or the author.

1.3 Outline of the Dissertation

The next several chapters of this dissertation covers the relevant background, the pertinent theoretical basis, and the numerical results that address the research objectives outlined in Section 1.2. Chapter 2 provides a comprehensive background on the theoretical basis on which Monte Carlo methods, deterministic radiation transport, and hybrid methods for radiation shielding are founded. In so doing, it provides context for the existing gaps for generating variance reduction parameters in highly anisotropic, deep-penetration radiation transport problems. It further highlights the most effective hybrid methods that can be applied to non-anisotropic, deep-penetration radiation transport problems.

The conclusion of Chapter 2 demarcates the transition from theoretical background work to the novel contributions of this project. Building on the knowledge presented in Chapter 2, Chapter 3 presents an overview of the theoretical basis of the method developed in this research. The theory contained in this chapter contributes to the larger body of hybrid methods research. This chapter also covers the software used for this project, and how it was modified to incorporate the novel theory presented herein. Next, Chapter 4 presents several problems with which the method is to be characterized. The results from these problems inform a parametric angle-informed study, presented in the latter portion of the chapter. Finally, Chapter 5 draws from the results presented in Chapter 4 to discuss the performance of the new method, summarize what was learned from the method characterization, and suggest future paths forward for future hybrid methods research.

Chapter 2

Literature Review

The following literature review aims to contextualize the work described in this dissertation within the realm of hybrid methods for deep-penetration neutron transport. In doing so, the pertinent theoretical information that is relevant to this topic is described. This description is supplemented by a discussion of the various efforts to implement these methods for applied problems, and the degree to which those efforts succeeded. First, a brief overview of variance reduction for Monte Carlo radiation transport is described in Section 2.1. Then, Section 2.1.3 expands on the various efforts to automate variance reduction techniques in Monte Carlo. Section 2.2.1 follows with an introduction of the concept of importance and how that relates to variance reduction. This section also focuses specifically on how the adjoint solution of the neutron transport equation relates to importance.

From this point, the chapter transitions from theory into existing implementations of variance reduction techniques used in modern software in the nuclear engineering community. Beginning in Section 2.3.1, a description of the consistent, adjoint-driven importance sampling method, or CADIS, which has been optimized for variance reduction of local solutions is presented. Next, Section 2.4 discusses the methods implemented to reduce the variance for global solutions. This discussion includes a description of the forward-weighted CADIS (FW-CADIS) method. The last section, 2.5, details the efforts to incorporate angular information into variance reduction methods for Monte Carlo. Sections 2.3.1-2.5 are each concluded with a description of the various software in which these methods have been implemented and the degree to which they improved the variance reduction for their target applications.

2.1 Monte Carlo Variance Reduction

Monte Carlo methods for radiation transport are used in the nuclear engineering community for a wide spectrum of application problems. Monte Carlo methods aim to emulate the transport of a particle from birth, through physical interaction, to death by randomly sampling the probabilities of physics that the particle could encounter, e.g. particle produc-

tion, elastic and inelastic scattering, absorption, and so forth. This process of transporting a single particle is repeated many times, to simulate the transport of many particles throughout the problem. When the user achieves a sufficient number of samples–or particles–to reach the desired statistical precision for the region of interest, the simulation is complete. However, this naive approach to simulating each particle–disregarding whether it is likely to contribute to the tallied result–can be extraordinarily computationally inefficient depending on the problem. A code could waste time simulating millions of "unusable" particles and still not reach the desired statistical precision for the tally. Variance reduction techniques were developed to address this issue. In general, these techniques bias the Monte Carlo transport to more effectively contribute to a particular result, while not fundamentally changing the nature of the problem being solved.

2.1.1 Statistical Background

Variance reduction techniques are rooted in statistics, so we begin our discussion of variance reduction techniques with a brief primer on the statistical background relevant to Monte Carlo radiation transport. Sections 2.1.1.1 through 2.1.1.3 are summarized from [7] and [8]. Monte Carlo methods transport many randomly sampled particles, and when those particles reach a region of interest, they are scored in a tally. The statistical precision of the tally will reflect the total number of particles that were sampled in a chosen region or at a chosen surface. The reliability of the answer obtained in this region is then dependent on the quantity and the history of the particles sampled.

2.1.1.1 Population Statistics

In radiation transport, one desires to estimate some response in phase-space. This response is the average behavior of the physical interactions in some differential phase-space in energy, space, and time. If the probability density function, $f(x)$, for the response is known exactly, then the response in dx can be calculated exactly by the true mean, or

$$\bar{x} = \int_{-\infty}^{\infty} x f(x) dx. \tag{2.1}$$

Rarely is $f(x)$ known exactly, so instead it is sampled. Using N randomly sampled particles, the estimate of the true mean value is given as

$$\hat{x} = \frac{\sum_{i=1}^{N} x_i}{N}, \tag{2.2}$$

where x_i is the ith event. $\hat{x}$ is the sample mean, or the estimated value of $\bar{x}$ based on the N number of samples that were used to calculate $\hat{x}$. As $N \to \infty$, $\hat{x}$ will $\to \bar{x}$, which is given by the Strong Law of Large Numbers [8]. $\hat{x}$ in itself is a useful measure, but determining the

spread of values about $\hat{x}$ is also an important measure. This is called the variance. The true variance of the distribution is

$$\sigma^2(x) = \bar{x^2} - \bar{x}^2, \tag{2.3}$$

and the standard deviation is the square root of the variance

$$\sigma(x) = \left(\bar{x^2} - \bar{x}^2\right)^{1/2}. \tag{2.4}$$

The variance of the sampled distribution differs, as a finite number of samples are used to calculate $\bar{x}$ and σ. The sample variance is defined by:

$$S^2 = \sum_{i=1}^{N} \frac{(x_i - \hat{x})^2}{N-1} \cong \widehat{x^2} - \hat{x}^2, \tag{2.5}$$

where

$$\widehat{x^2} = \frac{1}{N} \sum_{i=1}^{N} x_i^2, \tag{2.6}$$

and the sample standard deviation is given by

$$S = \left(\widehat{x^2} - \hat{x}^2\right)^{(1/2)}. \tag{2.7}$$

For (2.5) to hold true, the number of N samples must be large. S^2 is the sample estimate of the true variance, σ^2. The variance of the estimate of the mean value about $\bar{x}$ is:

$$S_{\hat{x}}^2 = \frac{S^2}{N}. \tag{2.8}$$

From (2.8), one can see the relationship between the sample standard deviation and the standard error of $\hat{x}$ about $\bar{x}$ is

$$S_{\hat{x}} = \sqrt{\frac{S^2}{N}} = \frac{S}{\sqrt{N}}. \tag{2.9}$$

$S_{\hat{x}}$ is the standard error of the estimate of the sample mean. The relative error normalizes the standard error by the estimate of the mean

$$R = \frac{S_{\hat{x}}}{\hat{x}}. \tag{2.10}$$

As a result, S, R, and N follow the relationship

$$S^2 \propto R^2 \propto \frac{1}{N}. \tag{2.11}$$

2.1.1.2 The Central Limit Theorem

Suppose $\hat{x}$ is calculated from several independent random particles to estimate $\bar{x}$. At what point does one conclude that $\hat{x}$ sufficiently reflects $\bar{x}$? The central limit theorem (CLT) [7, 8] is a very powerful supplement to the quantities described in Section 2.1.1.1. The CLT states that for large N, $\hat{x}$ will have a limiting distribution $f_N(\hat{x})$, and that distribution will be a normal distribution

$$f_N\big(\hat{x}\big) \approx \frac{1}{\sqrt{2\pi}\sigma(\hat{x})}\ \exp\left[\frac{-\big(\hat{x}-\bar{x}\big)^2}{2\sigma^2(\hat{x})}\right], \quad N \to \infty. \tag{2.12}$$

The standard deviation of $\hat{x}$ can be related to the standard deviation of the samples by

$$\sigma(\hat{x}) = \frac{\sigma(x)}{\sqrt{N}}. \tag{2.13}$$

Using the definition from Eq. (2.13) in Eq. (2.12) results in

$$f_N\big(\hat{x}\big) \approx \sqrt{\frac{N}{2*\pi}}\frac{1}{\sigma(x)}\ \exp\left[\frac{-N\big(\hat{x}-\bar{x}\big)^2}{2\sigma^2(x)}\right], \quad N \to \infty. \tag{2.14}$$

This allows us to use known values for $\hat{x}$ and an approximation of $\sigma(x)$–using S–to determine the probability density function of the sample means $f_N(\hat{x})$. Because $f_N(\hat{x})$ is normally distributed, we can find the probability that $\hat{x}$ lies in $\bar{x} \pm \epsilon$ with

$$P\big\{\bar{x}-\varepsilon < \hat{x} \le \bar{x}+\varepsilon\big\} = \int_{\bar{x}-\varepsilon}^{\bar{x}+\varepsilon} f_N\big(\hat{x}\big)d\hat{x}. \tag{2.15}$$

Placing our definition for the distribution of $\hat{x}$, which is $f_N(\hat{x})$, into Eq. (2.15), changing the limits of integration, and changing the variables such that

$$t = \sqrt{N/2}\big[(\hat{x}-\bar{x})/\sigma(x)\big],$$

this becomes

$$P\big\{\bar{x}-\varepsilon < \hat{x} \le \bar{x}+\varepsilon\big\} = \frac{2}{\sqrt{\pi}}\int_0^{(\sqrt{N/2})(\varepsilon/\sigma(x))} e^{-t^2}dt\,. \tag{2.16}$$

Recalling the definition of the error function, Eq. (2.16) becomes

$$P\big\{\bar{x}-\varepsilon < \hat{x} \le \bar{x}+\varepsilon\big\} = \text{ erf}\left[\sqrt{\frac{N}{2}}\frac{\varepsilon}{\sigma(x)}\right]. \tag{2.17}$$

Then, using the calculated estimation for $\sigma(x)$ (S), and also recalling that $S_{\hat{x}} = S/\sqrt{N}$ (Eq. (2.9)), the error function reduces to a function of ε and $S_{\hat{x}}$, or:

$$\text{erf}\left[\sqrt{\frac{N}{2}}\frac{\varepsilon}{\sigma(x)}\right] = \text{ erf}\left[\sqrt{\frac{1}{2}}\frac{\varepsilon}{S_{\hat{x}}}\right]. \tag{2.18}$$

Should ε be chosen to be a function of $S_{\hat{x}}$, the error function reduces further and becomes merely an evaluation as multiples (M) of $S_{\hat{x}}$ and $\sqrt{1/2}$. For the first few multiples of the standard error, this is evaluated as

$$P\{\bar{x} - MS_{\hat{x}} < \hat{x} \leq \bar{x} + MS_{\hat{x}}\} = \begin{cases} .683, & M = 1, \\ .954, & M = 2, \\ .997, & M = 3 \end{cases}. \tag{2.19}$$

The central limit theorem tells us that the sample mean follows a normal distribution, regardless of the distribution of the underlying sample, as the number of samples approaches infinity. This means that no matter what distribution is being sampled, the sampled mean will have this expected behavior. As a result, given a calculated value for $\hat{x}$ and S, the probability that $\hat{x}$ is near $\bar{x}$ is known and calculable. Further, the central limit theorem shows that this distribution is approached very quickly as N increases, with most problems only requiring $N > 30$ [7]. Note that N is not the total number of samples, but the number of samples required to calculate each mean.

However, for the central limit theorem to hold a number of requirements must be satisfied. All of the quantities in Section 2.1.1.1 have the underlying assumption that each x_i is assumed to be randomly sampled and independent of other x_i. If some region of phase space is omitted accidentally, these values will not be reflective of the true $f(x)$, and so $\hat{x}$ will not approximate $\bar{x}$. Further, for S to be a good approximation of $\sigma(x)$, a large number of N samples must contribute to the calculation of $\hat{x}$. The central limit theorem also assumes that $f(x)$ is a probability density function that can be sampled and has a variance that exists. As a result, one must be reasonably sure that all of these requirements are satisfied if using Monte Carlo sampling methods.

2.1.1.3 The Figure of Merit

The equations in the preceding sections describe how to estimate the statistics of a population given a finite number of samples. In radiation transport, a user seeks to estimate some response, the relative error associated with that response solution, and the time it takes to obtain those values. Equation (2.11) described the relationship between the sample variance, the relative error, and the number of particles as

$$S^2 \propto R^2 \propto \frac{1}{N}.$$

The relationship between the relative error, R, and the number of particles, N, (recall that $R^2 \propto \frac{1}{N}$) will be some constant value (C):

$$C_1 = R^2 N.$$

As a problem is simulated, the number of particles run, N, will increase proportionally to the computational transport time, T. Therefore, the relationship between R and T should

also be a constant.

$$C_2 = R^2 T$$

The figure of merit (FOM) shown in Eq. (2.20) is the most commonly reported metric using this relationship that is reported. It is widely used in quantifying the effects of variance reduction methods. Because it uses the inverse quantity of the relative error and time, a "good" result would be obtained from a low relative error in a short amount of time, resulting in a FOM with a high numerical value.

$$FOM = \frac{1}{R^2 T} \tag{2.20}$$

Further, a user may desire to determine how long a problem must be run to obtain a desired relative error. In that case, Eq. (2.20) can simply be rearranged to

$$R = \frac{1}{(FOM * T)^{1/2}}.$$

The figure of merit is a very useful tool, but it is limited by statistical precision in calculating R. It is worth noting that early on in a transport simulation, when too few particles have been simulated to effectively capture S or $\hat{x}$, the FOM will oscillate. Eventually, the FOM will converge to a relatively constant value. This behavior can also be used to determine whether one has sufficiently sampled the region in which they are quantifying the response.

2.1.2 Variance Reduction Methods for Monte Carlo Radiation Transport

Now that the different parameters that affect the variance in a problem have been introduced, let us transition to different variance reduction techniques that are available in Monte Carlo radiation transport packages. Variance reduction techniques in radiation transport methods fall into four general categories: truncation methods, population control methods, modified sampling methods, and partially-deterministic methods. Of importance for this project are population control methods and modified sampling methods, which are discussed in a number of the papers referenced herein. Truncation methods and partially-deterministic methods do not contribute to and are not the focus of this work, so will only be touched upon briefly.

A later section (3.3) of this dissertation will discuss the choice of software packages used for this project. In particular, our hybrid methods software package is designed to accelerate the Monte Carlo radiation transport package MCNP [10, 9, 8]. Variance reduction methods are available in a number of other Monte Carlo radiation transport packages, and are by no means limited to a particular code. However, the implementation of methods differs between software and the specifics may differ slightly. The discussion for the remainder of this subsection will be centered around the specifics of the code used for this project.

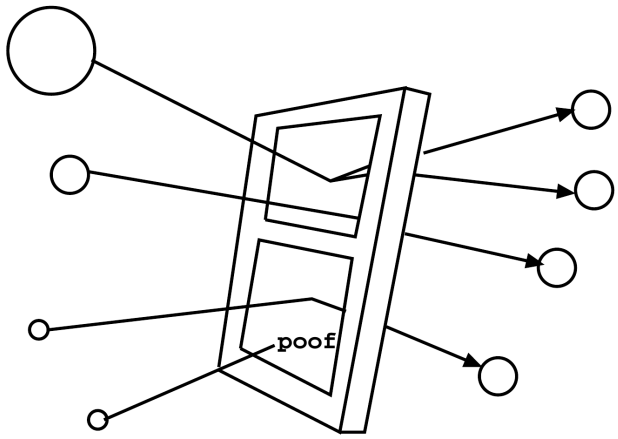

Figure 2.1: Cartoon illustration of a weight window, adapted from [9, 11]

Population Control Methods

Population control methods adjust the particle population in the problem to obtain better sampling in regions of interest by preferentially increasing or decreasing the particle population. The first two types of population control methods that will be discussed are called splitting and rouletting. Splitting is a method by which the particle population can be increased by splitting a single higher-weight particle into several lower-weight particles. Rouletting, conversely, reduces the particle population by stochastically killing particles. Particles that survive a rouletting routine have their weight adjusted higher, thereby conserving weight in the routine. Both splitting and roulette maintain a fair game by adjusting the particle weights as each routine is performed; statistically, the sum of the child particle weights is the same as the parent weight as it entered the routine.

To use population control methods effectively as a variance reduction technique, splitting is performed in high-importance regions to increase the particle count, and thus the sampling, in important regions. Conversely, rouletting is performed in low-importance regions to reduce the particle population in regions that are unimportant to the tally result. Splitting and rouletting can be applied to include geometry, energy and time.

The weight window combines splitting and rouletting to keep particles within a desired weight range. Figure 2.1 illustrates the different processes a particle may go through when passing through a weight window. The top particle entering the weight window is a single, high-weight particle. The weight of this particle is above the weight window bounds, so as it enters the weight window it is split into multiple particles whose weight is within the window bounds. The second particle entering the window is within the weight window bounds, so it retains its weight and is not split or rouletted. The last two particles entering the window have weights lower than the bound. They undergo a rouletting routine and one particle is killed and the surviving particle is increased in weight. As these particles leave the window, all of them have weights within the range of the window. This will reduce the variance of

the particles contributing to a tally in that region.

While the use of weight windows in a problem helps to keep a more ideal distribution of particle weights, the user is faced with calculating a significant number of parameters to determine weight windows for the entire problem. In the best case with an experienced user, this may just take time. With an inexperienced user or a complex problem this can be insurmountable, and may be too difficult to do without some automated assistance.

It should be noted that while splitting and rouletting can be performed on a single variable–angle, energy, space, or time–the weight windows generally used are either energy-space dependent or space-time dependent. Further, the weight window will split or roulette depending on the particle weight entering the window. Splitting and rouletting on their own either increase or decrease the particle weight proportional to the ratio of cell importances, or I'/I, no matter what the entering particle weight is. As a result, poorly chosen splitting or rouletting parameters can still have significant tally variance, because particle weights may still span a wide range.

Modified Sampling Methods

Modified sampling methods adjust transport by sampling from a different probability distribution function than the actual distribution for the problem. This is possible if, as with population control methods, the particle weights are adjusted accordingly. The new probability distribution function should bias particles in regions of high importance to the problem tallies. In MCNP, a number of modified sampling methods exist. These include the exponential transform, implicit capture, forced collisions, source biasing, and neutron-induced photon production biasing.

The exponential transform modifies particle transport from the analog problem by artificially modifying the macroscopic cross section, and thus the distance-to-collision, to move particles in important directions. In directions of higher importance, the cross section is reduced, and particles can flow more freely. In directions of lower importance, the cross section is increased, and particles more frequently interact, thereby increasing their probability of directional change or absorption. The transformed cross section used by the exponential transform is defined by

$$\Sigma_t^* = \Sigma_t(1 - p\mu), \tag{2.21}$$

where Σ_t^* is the transformed total cross section, Σ_t is the true total cross section, p is the transform parameter, and μ is the cosine of the angle between the preferred direction and the particle's transport direction [8, 11, 10].

Because the particle's transport is adjusted in the exponential transform, the particle weight must be adjusted accordingly. This is given by

$$\begin{aligned} w^* &= \frac{\Sigma_t e^{-\Sigma_t s}}{\Sigma_t^* e^{-\Sigma_t^* s}} \\ &= \frac{e^{-\rho\Sigma_t \mu s}}{1 - p\mu}, \end{aligned}$$

where s is the phase space of particle residence. This weight adjustment ensures that the particle weight is conserved throughout transport, even as the cross section is altered. Because the cross section in the problem is both energy and material dependent (depending on the geometry), the exponential transform will be dependent on space and energy, and particles will be biased in both. While a powerful method, the exponential transform is quite difficult to use and if p is ill-chosen this method can perform quite poorly. Further, the user has to know quite a bit about the problem physics and material to choose an optimal quantity for p.

Source biasing, rather than preferentially adjusting particles' directionality by way of adjusting the cross sections, biases particles from their origin. Source biasing has the option to bias particles in energy, direction, and space (if the source is volumetric). This allows the user to choose importance separately for each variable. First, the source variable (let us consider energy for the moment) is defined as a series of bins or a function. Second, the bins are assigned probabilities of occurrence according to their importance. An energy bin with a high importance will be assigned a high probability of occurrence, and a bin with low importance will be assigned a low probability of occurrence. As particles are born in the bins with higher importances, they will have their weights adjusted to the inverse of their probability of occurrence, or $w^* = p/p^*$. Here p refers to the probability density function for the source particles; it bears no relation to the exponential transform factor.

Source biasing is a very simple method that can reduce the solution variance significantly. However, if a user chooses bin sizes or a function that does not properly reflect the particles importances in the problem, the source will be poorly sampled. As a result, sampling may be very inefficient and the figure of merit will decrease. In MCNP, if poor parameters are chosen for this method, the user is given a warning.

Truncation Methods

Truncation methods stop tracking particles in a region of phase-space that is of low-importance to the tally. These methods can be used in space (a vacuum boundary condition), energy (eliminate particles above or below a specified energy), or time (stop tracking after a given time). To effectively use these methods, the user must be aware of particles' importance to a tally result. If particles that are important to a result are eliminated with a truncation method, the tally will lack the contribution from that particle's phase-space, and will be underestimated as a result. Further, as discussed in Section 2.1.1.2, the central limit theorem only holds assuming that the histories tracked are independent and drawn from identical distributions. Truncating particles of high importance removes the independence from the sampling and modifies the underlying PDF being sampled, so the estimate of the response will be wrong.

It is important in using any variance reduction technique to ensure that a fair game is being played. The user must ensure that the fundamental nature of the problem is not being changed by using a variance reduction technique, or the answer will not be representative of the original problem. Automated variance reduction techniques aim to eliminate this

uncertainty for the user by estimating the importance of particles in some way and then setting up variance reduction parameters automatically. The remainder of this chapter review will focus on efforts to automate population control methods and modified sampling methods for variance reduction.

2.1.3 Automated Variance Reduction Methods for Monte Carlo Radiation Transport

Section 2.1.2 described some methods that one may use to reduce the variance in Monte Carlo radiation transport tallies. These methods, if used correctly, can significantly increase the transport efficiency in a Monte Carlo simulation. However, correct use of these methods often requires intelligent selection of variance reduction (VR) parameters, which is a non-trivial task. Users have found themselves often performing several trial runs before choosing final quantities for the VR parameters in their problems, which was computationally inefficient and required significant knowledge of Monte Carlo and variance reduction to execute well [12].

This has been addressed by using Monte Carlo to sample the problem in an initial calculation to determine more favorable variance reduction parameters automatically. Booth and Hendricks, recognizing that choosing optimal weight window values for energy- and space-dependent weight windows was difficult even for experienced users, proposed two tools for Monte Carlo variance reduction in parallel. The first was a Monte Carlo importance generator [12] that could be used to make informed decisions on cell importances throughout the problem. The second method, a Monte Carlo generated weight window generator, calculates the weight window values automatically for a given problem [13]. The importance generator estimates a cell's importance by tracking the weights of the particles in the cell, or

$$Importance = \frac{\text{score of particles leaving the cell}}{\text{weight leaving the cell}}. \tag{2.22}$$

The weight window generator calculates weight window values with

$$W_{i,low} = \frac{1}{kN}\left(\Sigma W_{i,in} + \Sigma W_{i,out}\right) \tag{2.23a}$$

$$W_{i,high} = \begin{cases} k * W_{i,low} & \text{if } W_{i,low} \neq 0 \\ \infty & \text{if } W_{i,low} = 0 \end{cases}, \tag{2.23b}$$

where $W_{i,low}$ and $W_{i,high}$ are the weight window lower and upper weight bounds respectively, $W_{i,in}$ and $W_{i,out}$ are the total weight entering and leaving the cell, N is the number of source particles, and k is some weight window width (a constant that Hendricks set to 5).

In his paper, Booth notes that the weight window target value derived from the importance generator was chosen so that the track weight times the expected score in the tally region (for unit track weight) was approximately constant. Booth's importance generator

saw improvements in the FOM between 1.5-8x when compared to the analog run for the test problem presented.

Booth and Hendricks combined these two methods to automate weight window generation based on phase-space importance [14, 15]. They showed that the combination of the importance estimator and the weight window generator was a successful way to perform variance reduction in deep-penetration problems. However, their method depended on several iterations of importance-determining runs to obtain a satisfactory estimation of the importance. For a 300 cm slab problem, the FOM was increased from 1.9 to 75, but took 10 subsequent runs to obtain the FOM of 75, and these runs ranged from 1.2 min (for the analog problem) to 42 minutes (for the 9th run [15]).

It should be noted that both the importance generator and the weight window generator use a lower-fidelity Monte Carlo run to gain an initial estimate for a cell's importance and generate variance reduction parameters from them to bias a more computationally-intensive and higher-fidelity run. Naturally, the variance reduction parameters generated by using these techniques are limited by the statistical precision in the regions used to generate them. Hendricks also pointed out that the weight window generator tended to populate all regions of phase space equally, which he conceeded was not ideal for all problems [13]. Furthermore, for deep-penetration particle transport, the variance reduction parameters for low flux regions are exceedingly difficult to generate, resulting in unfavorable VR parameters.

The MCNP [8, 9] weight window generator has been extended beyond the initial space- and energy-implementation described in Booth's paper. It now has the ability to automatically generate space- energy- and angle-weight windows. The importance generator in MCNP also has been extended to time-importance; the values of which can be used for splitting or rouletting parameters [9], and can be optimized on a grid independent from the MCNP geometry [16].

As with Booth and Hendricks' original implementations, this updated weight window generator still relies on adequate sampling to obtain sufficient weight window parameters. When additional degrees of freedom, like angle-dependence, are added, the time to converge on those parameters takes even longer. The weight window generator also only allows for a single tally to be optimized at once, so multiple tallies cannot be optimized simultaneously. Finally, the weight window generator still requires user input and updating to seed the weight window solution. The user must choose the meshing of the problem and have some intuition as to how the problem should be subdivided. In the paper by Van Riper et al, it was found that depending on user experience, the weight window generator can have differences in the FOM from 2 to 10 times [17] for the problems that they investigated.

2.2 Importance Functions for Variance Reduction

The effective use of variance reduction techniques can lead to a faster time to a desired solution and a reduced variance in the specified tally. However, specifying variance reduction parameters is not always a straightforward procedure. In simple geometries, a user might

intuitively understand which regions of a problem may contribute more to a desired solution, but for more complex geometries, this may not be so obvious. In the following subsections, the theory in determining which regions of a problem are important to eliciting a tally response will be described. The first topic discussed will be the concept of importance and obtaining a measure of importance with Monte Carlo sampling. Second, the adjoint equation and its relation to importance will be introduced. Last, the contributon solution and how its relation to tally responses is reviewed.

2.2.1 The Concept of Importance

The concept of importance is, in essence, a means of defining which regions of a problem that are likely to contribute to a response and which are less likely to contribute to a response. The regions that are more likely to generate a response will have a higher importance than those that do not. If an importance function for a system can be obtained computationally, that importance function can be strategically used in variance reduction techniques to speed up the Monte Carlo calculations.

As described in Section 2.1.3, Booth [12] proposed a method to quantify a cell's importance within a Monte Carlo simulation (Eq. (2.22)). In this method, Booth suggested estimating the cell's importance using Monte Carlo transport as:

$$Importance = \frac{\text{score of particles leaving the cell}}{\text{weight leaving the cell}}.$$

This particular calculation of importance follows from the intuitive explanation for importance in the preceding paragraph. Recall from Section 2.1.2 that in variance reduction methods, the population of particles is increased in important regions such that the number of samples or particles contributing to a tally increases, but the total problem weight is conserved. More important regions should have many lower-weight particles to reduce the tally variance. Using Booth's bookkeeping method for estimating regional importance, if a cell has a greater weight leaving the cell than the number of particles, that means that the relative contribution of that cell to the tally is likely to be lower than other regions. If, instead, the number of particles leaving the cell is greater than the weight leaving the cell, then that region is more important to the tally response, because that particle population is higher than other cells.

While this estimation of the importance requires only a Monte Carlo forward calculation of the problem, it was referred to as the forward-adjoint importance generator [12, 14, 15] because the bookeeping tracked by Eq. (2.22) was a forward-approximation of the adjoint. Adjoint theory and how it relates to importance will be discussed in Section 2.2.2. Booth's estimation of importance was used to generate weight window target values inversely proportional to the importance. In this case, the track weight times the expected score is approximately constant in the problem. Choosing this inverse relationship between the weight window and importance is common practice in variance reduction, and is often a good choice because it is nearly optimal over a broad range of a problem phase-space [18].

It should be noted that Booth's method is reliant on the statistical precision of the cells sampled to generate their importances. For deep-penetration problems, obtaining a "good" estimate of the cell importances many mean free paths from the forward source takes several iterations. With large fluctuations between iterations, this has the potential to be a very slow and computationally inefficient way to calculate importance in a problem. Using a solution of the adjoint that is equally valid across all of the problem space is more ideal for deep-penetration problems.

2.2.2 The Adjoint Solution for Importance

Using the solution of the adjoint formulation of the neutron transport equation is one of the most widely recognized methods for generating an importance function. This subsection will begin with a brief summary of adjoint theory. A discussion on how the adjoint solution differs physically from the forward solution for a particular problem follows. Last, some early investigations on how the adjoint and importance are related are summarized.

2.2.2.1 Theory

In previous sections we have reviewed the statistical precision of Monte Carlo-based methods, and how sampled results in Monte Carlo can be obtained in less time with variance reduction methods. We have also briefly addressed the forward and the adjoint solutions for a particular problem. In neutron transport, the integral form of the forward, steady-state, particle transport equation can be defined as:

$$\hat{\Omega}\cdot\nabla\psi(\vec{r},E,\hat{\Omega})+\Sigma_t(\vec{r},E)\psi(\vec{r},E,\hat{\Omega})= \int_{4\pi}\int_0^{\infty}\Sigma_s(E'\rightarrow E,\hat{\Omega}'\rightarrow\hat{\Omega})\psi(\vec{r},E',\hat{\Omega}')dE'\,d\hat{\Omega}'+q_e(\vec{r},E,\hat{\Omega}), \quad (2.24)$$

where $\vec{r}$, E, and $\hat{\Omega}$, are direction, energy, and angle, respectively, giving six dimensions of phase-space in total. ψ is the neutron flux, Σ is the neutron interaction (scattering, absorption, total) cross section, and q_e is the external fixed source. Alternatively, this can be written in operator form,

$$H\psi = q_e\,, \quad (2.25)$$

where H represents the streaming, scattering, and absorptive terms from Eq. (2.24), ψ is the angular flux as it is in Eq. (2.24), and q_e is the source term.

The forward transport equation tells us where particles are moving throughout the system. Of note: the particles move in the scattering term from E' into E, and from $\hat{\Omega}'$ into $\hat{\Omega}$. Therefore, for a particular problem with a given q_e, particles start at q_e and move throughout the system, either downscattering in energy, streaming out of the problem, absorbed by the problem materials, or induce a response at the tally location.

The adjoint equation of the same form, in contrast, can be expressed as:

$$-\hat{\Omega}\cdot\nabla\psi^{\dagger}(\vec{r},E,\hat{\Omega})+\Sigma_t(\vec{r},E)\psi^{\dagger}(\vec{r},E,\hat{\Omega})= \int_{4\pi}\int_{0}^{\infty}\Sigma_s(E\rightarrow E',\hat{\Omega}\rightarrow\hat{\Omega}')\psi^{\dagger}(\vec{r},E',\hat{\Omega}')dE'\,d\hat{\Omega}'+q_e^{\dagger}(\vec{r},E,\hat{\Omega}), \quad (2.26)$$

or in operator form as

$$H^{\dagger}\psi^{\dagger}=q_e^{\dagger}, \quad (2.27)$$

where the variables with † signify the adjoint-specific variables for the problem: the adjoint flux $\psi^{\dagger}$ and the adjoint source $q_e^{\dagger}$. Note here that the particles in the adjoint equation move from E into E', and from $\hat{\Omega}$ into $\hat{\Omega}'$, which indicates an upscattering in energy and a reversal of direction when compared to the forward problem. The external source, too, is different, changing from q_e to $q_e^{\dagger}$.

To solve the adjoint problem the adjoint source, $q_e^{\dagger}$, can be chosen such that it has the potential to reveal information about the forward problem. In MC variance reduction, we seek to obtain information on the detector or tally response for the system. The response for the forward problem given a defined source distribution $q(\vec{r},E,\hat{\Omega})$ is

$$R_{tally}=\int_{4\pi}\int_{V}\int_{E}\psi(\vec{r},E,\hat{\Omega})\Sigma_{tally}(\vec{r},E,\hat{\Omega})dEdVd\hat{\Omega}, \quad (2.28a)$$

where $dE\ dV$ and $d\Omega$ are the differential spaces of energy, volume, and angle in the tally region. This can be simplified using bracket notation, where the brackets indicate an integration over all phase-space,

$$R_{tally}=\langle\psi\Sigma_{tally}\rangle. \quad (2.28b)$$

ψ is the angular flux and Σ_{tally} is the effective tally response function.

For a simple source-detector problem, we choose $q_e^{\dagger}$ to be Σ_{tally}; or the adjoint source is the tally/detector response function for the system. Therefore, the adjoint particles start at low energy at the detector location, move away from the adjoint source (the detector location), and scatter up in energy. By making the choice that $q_e^{\dagger}=\Sigma_{tally}$, the response function can be written as a product for the forward flux and the adjoint source

$$R_{tally}=\langle\psi q^{\dagger}\rangle. \quad (2.29)$$

By using the adjoint identity and the same operators H from Eqs. (2.25) and (2.27)

$$\langle\psi,H^{\dagger}\psi^{\dagger}\rangle=\langle\psi^{\dagger},H\psi\rangle. \quad (2.30)$$

Eq. (2.29) can be written as a function of the adjoint flux and the forward source distribution

$$R=\langle\psi^{\dagger}q\rangle. \quad (2.31)$$

At this point, we know that the solution to the adjoint problem transports particles from the adjoint source (which is the detector or tally location) into the problem phase-space. The

adjoint particles are upscattered in energy and are transported in $-\Omega$ relative to the forward problem. However, it may not be immediately obvious how this adjoint solution relates to importance for the forward solution. Let us start with a simple illustrative example: a monoenergetic, monodirectional, point source. The forward source takes the form of a delta function:

$$q(\vec{r}, E, \hat{\Omega}) = \delta(\vec{r} - \vec{r}_0)\delta(E - E_0)\delta(\hat{\Omega} - \hat{\Omega}_0).$$

Using this definition of the forward source and evaluating Eq. (2.31), we obtain

$$\begin{aligned} R &= \langle \psi^\dagger q \rangle \\ &= \int_V \int_E \int_\Omega \psi^\dagger(\vec{r}, E, \hat{\Omega}) q(\vec{r}, E, \hat{\Omega}) d\hat{\Omega} dE dV \\ &= \psi^\dagger(\vec{r}_0, E_0, \hat{\Omega}_0). \end{aligned}$$

This result shows that the solution to the adjoint equation is the detector response for the forward problem. As a result, the adjoint flux can be used as an indicator of a particle produced in $\vec{r}, E, \hat{\Omega}$ contributing to a response in the system. This indicator can be thought of as the particle's importance to achieving the tally or response objective. Consequently, it is often said that the adjoint is the importance function for the problem.

The adjoint solution is used in nuclear engineering for a number of applications, including reactor physics and perturbation theory [19, 21, 20, 22]. However, Goertzel and Kalos' early work recognized its application for deep-penetration radiation shielding. Goertzel and Kalos [23] showed analytically that the exact adjoint solution, if used as an importance or weighting function for the forward Monte Carlo calculation, will result in a zero variance solution for the forward Monte Carlo problem. Further, Kalos [24] showed in a 1D infinite hydrogen slab problem that an analytically-derived adjoint importance function significantly improved the speed to convergence for neutron transport in deep-penetration problems.

Goertzel and Kalos' finding that an exact adjoint can lead to a zero variance solution means that if a single particle is transported with the adjoint weighting function, its score will be the same as the total system response. Only a single particle is required to get an exact solution for the forward problem. This is prohibitive because obtaining an exact adjoint solution is just as computationally expensive as getting an exact forward solution. Instead, one seeks to obtain a good, but fairly inexpensive, estimate of the adjoint solution based on computational limitations. A good importance estimate should help reduce the variance in a reasonable amount of time and be relatively computationally inexpensive. A Monte Carlo solution can provide a continuous solution over the problem phase-space. However, as discussed in Section 2.1.2, the quality of this adjoint solution relies on the number of samples used to calculate it and that may take a significant amount of time. A deterministic solution has the potential to offer equal or better solution confidence across the entire problem. However, it is discretized in space, energy, and angle. For deep-penetration importance functions, we opt for deterministically-obtained solutions due to the solution's equally distributed validity.

2.2.2.2 Implementation

Coveyou, Cain, and Yost [25] expanded on Goertzel and Kalos' work by interpreting in which ways the adjoint solution could be adapted for Monte Carlo variance reduction. In particular, they investigated the choice of biasing schemes and how effective they were at variance reduction for a simple one-dimensional problem. They reiterated that the adjoint solution is a good estimate for importance, but should not be calculated explicitly, and rather estimated by a simpler model. The adjoint function is not necessarily the most optimal importance function; however, it is likely the closest and most obtainable estimate of importance that can be calculated [25]. They concluded that source biasing by the solution to the adjoint equation or by the expected response is the best choice for Monte Carlo variance reduction, as it can be used independently from any other variance reduction technique, and provides good results.

Tang and Hoffman [26] built off of the parameters derived by Coveyou et al. [25] to generate variance reduction parameters automatically for fuel cask dose rate analyses. In their work, Tang and Hoffman used the 1D discrete ordinates code XSDRNPM-S to calculate the adjoint fluxes for their shielding problems. The results from this calculation were then used to generate biasing parameters for Monte Carlo; specifically, they aimed at generating parameters for energy biasing, source biasing, Russian roulette and splitting, and next event estimation probabilities. They implemented their work in the SAS4 module in SCALE [27]; it was one of the earlier implementations of a fully-automated deterministic biasing procedure for Monte Carlo.

2.2.3 The Contributon Solution for Importance

Contributon theory is another useful concept that can be used as a measure of importance [28, 29, 30]. However, contributon theory quantifies importance differently than adjoint theory. In contributon transport, a pseudo-particle, the *contributon*, is defined. The contributon carries response in the problem system from the radiation source to a detector. The total number of contributons in a system are conserved by the *contributon conservation principle*: all contributons that are emitted from the source eventually arrive at the detector. Much of the work in this realm has been done by Williams and collaborators [28, 29, 30].

The contributon transport equation can be derived in a form analogous to the forward (Eq. (2.24)) and adjoint (Eq. (2.26)) equations. The derivation of Eq. (2.33) and its corresponding variables is available in a number of the sources referenced in this section, so we will abstain from re-deriving it here. The angular contributon flux is defined as the product of the forward and adjoint angular fluxes:

$$\Psi(\vec{r}, E, \hat{\Omega}) = \psi^{\dagger}(\vec{r}, E, \hat{\Omega})\psi(\vec{r}, E, \hat{\Omega}) \, . \tag{2.32}$$

The contributon transport equation is:

$$\hat{\Omega}\cdot\nabla\Psi(\vec{r},E,\hat{\Omega})+\widetilde{\Sigma}_t(\vec{r},E,\hat{\Omega})\Psi(\vec{r},E,\hat{\Omega})= \int_{4\pi}\int_0^\infty \widetilde{p}(\vec{r},\hat{\Omega}'\to\hat{\Omega},E'\to E)\widetilde{P}(\vec{r},\hat{\Omega}',E')\widetilde{\Sigma}_t(\vec{r},E',\hat{\Omega}')\Psi(\vec{r},E',\hat{\Omega}')dE'\,d\hat{\Omega}'+\hat{p}(\vec{r},E,\hat{\Omega})R. \tag{2.33}$$

The units of phase-space are the same as observed in the forward and adjoint transport equations. The symbols decorated with tildes denote variables that are unique to the contributon equation; $\widetilde{p}$ and $\widetilde{P}$ are both probability functions related to scattering and $\widetilde{\Sigma}$ are effective cross sections. The effective cross sections are given by:

$$\begin{aligned}\widetilde{\Sigma}_t(\vec{r},E,\hat{\Omega}) &= \widetilde{\Sigma}_s(\vec{r},E,\hat{\Omega})+\widetilde{\Sigma}_a(\vec{r},E,\hat{\Omega})\\ &= \frac{\iint\Sigma_s(\vec{r},\hat{\Omega}''\cdot\hat{\Omega},E\to E'')\psi^\dagger(\vec{r},\Omega'',E'')d\Omega''dE''}{\psi^\dagger(\vec{r},E,\hat{\Omega})}+\frac{Q^\dagger(\vec{r},E,\hat{\Omega})}{\psi^\dagger(\vec{r},E,\hat{\Omega})}.\end{aligned} \tag{2.34}$$

Note here that the effective scattering and absorption cross sections are adjoint flux-dependent. Where the adjoint flux becomes small, the interaction probabilities will become large. As a result, regions where the adjoint flux is high interaction probabilities become low, causing fewer interactions and more streaming. Conversely, regions with low adjoint fluxes–like the problem boundary–will have a very high cross section, thus encouraging particle transport back towards the adjoint source. This increased probability of interaction in low flux regions encourages response particle (contributon) transport towards the detector or tally, thus contributing to a response.

The scattering probability of a contributon at position $\vec{r}$, E', and $\hat{\Omega}'$ is:

$$\widetilde{P}(\vec{r},\hat{\Omega}',E')=\frac{\widetilde{\Sigma}_s(\vec{r},E',\hat{\Omega}')}{\widetilde{\Sigma}_t(\vec{r},E',\hat{\Omega}')}\,, \tag{2.35}$$

and the probability that a contributon scattering at $\vec{r}$, E', and $\hat{\Omega}'$ will scatter into $d\hat{\Omega}\;dE$ is

$$\widetilde{p}(\vec{r},\hat{\Omega}'\to\hat{\Omega},E'\to E)=\frac{\Sigma_s(\vec{r},\hat{\Omega}'\cdot\hat{\Omega},E'\to E)\psi^\dagger(\vec{r},E,\hat{\Omega})}{\iint\Sigma_s(\vec{r},\hat{\Omega}'\cdot\hat{\Omega}'',E'\to E'')\psi^\dagger(\vec{r},E'',\hat{\Omega}'')d\hat{\Omega}''dE''}. \tag{2.36}$$

The distribution function governing the contributon source is

$$\hat{p}(\vec{r},E,\hat{\Omega})=\frac{\psi^\dagger(\vec{r},E,\hat{\Omega})Q(\vec{r},E,\hat{\Omega})}{\int\int\int\psi^\dagger(\vec{r'},E',\hat{\Omega}')Q(\vec{r'},E',\hat{\Omega}')d\hat{\Omega}'dE'dV'}, \tag{2.37}$$

note that the contributon source is actually defined in Eq. (2.33) by the product of $\hat{p}$ and R. R is contributon production rate; it is given by integral of the adjoint flux and the forward source

$$\begin{aligned}R &= \int\int\int\psi^\dagger(\vec{r},E,\hat{\Omega})Q(\vec{r},E,\hat{\Omega})d\hat{\Omega}dEdV\\ &= \langle\psi^\dagger Q\rangle\end{aligned}\,, \tag{2.38}$$

which is recognizable as the system response described in Section 2.2.2. It can also be shown by integrating Eq. (2.33) over all phase space and ensuring that the function $\hat{p}$ is normalized, that

$$R = \langle \widetilde{\Sigma}_a \Psi \rangle, \tag{2.39}$$

or the rate at which contributons die in the detector is the same as the rate at which they are produced by the contributon source. Knowing that R is the contributon production rate, let us consider the probability that a particle will be absorbed in the detector, or P, given by

$$P = \langle \Sigma_a \psi \rangle. \tag{2.40}$$

Adding a factor of $\psi^\dagger/\psi^\dagger$ to the terms on the right hand side, this becomes

$$P = \left\langle \frac{\Sigma_a}{\psi^\dagger} \psi \psi^\dagger \right\rangle. \tag{2.41}$$

By using the identities from the contributon equation, this is also

$$P = \langle \widetilde{\Sigma_a} \Psi \rangle. \tag{2.42}$$

Next, substituting the definition from Eq. (2.39) into this equation, it follows that

$$P = R. \tag{2.43}$$

This is the same *contributon conservation principle* introduced at the beginning of this section. Williams noted that one could go so far as to transport contributons rather than real particles with Monte Carlo. Because every particle transported would eventually reach the detector and give an exact value for R (as shown by Eq. (2.43)), this would lead to a zero variance solution. However, the nature of solving the contributon equation with Monte Carlo (or any other transport mechanism) involves knowing the exact solution to the adjoint equation, and so relies on the same computational obstacles as solving the adjoint transport equation.

As mentioned in the previous section, the adjoint flux is an indicator of a particle's importance to inducing a response. Conversely, the contributon flux describes the importance of a particle to the solution. Becker's thesis [31] aptly points out that this is illustrated most dramatically in a source-detector problem, where the forward source has little importance to the adjoint source, but does have importance to the problem solution. As a result, both the contributon solution and the adjoint solution can be considered importance functions for a problem, but the importance that they describe differs.

Williams recognized the applications of contributons to shield design and optimization in an extension of contribution theory called spatial channel theory. In particular, Williams noted that variables relevant to contributon response were useful in determining transport paths through media [30, 32]. A study of different contributon values throughout the system could enlighten users on regions with higher response potential. This could then be used to

intelligently choose regions for detector locations or add to shielding. The contributon values in this theory include the contributon flux, the contributon density, the contributon current, or the contributon velocity [33]. In this way, the user could find the particles most influential to the response of the system. A region with high response potential is the most important to a detector tally. The variables of response described by Williams are the response potential, the response current, and the response vorticity [29].

Contributon theory and spatial channel theory have been applied successfully to shielding analyses [34, 32] due to their ability to show particle flow between a source and response effectively. Williams and Engle showed that spatial channel theory can be used in reactor shielding analyses. In their work, they used contributon currents to determine preferential flow paths through the Fast Flux Test Facility (FFTF) [32]. Seydaliev [34] used angle-dependent forward and adjoint fluxes and currents to visualize the contributon flux for simple source-detector problems. In this work, he showed that contributon flow in the system behaves much like a fluid between the source and detector, following preferential flow paths more densely. Seydaliev also observed ray effects in the contributon flux for high energy photons, and traditional methods like using a first collision source, did not remedy the issue. The contributon formulation of particle transport can show important particle flow paths between a source and a detector, but it is still not immune to computational obstacles that exist for standard forward- and adjoint- transport.

The past few subsections have described the different means by which importance can be defined or quantified for a problem. As discussed in Section 2.2.1, generating an importance function with Monte Carlo is limited in that the quality of the importance map is only as good as the regions that are sampled. For deep-penetration problems, it may be prohibitively difficult to obtain adequate importance sampling with traditional Monte Carlo methods.

Deterministically-obtained importance functions, however, offer the benefit of a solution that is equally valid across all of the problem solution-space. This is because the deterministic solution's precision is limited to convergence criteria, not sampling of individual particles. Using a deterministic solution is often faster and much less computationally-intensive than Monte Carlo for importance quantification. As a result, many hybrid methods opt to use deterministically-obtained importance functions to generate variance reduction parameters for Monte Carlo transport.

2.3 Automated Variance Reduction Methods for Local Solutions

The next several sections (2.3 through 2.5) describe different ways that deterministically-obtained importance functions can be applied to variance reduction methods in practice. Local variance reduction methods are those that optimize a tally response in a localized region of the problem phase-space. These types of problems may be the most immediately physically intuitive to a user, where a person standing x meters away from a source may wish

to know their personal dose rate. In this section, notable automated deterministically-driven variance reduction methods that have been designed for such localized response optimization are described. Recall that Booth's importance generator (Section 2.1.3) was also designed for localized tally results, but will not be elaborated upon here.

2.3.1 CADIS

In 1997, Haghighat and Wagner introduced the Consistent Adjoint-Driven Importance Sampling method (CADIS) [1, 3, 2] as a tool for automatic variance reduction for local tallies in Monte Carlo. CADIS was unique in that it used the adjoint solution from a deterministic simulation to consistently bias the particle distribution and particle weights. Earlier methods had not ensured the consistency between source biasing and particle birth weights. CADIS was applied to a large number of application problems and performed well in reducing the variance for local tallies [35].

The next several paragraphs present and discuss the theory supporting CADIS. Note that the theory presented is specific to space-energy CADIS, which is what is currently implemented in existing software. The original CADIS equations are based on space and energy $(\vec{r}, E)$ dependence, but not angle, so $\phi^\dagger$ can be used rather than $\psi^\dagger$. This does not mean that CADIS is not applicable to angle. This is merely a choice made by the software and method developers given the computational resources required to calculate and store full angular flux datasets, and the inefficiency that using angular fluxes might pose for problems where angle dependence is not paramount.

In trying to reduce the variance for a local tally, we aim to encourage particle movement towards the tally or detector location. In other words, we seek to encourage particles to induce a detector response while discouraging them from moving through unimportant regions in the problem. Recall from Eqs. (2.29) and (2.31) that the total system response can be expressed as either an integral of $\psi^\dagger q_e$ (the adjoint flux and the forward source), or $\psi\, q_e^\dagger$ (the forward flux and the adjoint source). Also recall that the adjoint solution is a measure for response importance.

To generate the biased source distribution for the Monte Carlo calculation, $\hat{q}$, should be related to its contribution to inducing a response in the tally or detector. It follows, then, that the biased source distribution is the ratio of the contribution of a cell to a tally response to the tally response induced from the entire problem. Thus, the biased source distribution for CADIS is a function of the adjoint scalar flux and the forward source distribtion q in region $\vec{r}, E$, and the total response R

$$\begin{aligned} \hat{q} &= \frac{\phi^\dagger(\vec{r}, E) q(\vec{r}, E)}{\iint \phi^\dagger(\vec{r}, E) q(\vec{r}, E) dE d\vec{r}} \\ &= \frac{\phi^\dagger(\vec{r}, E) q(\vec{r}, E)}{R}. \end{aligned} \tag{2.44a}$$

The starting weights of the particles sampled from the biased source distribution ($\hat{q}$) must be adjusted to account for the biased source distribution. As a result, the starting weights

are a function of the biased source distribution and the original forward source distribution:

$$\begin{aligned} w_0 &= \frac{q}{\hat{q}} \\ &= \frac{R}{\phi^\dagger(\vec{r}, E)}. \end{aligned} \tag{2.44b}$$

Note that when Eq. (2.44a) is placed into Eq. (2.44b), the starting weight is a function of the total problem response and the adjoint scalar flux in $\vec{r}, E$. The target weights for the biased particles are given by

$$\hat{w} = \frac{R}{\phi^\dagger(\vec{r}, E)}, \tag{2.44c}$$

where the target weight $\hat{w}$ is also a function of the total response and the adjoint scalar flux in region $\vec{r}, E$. The equations for $\hat{w}$ and w_0 match; particles are born at the same weight of the region they are born into. Consequently, the problem limits excessive splitting and roulette at the particle births, in addition to consistently biasing the particle source distribution and weights. This is the "consistent" feature of the CADIS method.

CADIS supports adjoint theory by showing that using the adjoint solution ($\phi^\dagger$) for variance reduction parameter generation successfully improves Monte Carlo calculation runtime. CADIS showed improvements in the FOM when compared to analog Monte Carlo on the order of 10^2 to 10^3, and on the order of five when compared to "expert" determined or automatically-generated weight windows [3, 4] for simple shielding problems. For more complex shielding problems, improvements in the FOM were on the order of 10^1 [1, 3]. Note that CADIS improvement is dependent on the nature of the problem and that these are merely illustrative examples.

2.3.2 Becker's Local Weight Windows

Becker's work in the mid- 2000s also explored generating biasing parameters for local source-detector problems [31]. Becker noted that in traditional weight window generating methods, some estimation of the adjoint flux is used to bias a forward Monte Carlo calculation. The product of this weight window biasing and the forward Monte Carlo transport ultimately distributed particles in the problem similarly to the contributon flux. In his work, Becker used a formulation of the contributon flux, as described in Eq. (2.32) to optimize the flux at the forward detector location. The relevant equations are given by Eqs. (2.45a) - (2.45f).

First, the scalar contributon flux ϕ^c, which is a function of space and energy is calculated with a product of the deterministically-calculated forward and adjoint fluxes, where

$$\phi^c(\vec{r}, E) = \phi(\vec{r}, E)\phi^\dagger(\vec{r}, E). \tag{2.45a}$$

This is then integrated over all energy to obtain a spatially-dependent contributon flux

$$\tilde{\phi}^c(\vec{r}) = C_{norm} \int_0^\infty \phi^c(\vec{r}, E) dE, \tag{2.45b}$$

where the normalization constant, C_{norm}, for a given detector volume, V_D, is:

$$C_{norm} = \frac{V_D}{\int_{V_D}\int_0^\infty \phi^c(\vec{r},E)dEdV}. \tag{2.45c}$$

The space- and energy-dependent weight windows are given by:

$$\bar{w}(\vec{r},E) = \frac{B(\vec{r})}{\phi^\dagger(\vec{r},E)}\,, \tag{2.45d}$$

where

$$B(\vec{r}) = \alpha(\vec{r})\tilde{\phi}^c(\vec{r}) + 1 - \alpha(\vec{r})\,, \tag{2.45e}$$

and

$$\alpha(\vec{r}) = \left[1 + \exp\left(\frac{\tilde{\phi}^c_{max}}{\tilde{\phi}^c(\vec{r})} - \frac{\tilde{\phi}^c(\vec{r})}{\tilde{\phi}^c_{max}}\right)\right]^{-1}. \tag{2.45f}$$

Becker found that this methodology compared similarly to CADIS for local solution variance reduction for a large challenge problem comprised of nested cubes. The particle density throughout the problem was similar between CADIS and Becker's local weight window. The FOMs were also relatively similar, but were reported only with Monte Carlo calculation runtimes (meaning that the deterministic runtimes were excluded). Note that Becker's method requires both a forward and an adjoint calculation to calculate the contributon fluxes, while CADIS requires only an adjoint calculation.

2.4 Automated Variance Reduction Methods for Global Solutions

Variance reduction methods for global solutions are designed to obtain an even distribution of error across several tallies or a tally map that spans the entire problem phase-space. The previous section detailed several methods that automate variance reduction for localized tallies. However, for global solutions these methods do not work well. The global tally suffers from a large range in variance across the physical problem space, and the solution is dependent on the flux distribution throughout the problem.

This section describes several methods that provide automated variance reduction for global solutions or multiple tallies. The general principle that these methods follow is that by distributing particles evenly throughout the Monte Carlo problem, a global tally will have approximately the same sample size in each region, resulting in a uniform variance across the tally. This often requires a forward deterministic solution to determine the density of forward particles throughout the problem, and subsequently using that forward distribution to aid in generating an importance map. This section summarizes the theory behind a number of existing global variance reduction methods. The section is concluded with a summary of how the methods performed and in which problems they performed well.

2.4.1 Cooper's Isotropic Weight Windows

Cooper and Larsen developed a weight window technique to reduce the variance of Monte Carlo global solutions [36] using a calculation of the forward flux from solutions obtained from diffusion, quasidiffusion [37], or pure Monte Carlo. In their work, Cooper and Larsen utilized a forward solution to the transport equation to generate weight window values to uniformly distribute particles throughout the problem. By doing so, the variance in the scalar flux remained relatively constant throughout the problem for a problem-wide tally, rather than rising significantly with increasing distance from the forward source. Cooper's "isotropic" weight windows (named because they were not dependent on $\hat{\Omega}$) dependent on $\vec{r}$ are given by:

$$\bar{ww}(\vec{r}) = \frac{\phi(\vec{r})}{\max \phi(\vec{r})} \,, \tag{2.46a}$$

$$ww(\vec{r})_{top} = \rho \bar{ww}(\vec{r}) \,, \tag{2.46b}$$

and

$$ww(\vec{r})_{bottom} = \frac{\bar{ww}(\vec{r})}{\rho} \,, \tag{2.46c}$$

where ρ is the weight window scaling factor. Note that by setting the weight window target value to be inversely proportional to the total flux in the cell, the density of particles throughout the problem ends up as roughly constant. Also note from Eq. (2.46a) that the weight windows are depend on space only.

In practice, Cooper's algorithm iteratively switches between solving the diffusion equation with transport correctors (Eddington factors described by [38]), and Monte Carlo solutions; this process is known as quasidiffusion [38, 37]. An initial quasidiffusion solution is used to generate weight windows, and then after a relatively short runtime, the Monte Carlo solution is used to generate updated Eddington factors for the quasidiffusion solution.

Because Cooper's method depends on Monte Carlo to generate the Eddington factors for the quasidiffusion problem, this method is limited by the iterative switch between the quasidiffusion solution and the Monte Carlo solution. The frequency with which this switching happens is entirely up to the user, but may drastically affect the efficiency of the method. Further, Cooper notes that we do not know at what point in time (for which number of N particles) the Monte Carlo solution becomes more accurate than the quasidiffusion solution, which is an important issue in choosing solution parameters.

2.4.2 Becker's Global Weight Windows

Becker, in addition to developing the local VR method discussed in Section 2.3.2, developed a global space-energy weight correction method both with (Section 2.5) and without directional biasing [39, 31]. Becker's global method uses a formulation of the space-dependent contributon flux, as with the local weight windows described in Section 2.3.2. For reference, those are defined in Eqs. (2.45a) and (2.45b).

Becker defines the spatially-dependent contributon flux parameter as $B(\vec{r})$, where

$$B(\vec{r}) = \tilde{\phi}^c(\vec{r}). \tag{2.47}$$

Becker's method defines a different adjoint source distribution depending on the response desired for the calculation. To optimize the flux the adjoint source is defined as:

$$q^\dagger(\vec{r}, E) = \frac{1}{\phi(\vec{r}, E)}. \tag{2.48a}$$

If the detector response is desired then

$$q^\dagger(\vec{r}, E) = \frac{\sigma_d(\vec{r}, E)}{\int_0^\infty \phi(\vec{r}, E)\sigma_d(\vec{r}, E)dE}, \tag{2.48b}$$

can be used instead. The space- and energy-dependent weight windows are then a function of the contributon flux, where

$$\bar{w}(\vec{r}, E) = \frac{B(\vec{r})}{\phi^\dagger(\vec{r}, E)}\ . \tag{2.49}$$

The process followed by Becker's global method uses two deterministic calculations to generate weight windows for the Monte Carlo calculation. First, the forward flux is calculated deterministically and used to construct the adjoint source distribution. After the adjoint solution is run, the contributon flux is calculated. The contributon flux and the adjoint flux are then used to construct the weight windows.

Becker's method aims to distribute response evenly throughout the problem. However, like FW-CADIS (discussed below in Section 2.4.3), the global response weight windows are proportional to the forward response,

$$\bar{w}(\vec{r}, E) \propto \frac{\int \sigma(\vec{r}, E)\phi(\vec{r}, E)dE}{\sigma(\vec{r}, E)} \tag{2.50}$$

rather than the forward flux as in Cooper's method, where $\bar{w}(\vec{r}, E) \propto \phi(\vec{r}, E)$.

In implementation, both Becker and Cooper's global methods undersampled the source (in comparison to FW-CADIS, which will be described in Section 2.4.3) for a specified calculation time. However, Becker's method sampled $\sim$1/3 the number of particles that Cooper's method did. Notably, Becker's method did obtain better relative uncertainties for low flux-regions in the problem.

2.4.3 FW-CADIS

In 2007, Peplow, Blakeman, and Wagner [40] proposed three methods by which variance reduction could be decreased in global mesh tallies in deep-penetration radiation transport problems. The first method, using a CADIS calculation where the adjoint source is defined at the problem boundary, aimed at moving particles outward to the problem edges. The second

method used standard CADIS, but instead defined each cell as equally important, so the adjoint source was defined equally throughout the problem phase-space. The last method, called Forward-Weighted CADIS (FW-CADIS), distributed the adjoint source across mesh cells as an inverse relation to the forward response of the cell. In their work, Peplow et al. found that the first method had large uncertainties in areas of the problem far from the boundary; the second method performed slightly, but not significantly, better than analog; and the third method had the most uniform uncertainty distribution.

FW-CADIS [5, 6, 41] built off of the work by Cooper and the CADIS method. Like Becker's method, FW-CADIS uses a forward deterministic calculation to determine the source distribution for the adjoint calculation. Unlike Becker's method, which used contributon fluxes to construct weight windows, the CADIS method uses adjoint fluxes as the basis of the weight window values. Similar to Cooper's method, however, FW-CADIS uses the forward calculation to determine how to evenly distribute particles throughout the problem. Like CADIS, FW-CADIS uses the adjoint solution from the deterministic calculation to generate consistent source biasing, weight windows, and particle birth weights.

The adjoint source for the adjoint calculation is dependent on the desired response for the system. The generic description for the adjoint source is given by Eq. (2.51) and more specific parameters are given by Eqs. (2.52a)-(2.52c). First, we can describe a general form of the adjoint source definition for all phase-space, P, as:

$$q^{\dagger}(P) = \frac{\sigma_d(P)}{R}. \tag{2.51}$$

Thus the adjoint source is dependent on the detector (or tally) cross-section and whatever response is being calculated in the system. Depending on whether the response is a flux or a dose rate, the adjoint source will differ. For example, the adjoint source for the spatially dependent global dose, $\int \phi(\vec{r}, E)\sigma_d(\vec{r}, E)dE$ is:

$$q^{\dagger}(\vec{r}, E) = \frac{\sigma_d(\vec{r}, E)}{\int \sigma_d(\vec{r}, E)\phi(\vec{r}, E,)dE}. \tag{2.52a}$$

The adjoint source for the spatially dependent total flux $\int \phi(\vec{r}, E)dE$ is:

$$q^{\dagger}(\vec{r}) = \frac{1}{\int \phi(\vec{r}, E)dE}. \tag{2.52b}$$

Last, the adjoint source for the energy- and spatially- dependent flux $\phi(\vec{r}, E)$ is:

$$q^{\dagger}(\vec{r}, E) = \frac{1}{\phi(\vec{r}, E)}. \tag{2.52c}$$

The process followed by FW-CADIS is to initially run a deterministic forward calculation to obtain the forward response. This solution is used to create the source distribution for the adjoint problem. A second deterministic calculation is run to obtain the adjoint solution. The adjoint solution is then used to generate variance reduction parameters in the same manner as CADIS.

2.4.4 Other Notable Methods

Baker and Larsen showed that the exponential transform can be used to generate VR parameters for global low-variance solutions in Monte Carlo [42]. In this work, Baker used a forward diffusion solution to generate parameters for a combination of VR techniques: implicit capture and weight cutoff, geometry splitting / rouletting with implicit capture and weight cutoff, and the exponential transform combined with implicit capture and a weight cutoff. The exponential transform method was then compared to the other combinations of VR techniques to quantify its success. In their work, Baker and Larsen found that the exponential transform approach did not work well for highly scattering problems, where geometry splitting and Russian roulette were generally better options. Their work did not focus on generating weight window values, nor was it tested on deep-penetration shielding problems.

While the aforementioned methods in this and the previous sections use deterministically-obtained solutions to generate importance maps, it should be noted that not all methods use this approach. Booth and Hendricks' methods used initial Monte Carlo calculations to reduce the relative error in tallies. Two methods in the global variance reduction realm are notable in that they too use Monte Carlo estimates of the flux to generate variance reduction parameters [44, 43]. Van Wijk et al. [44] developed an automated weight window generator that used a Monte Carlo calculation of the forward flux to generate weight window values. The weight window target values could be determined based on either a flux-centered scheme like Cooper's (Eq. (2.46a)) or by using a ratio of the square roots of the fluxes. The second method is a combination of Cooper's weight window target values and knowing that the relative error in a region is proportional to the square root of the number of particles. Van Wijk et al. applied their methods to a PWR facility and observed a FOM increase by a factor of >200 when compared to analog Monte Carlo. However, as with other Monte Carlo-generated VR parameters, for deep-penetration problems this approach relies on adequate sampling of all phase-space, which could be computationally prohibitive.

The Method of Automatic Generation of Importances by Calculation (MAGIC) method was proposed in parallel by Davis and Turner [43]. As with Van Wijk's method, the MAGIC method uses an analog forward Monte Carlo –potentially with several iterations–calculation to generate weight windows. The initial Monte Carlo runs used to generate the importance map took less time to converge by using multigroup (rather than continuous energy) cross section data as well as energy cutoffs. MAGIC converged on a finalized importance map by iteratively running several lower-fidelity Monte Carlo calculations.

Davis and Hendricks compared three variants of MAGIC to FW-CADIS in ITER fusion energy systems. These three variants used different weight window adjustments for importances: weight windows in cells based on existing weight information, weight windows in mesh cells based on flux information, and weight windows in cells based on population density. It was concluded that the most effective method for variance reduction of those proposed in the paper was MAGIC's weight window in mesh cells based on flux information. In this case, FW-CADIS' FOM was 65% that of MAGIC's. This compared similarly to Van

Wijk's method, where the flux-based results continued improving the FOM as the computational time increased. The authors did not make it clear how many iterations were required, on average, to generate the finalized weight window map or if the time to iteratively generate the importance map was included in the FOM. While FW-CADIS' FOM was lower than MAGIC's, FW-CADIS had the highest fraction of cell voxels with very low relative errors.

Peplow et al. [45] compared the performance of Cooper's method, Van Wijk's method, Becker's method, and FW-CADIS across a number of shielding calculations. For a simple shielding problem, FW-CADIS had the shortest runtime, which included the forward and adjoint deterministic runtimes, and had a FOM 80x higher than the analog calculation, and more than 3x higher than the next best hybrid method. Van Wijk's method was the only method other than FW-CADIS to pass all statistical convergence checks for the problem, but its reported FOM was lower than either Becker's method or FW-CADIS. In a second deep penetration shielding problem, FW-CADIS was the only method that passed all statistical convergence checks. FW-CADIS also had the highest reported FOM for this problem. The timing for all of the methods were comparable. Peplow et al. also ran two "challenge" problems. As with the first two problems, FW-CADIS outperformed the other methods and passed all statistical checks. Becker's method was consistently comparable to FW-CADIS in reported FOMs, but only passed all of the statistical checks in a single challenge problem. Becker's method also performed relatively better than the other methods in deep-penetration challenge problems.

The ubiquity and continued development of global variance reduction methods illustrates the need and desire for them in the nuclear engineering community. Some of the methods discussed in this section–including Becker's global weight windows, Cooper's weight windows, Van Wijk's method, and FW-CADIS–have been applied to large application problems and compared to other methods. All of the methods reduce the time to a "good" solution–thus improving the final FOM–when compared to analog Monte Carlo. When compared against one another, FW-CADIS consistently outperforms the other methods.

2.5 Automated Angle-Informed Variance Reduction Methods

In a number of problems, the angular dependence of the flux is significant enough that biasing in space and energy exclusively is not sufficient. As a result, a subset of hybrid methods were developed to incorporate some degree of the flux anisotropy in variance reduction parameters. Without explicitly calculating the angular flux, which is memory- and storage-intensive, methods attempted to approximate the angular flux using other information more readily accessible to them. These approaches are broadly categorized as methods that bias using population control methods (such as weight windows), and methods that bias with modified sampling methods (such as the exponential transform). Initial approaches to angular biasing focused on approximating the angular flux, ψ, as a separable function of the scalar flux

and an angle-dependent multiplier. These approximations of the flux were then used to generate biasing parameters dependent on angle for highly angular-dependent problems. In this section, methods that generate variance reduction parameters dependent on angle or that include angular information are described.

2.5.1 Angular Biasing with Population Control Methods

2.5.1.1 AVATAR

The AVATAR [17, 46] (Automatic Variance and Time of Analysis Reduction) method generates three-dimensional, space-, energy- and angle-dependent weight windows for Monte Carlo. The implementation of AVATAR by the authors uses a relatively course-mesh and few-angle deterministic calculation in THREEDANT, approximating the angular flux as a function of the scalar flux, and then subsequently passes those flux values through a postprocessing code, Justine, to generate weight windows for MCNP [8]. The AVATAR approach to determining the angular flux uses an approximation of the angular flux based on the maximum entropy distribution, which is briefly summarized in the next few paragraphs.

Information Theory

First, for a given set of discrete values x_i, $i = 1, 2, \cdots n$ that are passed to a function, $f(x)$, the expectation value of that function is given by

$$\big\langle f(x) \big\rangle = \sum_{i=1}^{n} p_i f(x_i). \tag{2.53}$$

For the probability distribution $p_i = p(x_i)$, $i = 1, 2, \cdots n$, the entropy of p is defined as

$$H(p) = -K \Sigma_i p_i \ln p_i \,, \tag{2.54}$$

where K is a positive constant. A proof that this is indeed the associated maximal entropy associated with all p_i is given in [47]. For a continuous probability density function $p(x)$ over the interval I, the entropy of the continuous function is

$$H(p) = -K \int_I p(x) \ln p(x) dx. \tag{2.55}$$

To maximize either of these distributions, while also maintaining that $\Sigma p_i = 1$, one can use Lagrangian multipliers λ and μ

$$p_i = e^{-\lambda - \mu f(x_i)}. \tag{2.56}$$

This set of equations can be solved using

$$\big\langle f(x) \big\rangle = -\frac{\partial}{\partial \mu} \ln Z(\mu) \,, \tag{2.57a}$$

and

$$\lambda = \ln\left[Z(\mu)\right], \tag{2.57b}$$

where

$$Z(\mu) = \Sigma_i e^{-\mu f(x_i)}. \tag{2.57c}$$

Jaynes [47, 48] showed that the maximum entropy probability distribution function corresponding to the previous equations is given by

$$p_i = \exp\left[-\left(\lambda_0 + \lambda_1 f_1(x_1) + \cdots + \lambda_m f_m(x_i)\right)\right], \tag{2.58}$$

and the entropy of this distribution is given by

$$S_{max} = \lambda_0 + \lambda_1\big\langle f_1(x)\big\rangle + \cdots + \lambda_m\big\langle f_m(x)\big\rangle. \tag{2.59}$$

In this case, the constant K from Eq. (2.54) has been set to 1.

The maximum entropy approach to calculating a probability distribution function is an attractive option given limited information about that distribution. This method's power lies in that it deduces a function given limited information, but does not place too great of an importance on missing or unwarranted information. Furthermore, a distribution ascertained from this methodology will encompass all distributions with smaller entropies that satisfy the same constraints. Thus, the method provides the most widely applicable probability distribution function for the system that has been defined.

Moskalev showed that by using the maximum entropy approach, a distribution function could be reconstructed from a (truncated) Legendre expansion [49]. This is particularly applicable to radiation transport because scattering terms are often truncated Legendre expansions. In his application, Moskalev derived a generalized form of reconstructing a probability distribution from a truncated expansion, where the true function represented by a Legendre polynomial series,

$$f(L,\mu) = \sum_{l=0}^{L} -\frac{2l+1}{2} f_l P_l(\mu)\,, \tag{2.60}$$

could be associated with an adjusted function (obtained from maximizing the entropy of the known values),

$$\tilde{f}(L,\mu) = \exp\big(\sum_{l=0}^{L} \lambda_l P_l(\mu)\big)\,, \tag{2.61}$$

such that

$$(f, P_l) = (\tilde{f}, P_l); \quad l = 0, \cdots, L. \tag{2.62}$$

Here, λ_l are the Lagrange multipliers, $\tilde{f}$ and f are $\in \phi$, and are assumed to be a function of μ such that $f(\mu) \geq 0, \mu \in [-1, 1]$. These generalized equations were then applied to group-to-group scattering probability distribution functions, as well as reconstructing a $L = 3$ function. The reconstruction showed agreement except near the extrema of μ.

Walters and Wareing [51, 50] showed that the angle-dependent source definition for a discrete ordinates transport problem could be calculated using Moskalev's approach [49]. In their method, they used this approach to reconstruct the source distribution of particles in each cell from the source moments. For standard methods, the source in a cell expanded in Legendre moments is

$$S_m(x) = S_{m,j}\left[P_0(x) + \frac{S^x_{m,j}}{S_{m,j}}P_1(x)\right], \tag{2.63}$$

where $S_{m,j}$ is the average source in cell j, direction m, $S^x_{m,j}$ is the $P_1(x)$ moment of the source, and the P_0 and P_1 are the associated Legendre polynomials. Using a normalized source distribution $s_m(x)$ where

$$S_m(x) = s_m(x)S_{m,j},$$

and the normalized distribution is

$$s_m(x) = \left[s_0 + s_1P_1(x)\right]. \tag{2.64}$$

In this equation, s_0 and s_1 are the zeroth and first Legendre moments of the source, respectively. The source distribution derived from the maximum entropy distribution is

$$\tilde{s}(x) = \frac{\lambda_{1,k}}{\sinh(\lambda_{1,j})}\ e^{\lambda_{1,j}P_1(x)}. \tag{2.65}$$

$\tilde{s}$ has normalized Legendre moments s_0 and s_1 that match $s_m(x)$. Because $\tilde{s}$ satisfies the information that can be obtained about s_m, it can be used to reconstruct $S_m(x)$:

$$S_m(x) = \tilde{s}_m(x)S_{m,j}. \tag{2.66}$$

$\lambda_{1,j}$ can be found with

$$s_1 = 3\left[\coth(\lambda_{1,j} - \frac{1}{\lambda_{1,j}})\right]. \tag{2.67}$$

It should be noted that the same methodology that Walters and Wareing use to reconstruct the source distribution from the source moments can be used to reconstruct the angular flux in cells based on moments of the angular flux (i.e. the scalar flux and current) [51].

In their paper, Walters and Wareing [50] suggested that in place of solving Eq. (2.67) for $\lambda_{1,j}$, that a rational polynomial be used in its place to reduce computational time. The suggested polynomial for $0 \leq \lambda_{1,j} \leq 5$ is:

$$\lambda_{1,j} = \frac{2.99821(\frac{s_{1,j}}{3}) - 2.2669248(\frac{s_{1,j}}{3})^2}{1 - 0.769332(\frac{s_{1,j}}{3}) - 0.519928(\frac{s_{1,j}}{3})^2 + 0.2691594(\frac{s_{1,j}}{3})^3}, \tag{2.68}$$

and for $\lambda \geq 5$:

$$\lambda_{1,j} = \frac{1}{1-\bar{\mu}}. \tag{2.69}$$

A full derivation of Eq. (2.67) and how it satisfies the maximum entropy requirements can be found in Appendix A of Ref. [50].

In their application, Walters and Wareing found that this method was accurate over a fairly course mesh for the problems analyzed, and the computed fluxes remained positive over the solution space. When compared to other methods, this approach performed much better on coarse meshes. However, the analysis was limited to 1D problems. As mesh size grew finer, the method performed similarly to other methods. Near vacuum boundary conditions, $\lambda_{1,j} \to \infty$ at the cell boundary, causing issues in calculating the flux in these cells.

AVATAR Implementation

AVATAR uss a deterministically-obtained solution of the adjoint scalar flux and adjoint currents to reconstruct the angular flux distribution. The angular flux distribution is then used to generate weight windows. AVATAR built off of the methodology described by Walters and Wareing [51, 50], but instead of reconstructing the source distribution inside the cell, the maximum entropy method was used to reconstruct the angular fluxes. Thus the angular flux, ψ, was reconstructed with the scalar flux, ϕ, and the current, J.

AVATAR avoided generating explicit angular fluxes with THREEDANT by assuming that the adjoint angular flux is symmetric about the average adjoint current vector, $J^\dagger$:

$$\psi^\dagger(\hat{\Omega}) = \psi^\dagger(\hat{\Omega} \cdot n)\,, \tag{2.70a}$$

where

$$n = \frac{J^\dagger}{\|J^\dagger\|}. \tag{2.70b}$$

Note that n, J, ψ, and ϕ all have implied dependence on $(\vec{r}, E)$. The angular flux could then be reconstructed assuming that the angular flux is a product of the scalar flux and some angle-dependent function

$$\psi^\dagger(\hat{\Omega} \cdot n) = \phi^\dagger f(\hat{\Omega} \cdot n). \tag{2.70c}$$

Note that Eq. (2.70c) takes the form of Eq. (2.66). Thus f is derived from the maximum entropy distribution:

$$f(\hat{\Omega} \cdot n) = \frac{\lambda e^{(\hat{\Omega} \cdot n)\lambda}}{2 \sinh \lambda}\,, \tag{2.70d}$$

and λ is a function of the average cosine $\bar{\mu}$

$$\begin{aligned} \lambda &= \frac{2.99821\bar{\mu} - 2.2669248\bar{\mu}^2}{1 - 0.769332\bar{\mu} - 0.519928\bar{\mu}^2 + 0.2691594\bar{\mu}^3} \\ &= \frac{1}{1 - \bar{\mu}} \end{aligned} \tag{2.70e}$$

for $0 \leq \bar{\mu} < 0.8001$ and $0.8001 \leq \bar{\mu} < 1.0$, respectively. Also, μ is given by

$$\bar{\mu}(\vec{r}, E) = \frac{\left\| J^{\dagger}(\vec{r}, E) \right\|}{\phi^{\dagger}(\vec{r}, E)}. \tag{2.70f}$$

Equations (2.70e) and (2.70f) are exact in both isotropic and streaming conditions [17].

Using the calculation of the angular flux described in Eqs. (2.70a) through (2.70f), angle-dependent weight windows can be constructed. AVATAR's space- energy- and angle-dependent weight window is given by

$$\bar{w}(\vec{r}, E, \hat{\Omega}) = \frac{k}{\phi^{\dagger}(\vec{r}, E) f(\hat{\Omega} \cdot n)}, \tag{2.71}$$

where k is a constant that can be adjusted to match the source distribution. In the case of AVATAR, k was used as a normalization factor to ensure that source particles are born with weights within the weight window. AVATAR exclusively generated weight windows, and did not attempt to consistently bias the source distribution. Physically, the assumption behind AVATAR is that the adjoint angular flux is locally one-dimensional, so azimuthal symmetry is assumed.

AVATAR Results

The authors of AVATAR showed that AVATAR's angularly-dependent weight windows improved the FOM (from 5x to 7x) for a multiple-tally well-logging problem compared to the MCNP weight window generator. AVATAR was also compared to other methods in subsequent papers [16]. In an update of the MCNP weight window generator, AVATAR was compared to variants of the weight window generator and had a FOM of 79 while variants of the weight window generator had FOMs ranging from 105 to 119 [16]. However, the MCNP weight window generator required multiple iterations of Monte Carlo transport to converge on weight window values while AVATAR did not. Total runtimes for iteratively converging on weight window values were in the 200 to 300 minute range, while AVATAR took roughly 5 minutes to converge on weight window values for the problem. Whether these calculations were performed in serial or parallel were not discussed.

The MCNP weight window generator has also been adapted to use weight window values seeded by a solution from AVATAR [16]. This method had FOMs comparable to the default MCNP weight window generator, but only required 1 iteration to converge rather than 3. This reduced the total transport runtime from roughly 260 minutes to 140 minutes, but still required user experience and input to adequately set up and prepare the deterministic input for AVATAR.

The method used by AVATAR to produce angle-dependent weight windows successfully incorporated angular information into variance reduction parameters for Monte Carlo with very little additional computational burden. However, because AVATAR was not fully automated, the user had to have knowledge on the use of the S_N deterministic solver in addition

to the Monte Carlo methods they were trying to optimize. As a result, the user needed to adequately prepare the deterministic inputs, correctly specify the adjoint source for the deterministic solve, and then pass these values to postprocessing software [52, 16]. The FOMs reported with AVATAR did not incorporate the additional time required for user setup and preparation of inputs. Though this is not a customary time inclusion, the burden of time for this process may be significant. Though more computationally efficient than the weight window generator, this aspect of AVATAR may be too substantive of an obstacle for new-user approachability. Further, it leaves more room for user-induced error.

The AVATAR method [17, 46] used an approximation of the angular flux–without explicitly calculating it–to generate angle-dependent weight windows. It operated with the approximation that the angular flux was separable and symmetric about the average current vector. The angular flux was then calculated using a product of a deterministically-obtained scalar flux and an exponential function, derived from the maximum entropy distribution, that was a function of the scalar flux and the current. Space-, energy-, and angle-dependent weight windows for the Monte Carlo problem were then generated from the inverse of the angular flux. AVATAR improved the FOM for sample problems from 2 to 5 times, but did not apply to problems where the flux was not azimuthally symmetric.

2.5.1.2 Simple Angular CADIS

Simple Angular CADIS [52] is built on the theory of CADIS and FW-CADIS, but incorporates angular information in the methods. Simple Angular CADIS does so without explicitly using angular flux solutions from the deterministic solution. Instead, the method reconstructs the angular flux in the same manner employed by AVATAR, and additionally consistently biases the source distribution with the weight windows using the same methodology as CADIS and FW-CADIS. Recall that the original implementation of AVATAR did not have consistent source biasing. In their work, Peplow et al. implemented simple angular CADIS in MAVRIC, a hybrid methods software package distributed with the SCALE codebase [27]. The Simple Angular CADIS method was implemented with two different approaches to variance reduction: directionally-dependent weight windows with directionally-dependent source biasing and directionally-dependent weight windows without directional source biasing.

Theory

The Simple Angular CADIS approach, like AVATAR, uses a reconstruction of the angular flux derived from the maximum entropy distribution (Section 2.5.1.1). In Simple Angular CADIS, the authors approximate the adjoint angular flux such that

$$\psi^{\dagger}(\vec{r}, E, \hat{\Omega}) \cong \phi^{\dagger}(\vec{r}, E)\frac{1}{2\pi}f(\hat{\Omega}\cdot\hat{n})\,, \tag{2.72}$$

where $f(\hat{\Omega}\cdot\hat{n})$ is given by the same Eqs. (2.70d), (2.70e), (2.70f) as AVATAR. Note that this differs from AVATAR's reconstruction of the angular flux, Eq. (2.70a), by a factor of $1/2\pi$.

As it was only dependent on μ, AVATAR's original approach assumed azimuthal symmetry, but did not incorporate any factor of integration into the angular flux reconstruction. By including the azimuthal integration factor of $1/2\pi$, this version of $\psi^\dagger$ satisfies

$$\phi^\dagger(\vec{r}, E) = \int \phi^\dagger \frac{1}{2\pi} f(\hat{\Omega} \cdot \hat{n}) d\hat{\Omega}.$$

The corresponding angle-dependent weight windows are then given by:

$$\bar{w}(\vec{r}, E, \hat{\Omega}) = \frac{2\pi k}{\phi^\dagger(\vec{r}, E) f(\hat{\Omega} \cdot n)} \,. \tag{2.73}$$

For the variant method with directionally-dependent weight windows and without directional source biasing, the biasing parameters are given by Eqs. (2.74). The biased source distribution, $\hat{q}(\vec{r}, E, \hat{\Omega})$, is given by a combination of the standard CADIS biased source, $\phi^\dagger(\vec{r}, E)$ and the original directional source distribution, $q(\hat{\Omega} \cdot \hat{d})$ such that

$$\begin{aligned} \hat{q}(\vec{r}, E, \hat{\Omega}) &= \frac{1}{R} q(\vec{r}, E) \phi^\dagger(\vec{r}, E) \frac{1}{2\pi} q(\hat{\Omega} \cdot \hat{d}) \\ &= \hat{q}(\vec{r}, E) \frac{1}{2\pi} q(\hat{\Omega} \cdot \hat{d}). \end{aligned} \tag{2.74a}$$

The direction $\hat{d}$ is sampled using the original directional source distribution $q(\hat{\Omega} \cdot \hat{d})$. The birth weight matches standard CADIS with

$$\begin{aligned} w_0(\vec{r}, E, \hat{\Omega}) &= \frac{q(\vec{r}, E, \hat{\Omega})}{\hat{q}(\vec{r}, E, \hat{\Omega})} \\ &= \frac{R}{\phi^+(\vec{r}, E)}, \end{aligned} \tag{2.74b}$$

and the weight window target value is given by

$$\begin{aligned} \bar{w}(\vec{r}, E, \hat{\Omega}) &= \frac{R}{\phi^\dagger(\vec{r}, E)} \frac{f(\hat{\Omega}_0 \cdot n(\vec{r_0}, E_0))}{f(\hat{\Omega} \cdot n)} \\ &= \bar{w}(\vec{r}, E) \frac{f(\hat{\Omega}_0 \cdot n(\vec{r_0}, E_0))}{f(\hat{\Omega} \cdot n)}. \end{aligned} \tag{2.74c}$$

Note that the biased source distribution, $\hat{q}(\vec{r}, E, \hat{\Omega})$, is a function of the biased source distribution from standard space- energy-CADIS and of the original directional source distribution. This is why this method has directional weight windows, but not directional source biasing. For the second method, with directionally-dependent weight windows and with directional source biasing, the biasing parameters are given by the equations summarized in Eqs. (2.75). The biased source distribution is given by a combination of the space-energy biased source

distribution, the original directional source distribution, and a directionally-dependent biased source distribution, $f(\hat{\Omega} \cdot \hat{n_0})$, such that

$$\begin{aligned}\hat{q}(\vec{r}, E, \hat{\Omega}) &= \frac{1}{Rc} q(\vec{r}, E, \hat{\Omega}) \phi^{\dagger}(\vec{r}, E, \hat{\Omega}) \\ &= \left[\frac{1}{R} q(\vec{r}, E) \phi^{\dagger}(\vec{r}, E)\right] \left[\frac{1}{c} \frac{1}{2\pi} q(\hat{\Omega} \cdot \hat{d}) \frac{1}{2\pi} f(\hat{\Omega} \cdot n_0)\right] \\ &= \hat{q}(\vec{r}, E) \left[\frac{1}{c} \frac{1}{2\pi} q(\hat{\Omega} \cdot \hat{d}) \frac{1}{2\pi} f(\hat{\Omega} \cdot n_0)\right].\end{aligned} \tag{2.75a}$$

The constant c is given by

$$c = \int \frac{1}{2\pi} q(\hat{\Omega} \cdot \hat{d}) \frac{1}{2\pi} f(\hat{\Omega} \cdot n_0) d\hat{\Omega}. \tag{2.75b}$$

The birth weights are also a function of direction, where

$$\begin{aligned}w_0(\vec{r}, E, \hat{\Omega}) &= \frac{q(\vec{r}, E, \hat{\Omega})}{\hat{q}(\vec{r}, E, \hat{\Omega})} \\ &= \frac{R}{\phi^{+}(\vec{r}, E)} \frac{2\pi c}{f(\hat{\Omega} \cdot n_0)},\end{aligned} \tag{2.75c}$$

as are the target weights

$$\begin{aligned}\bar{w}(\vec{r}, E, \hat{\Omega}) &= \frac{R}{\phi^{\dagger}(\vec{r}, E)} \frac{2\pi c}{f(\hat{\Omega} \cdot n_0)} \\ &= \bar{w}(\vec{r}, E) \frac{2\pi c}{f(\hat{\Omega} \cdot n)}.\end{aligned} \tag{2.75d}$$

Details about how the aforementioned equations were practically implemented are detailed in Ref. [52]. The motivated reader may explore this reference for details on the calculation of λ, $\bar{\mu}$, $\left\|J^{\dagger}(\vec{r}, E)\right\|$, and $f(\hat{\Omega} \cdot \hat{n_0})$

Results

To test these two modifications of CADIS, the authors ran a number of test problems and compared them against standard implementations of CADIS and analog Monte Carlo runs. For a spherical boat test problem, Simple Angular CADIS without directional biasing improved the FOM by a factor of 2 to 3. Note that because the source is monodirectional, directional source biasing was not compared. Simple Angular CADIS with- and without-directional source biasing improved the FOM for active interrogation sample problems and for simple duct streaming problems. The methods did not improve the FOMs for sample problems using a neutron porosity tool or a gamma-ray litho-density tool.

The range in performance for angle-dependent problems was explained by the authors as a failure of the angular flux approximation to capture the true distribution of the angular flux. Because Simple Angular CADIS uses the same approximation in calculating the angular flux (Eq. (2.72)) as AVATAR, it is limited in the types of anisotropy that it can capture. As a result, the biasing parameters for a problem are unlikely to adequately reflect the flux distribution in problems where the flux is not captured effectively by the P_1 expansion.

The authors also noted that because the weight window is dependent on space/energy/angle, the source birth weights only matched the weight window target values at a specific point in the weight window region. If the weight window covered a substantial region of phase-space, this could result in particle birth weights that do not adequately correspond to the importance of the region that they are born into, resulting in increased runtime and a more computationally-intensive calculation.

2.5.1.3 Cooper's Weight Windows

Cooper and Larsen, in addition to generating global isotropic weight windows from a deterministic forward solution (as described in Section 2.4.1), also developed angle-dependent weight windows [36]. Here, the forward angular flux is calculated in a similar manner as the AVATAR method, where the angular flux is a product of the scalar flux and an angle-dependent function. In this case, the adjustment factor also includes a factor of 4π,

$$\psi(\vec{r},\hat{\Omega}) \approx A(\vec{r})e^{\vec{B}(\vec{r})\cdot\hat{\Omega}}, \tag{2.76a}$$

where $A(\vec{r})$ and $\vec{B}(\vec{r})$ are given by:

$$A(\vec{r}) = \frac{\phi(\vec{r})}{4\pi}\frac{B(\vec{r})}{\sinh B(\vec{r})} \tag{2.76b}$$

$$\vec{B}(\vec{r}) = B(\vec{r})\frac{\vec{\lambda}(\vec{r})}{\left|\vec{\lambda}(\vec{r})\right|} \tag{2.76c}$$

and

$$\lambda(\vec{r}) = \coth B(\vec{r}) - \frac{1}{B(\vec{r})}. \tag{2.76d}$$

If both $A(\vec{r})$ and $\vec{B}(\vec{r})$ are inserted into the equation for $\psi(\vec{r},\hat{\Omega})$, Eq. (2.76a), the formulation will be very similar to AVATAR's reconstruction of the angular flux. However, Cooper's method differs from AVATAR in the calculation of $\lambda(\vec{r})$. Cooper noted that $\lambda(\vec{r})$ could be estimated with either the scalar fluxes and currents from a fairly low-cost quasidiffusion calculation,

$$\begin{aligned}\lambda_i(\vec{r}) &= \frac{J_i(\vec{r})}{\phi(\vec{r})} \\ &= \frac{1}{\Sigma_{tr}(\vec{r})\phi(\vec{r})}\frac{\partial}{\partial r_j}E_{ij}(\vec{r})\phi(\vec{r}) \,,\end{aligned} \tag{2.76e}$$

or with the scalar fluxes and currents directly from the Monte Carlo solution (recall that $E_{ij}(\vec{r})$ is the Eddington factor described in Section 2.4.1). Cooper noted that because Monte Carlo robustly calculates these values, it is the more optimal choice. After obtaining these values from the deterministic calculation, Cooper's angle-dependent weight window could be calculated with

$$ww_{i,j}(\hat{\Omega}) = \frac{\psi_{i,j}(\vec{r},\hat{\Omega})}{max\phi_{i',j'}/4\pi}. \tag{2.76f}$$

As mentioned in Section 2.4.1, Cooper's method was limited in that it used an iterative quasidiffusion / Monte Carlo solution to generate the biasing parameters for the problem. This method was not automated; and the ideal frequency between iterations was never explored. However, Cooper showed in two-dimensional example problems that the angularly-dependent weight windows significantly improved the figure of merit as compared to analog Monte Carlo. The distributions of the FOM and the resulting tally were also much smoother with the approach described in their work. Further, the angular weight windows performed slightly better than the isotropic weight windows in evenly distributing the particles, even in problems where the anisotropy was not significant. However, like AVATAR, this method is limited in the types of anisotropy it can quantify due to the approximations it uses to reconstruct the angular flux. In generating the estimates for $\vec{\lambda}$, the authors found that using a quasidiffusion estimate was more efficient than using Monte Carlo estimates, likely because the estimates of the factors could be periodically updated as the solution iteratively converged.

2.5.2 Angular Biasing Using the Exponential Transform

2.5.2.1 Early Work

As discussed in Section 2.1.2, the exponential transform is a modified sampling method that adjusts the distance-to-collision in Monte Carlo transport to encourage particle transport in preferential regions. This is done by modifying the sampled cross section. Recall from Eq. (2.21) that the exponential transform is dependent on a transform parameter p and the cosine angle μ, such that $\Sigma_t^* = \Sigma_t(1 - p\mu)$. When used without angle biasing,

$$\psi_g^\dagger(r,\Omega) \approx e^{\Sigma_t \lambda \cdot r}\ , \tag{2.77}$$

the exponential transform can have undesirable weight fluctuations [2], especially as the number of collisions to reach a tally increases [53]. Eq. (2.77) shows that the importance function (the adjoint flux) can be approximated as an exponential function varying in space, dependent on the total cross section Σ_t, distance traveled r, and a parameter defining the amount and direction of biasing λ.

Dwivedi [54] showed that by adding an angle-dependent collision biasing scheme in addition to the exponential transform, the problematic weight fluctuations could be mitigated.

The collision biasing scheme introduced with the exponential transform takes the form

$$\psi_g^{\dagger}(r,\Omega) \approx \frac{\sigma_{s,0} e^{\Sigma_t \lambda \cdot r}}{4\pi\sigma_t(1-\lambda\cdot\Omega)}. \tag{2.78}$$

Note that the ratio of cross sections outside of the exponential function $\sigma_{s,0}/\sigma_t$, where $\sigma_{s,0}$ is the zeroth moment of the scattering cross section, the ratio of the cross sections is the survival probability in an interaction event, and the $(1-\lambda\cdot\Omega)$ term is consistent with the weight adjustment required for the exponential transform (Eq. (2.1.2)). This was applied to a monoenergetic problem with slab geometry and isotropic scattering, and the variance was reduced by a factor of more than 100 when compared with other exponential transform methods.

Gupta and Dwivedi's subsequent work [53] adjusted the factor described in the preceding paragraph by applying the exponential transform with angle biasing to deep-penetration problems with anisotropic scattering. The authors did not explicitly use the true distribution for anisotropic scattering, but rather chose to approximate the biased kernel to be a function of the isotropic angular distribution. The authors observed a reduction in the variance by a factor of 10, but they acknowledged that, while the combination of the biased kernel and exponential biasing reduced weight fluctuations, it also had the potential to introduce other weight fluctuations due to anisotropies in the flux.

Ueki and Larsen [55] generalized Dwivedi's importance transform and applied it to isotropic, linearly anisotropic, and quadratically anisotropic scattering. They observed that Dwivedi's method and the generalized Dwivedi method outperformed non-angle-dependent exponential biasing for all types of scattering, and that their generalized method outperformed Dwivedi's original method in higher order scattering. The work of Dwivedi, Gupta, Ueki and Larsen was applied and each compared with one-dimensional sample problems. Ueki and Larsen pointed out that their method could be extended to three-dimensional problems using Turner and Larsen's methodology (described in Section 2.5.2.2) [55].

In 1985, Henricks and Carter [56] described a method by which photon transport could be biased in angle with an exponential transform adjustment factor. In this study, the authors performed studies on three test problems with the exponential transform adjustment factor and with a synergistic angular bias and exponential transform adjustment. In all studies, the synergistic biasing outperformed the exponential transform adjustment alone. However, their method performed best in highly absorbing media. The authors noted that this performance was due to the fact that the biasing could be strong without undersampling scattering in the problem. They also pointed out that, while the weight window method was comparable in efficiency to the method described, their method avoided choosing importances and weight window values for biasing. Their method was limited to exclusively photon transport biasing, and not neutron transport. However, the authors were optimistic that the method could be extended to neutron transport with relative ease. Both, Niemal, and Vergnaud [57] also derived VR parameters for the exponential transform and for collision biasing based on the adjoint solution as a measure of importance.

2.5.2.2 LIFT

The LIFT [58, 59] method developed by Turner and Larsen, and like Dwivedi's exponential transform, is a modification of the zero variance solution (see Section 2.2.3). Consequently, the LIFT method uses a calculation of the adjoint flux as a measure for importance in the problem to distribute particles according to the contributon density in the problem. LIFT uses a deterministic calculation to generate biasing parameters for the exponential transform and weight window variance reduction techniques.

As with the form of the importance function derived by Dwivedi (Eq. (2.78)), the LIFT method generates an angle-dependent importance function by taking the product of a space-based exponential function and an angle-informed collision estimator. Additionally, LIFT uses a deterministic calculation of the adjoint scalar flux to inform the angular flux reconstruction. The adjoint angular flux is approximated as piecewise continuous in space and angle with Eqs. (2.79a) through (2.79d):

$$\psi^{\dagger}_{g,n}(r,\Omega) \approx \phi^{\dagger}_{g,n} V_n \left[\beta_{g,n} \frac{\sigma_{s_0,g\to g,n} b_{g,n}(\Omega)}{\sigma_{t,g,n} - \rho_{g,n}\cdot\Omega} e^{\rho_{g,n}\cdot(r-r_n)} \right] , \tag{2.79a}$$

where the physical system is comprised of N regions of volume V_n, and $\psi^{\dagger}_{g,n}$ is the approximation of the angular flux for group g and region n. Further, β, the normalization factor, is given by:

$$\beta_{g,n} = \frac{1}{\int_{V_n} e^{\rho_{g,n}\cdot(r-r_n)} dr \int_{4\pi} \frac{\sigma_{s_0,g\to g,n} b_{g,n}(\Omega)}{\sigma_{t,g,n}-\rho_{g,n}\cdot\Omega} d\Omega} ; \tag{2.79b}$$

$b_{g,n}$, the linearly anisotropic factor, is

$$b_{g,n}(\Omega) = 1 + 3\mu_{g\to g,n} \frac{\sigma_{t,g,n} - \sigma_{s_0,g\to g,n}}{|\rho_{g,n}|^2} \rho_{g,n}\cdot\Omega ; \tag{2.79c}$$

and the biasing parameter $\rho_{g,n}$ is given by the product of the cross section and the biasing parameter λ seen previously in Eqs. (2.77) and (2.78),

$$\rho_{g,n} = \sigma_{t,g,n}\lambda_{g,n}. \tag{2.79d}$$

Turner showed that $\rho_{g,n}$ can be obtained from the deterministic solution to the adjoint equation, rather than from the cross section and λ, which requires some assumptions on the distribution of particles. Instead, Turner showed that ρ can be found in terms of the deterministic scalar fluxes, where

$$\rho_{x,g,n} = \frac{1}{\Delta x_n} \ln\left(\frac{\phi^{\dagger}_{g,i+1/2}}{\phi^{\dagger}_{g,i-1/2}} \right) \tag{2.80a}$$

$$\rho_{y,g,n} = \frac{1}{\Delta y_n} \ln\left(\frac{\phi^{\dagger}_{g,j+1/2}}{\phi^{\dagger}_{g,j-1/2}} \right) \tag{2.80b}$$

and

$$\rho_{z,g,n} = \frac{1}{\Delta z_n} \ln\left(\frac{\phi^\dagger_{g,k+1/2}}{\phi^\dagger_{g,k-1/2}}\right) \tag{2.80c}$$

are all defined using cell-edge flux values in Cartesian coordinates.

Eq. (2.79a) is an adjustment of the exponential transform described by Dwivedi [54]. However, rather than relying upon an isotropic scattering law, like earlier implementations of the exponential transform, the LIFT method adjusts the transform to instead be linearly anisotropic in angle. The derivation of this equation for both linearly anisotropic scattering and isotropic scattering is available in [58]. To summarize: the parameters $\beta_{g,n}$, $b_{g,n}$, and $\rho_{g,n}$ are calculated from values obtained from the deterministic calculation and are used to calculate $\psi^\dagger_{g,n}$.

In addition to using the exponential transform to bias the particles in angle, the LIFT method also uses weight windows for particle weight adjustment. However, the computational cost of generating angle-dependent weight windows from the previous equations led the authors to choose space-energy exclusive weight windows. The weight window target values were calculated to be inversely proportional to the adjoint solution, as with other methods

$$ww_{center,g,n} = \frac{\phi^\dagger_{g,src}}{\phi^\dagger_{g,n}}. \tag{2.81}$$

The LIFT method [58, 59], like AVATAR, calculated the angular flux for a region by assuming the angular flux was a product of the scalar flux and an exponential function. The angular flux values were then used to generate values for the exponential transform variance reduction technique to bias the particles in space, energy, and angle. Like AVATAR, LIFT also generated weight window parameters. However, generating a full angle-dependent weight window map and running Monte Carlo transport with those weight windows was computationally limiting, and the authors chose to only generate space- and energy-dependent weight windows. Turner showed that LIFT outperformed AVATAR for several example problems, but both methods performed poorly in voids and low-density regions.

Turner compared a number of variants of LIFT [59] against AVATAR to determine the efficiency of LIFT. In his investigation, Turner compared LIFT and AVATAR using approximations for the adjoint solution with diffusion and S_N transport calculations, and with various methods to calculate weight window parameters, including using LIFT combined with AVATAR's weight window parameters. In most cases, LIFT outperformed AVATAR. In problems with voids and low-density regions, the efficiency of the LIFT method decreased, but so did AVATAR. This independently confirmed the findings of the previous study. However, an important note that Turner mentioned was that while increasing the accuracy of the deterministic solution may decrease the variance, it is not necessarily the best for the FOM. This is a valuable lesson for all automated variance reduction methods: an overly accurate solution for the adjoint problem may reduce the variance but come at such a high computational cost such that it decreases the FOM.

More recently, Keady and Larsen showed that LIFT could be improved upon further by using cell-averaged currents and fluxes rather than cell-edge values for angular biasing [60]. By using this modified variation of LIFT, material interfaces do not create strong flux discontinuties on cell edges, resulting in a solution that is both smoother and more realistic. Results were presented for a one-dimensional monoenergetic slab problem with material interfaces. The modified version of LIFT outperformed both the original LIFT method and Monte Carlo weight windows generated with forward deterministic weight windows.

2.6 Variance Reduction in Large Application Problems

Variance reduction methods exist for Monte Carlo methods to achieve a more accurate answer in a shorter amount of time. Automated variance reduction methods have been designed to aid users in generating variance reduction parameters where it might not be intuitive or obvious what variance reduction parameters are best for a problem. The most successful variance reduction methods construct or estimate an importance function for the desired response from a preliminary calculation. This importance function may be derived from the adjoint solution to the transport equation, or it may be derived from contributon theory.

The methods described in Sections 2.3 through 2.5 have been implemented and tested in a number of software packages. The problem spaces over which they have been applied is extensive, and show that a large subset of application problems can be successfully simulated with the assistance of existing variance reduction techniques. Local variance reduction methods can be used to reduce the variance in source-detector problems where the detector constitutes a small subset of the problem phase-space. Global variance reduction methods can be used to distribute response sampling equally throughout several tallies or a problem-wide tally. Angle-based variance reduction methods are used in problems where space- and energy- variance reduction methods alone are not sufficient. For large and complex problems, automated versions of each of these methods are required as the user expertise to obtain even remotely adequate parameters is significant. Here, the existing state of automated variance reduction methods and the applications on which they have been tested will be summarized.

Presently, numerous hybrid methods packages that use the methods described in the preceeding sections are available. These packages are targeted towards deep-penetration radiation transport and shielding applications. The CADIS and FW-CADIS methods are distributed with MAVRIC [27, 40] and ADVANTG [61] from Oak Ridge National Laboratory (ORNL), which use the discrete ordinates code Denovo [62] to make VR parameters for the Monte Carlo codes Monaco [27] and MCNP[8], respectively. CADIS and FW-CADIS are also available in Tortilla [63], which uses the hybrid methods software using the deterministic code Attilla [64]. Tortilla also includes a version of LIFT and LIFT-based weight windows. The Deterministic Adjoint Weight Window Generator (DAWWG) from Los Alamos National Laboratory (LANL) [65] uses the adjoint solution from a deterministic solve in PARTISN

[66] to generate biasing parameters for MCNP, and also includes AVATAR functionality. MCNP [8] is distributed with a weight window generator (WWG) that uses a preliminary Monte Carlo solution to estimate an importance function for the problem. Though this list is not exhaustive, it illustrates the present ubiquity and need for hybrid methods to analyze realistic problems. In the analysis of realistic problems, ensuring that a "good" answer is achieved is necessary for safety and security. In the next few paragraphs, how and how effectively each of these methods have been applied to application problems is summarized. The degree to which each is successful is also discussed.

CADIS and FW-CADIS have been used for a number of studies of spent fuel storage facilities. Radescleu et al. used FW-CADIS in MAVRIC to calculate spent fuel dose rates of a single dry cask with finely detailed geometry and spent fuel isotopic compositions [67]. Chen et al. used MAVRIC [27] to analyze dose rates on spent fuel storage containers [68]. The fueled region of the storage container was homogenized into an effective fuel region. They found that in a coarse energy group calculation (27G19N) MAVRIC underestimated neutron dose rates at high energies. However, MAVRIC's ability to generate importances in three dimensions allowed it to have better problem-wide results, while the compared to methods (SAS4) struggled generating satisfactory results in the axial direction. This was demonstrated to a greater extent in an analysis of an independent spent nuclear fuel storage installation (ISFSI) [69] by Sheu et al. The FOM achieved by MAVRIC appeared inferior to those obtained with SAS4 or TORT/MCNP in a single cask. However, when applied to a storage bed of 30 casks MAVRIC was able to generate VR parameters at all, which were unfeasible for the other two methods. These studies demonstrated that CADIS and FW-CADIS are desirable methods for which to obtain global and three-dimensional variance reduction parameters for realistic problems.

ADVANTG [61], developed at ORNL [70, 35, 71] is a hybrid methods package for automated variance reduction of the Monte Carlo transport package, MCNP [11]. ADVANTG uses the deterministic transport code Denovo [62] to perform the forward and adjoint calculations for CADIS and FW-CADIS. At its inception, ADVANTG was used to analyze various threat-detection nonproliferation problems [61]. FOM improvements on the order of 10^2 to 10^4 when compared with analog Monte Carlo have been observed. However, Mosher et al. noted that the methods struggled with problems exhibiting strongly anisotropic behavior. In particular, they noted that low-density materials and strongly directional sources posed issues. This indicated that while CADIS and FW-CADIS are very useful methods, they have limitations in highly angle-dependent applications.

The deterministic adjoint weight window generator (DAWWG), utilizes the discrete ordinates code PARTISN [65] to generate space- energy- and angle-dependent weight windows. It is an internal feature of MCNP. The angle-dependent weight windows are calculated with the same methodology as AVATAR [65, 17]. Sweezy and colleagues compared DAWWG to the standard MCNP WWG on an oil well logging problem, a shielding problem, and a dogleg neutron void problem. The deterministic weight window generator obtained similar relative errors as the standard WWG for the first two problems, but in a fraction of the time. However, for the dogleg void problem, which exhibited strong angular dependence in the neutron

flux, the authors noted that DAWWG was not as effective as the standard MCNP WWG. This was attributed to ray effects from the S_N transport influencing the weight windows obtained by DAWWG, which is not an issue for the standard WWG.

A variety of automated variance reduction methods, including CADIS and LIFT have been implemented into the Attila / Tortilla deterministic and hybrid transport code packages [63]. These methods were used on several nonproliferation test problems. For the most part, LIFT and LIFT combined with weight windows outperformed CADIS' weight windows and source biasing, indicating that the addition of angular information was of benefit for these more realistic nonproliferation application problems.

Peplow et. al. formulated an adjustment to CADIS in the ORNL code suite [52] to incorporate angular information into the VR parameters (see Section 2.5.1.2. Two different methods to generate weight windows and source biasing parameters were investigated: CADIS with directional source biasing, and CADIS without directional source biasing. For the method without directional source biasing, the biased source distribution matched that of the original CADIS, but the weight window values were directionally-dependent. The method with directional source biasing used the transform function to obtain directionally-dependent weight windows and directional source biasing. Peplow and his colleagues found that these methods generally increased the FOM by a factor of 1-5 as compared to traditional CADIS, but in some cases decreased the FOM. This was attributed to the P_1 approximation used to calculate the angular flux, which limited the physical applicability of the method, just as with AVATAR.

CADIS and FW-CADIS have shown to be the existing "gold standard" of local and global variance reduction methods for large application problems, a selection of which were described in the preceding paragraphs. These problems include active interrogation of cargo containers [61], spent fuel storage casks [68, 67] and beds [69], and other nonproliferation and shielding applications [63]. For additional applications, one may refer to [35]. In some of these application problems, the parameters generated by CADIS or FW-CADIS were sufficient for the problem application. However, for other problems that had strong angular dependence or geometric complexity, the parameters were insufficient [68, 63, 52]. This can be remedied with additional angular information in the variance reduction parameters, such as LIFT [63], but the benefits of consistent source biasing are lost in this case. Alternatively, the angular flux can be reconstructed in a manner similar to AVATAR [65, 52] to generate angle-dependent weight windows, but this approximates the angular flux to be linearly anisotropic in angle (from the P_1 reconstruction), and is also dependent on the deterministic flux not having ray effects [65].

Although numerous methods have been proposed and implemented to obtain adequate angle-informed variance reduction parameters for application problems, they have limited applicability, and determining in which problems they will be useful is not always straightforward. No single method has been successful for problems with all types of anisotropy, and no existing angle-informed method captures the anisotropy in the flux without significant approximation. For large-scale, highly anisotropic, deep-penetration radiation transport problems, there exists a need for improvements in hybrid methods.

Chapter 3

Methodology

The objective of this work is to develop a method that, like CADIS and FW-CADIS, automatically generates variance reduction parameters for fixed-source, deep-penetration radiation transport problems. In general, the variance reduction parameters generated by CADIS and FW-CADIS are not sufficient for problems that are strongly anisotropic with respect to the flux. This method will extend existing methods to generate importance maps–that in turn generate variance reduction parameters–that are informed by angle to remedy this issue. The first section in this chapter describes the mathematical foundation of this new method. A discussion on how the method's performance will be quantified follows. Finally, a description of the software being used and how the method is added to this software concludes this chapter.

3.1 Theory: Angle-Informed Importance Maps for CADIS and FW-CADIS

There exist methods to generate variance reduction parameters for deep penetration radiation transport problems with strong anisotropy in the flux. These methods have shown to have varying success, and may not be fully automated. The solution proposed in this dissertation is a formulation that we have named the Ω-CADIS-methods. This section will commence with a brief discussion of the foundational research on which the Ω-CADIS-methods are built. That discussion serves as a primer for the subsequent section, which is an introduction to the Ω-CADIS-methods and a discussion on how they differ from their predecessors.

3.1.1 Previous Work

As discussed in Sections 2.3.1 through 2.5, the existing gold standard for automatically generating variance reduction parameters for deep penetration fixed-source radiation transport problems are CADIS and FW-CADIS. Both of these methods are very effective at generating

variance reduction parameters for local and global solutions, respectively. However, CADIS and FW-CADIS have only been implemented to perform variance reduction in space and energy, not angle. As a result, solutions for problems with strong anisotropy in the flux are not always optimized with these methods, resulting in slow convergence times and low FOM values. Problems with strong anisotropies in the flux require more than just space- and energy- variance reduction techniques. A number of angle-informed variance reduction methods have been investigated, most notably AVATAR, LIFT, and a modified version of CADIS using AVATAR-type angular parameters.

LIFT, AVATAR, and Simple Angular CADIS all showed that by including angular information into Monte Carlo variance reduction parameters the FOM can be improved. However, none of these methods used the actual angular flux to calculate the variance reduction parameters for the problem they were optimizing. Without explicitly using the angular flux solutions they were limited in which types of problems they were applicable, because some assumption of the degree of anisotropy of the flux was made. Further, LIFT and Simple Angular CADIS showed that by including substantial angular biasing in the weight windows in problems where the approximation to the angular flux is not sufficient, the FOM can decrease not unsubstantially, defeating the purpose of using these methods.

3.1.2 The Ω Methods

The foundation of the Ω-methods is built upon CADIS and FW-CADIS. As with both methods, the Ω-methods will use a version of the adjoint scalar flux to consistently bias a Monte Carlo problem with the intention of reducing the variance. In Section 2.2.1 the concept of importance was introduced. Notably, it was shown that the adjoint flux is a good marker for the likelihood of particles to contribute to a tally, which is the particle's importance. It was also shown that the product of the forward and adjoint fluxes generates a pseudo-particle flux called the contributon flux, where contributons are "importance particles". These importance particles can be used to show preferential flow paths from a source to a tally or desired location.

By using a version of the adjoint scalar flux that has been formulated with the contributon flux, the direction of particle flow will be incorporated into the importance map and, consequently, the variance reduction parameters. By using this variant of the adjoint scalar flux, the method, like traditional CADIS, will show increasing importance as the particles travel near the adjoint source. However, because this variant of the adjoint flux incorporates directionality of the particle flow, not all regions near the adjoint source are equally important. In this way, the adjusted flux incorporates features from both the adjoint- and contributon- fluxes.

The adjusted adjoint scalar flux quantity, or the Ω-adjoint scalar flux, is

$$\phi^{\dagger}_{\Omega}(\vec{r}, E) = \frac{\int_{\Omega} \psi^{\dagger}(\vec{r}, E, \hat{\Omega})\psi(\vec{r}, E, \hat{\Omega})d\hat{\Omega}}{\int_{\Omega} \psi(\vec{r}, E, \hat{\Omega})d\hat{\Omega}}. \tag{3.1}$$

The Ω-flux is a hybridization of the adjoint scalar flux and the contributon flux. It is both a normalized contributon flux and a forward-weighted adjoint flux. As a result, it should inherit some of the advantages of each of the traditional adjoint and the contributon fluxes. Because it maintains dimensionality of the traditional adjoint scalar flux, it can be used in place of the standard adjoint scalar flux in both CADIS and FW-CADIS variance reduction parameter generation. This means that the method can capitalize on existing infrastructure used to generate variance reduction parameters for CADIS and FW-CADIS, and only the software handling the transport and flux-generation requires modification.

3.1.2.1 CADIS-Ω

As with CADIS, CADIS-Ω consistently biases a problem's source and particle weights according to their importance. However, CADIS-Ω uses the Ω-adjoint scalar flux rather than the standard adjoint scalar flux to generate the biased source distribution, weight windows, and the particle birth weights. Furthermore, because $\phi^\dagger_\Omega$ is used to calculate these values in CADIS-Ω, the consistent-biasing hallmark for which CADIS is known is maintained. The adjusted formulation of CADIS using the Ω fluxes is given by Eqs. (3.2). The biased source distribution used by CADIS-Ω is formulated just as it is in CADIS, except the adjusted adjoint fluxes are used:

$$\begin{aligned}\hat{q}_\Omega &= \frac{\phi^\dagger_\Omega(\vec{r},E)q(\vec{r},E)}{\iint \phi^\dagger_\Omega(\vec{r},E)q(\vec{r},E)dEd\vec{r}} \\ &= \frac{\phi^\dagger_\Omega(\vec{r},E)q(\vec{r},E)}{R_\Omega}.\end{aligned} \tag{3.2a}$$

The starting weights of the particles sampled from the biased source distribution, $\hat{q}$ are given by

$$\begin{aligned}w_{0,\Omega} &= \frac{q}{\hat{q}_\Omega} \\ &= \frac{R_\Omega}{\phi^\dagger_\Omega(\vec{r},E)},\end{aligned} \tag{3.2b}$$

and the new target weights for the particle are

$$\hat{w}_\Omega = \frac{R_\Omega}{\phi^\dagger_\Omega(\vec{r},E)}. \tag{3.2c}$$

3.1.2.2 FW-CADIS-Ω

FW-CADIS differs from CADIS in that it requires a forward deterministic calculation to generate $q^\dagger$, which is used as the source distribution in the adjoint deterministic problem

(recall that CADIS sets $q^\dagger = \sigma_d$). Depending on the type of global response desired, FW-CADIS runs a deterministic forward calculation to approximate the global response in the problem. The inverse of these responses is then used to generate the biased adjoint source distribution for the adjoint deterministic run. Therefore, the behavior of FW-CADIS-Ω in the forward biasing portion of the calculation will remain unchanged from FW-CADIS. The generalized form for the adjoint source definition is given by the fraction of the response in a region of phase space, P, over the total response in the problem, or

$$q_\Omega^\dagger(P) = q^\dagger(P) = \frac{\sigma_d(P)}{R}.$$

When applied to the spatially-dependent global dose, $\int \phi(\vec{r}, E)\sigma_d(\vec{r}, E)dE$, the adjoint source will be

$$q_\Omega^\dagger(\vec{r}, E) = q^\dagger(\vec{r}, E) = \frac{\sigma_d(\vec{r}, E)}{\int \sigma_d(\vec{r}, E)\psi(\vec{r}, E,)dE}.$$

The adjoint source for the spatially-dependent total flux $\int \phi(\vec{r}, E)dE$ is

$$q_\Omega^\dagger(\vec{r}) = q^\dagger(\vec{r}) = \frac{1}{\int \phi(\vec{r}, E)dE}.$$

The adjoint source for the energy- and spatially-dependent flux $\phi(\vec{r}, E)$ is

$$q_\Omega^\dagger(\vec{r}, E) = q^\dagger(\vec{r}, E) = \frac{1}{\phi(\vec{r}, E)}.$$

One advantage of FW-CADIS-Ω is that, from a transport perspective, the Ω-method is no more expensive than standard FW-CADIS. Because both versions require a forward and adjoint deterministic calculation, an extra transport step is not required as it is for CADIS-Ω. This is attractive, but the nature of FW-CADIS might not be the most well-suited for the Ω-methods. Because FW-CADIS attempts to evenly distribute particles throughout the problem using the forward-biased adjoint fluxes, the additional forward normalization with the Ω-methods will likely skew the particle distribution in the problem in the forward direction, and it may place too great of importance on the forward-moving particles in generating the variance reduction parameters.

3.2 Computational Success Metrics

3.2.1 Anisotropy Quantification

As the Ω-methods are analyzed, it is important to determine the types of problems in which the methods are successful. In addition to describing the physics that induce anisotropy in the flux, quantifying the degree of anisotropy of the problem is useful in characterizing the

method. In this section, a number of methods by which the anisotropy can be quantified in these problems are proposed. A brief description of how these methods capture anisotropy in the problem is also included. While each metric proposes an avenue by which the problem can be analyzed, there are certainly other methods that one may propose. The methods described in the following subsections are proposed because they use data generated from the existing method. The degree to which they impose a computational burden will be addressed in their analysis.

3.2.1.1 The Scalar Contributon Ratio

The hybrid methods software that will be used for this project is ADVANTG, developed at ORNL. Section 3.3 explains how the software used interacts with other pieces of software and how they were modified to execute this method. The standard release of ADVANTG provides the contributon flux as an output option, which can then be used to analyze problem physics by a user. If this option is selected as an output, a SILO file containing the contributon fluxes for each discretized cell in space and energy is created. This is useful for problem analysis as the user may see preferential streaming paths for particles in the problem using this metric. The contributon flux generated in this process is given by the product of the scalar adjoint and forward fluxes (Eq. (3.4)).

As mentioned in Section 2.2.3, the contributon flux can be calculated by using the product of the forward and adjoint fluxes. In standard software packages that calculate the contributon flux, like ADVANTG, the scalar contributon flux is calculated by the product of the scalar adjoint and forward fluxes. This can be written as

$$\phi^c(\vec{r}, E) = \phi^\dagger(\vec{r}, E)\phi(\vec{r}, E). \tag{3.4}$$

A more precise calculation of the contributon flux could be generated from integrating the angular contributon flux over all angle, as

$$\begin{aligned} \Phi^c(\vec{r}, E) &= \int_\Omega \psi^c(\vec{r}, E, \hat{\Omega}) d\hat{\Omega} \\ &= \int_\Omega \psi^\dagger(\vec{r}, E, \hat{\Omega})\psi(\vec{r}, E, \hat{\Omega}) d\hat{\Omega}. \end{aligned} \tag{3.5}$$

Both Eqs. (3.4) and (3.5) calculate the contributon flux as a function of space and energy, but the differences in their calculation is addressed in their notation, namely using ϕ^c or Φ^c. The standard release of ADVANTG only has access to the scalar fluxes, so Eq. (3.5) is not an accessible option for a user. Because the Ω calculations require full angular flux map, the scalar contributon flux can be calculated with the latter formulation, rather than the former in the modified version developed to support this work.

The first measure of anisotropy quantification that will be evaluated is the ratio between these two quantities, as described by Eq. (3.6). The ratio between these two values is evaluated for every cell, x, y, z, and energy group, E_g. If the adjoint or forward angular

flux is significantly peaked in Ω, this will result in a deviation between ϕ^c and Φ^c, because there will be a multiplicative effect in the angular flux captured in Φ^c but not ϕ^c. The more isotropic the flux in $\vec{r}$ and E, the closer these values will be and the quantity will approach unity.

$$M_1 = \left.\frac{\phi^c}{\Phi^c}\right|_{x,y,z,E_g} \tag{3.6}$$

3.2.1.2 The Ratio of Adjoint Fluxes

As discussed in previous sections, the Ω-methods use the Ω-scalar flux in place of the standard adjoint scalar flux. Therefore the ratio between these two quantities would also provide a useful metric for comparing which regions have significantly differing bias parameters in standard-adjoint and Ω-adjoint situations. This metric will deviate from unity if the forward flux is anisotropic. This metric is calculated for every cell and every energy group in the problem, as shown in Eq. (3.7).

$$M_2 = \left.\frac{\phi^\dagger_\Omega}{\phi^\dagger}\right|_{x,y,z,E_g} \tag{3.7}$$

Metrics one and two both reasonably appear to compute the anisotropy in the flux using versions of the contributon and adjoint fluxes, respectively. However, by expanding the Ω-adjoint scalar flux in metric two,

$$\begin{aligned} M_2 &= \left.\frac{\phi^\dagger_\Omega}{\phi^\dagger}\right|_{x,y,z,E_g} \\ &= \left.\frac{\int_\Omega \psi^\dagger(\hat{\Omega})\psi(\hat{\Omega})d\hat{\Omega}}{\int_\Omega \psi(\hat{\Omega})d\hat{\Omega}}\frac{1}{\phi^\dagger}\right|_{x,y,z,E_g}, \end{aligned}$$

integrating the forward angular flux over all angle,

$$= \left.\frac{\int_\Omega \psi^\dagger(\hat{\Omega})\psi(\hat{\Omega})d\hat{\Omega}}{\phi}\frac{1}{\phi^\dagger}\right|_{x,y,z,E_g},$$

and rearranging the terms,

$$
\begin{aligned}
&= \left.\frac{\int_\Omega \psi^\dagger(\hat{\Omega})\psi(\hat{\Omega})d\hat{\Omega}}{\phi\phi^\dagger}\right|_{x,y,z,E_g} \\
&= \left.\frac{\Phi^c}{\phi^c}\right|_{x,y,z,E_g} \\
&= \left.\frac{1}{M_1}\right|_{x,y,z,E_g},
\end{aligned}
$$

it becomes evident that the ratio of adjoint fluxes is the inverse of the scalar contributon ratio. As a result, metric one will not be used in the analyses of the characterization problems.

3.2.1.3 The Maximum to Average Flux Ratio

An alternative metric to quantify anisotropy is to calculate the ratio between the maximum and average angular contributon flux in each $\vec{r}, E$ voxel. The higher this quantity, the more peaked the contributon flux is in Ω. Note that while using the Ω-flux would seem like the natural choice, no angular information is directly accessible once the Ω scalar flux has been calculated. One can compare the standard adjoint scalar flux and the Ω-adjoint scalar flux and infer how anisotropic the flux in the cell might be, but due to the normalization that occurs in Eq. (3.1), the variation of angular Ω fluxes throughout Ω for a cell in x, y, z, E_g is not calculated. As such, the contributon flux must be relied upon as a next-best evaluator of that metric:

$$
M_3 = \left.\frac{\psi^c_{Max}}{\psi^c_{Avg}}\right|_{x,y,z,E_g}. \tag{3.8}
$$

While Eq. (3.8) directly measures the anisotropy in the problem using the angular contributon fluxes, it doesn't compare the difference between the fluxes used in the Ω- and the standard adjoint methods. Metric three can be reformulated to incorporate this information using

$$
\begin{aligned}
M_4 &= \left.\frac{\frac{\psi^c_{Max}}{\psi^c_{Avg}}}{\frac{\psi^\dagger_{Max}}{\psi^\dagger_{Avg}}}\right|_{x,y,z,E_g} \\
&= \left.\frac{M_3}{\frac{\psi^\dagger_{Max}}{\psi^\dagger_{Avg}}}\right|_{x,y,z,E_g},
\end{aligned} \tag{3.9}
$$

as a measure between the anisotropies of the standard and contributon fluxes. This equation is a logical progression from metric two and metric three. This metric contains more information on how perturbed the contributon flux is when compared to the original adjoint

flux that is normally used in CADIS and FW-CADIS. In the case of a strongly anisotropic forward flux, the forward flux would significantly change the distribution of the contributon fluxes in a cell, but it would not affect the flux distribution of the standard adjoint angular fluxes. By comparing the anisotropy in the contributon fluxes to those in the standard adjoint, the perturbation of the Ω flux by the forward flux in the cell can be evaluated. In regions where the forward flux is not anisotropic, then the contributon anisotropy ratio should be approximately the same as the standard adjoint anisotropy ratio.

Further, because the contributon flux incorporates directionality of the forward and adjoint fluxes, the maximum to average ratio of the contributon flux can differ from the adjoint flux. In regions where the adjoint angular flux and the forward angular flux are traveling in the same direction, the contributon ratio should be greater than the adjoint ratio, and this metric will be greater than one. In regions where they are travelling in opposite or perpendicular directions, the contributon flux will evaluate to a more isotropic state, and metric four will be less than unity. This metric provides substantially more information than metric two because it compares the behavior of the directional contributon and adjoint fluxes, rather than comparing the overall behavior of the flux in the cell.

Both Eqs. (3.8) and (3.9) compare the maximum angular flux in a cell to the average flux in the same cell. Because the average angular flux is the normalization factor, the maximum flux in the cell is compared to some relative measure of the total flux behavior in that cell. If, for example, the flux has several directional peaks, the average will reflect that. The fact that Eq. (3.9) contains information on the global behavior in the contributon and average cell, the directionality of the fluxes, and the degree of isotropy of the forward flux is attractive. However, this is also a fairly computationally expensive calculation and it may not be worth the computational cost when compared to metrics two and three.

3.2.1.4 The Maximum to Minimum Flux Ratio

An additional metric to quantify anisotropy in the contributon flux distribution is to calculate the ratio between the maximum and minimum angular fluxes for each region of x, y, z, E_g phase-space, as described in metric five, or Eq. (3.10). This quantity incorporates information about the behavior of the local maximum relative to the local minimum angular flux in each cell.

$$M_5 = \left.\frac{\psi^c_{Max}}{\psi^c_{Min}}\right|_{x,y,z,E_g} \tag{3.10}$$

This metric may be more appropriate to describe the anisotropy of the flux in cells where the distribution of flux values in the cell are not well reflected by the average flux in the cell. As with metric three (Eq. (3.8)), metric five (Eq. (3.10)) only quantifies the anisotropy of the contributon flux in the cell. There is no comparison or normalization to compare the anisotropy with respect to another method. To compare it to the anisotropy of the flux in the standard adjoint problem, a ratio similar to that of Eq. (3.9) may be formulated:

$$M_6 = \left. \frac{\frac{\psi^c_{Max}}{\psi^c_{Min}}}{\frac{\psi^\dagger_{Max}}{\psi^\dagger_{Min}}} \right|_{x,y,z,E_g} = \left. \frac{M_5}{\frac{\psi^\dagger_{Max}}{\psi^\dagger_{Min}}} \right|_{x,y,z,E_g}. \tag{3.11}$$

As with Eq. (3.9), Eq. (3.11) uses a ratio from the standard adjoint formulation to normalize the anisotropy of the contributon flux. Equation (3.11) is consistent with Eq. (3.10) and normalizes using the maximum to minimum ratio of angular fluxes of the adjoint. These two metrics will show the relative behavior of the flux in the cell, but because neither incorporates information about the total flux behavior within the cell, they may be very sensitive to the variance of the angular flux within the cell. Using the ratio of both the contributon and adjoint fluxes may help to smooth this if the variance of flux distributions within the contributon and standard adjoint is similar in a particular cell. However, if these two differ significantly, then metric six (Eq. (3.11)) may have a synergistic effect and will over-emphasize the variance when quantifying the anisotropy of the cell.

Metrics one through six quantify anisotropy in the problem solved by using different parameters to capture the problem physics. These metrics will be compared to one another to determine which is the most consistently correlated with predicting the Ω-method's success. A user may want to know if the Ω-method will effectively generate variance reduction parameters for a Monte Carlo simulation, and this may be a prescriptive solution for that issue. However, all of these metrics do require full angular flux solutions for both the forward- and adjoint- problem, so some computational burden will be required. The analysis of using these metrics will include some information of benefit to burden, which likely will come at the cost of time. That said, because the Monte Carlo solution is more computationally demanding, generating these metrics from the deterministic solution should be substantially less of an obstacle.

3.2.2 Figure of Merit

The FOM is a commonly used metric to measure Monte Carlo runtimes and to gauge the effectiveness of various hybrid methods. As discussed in Section 2.1, the FOM relates the relative error of a solution to the time required to achieve that variance. This was introduced in Eq. (2.20) as:

$$\text{FOM} = \frac{1}{R^2 T},$$

where T is the time and R^2 is the square of the relative error.

3.2.2.1 Relative Error

In tallies with multiple regions and/or energy bins, the FOM is usually calculated from the tally average relative error, or R_{avg}. This value is meaningful as it reflects the overall tally behavior. However, it is often desirable that all portions of the tally lie below a desired relative error threshold. A region with very low particle contribution may have a much higher relative error than the tally average, and may also converge much slower to a desired relative error. This results in a substantially different FOM than the tally average. In the results presented in later chapters, both relative errors will be used to calculate different FOMs, respectively

$$\text{FOM}_{avg} = \frac{1}{R_{avg}^2 T}, \tag{3.12a}$$

and

$$\text{FOM}_{max} = \frac{1}{R_{max}^2 T}. \tag{3.12b}$$

In addition to reporting both FOMs for the entire problem, comparing the distribution of values of the relative error for problems will be a useful metric in method characterization. If, for example, FW-CADIS acquires desirable results in a calculation, then the problem should have a relatively even uncertainty distribution for all cells. Comparing the distribution of relative errors between the analog case and the hybrid case reveals whether the method is effectively generating variance reduction parameters for the entire problem or if it is more effective in particular regions.

3.2.2.2 Timing

The previous section described two different means by which the FOM could be calculated using different relative errors. The question that one must now consider is: what time should be used to calculate the FOM? In an analog Monte Carlo simulation, this time is the runtime of the Monte Carlo simulation, $T = T_{MC}$. In a hybrid method, one could choose either

$$T_{Hybrid} = T_{MC} + T_{Deterministic}, \tag{3.13}$$

or

$$T_{Hybrid} = T_{MC}. \tag{3.14}$$

The FOM should remain a constant–with the exception of very early on in an MC calculation where statistics are very poor–for a problem. The issue with using Eq. (3.13) to calculate the FOM is that the deterministic runtime does not change the relative error of the Monte Carlo simulation. Thus, the FOM is not a constant throughout the Monte Carlo simulation when using Eq. (3.13) as the time. However, it would be disingenuous to not include the deterministic runtime into reports for the hybrid method, as the total computational time required to achieve some desired relative error is ultimately what the user is

seeking. As such, two reports of the FOM are included with the results for each simulation:

$$\text{FOM}_{MC} = \frac{1}{R^2 T_{MC}}, \tag{3.15a}$$

and

$$\text{FOM}_{Hybrid} = \frac{1}{R^2 (T_{MC} + T_{Deterministc})}. \tag{3.15b}$$

Note that the deterministic time used in Eq. (3.15b) is the time to run the transport and generate source biasing and weight window values for each problem. It will not include the time used to quantify the anisotropy as outlined in Section 3.2.1, as those parameters will be computationally demanding but not normally included in a hybrid method computation.

In this section, four different equations to calculate the FOM were presented: two using different relative errors, and two using different quantities for time. In analyzing the method, all four will be presented: $\text{FOM}_{MC,avg}$, $\text{FOM}_{MC,max}$, $\text{FOM}_{Det,avg}$, and $\text{FOM}_{Det,max}$. Further, the improvement in the FOM for each problem will be reported as those values normalized by $\text{FOM}_{analog,avg}$ for the two FOMs calculated with the tally average relative error and $\text{FOM}_{analog,max}$ for the FOMs calculated with the tally maximum relative error. The success of the Ω-method will depend on its ability to improve each one of these FOM values.

3.3 Software

In this section, the software in which the methods presented in Section 3.1.2 are implemented is described. A brief summary of each piece of software and what was added in each is discussed. While the details of the inner-workings of the software will not be described here, both pieces of software have rich documentation and user guides which an interested reader may reference.

3.3.1 Denovo

Denovo S_N is a three-dimensional discrete ordinates transport solver developed at Oak Ridge National Laboratory [62]. Denovo is a module in the larger Exnihilo massively-parallel radiation trasnsport code suite. There exist several other modules in Exnihilo. In addition to Denovo, the most pertinent package being Omnibus, a frontend pre- and post-processing module. The Ω-fluxes are generated by running two independent (a forward and an adjoint) determinstic solves in Denovo. The setup and generation of each simulation input is automated through ADVANTG (see Section 3.3.2). After the calculation has reached the desired convergence criteria, the full angular flux maps for the forward and adjoint solves are saved to an HDF5 [72] file. Denovo was modified to output the full angular flux maps for a simulation. The Ω-fluxes are then generated by passing the angular flux maps through the postprocessing module in Omnibus. Using this module, the integration described in Eq. (3.1) is performed, the scalar Ω-fluxes are saved to a SILO file, and the scalar fluxes are

passed to ADVANTG for variance reduction parameter generation. Appendix A.1 contains the code added to Omnibus to perform this calculation.

3.3.2 ADVANTG

ADVANTG [70] is a software package originally designed to automatically generate variance reduction parameters for the Monte Carlo radiation transport solver MCNP [9] using the CADIS and FW-CADIS methods. For this project, the ADVANTG functionality was extended to process the Ω-fluxes provided by Denovo through Omnibus and to generate variance reduction parameters for CADIS and FW-CADIS using said fluxes. In addition to the modifications required to perform CADIS and FW-CADIS, ADVANTG was further modified to generate anisotropy quantification metrics and a modified version of the scalar contributon flux, both of which were summarized in Section 3.2.1. The piece of code used to reroute the Ω-fluxes through CADIS and FW-CADIS as well as to generate the anisotropy metrics in ADVANTG is included in Appendix A.2.

Summary

In summary, this chapter presented the novel theory behind the Ω-methods; the metrics by which the Ω-methods will be compared with existing hybrid methods; and the software that was modified to implement the Ω-methods into an existing codebase. Two variants of the Ω-methods were presented: CADIS-Ω and FW-CADIS-Ω, which are referred to together as FW/CADIS-Ω. CADIS-Ω is a modification of CADIS, and is designed to generate VR parameters for local solutions in problems with strong anisotropy. FW-CADIS-Ω is a modification of FW-CADIS, and is designed for generating VR parameters for global solutions in problems with strong anisotropy.

Both CADIS-Ω and FW-CADIS-Ω are implemented in well-used, well-documented, massively-parallel, state-of-the-art radiation transport and hybrid methods software. The radiation transport code suite Exnihilo is modified to generate the Ω-fluxes. The hybrid methods package ADVANTG is modified to generate VR parameters for the Ω-methods using the Ω-fluxes.

To understand the performance of the Ω-methods and compare it consistently to existing methods, several performance metrics were proposed. First, a few variants of the FOM were described. They include: $\text{FOM}_{MC,avg}$, $\text{FOM}_{MC,max}$, $\text{FOM}_{hybrid,avg}$, $\text{FOM}_{hybrid,avg}$. Together, they provide an overall picture of the performance of the Ω-method's performance with respect to relative error and time, rather than of a single criteria. Because anisotropy has the ability to affect energy groups differently, resulting in different relative errors achieved in different energy bins, separating out different FOMs helps to isolate interesting behavior in the methods.

The Ω-methods are designed to work in problems with strong anisotropies in the flux. As a result, several anisotropy metrics with which to investigate flux anisotropy were proposed.

Using these metrics and comparing them to the relative errors or FOMs in each tally region, we can try to understand the effect that anisotropy has on the Ω-method performance. Each metric quantifies the anisotropy in cells differently, so each has the potential to capture different information. Denovo was modified to output angular fluxes to generate the Ω-flux for the Ω-methods. As a result, the anisotropy metrics use data generated from the existing Ω-method calculation.

Using the methodology described in this chapter, the Ω-methods' performance can be fully characterized. Further, the characterization presented in this chapter has been extended from standard FOM performance metrics to include anisotropy quantification. By implementing the Ω-methods into production-level software, it is accessible to any user beyond the author. The generation of the anisotropy metrics is also incorporated into the codebase, meaning that any user could feasibly perform an investigation of the Ω-performance consistent with what is proposed herein. The use of the various FOMs and of the aniostropy metrics helps the understanding of the Ω-method performance as a function of time, error, and anisotropy.

Chapter 4

Characterization Problems and Results

The Ω-methods have been presented in the previous chapters. In this chapter, the CADIS-Ω-method is applied to a number of small, anisotropy-inducing problems. Recall that the Ω-methods are a version of CADIS and FW-CADIS that use an adjusted contributon-based flux rather than a pure-adjoint flux to generate biasing parameters. The CADIS-Ω-method's performance is compared to CADIS and standard nonbiased Monte Carlo. Because the Ω-methods have been designed to generate variance reduction parameters in problems where there is a strong degree of anisotropy in the flux, their characterization is dependent on testing them in anisotropic problems. This chapter begins with a presentation of the characterization problems that have been designed to induce anisotropy in the particle flux by different physical mechanisms. The results of the Ω-methods when applied to these problems follows. Two problems that highlight interesting aspects of the Ω-methods are subsequently used in a deeper parametric study to determine the Ω-method's sensitivity to different angular flux information. Using the results obtained from this study, recommendations on favorable parameters with which to run the Ω-methods are made.

4.1 Description of the Characterization Problems

In characterizing the Ω-methods, we aim to determine in which problems they perform well, and then quantify that success. First, we must determine how effective the Ω-methods are in reducing the variance for a tally result in Monte Carlo. This is done by assessing and comparing the FOMs between different VR methods. Also, the method must be investigated using a diverse set of anisotropic problems. By constructing problems that have different mechanisms causing or inducing anisotropy in the flux, potential strengths or weaknesses of the method can be isolated as a function of these mechanisms. In addition to comparing the FOMs or REs between methods, another desirable metric by which to measure the

method's success given the degree of anisotropy in the problem. Recall that different means of quantifying the flux anisotropy are described in Section 3.2.1. With a diverse selection of characterization problems, we obtain variation in the flux anisotropy in each problem as well as the resultant FOMs. This provides us with a path forward with which to use the Ω-methods in a deeper angular-sensitivity study.

4.1.1 Identification of Anisotropy-Inducing Physics

There exists a rich history of using hybrid methods in problems with strong angular dependence, as summarized in Chapter 2. Angular dependence may appear in a problem through several means–both physical and computational. Mosher et al. [61] noted in their threat-detection work with ADVANTG that problems with strongly directional sources and problems with "thin" materials like air were difficult for ADVANTG to effectively reduce the variance. They attributed this to strongly anisotropic behavior of the importance function that were not reflected well by the scalar flux. Sweezy [65] also found that weight windows obtained from a hybrid S_N calculation were not good for a dogleg void problem, where ray effects from the S_N calculation generated poorer weight windows than a method without ray effects [1]. Though they did not observe ray effects in the importance map for the problem, Peplow et al. [52] also found that CADIS struggled with thin material streaming in a spherical boat test problem.

The examples of angle-dependence in problems affecting hybrid methods' success illustrate that the flux can have anisotropy resulting from more than one mechanism. Based on these examples, we have identified several separate processes that affect the flux anisotropy. These processes can be grouped into three categories:

- anisotropy in the flux resulting from strongly directional sources,
- anisotropy resulting from strong differences between material properties (this can be due to differences in materials spatially or due to changes in interaction probabilities as a function of energy),
- anisotropy in the flux from algorithmic limitations (ray effects).

These processes overlap. Consequently, this section continues with a brief discussion about how each mechanism applies to anisotropic problems.

A strongly directional source is one that emits particles in a very small solid angle of angle-space. The most extreme example of this would be a monodirectional source, while an extreme opposite would be an isotropic source. This particular anisotropy-creating process is source-specific and does not depend on the rest of the problem configuration. Our characterization problems will have sources of both types to ensure the full parameter space is covered.

[1] Recall from Sections 2.2.3 and 2.6 that ray effects are a nonphysical effect seen in the flux solution that arise from the angular discretization of the problem. Ray effects are common in situations where there are strong streaming effects or if a strong source is emitting particles with long mean free paths in the material.

The next subset of anisotropy-inducing processes are those that result form strong differences between material properties. As noted, this can be from the geometric configuration of the problem, or from variations in the cross sections within a geometric location. To illustrate the differences in the way the problem can physically induce anisotropy in the flux, several simple thought experiments will be presented.

Consider first the extreme example of material A which has some low absorption probability, and material B which is a pure absorber. Only particles that travel through material A will eventually reach the tally location. This is an example of a type of problem with strong material heterogeneity. In constructing a set of characterization problems, creating channels through which particles will preferentially travel will induce anisotropy in the flux. These types of flow paths are also of interest in shielding application problems, and were discussed at length in Section 2.2.3. In this type of problem, material A can either have a low scattering probability (airlike), or it can be highly scattering. In scattering events, neutral particles can either lose very little energy with a high Z material, like lead, or they can lose a lot of energy with a low Z material. These are considered separately, because the energy spectrum of the particles affects the particle's interaction probability.

Consider another example of an isotropic point source immersed in a pure thin material. Because particles have a very low probability of interaction in the material, they will travel almost uniformly outwards away from the point source. At some distance from the point source, the majority of the particles in a cell will be traveling in the same direction. This is an example of a problem with streaming paths. To summarize, we have identified several sub-distinctions of this type of effect: regions with streaming where particles far from the source are primarily monodirectional, regions that are highly scattering where particles have a preferential flowpath through one material and are downscattered in energy, and regions with strong material heterogeneity where particles have preferential flowpaths but are not necessarily downscattered in energy. It should be noted that while streaming and scattering problems will almost always be subsets of problems with material homogeneity, it is possible to have a highly scattering or a streaming problem without material heterogeneity.

The last factor that can influence anisotropy in the flux solution is ray effects. While ray effects are a result of anisotropy in the flux solution, this is a nonphysical effect and can actually affect variance reduction performance. In the case of ray effects, we aim to see if the Ω-methods are more robust in avoiding them in generating VR parameters. Because ray effects are primarily seen in large regions with low interaction probabilities, some of the characterization problems must incorporate these types of regions into their geometries.

In this subsection, four primary physical mechanisms by which the flux may be anisotropic were identified. These are: streaming paths, problems with high scattering effects, problems with high material heterogeneity (specifically with materials with strong differences in scattering and absorption probabilities), and problems with monodirectional sources. As described in the preceding paragraphs, a few of these mechanisms may overlap with one another. Together, they compose an assortment of anisotropy-inducing physics. Combined with different geometric arrangements a diverse group of anisotropic problems can be formulated.

4.1.2 Problem Specifications

With the anisotropy-inducing physics described in Section 4.1.1, a set of characterization problems that have different combinations of each of these effects can be conceptualized. These problems provide an overview of how the Ω-methods perform in an assortment of anisotropic problems. As previously described, these fall into two broad categories: anisotropy caused by the problem materials and geometry, and anisotropy caused by the source definition. In the next several paragraphs, the material and geometric configuration of each problem will be described. This will be supplemented with an explanation of which anisotropy-inducing physics are contained in each problem. A summary of which physics are in each problem is provided in Table 4.1.

Labyrinths

The labyrinth problems have isotropic point sources on the left hand side of the problem emitting a Watt spectrum of neutrons approximating the energy spectrum emitted by that of ^{235}U fission. On the right hand side of the problem there is a NaI detector recording the flux. They are composed of a concrete maze with an air channel through the maze, and then open air channels at either end of the channels. The first variant of the labyrinth has a single turn, as illustrated in Figure 4.1, and the second labyrinth has multiple turns, as illustrated in Figure 4.2. These problems are both likely to have ray effects in the air region near the forward source. However, because far more scattering events will be required for a particle to exit the channel in the multi-turn maze, ray effects will likely be less prominent in the air region near the detector of that variant problem than in the single turn maze. Both problems have strong differences in interaction probabilities between the air and the concrete, thus they will have material heterogeneity. Further, because the concrete is composed of several lighter-mass elements, these will also be highly scattering.

Steel beam in Concrete

Figure 4.3 is a variant problem with a steel beam embedded in concrete. A NaI detector is located on the right hand side of the problem to record the response in CADIS problems. The source is a 80x80 centimeter sheet pointed in towards the steel structure in the $+x$ direction emitting 10 MeV neutrons. Because the particles have preferential flow through the steel but do do not have long streaming paths, this problem has material heterogeneity and will be highly scattering, but will not have streaming paths in the shielding region. Further, because the source is emitted from a thin plate in $+x$, it is monodirectional. This problem may have some ray effects occurring from backscattering off of the steel and concrete in the left side air region. It may also have ray effects exiting the beam on the right hand side. However, because significantly more scattering will happen in the concrete, the ray effects on the right hand side will be less pronounced than in the air exits of the labyrinths.

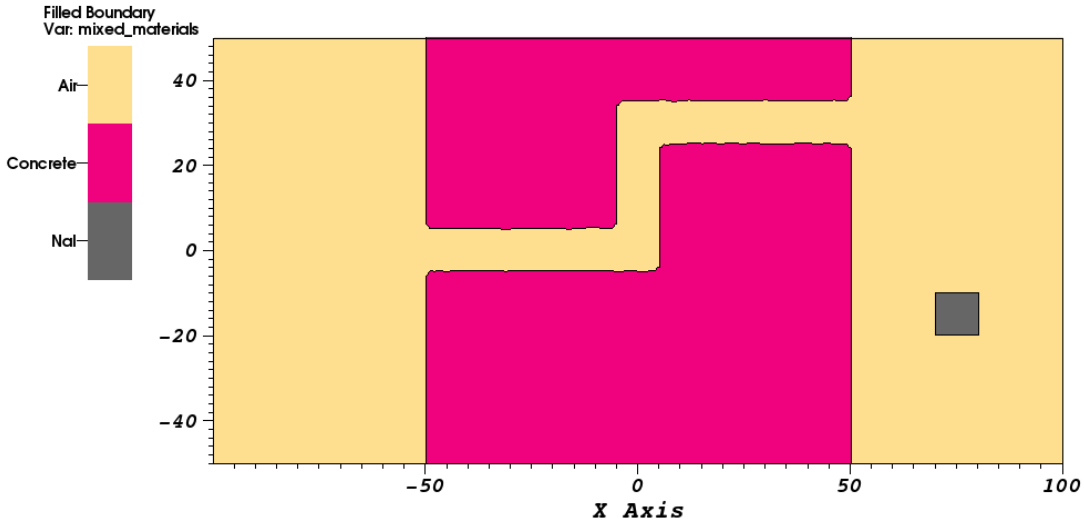

Figure 4.1: Single turn labyrinth geometry.

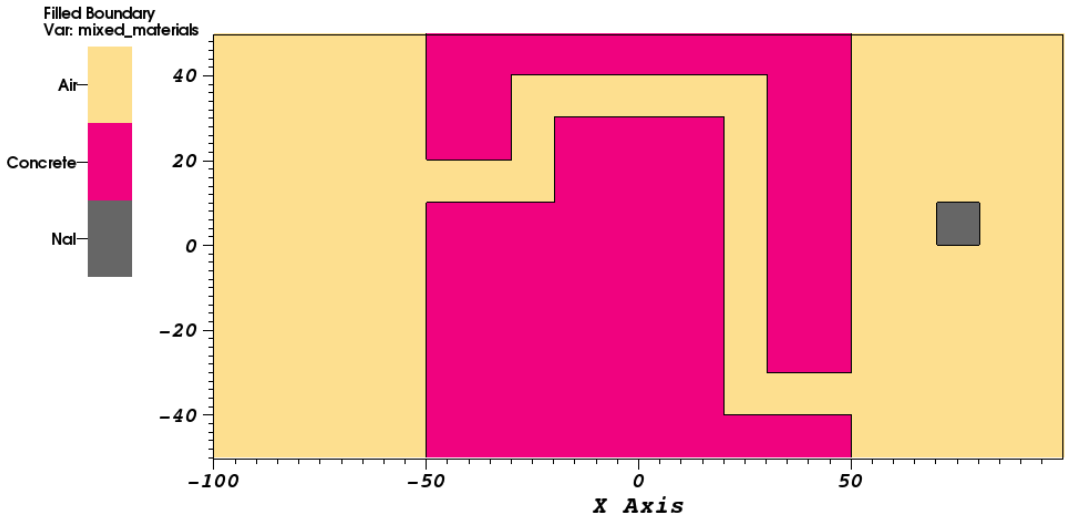

Figure 4.2: Multi-turn labyrinth geometry.

U-shaped corridor

The U-shaped corridor illustrated in Figure 4.4 is somewhat similar to the maze variants from Figs. 4.1 and 4.2. On the left-hand side of the corridor there is a point source emitting

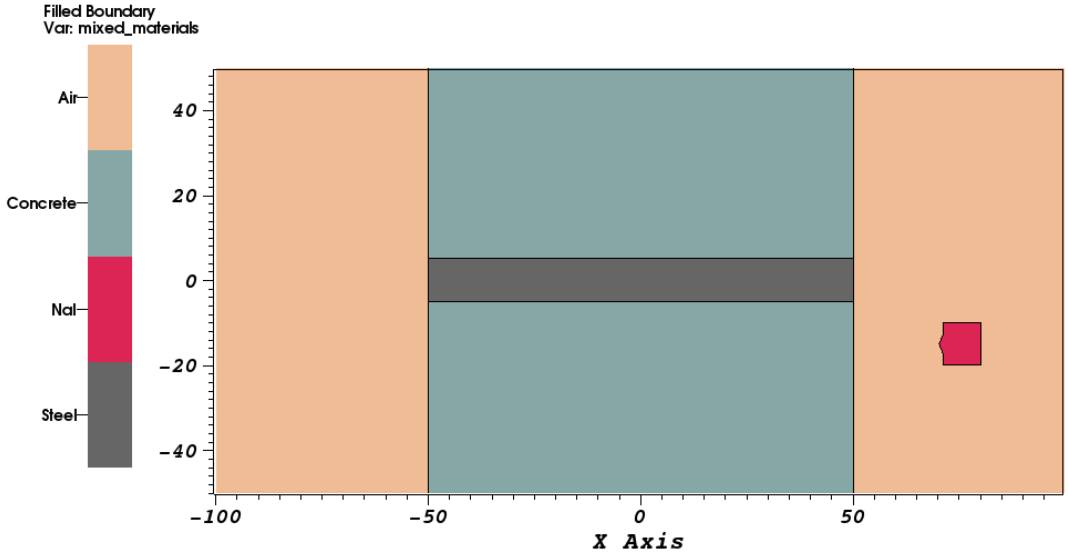

Figure 4.3: Steel plate embedded in concrete.

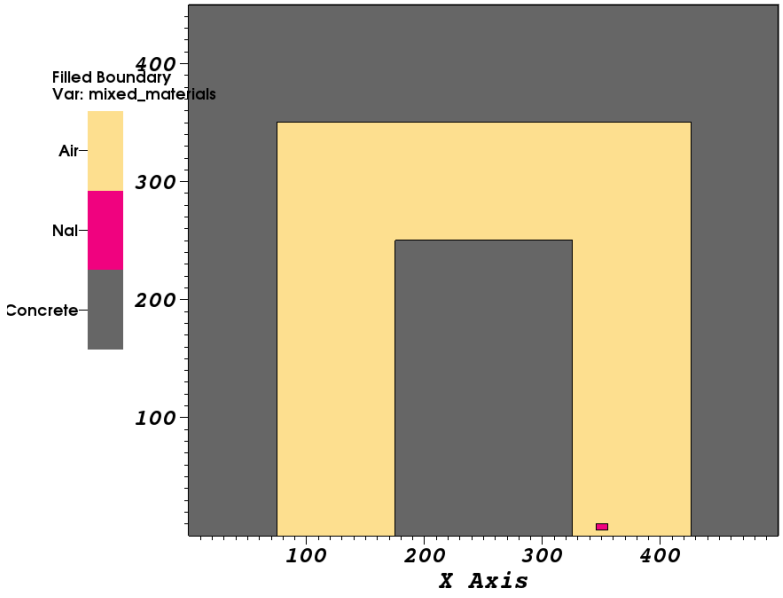

Figure 4.4: U-shaped corridor in concrete.

a Watt spectrum of ^{235}U neutrons. The right leg of the corridor has a NaI detector. Without the large air voids in the labyrinth variants, the U-shaped corridor will have less prominent

ray effects. The heterogeneity between the air and concrete will preferentially transport particles through the air, and particles interacting with the concrete will downscatter in energy.

Concrete shielding with rebar

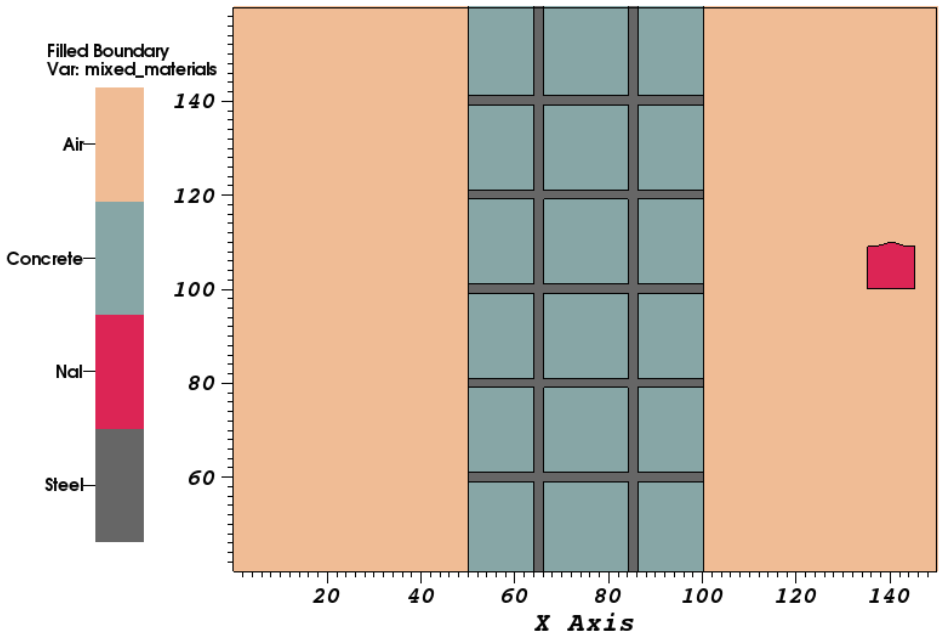

(a) Slice at $y = 100$ centimeters

The shielding material illustrated in Figure 4.5 is built off of the steel structural beam problem in Figure 4.3. However, this is a more realistic illustration of rebar in concrete. In this problem, a NaI detector is used to measure the response on the right hand side of the problem in yellow. The source is both space- and energy-dependent, emitting a Watt spectrum of neutrons characteristic of ^{235}U fission, and is distributed in a 100x160 centimeter plate on the left hand side of the problem. The source is monodirectional in $+x$. The two images provided show different xy-plane cutaways of the shielding, with steel rebar running through the concrete in different directions. This problem will have angular dependence, but preferential flowpaths through the concrete are not directed towards the detector location on the other side of the shielding in some of the rebar. This problem has material heterogeneity both in the concrete and between the concrete and air. This problem is highly scattering from the concrete, and is unlikely to have ray effects without a strong single preferential flowpath through the shield.

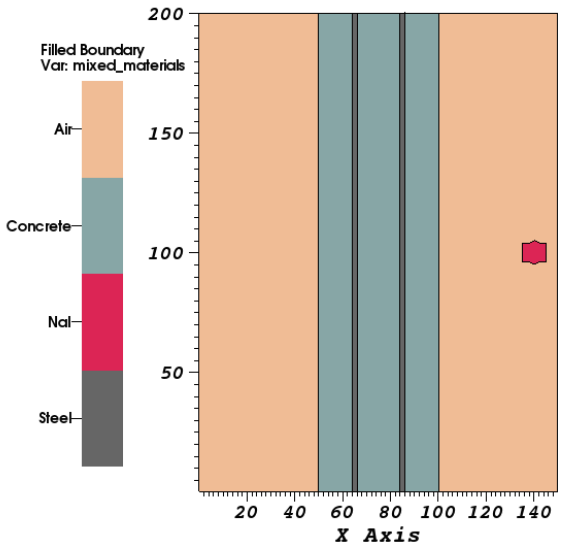

(b) Slice at $z = 105$ centimeters

Figure 4.5: Concrete shielding with rebar.

Nuclear medicine therapy room

A small application problem relevant to the interests of this project is the therapy room illustrated in Figure 4.6. This room has concrete walls, a water-based phantom that is being irradiated by a monodirectional source in the room, and a hallway where a therapy technician might walk. In a CADIS run of this problem, we seek to calculate the response in the technician in the hallway from particles that are not absorbed by the patient in the room. Because this problem is primarily air with concrete borders, it will have strong streaming effects in the air. Particles that do make it to the technician will be produced by emission from the patient in the room, by scattering off air or by scattering off walls. Because of the high fraction of air in this problem, we also anticipate ray effects to occur. While there will be scattering in this problem, it will not be as strong of an effect as other characterization problems.

Now that the broad subset of characterization problems have been described, the physics that each contains is summarized in Table 4.1. The table illustrates that it is difficult to separate one cause of flux anisotropy from another in a characterization problem. This is especially true in generating a problem that has ray effects without streaming paths, and in constructing a highly scattering problem that has preferential flow paths but does not have material heterogeneity. This is a deficiency of the characterization problem construction, and is certainly an area that may be improved upon in future work.

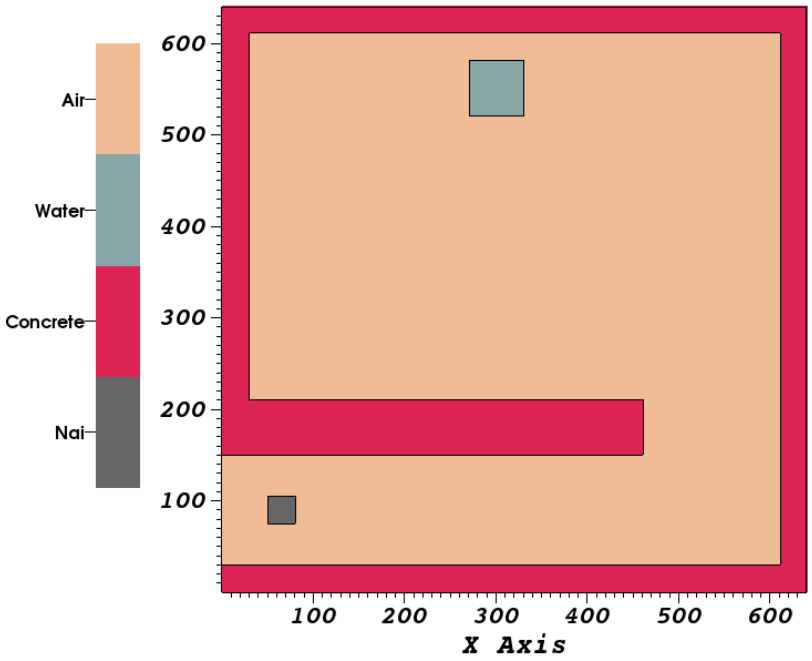

Figure 4.6: Therapy room geometry.

Problem Name	Problem Coverage				
	Streaming Paths	Highly Scattering	Material Hetero-geneity	Monodi-rectional Source	Ray Effects
Single turn labyrinth	x	x	x		x
Multi-turn labyrinth	x	x	x		x
Steel plate		x	x	x	x[†]
U-shaped corridor	x	x	x		
Shielding with rebar		x	x	x	
Therapy Room	x		x	x	x

[†] May have ray effects in low density region exiting the metal plate, but effects will be less pronounced than other problems.

Table 4.1: Anisotropy-inducing physics of each of the characterization problems. Each identified anisotropy-inducing physical metric is used in different combinations for the characterization problems. This will help to aid in extrapolating to which real problems the Ω-methods may be applied.

4.1.3 Introduction to Data Visualization and Analysis

At this point several characterization problems have been identified for their properties in inducing anisotropy in the particle flux. Prior to going through the results for each of the characterization problems, this section shows how the data for each problem is presented and walks through the reasoning behind this approach to the analysis. This starts with example tables and figures of the FOM and tally results. Then, plots explaining the anisotropy metrics follow. This is accompanied by a discussion about how the anisotropy metrics can be related to the FOM and the relative error.

Figure of Merit and Timing Tables

In Section 3.2.2 several equation variants of the FOM were presented as quantifications of method success. The FOMs for each characterization problem are presented in tabular form, similar to Table 4.2. As discussed in that section, the FOM is dependent on the relative error and the time to obtain that relative error. For the hybrid cases, six different FOMs will be presented: three FOMs based on the tally average relative error, the tally maximum relative error, and the tally minimum relative error, and two FOMs based on the Monte Carlo runtime and the hybrid runtime. The unbiased analog Monte Carlo does not have a deterministic runtime, so only the three FOM variants based on the relative error are presented for those runs. When analyzing the results in the FOM table for each characterization problem, consider that the tally average relative error is calculated from all particles contributing to all tally bins in the problem. Thus the FOM reported for the tally average relative error may be outside of the bounds of the tally minimum or the tally maximum relative error. Table 4.2 summarizes which equations were used to calculate each FOM; each equation number is noted in brackets.

	CADIS or CADIS-Ω		analog
FOM Variant	MC (3.15a)	MC_{hybrid} (3.15b)	MC
tally avg (3.12a)	$\text{FOM}_{avg,MC}$	$\text{FOM}_{avg,hybrid}$	$\text{FOM}_{avg,MC}$
max RE (3.12b)	$\text{FOM}_{max,MC}$	$\text{FOM}_{max,hybrid}$	$\text{FOM}_{min,MC}$
min RE	$\text{FOM}_{min,MC}$	$\text{FOM}_{min,hybrid}$	$\text{FOM}_{min,MC}$
time (mins)	T_{MC}	T_{hybrid} (3.13)	T_{MC}

Table 4.2: Table of FOM variants used to measure Ω performance. Relevant equations can be found in Section 3.2.2 and are referenced in the table in parentheses.

Tables calculating the FOMs summarized in Table 4.2 may not have evaluated FOMS in some locations. These will be noted with a dashed line, or "–". These values will generally be in the minimum relative error section of the FOM tables, and they represent a zero relative error. This does not mean that infinite particles have been sampled (so the relative error is infinitely small), but rather that no particles have been binned for that energy bin. This

technically results in an infinite FOM, but in reality represents a bin that will never converge. Because this value will hold no meaning in our quantification of the Ω-methods' success, the infinite valued FOM is not included.

Table 4.3 reports the times used to calculate the FOM values in Table 4.2 more detail. This table is split into three vertical regions: the MCNP time spent doing Monte Carlo transport (T_{MC}), the deterministic time spent in ADVANTG/Denovo (T_{det}), and the walltime (T_{hybrid}), which is the summation of the two. The deterministic time section contains further segmentations of timing. This is because processes in ADVANTG are run using different computational resources. ADVANTG itself is a driver script that can launch a paralellized run in Exnihilo/Denovo, but it also postprocesses the Denovo fluxes into source biasing and weight window parameters. The processes exclusive to ADVANTG, like generating the biasing parameters, are performed in serial on a single processor. Conversely, all of the Denovo calculation is run in parallel on any number of cores specified by the user. To ensure that a comparable time is used when calculating the adjusted FOM, we have chosen to calculate the total walltime spent in each calculation. Thus, the parallelized clock time is multiplied by the total number of cores to obtain T_{denovo}. This quantity is summed with the runtimes of the other serial tasks to obtain the total deterministic runtime.

		CADIS time (minutes)	CADIS-Ω time (minutes)	analog time (minutes)
MCNP time	total (T_{MC})	$T_{MC,cad}$	$T_{MC,cad-\Omega}$	$T_{MC,analog}$
deterministic time	advantg time (T_{adv})	0.18	0.18	–
	denovo time (T_{denovo})	5.69	25.64	–
	dispose time	0.00	0.16	–
	omega time (T_{Ω})	–	0.66	–
	total (T_{det})	T_{adv}+T_{denovo}	T_{adv}+T_{denovo}+T_{Ω}	–
wall time	total (T_{hybrid})	$T_{MC,cad}$ + $T_{det,cad}$	$T_{MC,cad-\Omega}$ + $T_{det,cad-\Omega}$	$T_{MC,analog}$

Table 4.3: Table of differing times used to measure Ω performance. These times are used to calculate the FOMS in Table 4.2.

Two other times are listed under the deterministic time that may or may not be included in T_{hybrid}, which are T_{Ω} and $T_{dispose}$. $T_{dispose}$ is the reported times that are not included in the calculation of T_{det} in either CADIS or CADIS-Ω. It is a sum of time results that either are not important to comparing the methods–like calculating the anisotropy metrics–or times that are accounted for by other tasks in T_{det}. This prevents overlap of times and provides a

more realistic comparison between the performance of both methods.

The reported Ω time, T_Ω, is the total time spent in the tasks unique to the Ω-methods. This includes reading in the angular flux files, performing the computation of Eq. (3.1), and writing the Ω-results to a file. The Ω time, though run in Denovo, is still a serial calculation so is separated out from the total Denovo time. The Ω-method tasks at this time are not parallelized, so the clock time is treated in the same way as the reported ADVANTG time. Because the majority of the Ω-flux generation infrastructure is implemented in Exnihilo rather than ADVANTG, future expansions of the method could be parallelized for faster clock times.

Because the adjusted FOM (the FOMs labeled FOM_{hybrid} in Table 4.2) uses T_{Hybrid}, which is the total runtime of the Monte Carlo calculation (T_{MC}) and the hybrid/deterministic run preceding it (T_{det}), it will differ between the Ω-methods, standard CADIS, and standard FW-CADIS. For CADIS, T_{det} is the sum of the ADVANTG runtime and the wall time of the Denovo transport. For CADIS-Ω, this is the sum of the ADVANTG runtime, the wall time of the Denovo transport, and the time spent in the Ω-flux calculation. How each time is calculated is summarized in Table 4.3.

Beyond adding the Ω-flux compute time, CADIS-Ω will generally have much longer Denovo runtimes than CADIS. This is a combination of the Ω-methods' requirement of both a forward and adjoint calculation (recall that CADIS requires only the adjoint calculation), and that the Ω-methods require full angular flux solutions to calculate the Ω-flux. While standard CADIS has the ability to print the full angular flux solutions as CADIS-Ω, it is neither a requirement nor is it standard practice. The I/O demands to both write the angular fluxes and then read them back in is a potential bottleneck in the method based on the current implementation.

Tally Result and Relative Error Plots

Each of the problems introduced in Section 4.1.2 has a 10x10x10 cm detector in which the tally response is calculated. The tallies are discretized in energy; the tally result and associated relative error are tabulated for each energy bin. Some of this information can be inferred from Table 4.2, but seeing the distribution of the relative errors for each energy bin for each method is a useful way of seeing how effective each method is at biasing particles all of the tally bins, without time effects. As described in the previous paragraph, CADIS-Ω's deterministic time will be longer than CADIS', so the FOM_{hybrid} may be lower for the Ω-methods, even if the relative errors are better. Presenting both the relative error distribution and the FOM will provide a clear picture of the performance of the Ω-methods.

The tally results and relative errors for CADIS, CADIS-Ω, and the nonbiased analog Monte Carlo will be presented in figures similar to 4.7a and 4.7b. In the case where the relative error of the nonbiased analog Monte Carlo far exceeds the errors achieved by CADIS and CADIS-Ω, it will be omitted. The example given in Figure 4.7b shows a result where this is the case. The hybrid methods will be marked with a dashed line; the nonbiased analog Monte Carlo will be a solid line.

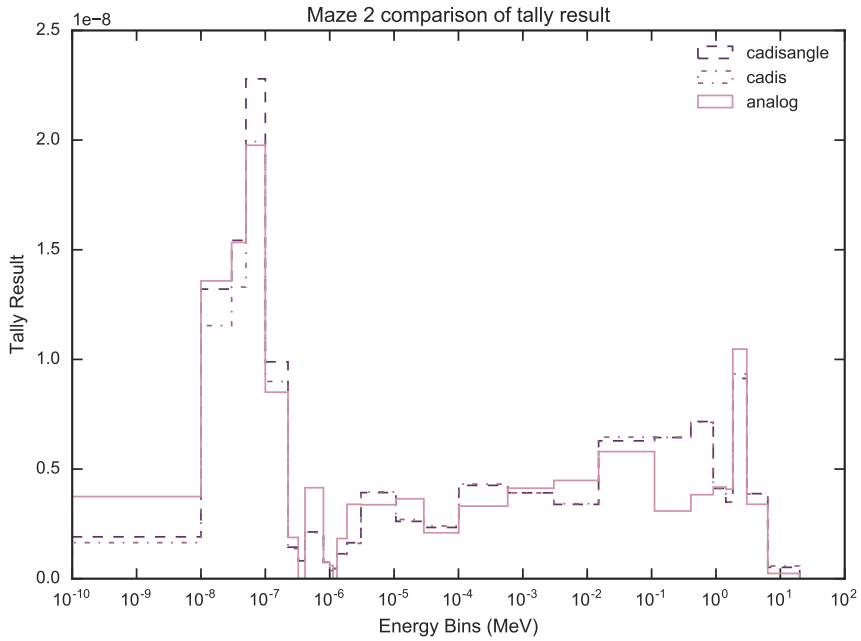

(a) Comparison between methods of the tally result.

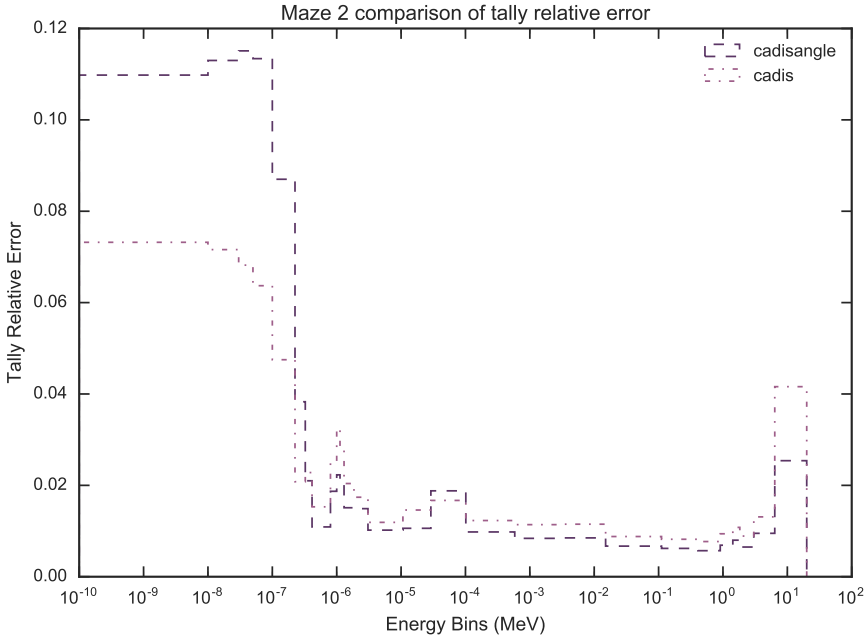

(b) Comparison between methods of the tally relative error.

Figure 4.7: Sample results for a characterization problem tally.

Anisotropy Metrics

Equations (3.6) through (3.11) in Section 3.2.1 presented several different ways by which the anisotropy of each problem could be quantified. As discussed in that section, Each metric will show slightly differing effects. For example, the ratio of the Ω- to adjoint-flux in metric two will differ significantly from the angular contributon max to average of metric three. The Ω-flux may be larger or smaller than the adjoint scalar flux depending on the directionality of the adjoint and forward particles relative to one another. If the particles are travelling in opposite directions, this will result in a larger omega flux than the adjoint flux. If they stream in the same direction (away from the tally detector, for example), then the resultant Ω flux will be smaller than the adjoint. In the case of the angular contributon max to average the distribution will have a lower limit where the maximum is very close to the average contributon flux. It can never be lower than the average. In a isotropic problem, the majority of the cells in the problem will be this ratio, whereas in a strongly anisotropic problem this distribution will shift upwards, but will still have the same limiting lower value as the isotropic case.

To illustrate the effect of how different the anisotropy metrics' distributions are, Figure 4.8 shows stripplots for all of the anisotropy metrics for three different energy groups in one of the characterization problems. The effects of thermalization–and consequently more induced isotropy–on each of the metrics can be seen clearly as one scans from Fig 4.8a to 4.8c.

The adjoint anisotropy metric, the forward anisotropy metric, and metric three are all shifted by a factor of 4π. Their natural lowest limit should be near unity but all lie lower. This may be corrected in the future, but for the purposes of this analysis we are more interested in the relative distribution and the consistent factor of 4π is not important to that effect.

A stripplot shows distinct data points, but easily can be overwhelmed if the full number of cells is used in a single strip. The figures in 4.8 contain a random selection of 1500 data points from the full anisotropy datasets, which is only a small fraction of the number of cells in the characterization problem meshes. There are other ways to visualize the full distribution of the dataset. Figure 4.9 shows three modes by which an anisotropy metric can be visualized. These plots, unlike Figure 4.8, show a single metric but all energy groups. The highest/fastest energy group is plotted in deep red, and the lowest or most thermal energy group is shown in blue.

All three subfigures in 4.9 show the effects of thermalization on the chosen metric distribution and density. The stripplot of 4.9a is a clear representation of the density, but not much more can be ascertained about the distribution of the metric. Figure 4.9b has box and whisker plots that show the data quartiles, the mean, and outliers. However, in the case where the distribution is heavily towards a limiting value, the mean is hard to separate from the distribution. Further, no data on how the metric is distributed beyond the quartile markers is provided. The violin plot of Figure 4.9c is a hybrid of the former two plots. The width of the violin is related to the density of values, but inside the violin the limits of the

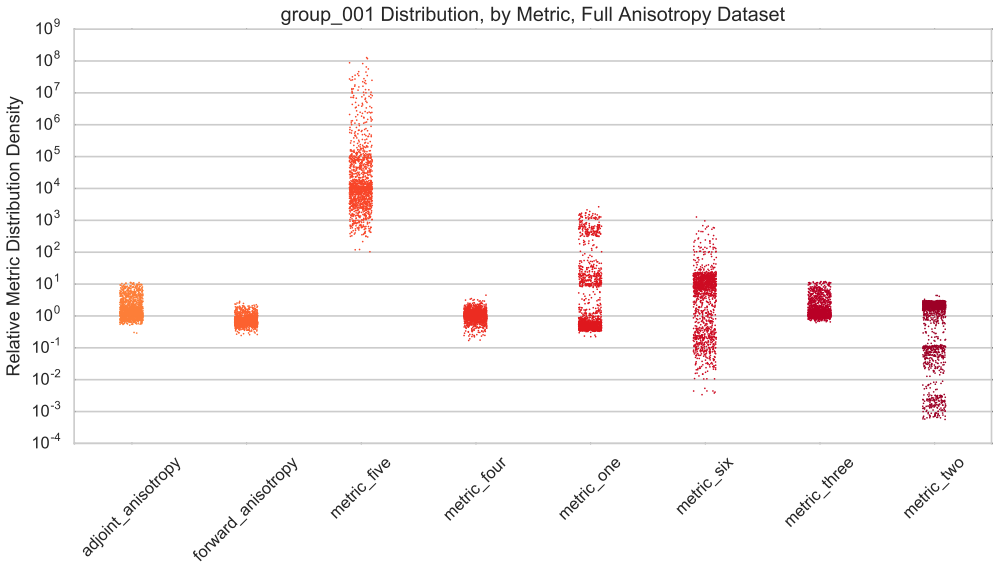

(a) Example distribution of anisotropy metrics for fastest energy group.

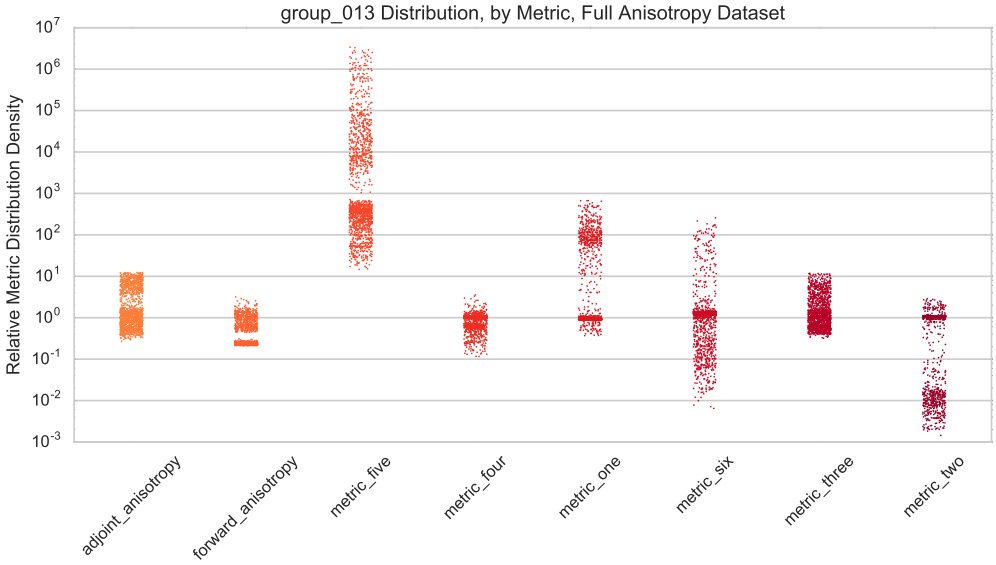

(b) Example distribution of anisotropy metrics for epithermal energy group.

box plots are marked in black. The violin limits extend to the outliers.

The analysis for each of the characterization problems look at the result for the tally average relative error, the tally maximum relative error, and the tally minumum relative error. Because we are interested in how the relative error in each energy bin changes with respect to CADIS-Ω and CADIS, the plots showing the distributions over all energy groups for a single metric is generally more applicable than the plots for a single energy group but with all metrics. As a result, future plots of the metrics will be in the style of those in Figure

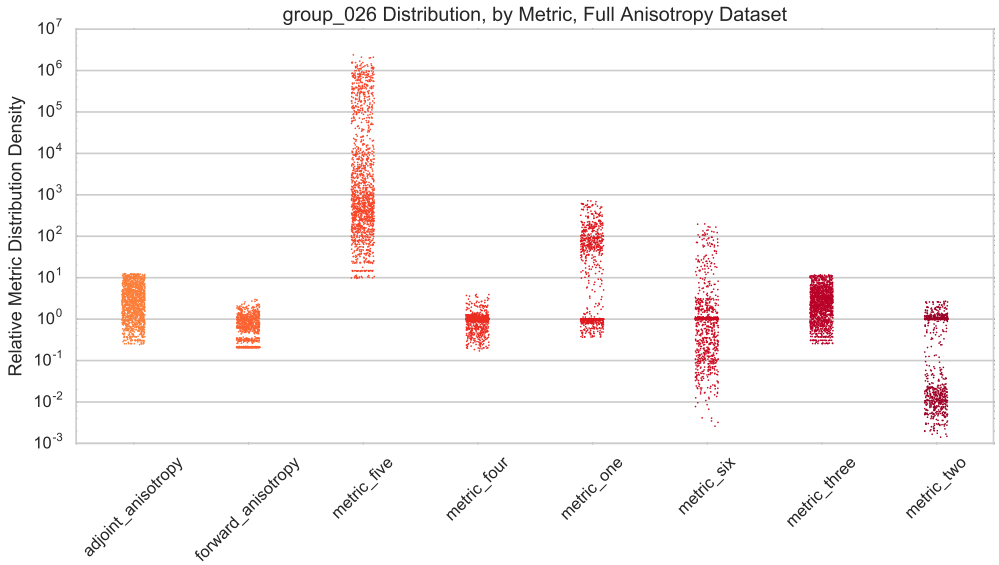

(c) Example distribution of anisotropy metrics for thermal energy group.

Figure 4.8: Example distribution of all anisotropy metrics for highest, intermediate, and lowest energy groups.

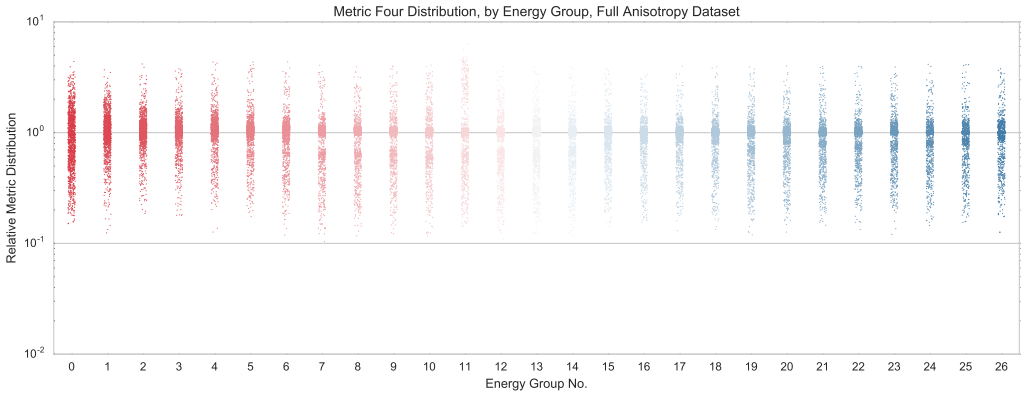

(a) Example distribution of M_4, all energy groups, strip plot.

4.9 rather than 4.8.

Filtered Anisotropy Metrics

Beyond plotting the anisotropy metrics as a function of energy group, we are interested in how the relative error or FOM will respond as a function of each metric. However, not all cells in the problem are as important as others to contributing to the tally. A cell on the problem boundary is very unlikely to contribute to the tally result when compared to a cell

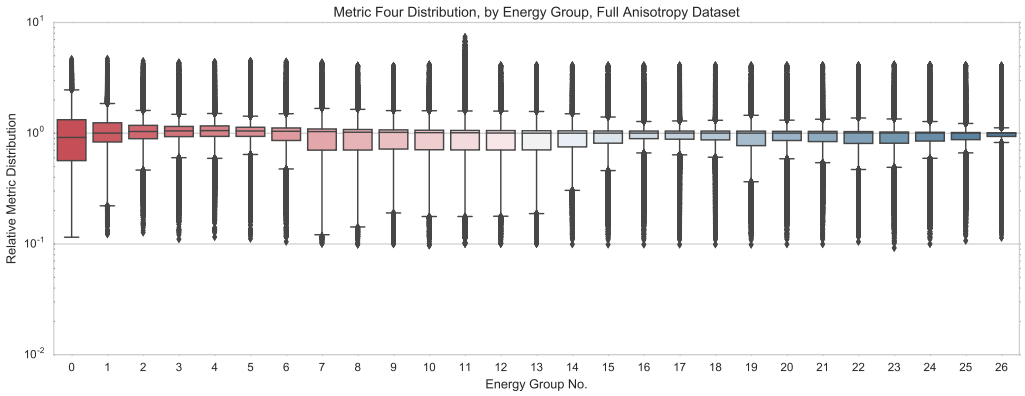

(b) Example distribution of M_4, all energy groups, box plot.

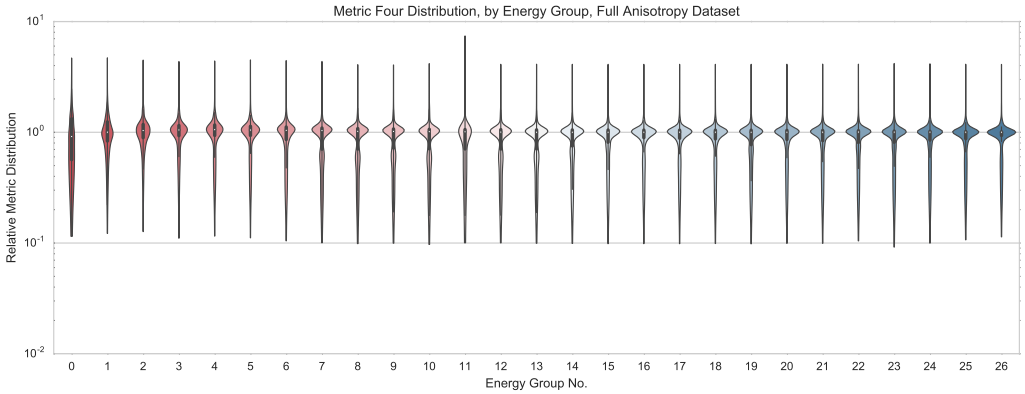

(c) Example distribution of M_4, all energy groups, violin plot.

Figure 4.9: Different ways of visualizing M_4 for a characterization problem.

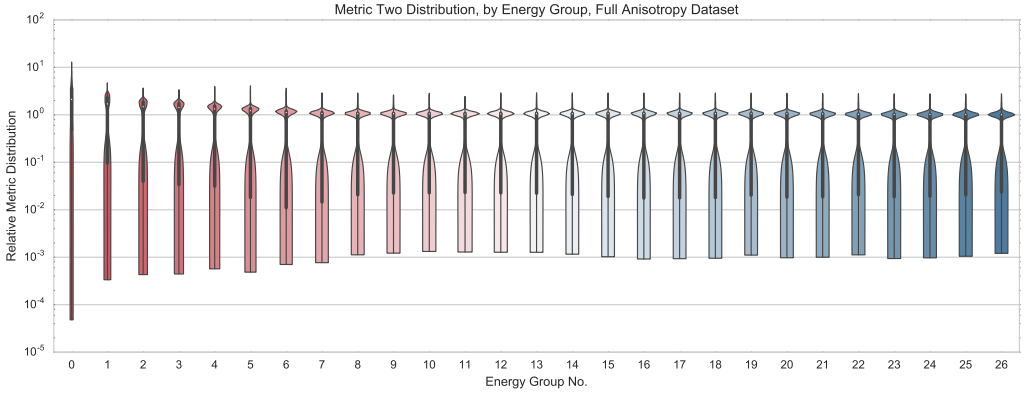

(a) Example distribution of M_2, all energy groups, violin plot

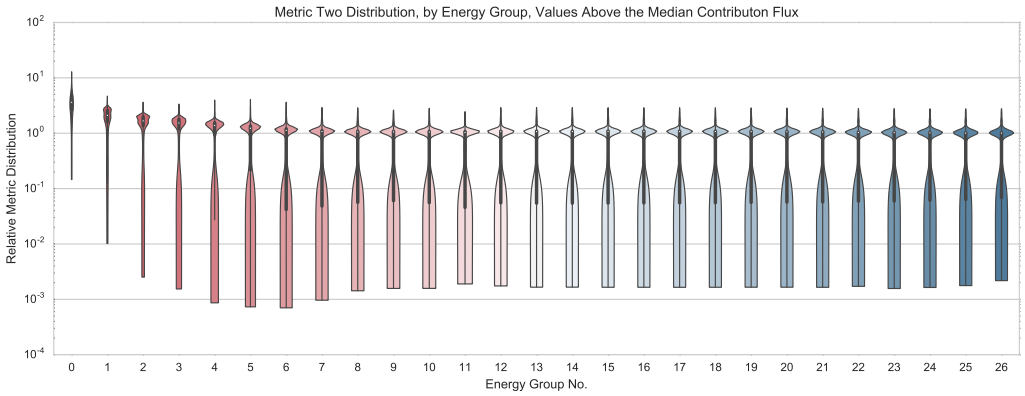

(b) Example distribution of M_2, all energy groups, violin plot using only datapoints above the median metric value in each energy group.

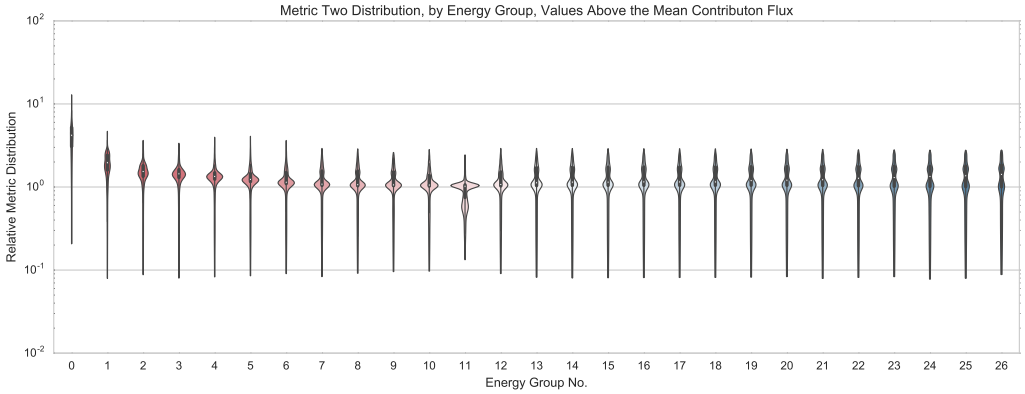

(c) Example distribution of M_2, all energy groups, violin plot using only datapoints above the mean metric value in each energy group.

Figure 4.10: M_2 violin plots using different selections of the metric data.

next to the adjoint source. As discussed in Section 2.2.3, the contributon flux measures the response importance of a cell. By selectively choosing anisotropy metrics from cells that are likely to induce a response, some of the noise of less important cells can be cut out.

To consistently cut out the same number of datapoints across all metrics, we have chosen to use a filtering algorithm based on the contributon flux in each cell. The first filter is choosing metric values from cells where the contributon flux is above the problem median contributon flux. This median is evaluated separately for each energy group to ensure that the same number of cells in each group is plotted. The second filter is choosing metric values from cells where the contributon flux is above the problem mean contributon flux. Again, the mean is computed separately for each energy group such that energy groups with higher contributon fluxes do not cut out important flux values from a different energy group.

However, unlike the median filter a different number of cells for each energy group will be filtered. This is dependent on the skew between the contributon mean and median value for each energy group. Because the filter is evaluated based on the contributon flux, it can be applied to each metric consistently, meaning that the same number of cells are filtered out between different metrics.

Figure 4.10 shows the effects of cutting out data from unimportant cells on the M_2 distribution. The first figure in the series, 4.10a, is the M_2 full distribution. As discussed previously, M_2 will be above unity in cells where the foward and adjoint angular fluxes travel in opposing directions, and will be below unity in cells where they travel in the same direction. Very unimportant cells should be below unity. Applying the first filter–selecting values above the contributon median–to this distribution results in Figure 4.10b. The bottom tails of all of the distributions have been shortened, but still many unimportant cells remain. This should be expected, as only half of cells have been removed. Applying the second filter results in Figure 4.10c. The unimportant tails have been almost completely removed from the M_2 distributions. Further, features in the metric distribution once obviscated by the tails are now visible.

Improvement Factor Correlations with Anisotropy

Now that a way of visualizing the metric distributions has been presented, we seek to find how the metric distributions relate to the relative error or FOM for a given problem. First, an improvement ratio for the relative error and FOM will be defined. For the relative error it is

$$I_{RE} = \left.\frac{RE_{CADIS-\Omega}}{RE_{CADIS}}\right|_{E_g}, \tag{4.1}$$

and for the FOM it is

$$I_{FOM} = \left.\frac{FOM_{CADIS-\Omega}}{FOM_{CADIS}}\right|_{E_g}. \tag{4.2}$$

These will be henceforth be referred to as the relative error and FOM improvement factors. With this definition of the improvement in the FOM or the relative error from CADIS to CADIS-Ω, we now have a comparison between the updated and standard methods. By relating this metric to the anisotropy metrics, we can see how anisotropy of the problem influences the improvement in the relative error or the FOM.

There are several ways in which the improvement factor I_{RE} or I_{FOM} may be compared against the anisotropy metrics. The first are against the metric mean and median values. A plot of I versus either of these values should look very simiar, with some shifting depending on the distribution. However, if the mean and median are shifted significantly, this would indicate a skew of the distribution. This skew may also be correlated with either of the I values. Last, it is possible that the spread of metric values may be correlated with the I factor. Figure 4.11a is an illustration of how I can be plotted with each of these measurements of the metric distribution.

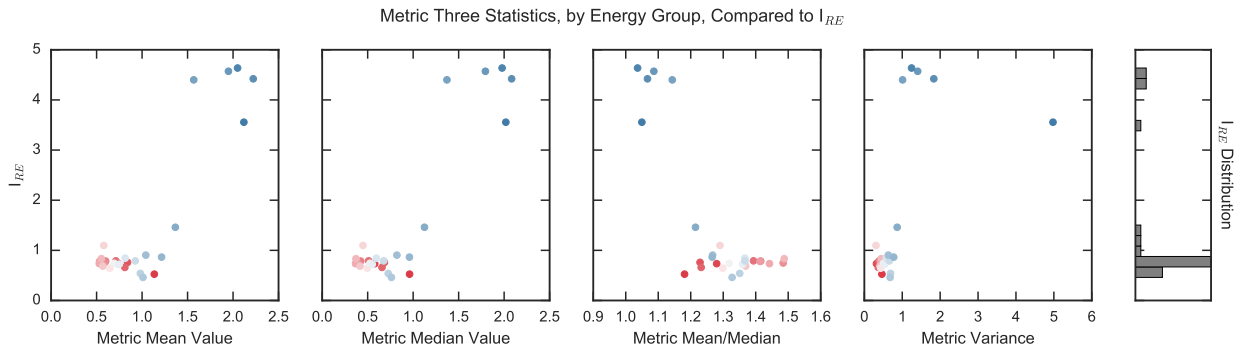

(a) M_3 average, mean, skew, and variance plotted against the relative error improvement I_{RE}

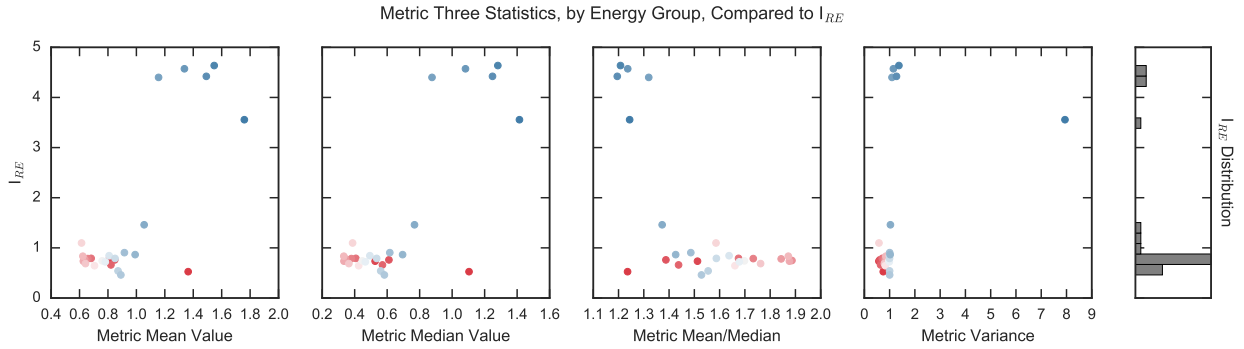

(b) M_3 data selection above the metric median for each energy group, value average, mean, skew, and variance plotted against the relative error improvement I_{RE}

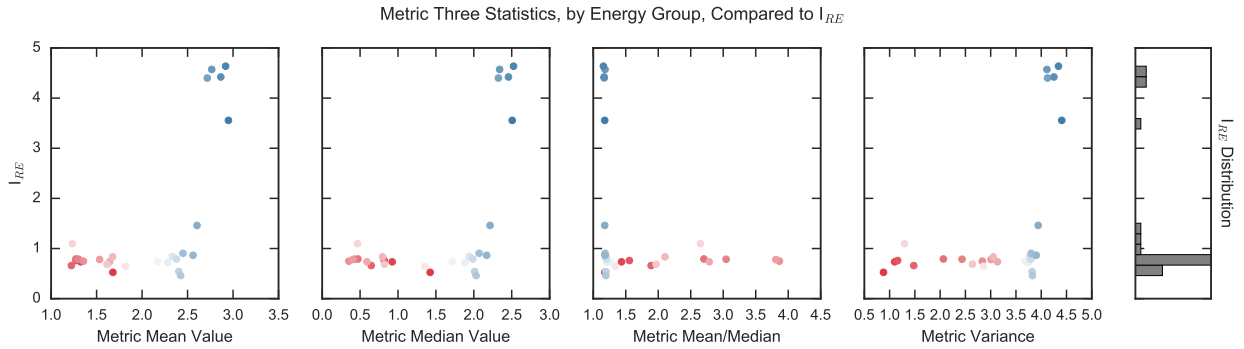

(c) M_3 data selection above the mean for each energy group, value average, mean, skew, and variance plotted against the relative error improvement I_{RE}

Figure 4.11: Sample scatterplots of the M_3 distribution against the relative error improvement factor, I_{RE}.

Similar to using the filtering algorithms in Figure 4.10, the data in the statistical trend plots can also be filtered. The subfigures in 4.11 illustrate how filtering out the data by the

contributon flux influences the location of I_{RE} for each energy group. Figure 4.11b calculates the metric mean, median, skew, and variance for each energy group using only metric values in cells above the contributon median. Conversely, Figure 4.11c calculates the metric mean, median, skew, and variance for each energy group using only metric values in cells above the contributon median value.

The dots in each plot correspond to the same energy groups plotted in 4.10. That is, the lowest energy is plotted in blue and the highest in red. Note that this type of plot is possible because the Monte Carlo tally has been discretized to have the same binning as the the deterministic code. It would be far more difficult if the energy bin widths of the Monte Carlo tally did not match the deterministic code.

The data that will be presented for each characterization problem can be subdivided into three distinct categories: data primarily obtained by the Monte Carlo calculation, data primarily obtained by the deterministic calculation, and data that is a combination of both. The FOM values using Monte Carlo runtimes, for example, is in the first category. The anisotropy metrics presented in Section 3.2.1 are an example of a determinstic-exclusive dataset. The results presented in Figure 4.11 are a combination of both deterministic and Monte Carlo-influenced results. In studying the Ω methods, we seek to understand how the Ω methods' performance influence the Monte Carlo results. Beyond observing the FOM and relative error distribution obtained in the Monte Carlo, the anisotropy metrics will provide another avenue by which to investigate Ω-method performance.

One may have deduced that the results for the characterization problems and the subsequent angle sensitivity study will be substantive. Only the most pertinent fraction of the available data will be presented with each problem in Sections 4.2 and 4.3. For example, in most cases only a single figure–and perhaps only a single metric–from the three presented in 4.11 will be presented for a particular problem, because only one will show a trend relevant to the Ω-methods' performance. A more extensive set of data and figures is accessible in the public repositories listed in Appendix A.

4.2 Characterization Problem Results

To quantify the Ω-method success for a variety of anisotropy-inducing physics, we will present various forms of the Figure of Merit, as described in Section 3.2. In the preceding subsections, a subset of flux anisotropy-inducing physics have been identified and a subset of problems that contain these physics have been conceived. In this section, the results for CADIS-Ω, CADIS, and nonbiased Monte Carlo will be presented for each of these problems. Explanations on the performance of the Ω methods will accompany the results for each problem. In some cases, variants of problems were run to confirm or refute observations seen in other problems.

4.2.1 Computational Specifications

As noted in a number of the previous sections, hybrid methods require both a deterministic and a Monte Carlo calculation to obtain a problem result. These transport codes require different computational parameters to obtain an answer. For the characterization problems the computational parameters are summarized in Table 4.4; the parameters for the deterministic and Monte Carlo calculations are demarcated in the table.

Parameter Type	Parameter Value
ADVANTG Values	
P_N Order	3
Quadrature Type	Quadruple Range
Quadrature Order	10
Spatial Solver	Step Characteristic
Energy Group Library†	27G19N
Boundary Conditions	vacuum
MCNP Values	
Particle Count	$1e7$
Boundary Conditions	vacuum

† Parameter type that has no default in ADVANTG.

Table 4.4: Default simulation values for the characterization problems. The values for ADVANTG primarily signify parameters used to run Denovo, with exceptions for calculating biasing parameters, which is done exclusively in ADVANTG. MCNP-specific values are those used for Monte Carlo runs.

The first portion of the table summarizes the values used by ADVANTG. Note that these values all pertain to the Denovo deterministic solver, which is set up by ADVANTG. The parameter types marked with a dagger have no default in ADVANTG. We have chosen to use a relatively course 27 group energy group library. Because the characterization problems are meant to identify the method's performance pertaining to flux anisotropy, and we expect the energy group structure to have less of an effect on anisotropy conditions than other parameters, we opted for a computationally inexpensive energy group mesh for the deterministic solver. Further, this group library was designed for radiation shielding applications, so it applies to the majority of the characterization problems.

The boundary conditions for all of the characterization problems will be vacuum. At this time, ADVANTG does not support reflective or mirror boundary conditions so this is a limitation in application space that we cannot address at this time. The Monte Carlo code we use does support vacuum boundary conditions, but a discrepancy in boundary conditions

between deterministic and Monte Carlo calculations would result in the simulation of a fundamentally different problem.

Unless noted, the values in this subsection of the table are ADVANTG default values. They are a good initial choice for characterization of the method because they are often chosen as the parameters for hybrid methods studies by experienced and inexperienced ADAVANTG users. Further, these values are defaults in ADVANTG for their computational stability, such as not having negative valued weights or fluxes, stable convergence, a relatively fast time to a solution, et cetera. Due to the good properties exhibited by the solver options and because users first using the Ω-methods are likely to choose these values, the values in Table 4.4 will be used for the characterization of the Ω-methods.

The latter section of the table summarizes the Monte Carlo code MCNP values for each of the problems. The value of $1e7$ particles as a particle cutoff was chosen because it made the error bins in the majority of the nonbiased Monte Carlo characterization problems less than 100%. In some problems that are extraordinarily difficult for Monte Carlo to solve without biasing, there were tally bins with very high errors. In the following subsections they will be clearly indicated and their results will not be plotted so as to not obfuscate the CADIS and CADIS-Ω results. Time cutoffs were not chosen because we decided to measure how effective the Ω methods were at reducing the variance per particle. Depending on the flux maps generated from CADIS and CADIS-Ω, the time to transport a finite amount of particles may vary. As a result, the reported times from a simulation can tell us whether the method requires more sampling than other methods in addition to how fast it takes to reach a desired relative error.

The responses in the NaI detectors of each of the problems was measured with an MCNP track length tally (f4). The tally was energetically binned to match the dataset of the multigroup dataset provided in ADVANTG, and the entire volume of the detectors were used with no spatial binning. It should be noted that while the tally is energetically binned, Monte Carlo transport is not discretized in space or energy like deterministic transport. In a nonbiased analog Monte Carlo calculation, transport is completely continuous in space, energy, and angle. In a hybrid calculation using VR parameters from a deterministic solution, the VR parameters will be discretized to reflect the solution obtained from the determinstic solver. As a result, the particle's transit throughout the problem will be a combination of sampling both continuous and discretized-energy dependent factors. Consider a particle that goes through a scattering event in shielding material. In this scattering event, the particle samples from a continuous-energy cross section and changes direction based on its energy. However, depending on how much energy it loses in the scattering event it may cross into the energy range of a lower-energy weight window and will require further sampling.

All characterization problems were run on Remus, a machine operated and maintained by the Radiation Transport and Nuclear Systems Division at Oak Ridge National Laboratory. The ADVANTG runs were run on 16 cores of a 32 core node, with 256Gb of memory. The MCNP runs were run on the same machine, with 256Gb of memory but using all 32 cores of the node.

Each problem presented in Section 4.2 will use the values specified in Table 4.4 unless

otherwise noted. Times to transport the Monte Carlo particle quantity varies between methods due to differences in sampling. Monte Carlo and ADVANTG inputs and directions on how to acquire them are provided in Appendix A.3.

4.2.2 Single Turn Labyrinth

The analysis of the characterization problems begins with the single turn labyrinth. The single turn labyrinth FOM results are summarized in Table 4.5, and are illustrated in Figures 4.12 and 4.13. The table has six FOM values for CADIS and CADIS-Ω results, and three FOM values for the analog (nonbiased) Monte Carlo results. The equations to calculate each of these FOMS is summarized in Table 4.2.

	CADIS		CADIS-Ω		analog
	MC	MC_{hybrid}	MC	MC_{hybrid}	MC
tally avg	18.6	14.9	2.36	1.56	17.4
max RE	2.76	2.21	0.481	0.318	0.0857
min RE	249	200	196	130	–
time (mins)	67.7	84.4	157	237	11.7

Table 4.5: Figure of Merit comparison for single turn maze. The relative errors used are the tally average relative error, the tally maximum relative error, and the tally minimum relative error; the times are total walltimes for the Monte Carlo calculation and the sum of the hybrid method software, the deterministic transport time, and the Monte Carlo calculation time.

		CADIS	CADIS-Ω	analog
		time (minutes)		
MCNP time	total	67.71	157.01	11.67
deterministic time	advantg_time	0.26	0.28	–
	denovo_time	16.41	78.19	–
	dispose_time	0.01	0.40	–
	omega_time	0.00	1.61	–
	total	16.67	80.08	–
wall time		84.38	237.09	11.67

Table 4.6: Detailed timing results for single turn maze.

In Table 4.5 the FOM results for CADIS, CADIS-Ω, and nonbiased Monte Carlo for the single turn maze are presented. In all cases, the CADIS FOMs are better than those obtained by CADIS-Ω. The FOMS calculated using the tally average relative error are better in the nonbiased analog Monte Carlo than CADIS-Ω as well. However, this is a

product of two effects: the time for the analog to run the same particle count is far shorter than either CADIS or CADIS-Ω. As a result, to obtain the same FOM, CADIS-Ω needs to have $R_1/R_2 = \sqrt{T_2/T_1}$ (this is from taking a ratio of the FOMs) the tally average relative error, or 0.27. Because this problem is highly scattering and many low-energy particles can make it through the concrete labyrinth, even the analog can have good sampling at low energies, resulting in a tally average FOM that reaches this threshold.

Table 4.6 contains more detailed timing information spent in each of the codes for each type of problem. We can see that the Monte Carlo runtime for CADIS-Ω is more than twice that of CADIS, and almost fifteen times that of the nonbiased analog Monte Carlo. The time to run just the hybrid/deterministic portion of the calculation is also four times longer for CADIS-Ω than it is for CADIS. These disparities in runtimes have a strong negative impact on the CADIS-Ω FOMs, which was observed in the FOM results in Table 4.5.

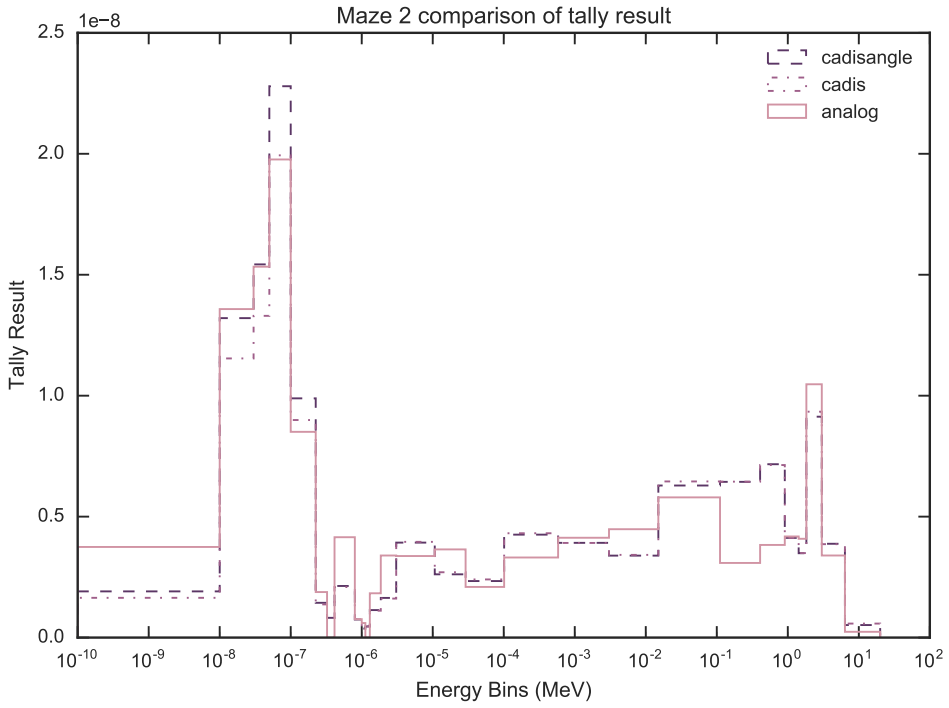

Figure 4.12: Tally results comparison between methods for single turn labyrinth.

Figures 4.12 and 4.13 show the tally result and the relative errors for each result in the single turn maze, respectively. This particular relative error plot, Figure 4.13, does not include the relative error bins of the analog result because they are significantly higher than the CADIS and CADIS-Ω results. This is further confirmed in Table 4.5, where the minimum relative error FOM is a non-tallied bin.

By inspecting Figure 4.12, one can observe that the CADIS and CADIS-Ω results are in agreement in bins greater that 10^{-7} MeV. At lower energy bins, CADIS-Ω generally

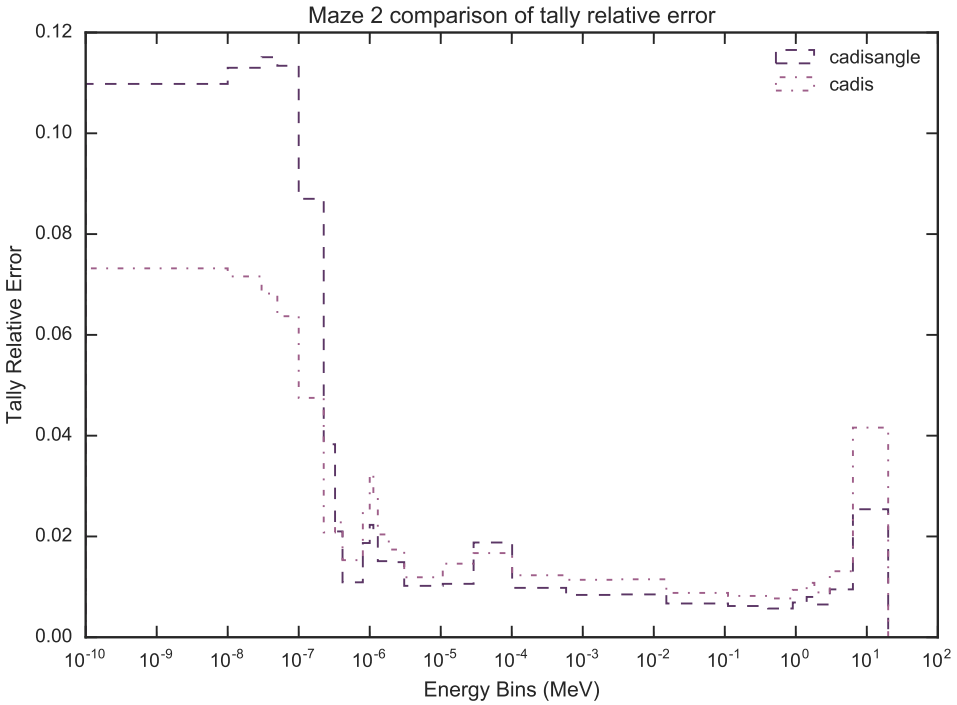

Figure 4.13: Tally relative error comparison between methods for a single turn labyrinth.

has a higher value for the tally result than standard CADIS. However, in comparing the errors for these low energy bins in Figure 4.13, CADIS has a lower relative error. This indicates that CADIS sampled many more low-weight particles than CADIS-Ω in these regions. Conversely, CADIS-Ω has a lower calculated relative error than CADIS for bins greater than $5 * 10^{-6}$ MeV. This is expected, as higher energy particles generally exhibit a stronger angular dependence than low-energy particles. In geometric and energetic regions where the angular dependence is stronger, the importance map generated by CADIS-Ω may show more of an effect in improving the relative error.

To aid in our understanding of how the Ω-method's importance map differs from the standard adjoint flux map, let us compare the flux distributions obtained by different deterministic solutions of the single turn labyrinth. Figure 4.14 shows several different flux distributions that represent the single turn labyrinth geometry. This figure is of the highest energy group for each flux type.

Figure 4.14a shows the forward flux for the labyrinth. It is clear that in this problem, particles emenate isotropically outwards from the source on the left side of the problem. Some particles travel towards the shield and enter the labyrinth. These particles travel 50cm and hit the wall in the first turn of the labyrinth. Many high energy particles reach fairly deep into the concrete past this turn, as indicated by the green channel partway through the concrete.

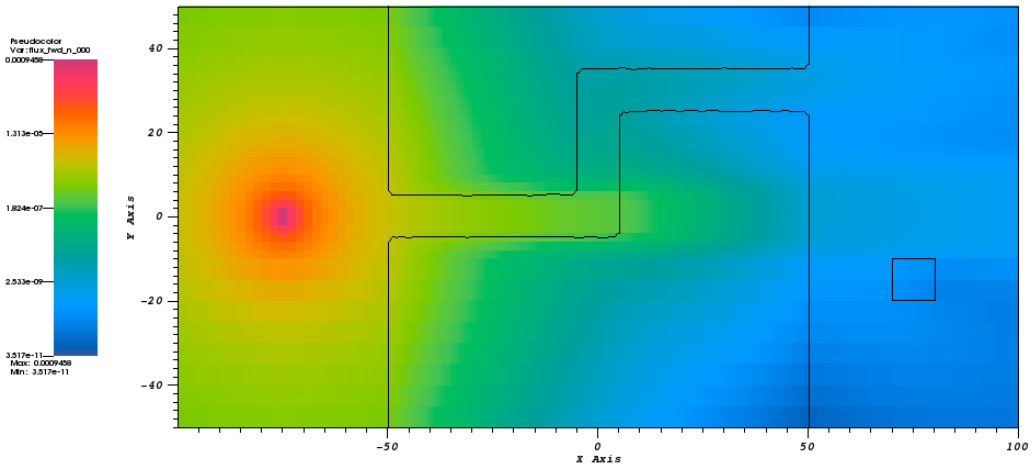

(a) Forward flux map for highest energy group, single turn labyrinth.

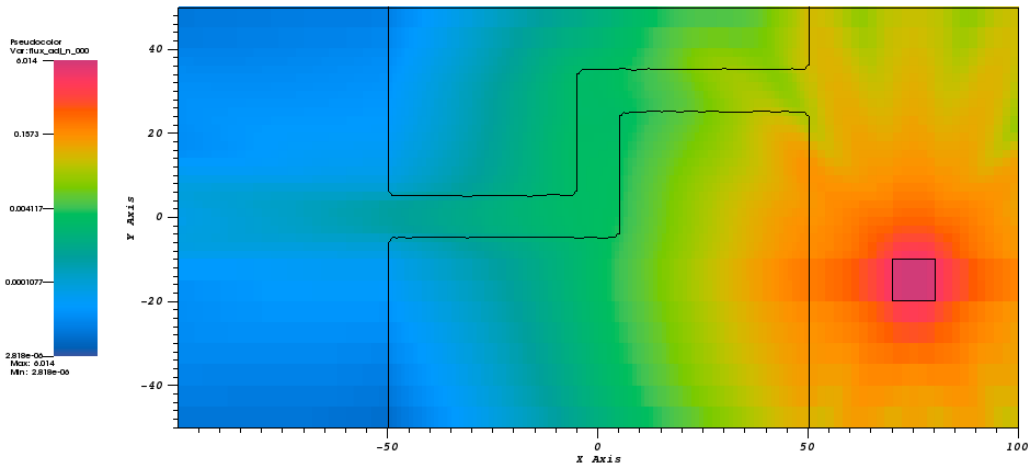

(b) Adjoint flux map for highest energy group, single turn labyrinth.

Figure 4.14b complements Figure 4.14a by showing the adjoint flux distribution for the fastest energy group. Recall that this distribution is what is used by CADIS to generate VR parameters. Particles are generated throughout the NaI detector and exit the detector

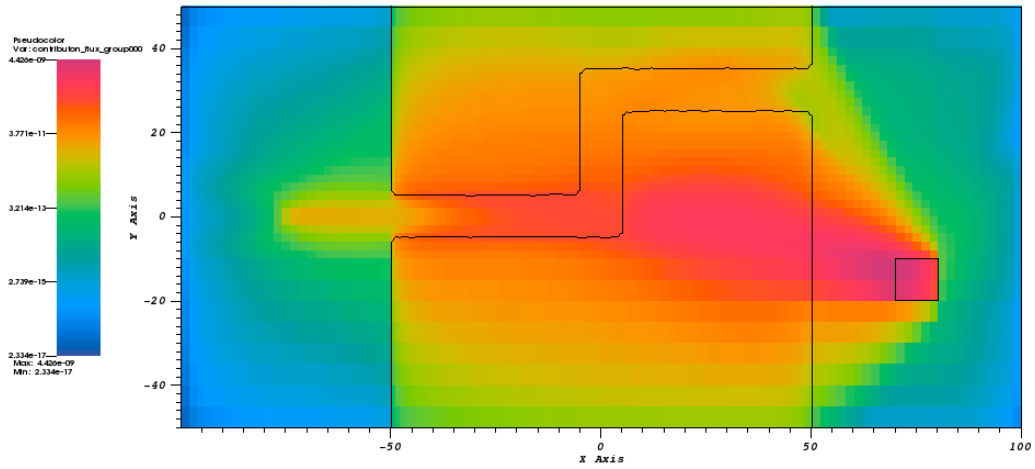

(c) Contributon flux map for highest energy group, single turn labyrinth.

in all directions. Because the source is not in line with the labyrinth entrance, particles end up colliding much closer to the labyrinth edge than in the forward distribution. There also exist some prominent ray effects in this distribution on the right hand side of the problem. In particular, the contrasting orange and green fingers of the ray effects show at least an order of magnitude change in the flux for forward particles exiting the maze in this region. In reality, the importance in this region should be close to a spherical surface some distance away from the adjoint source.

Recall that the Ω-flux is computed using the angle-integrated contributon flux in the numerator. For this problem, the contributon flux will be used to illustrate how the Ω-flux is a combination of the adjoint and the contributon flux. Figure 4.14c shows the distribution of angle-integrated contributon flux values for the single turn labyrinth. Interestingly, because so many forward particles penetrated deeply into the shield, the contributon flux points directly into this section of the shield. It is also clear that near the forward source, only particles moving in the direction towards the labyrinth entrance contribute to a high contributon flux. In the left-side of the labyrinth, we can observe directional importance in the labyrinth channels, but in the first turn this directional importance is no different than the concrete barriers surrounding the channels.

Figure 4.14d shows how the Ω-flux is built off of the adjoint and contributon fluxes by showing the Ω-flux distribution for the single turn labyrinth. Comparing this figure to 4.14c, the majority of high flux regions are pushed back towards the NaI detector. The flux gradient exiting the maze does not span as many orders of magnitude as it did in the contributon flux plot, too. Further, the importance of particles does not remain as high or

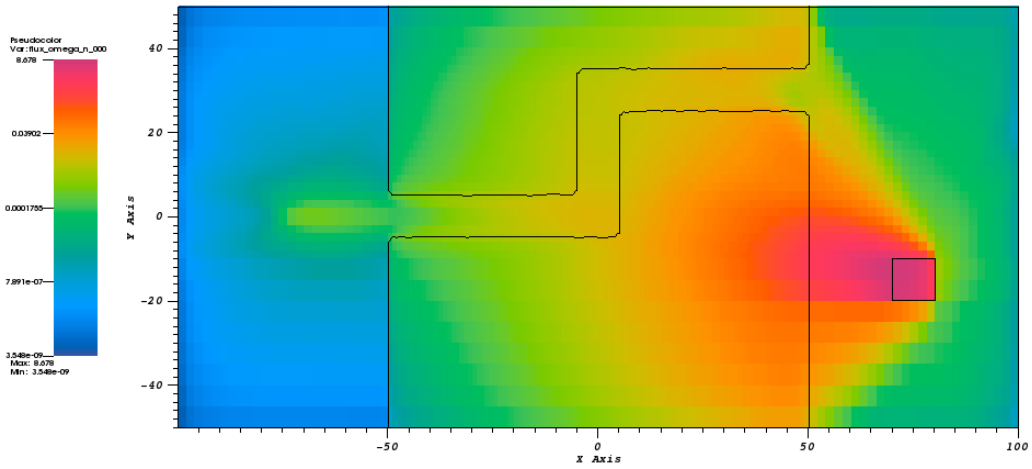

(d) Ω-flux flux map for highest energy group, single turn labyrinth.

Figure 4.14: Flux map slice of single turn labyrinth. Flux maps have scales normalized to maximum and minimum values for each slice; between plots the scales are not consistent. These plots show the highest energy group, group 000, for each cell in the problem midplane.

go as deep into the concrete shield as the contributon flux plot. This is because the Ω flux normalizes by the forward flux, resulting in reducing importance in regions where only the forward flux is strong. As with the contributon flux, the Ω-flux strongly reduces particle importance near the problem boundaries. Recall from Section 2.2.3 that in the contributon transport equation that the cross section becomes very high near problem boundaries, thus encouraging particles back towards the problem source and sink. Because the Ω-flux uses standard forward and adjoint transport, the cross section is not manipulated. However, the flux magnitude reflects importance consistent with contributon theory.

Both the Ω- and the contributon fluxes show a mitigation of ray effects on the right hand side of the problem. Note that there are no "fingers" of flux magnitude at distances several cm away from the NaI detector on the right side of the problem in either Figure 4.14c or 4.14d. Reducing these numerical appiritions is a positivie effect of the method. However, there exists a fairly strong gradient in flux magnitude for a particle travelling directly out of the maze exit. As a result, a particle traveling several cm of distance across this strong gradient line may move from a region of very low importance to very high importance, causing very significant sampling requirements for the Ω-importance that may not exist with the standard adjoint.

A description of filtering algorithms accompanied the discussion of the anisotropy metrics

in Section 4.1.3. The filtering algorithms are based on the contributon flux distribution in the problem, or 4.14c. Recall that the two filter matrices discussed included those from cells where the contributon flux is above the average contributon flux value, and where values are above the mean contributon flux value. For the single-turn labyrinth, the filter matrix in the highest energy group (Figure 4.14c) will use values in the orange and pink region of the figure and exclude values from the blue and green regions of the figure. As a result, only anisotropy metric values from within the maze will be used. The very anisotropic values near the edge of the problem (where significant particle streaming exists), will not be included because they are likely to be inconsequential to the tally response.

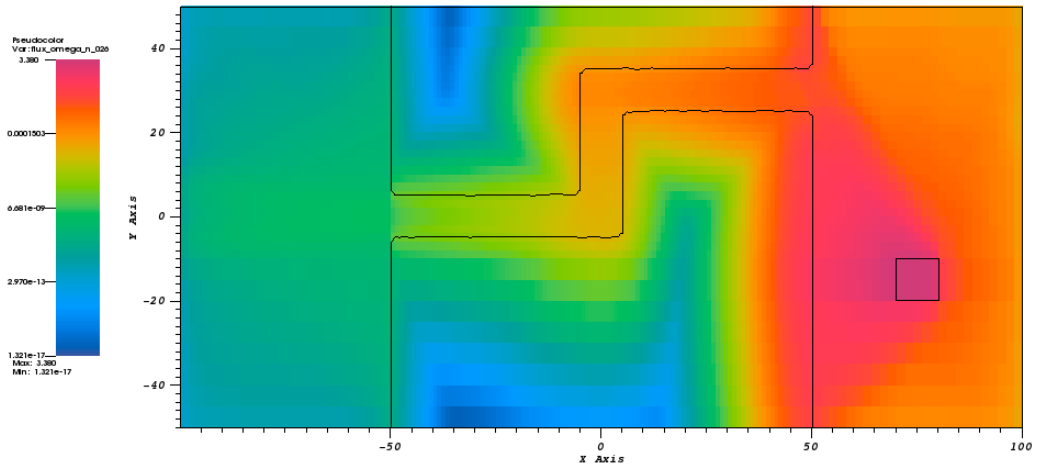

Figure 4.15: Ω-flux flux map for lowest energy group, single turn labyrinth.

Figure 4.15 shows the Ω-flux distribution for the lowest energy group. This differs quite a bit from 4.14d in that the flux in the labyrinth has a much stronger gradient once entering concrete than the higher energy group. This is expected, as the mean free path of a low energy neutron is much shorter than a high energy one, especially in a dense, hydrogenous material like concrete. As a result of the stronger flux gradient in concrete, low energy particles entering the concrete shield will be rouletted at a much greater frequency than high energy particles. Particles exiting the labyrinth also have a lower gradient of importance that they may cross than in the high energy flux map. As a result, particle splitting and rouletting in this air region will be less extreme at low energies than at high energies.

Comparing the figures of Ω-fluxes in 4.14d and 4.15, we can start to explain some of the timing behavior observed in Tables 4.5 and 4.6. High energy particles exiting the maze towards the tally detector have much longer mean free paths than the low energy particles,

and will generally show a much stronger effect in the Ω-flux in those regions. This is illustrated in Figure 4.14d. The shape of the Ω flux around the detector region is much more strongly dependent on direction in the high energy group 000 flux than it is for the lower energy group 026 flux. Despite having lower relative errors than CADIS at higher energies, CADIS-Ω has lower FOMs than CADIS for the FOMS calculated with the minimum relative error. As discussed previously, this is due to the long runtime of CADIS-Ω, which is more than twice as long as CADIS. From this, we can conclude that while CADIS-Ω is better at transporting particles in high energy regions than CADIS, achieving lower relative errors, the length of time to do so is prohibitive and achievable by CADIS should the runtimes be the same for both.

4.2.3 Multiple Turn Labyrinth

The multiple turn labyrinth is built off of the single turn labyrinth geometry. The labyrinth materials are much the same, but the geometry differs. Table 4.7 summarizes the Figure of Merit results for CADIS, CADIS-Ω and nonbiased Monte Carlo. Figures 4.16 and 4.17 show the results obtained by the track length tally in each method.

	CADIS		CADIS-Ω		analog
	MC	MC_{hybrid}	MC	MC_{hybrid}	MC
tally avg	327	248	224	71	0.054
max RE	1.46	1.11	1.02	0.322	0.0393
min RE	113	85.6	71	22.5	–
time (mins)	51.5	68	35.5	112	25.5

Table 4.7: Figure of Merit comparison for multiple turn maze.

		CADIS	CADIS-Ω	analog
		time (minutes)		
MCNP time	total	51.52	35.55	25.46
deterministic time	advantg_time	0.25	0.21	–
	denovo_time	16.28	74.85	–
	dispose_time	0.01	0.40	–
	omega_time	0.00	1.74	–
	total	16.53	76.80	–
wall time		68.05	112.35	25.46

Table 4.8: Detailed timing results for multiple turn maze.

In Tables 4.7 and 4.8 it is notable that the CADIS-Ω runtime is shorter in the Monte Carlo simulation than CADIS. This differs most of the other cases presented in this section.

However, it is also notable that because the deterministic time is so much longer for CADIS-Ω, T_{hybrid} ends up being greater for CADIS-Ω than CADIS.

Table 4.7 shows that both CADIS and CADIS-Ω outperform the analog by a factor of 10^2 or 10^3, indicating the necessity of variance reduction for a problem like this. In comparing the FOMs, CADIS slightly outperforms CADIS-Ω for all relative errors, meaning that the time to reach any relative error will be achieved faster by CADIS.

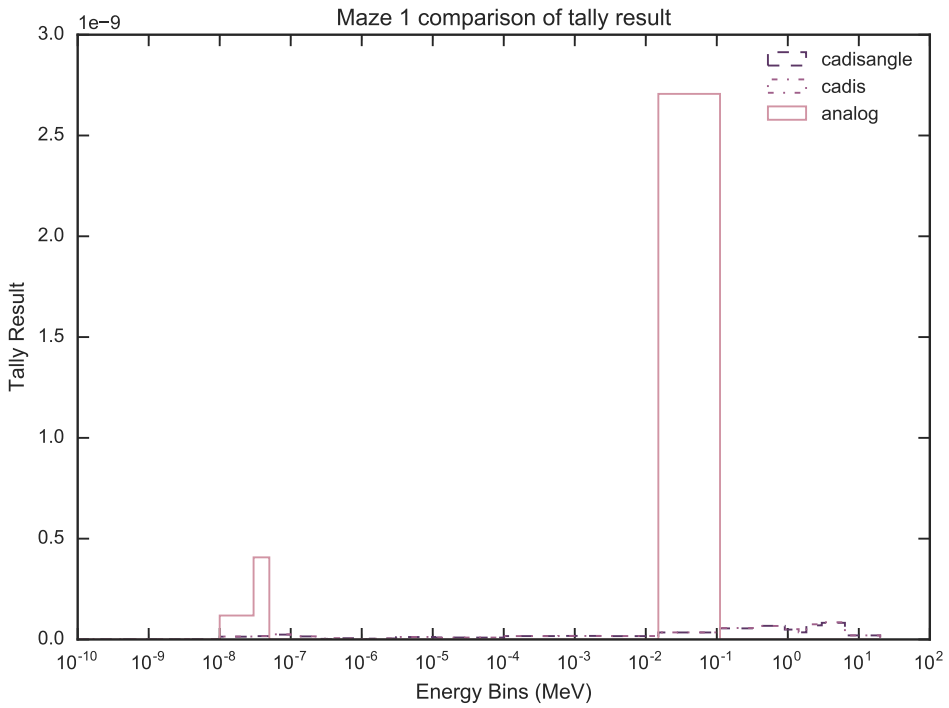

Figure 4.16: Tally results comparison between methods for multiple turn labyrinth.

Looking at Figures 4.16 and 4.17, we can see that the analog Monte Carlo results differ significantly from either CADIS or CADIS-Ω. Two distinct regions of tally bins have been recorded in the analog case: a high energy region comprised of particles that have scattered very few times before reaching the detector, and a much smaller low energy region, comprised of particles that are very thermal. These thermal particles have a very small mean free path in the concrete labyrinth, thus the majority of them were absorbed in the shield. However, given the errors on this result, these results are not trustworthy. In the case of this problem, some of what was discussed in the single-turn labyrinth is confirmed. This particular case requires that particles scatter several more times if they are to exit the labyrinth from the air duct. As a result, the spectrum is more thermal than the first case and the problem has less anisotropy from the scattering effects. As discussed in the single-turn labyrinth subsection, CADIS outperformed CADIS-Ω in problems in energy bins that had less angular dependence. Because this problem has far more scattering event, it overall has less angular

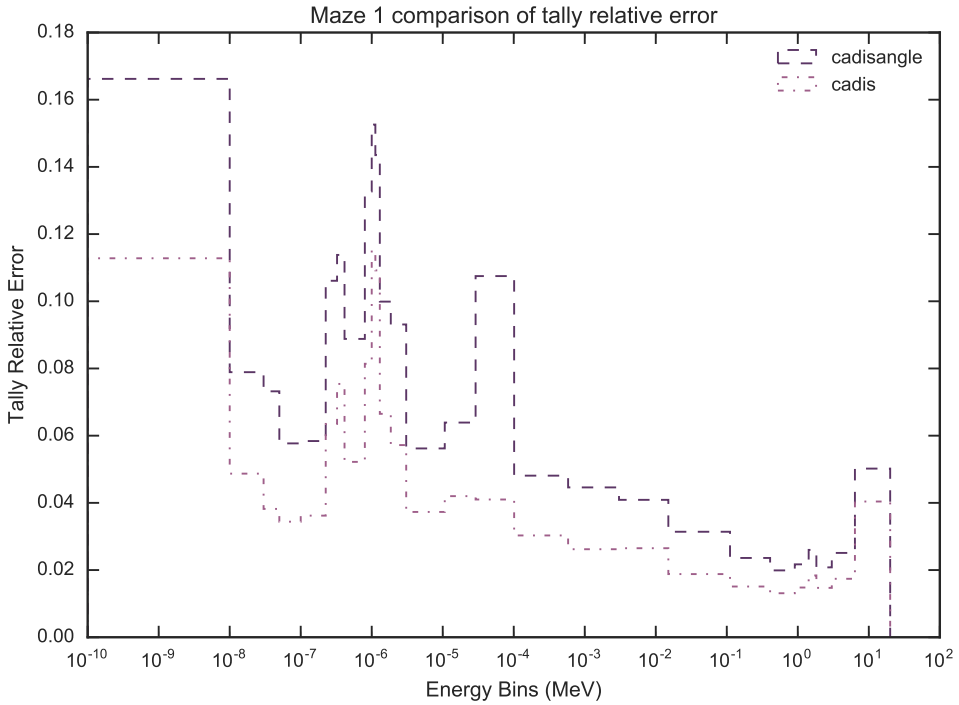

Figure 4.17: Tally relative error comparison between methods for a multiple turn labyrinth.

dependence and CADIS outperforms CADIS-Ω in all energy bins. This problem is poorly suited to CADIS-Ω.

Figure 4.18 shows the adjoint and Ω flux maps for the lowest energy group at the problem midplane for the multiple turn labyrinth. These figures look remarkably similar, showing that this problem does not have significant anisotropy to capture. The region that does differ is near the detector region, where the region of high importance is focused towards the labyrinth and the laybrinth exit. The other region with noticeable difference is located at the entrance to the maze. These figures show the lowest energy group particles, so for forward particles of this energy to go the same direction as adjoint particles, they must have gone into the labyrinth, scattered back out, and then scattered again. As a result, we do not see a strong directional dependence in the Ω-flux plot in the region near the forward source. The adjoint flux plot shows more of a streaming effect from the adjoint particles that exit the maze.

In Section 4.2.2, it was discussed that higher energy regions that contribute to the tally are more anisotropic, and that these regions benefit more from the Ω-flux map than they do with standard CADIS' importance map. Using the anisotropy metrics from Section 3.2.1, let us compare the anisotropy distributions of the single turn and multiple-turn labyrinth problems. Figure 4.19 are violin plots of the M_3 distributions of the labyrinth problems. To filter out values of the metric distribtuion that do not have a strong importance to

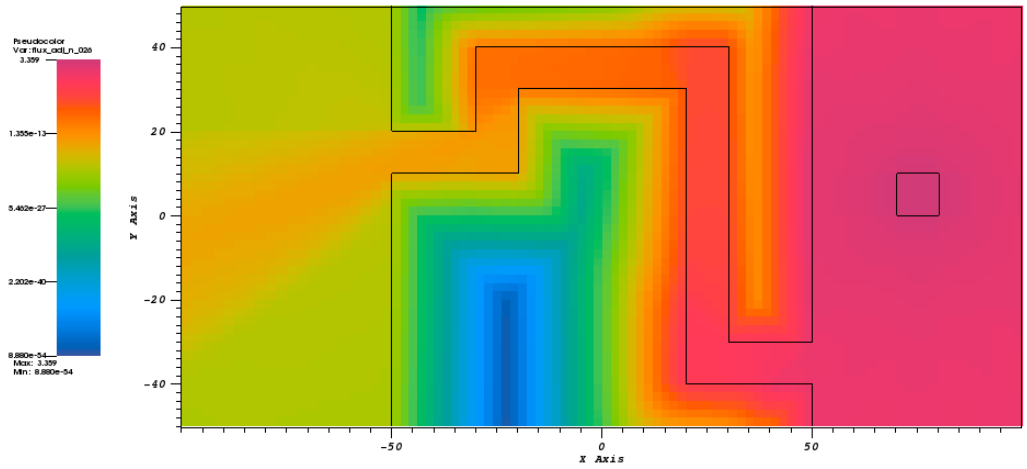

(a) Adjoint flux map for lowest energy group, multiple turn labyrinth.

contributing to the tally, only values from cells above the contributon flux mean value are included in the violins.

First, looking at the metric three distributions for both the single- (4.19a)and multiple-turn (4.19b) labyrinths, we can see that the violins in both plots shift from a fairly small grouping of values at high enrgies to a broad range of values at low energies. The bottom of the violin in each group also tells us a bit about the metric distribution. Because only values from "more important" cells have been included in these distributions, the bottom cutoff tells us how anisotropic the cells of median importance might be. It also tells us how many cells have high-valued anisotropy metrics. For both the single- and multi-turn labyrinths, we see higher-valued cutoff point in high energies than in low energies. This indicates that more cells in high energies have higher values of M_3.

The violin plots of the multi-turn labyrinth (Fig. 4.19b) tend to span a larger range of values. That is, the violins tend to be longer. All of the violins in both plots have a bounding upper limit, meaning that in every energy group there are some very anisotropic cells. Interestingly, it appears that for the multi-turn labyrinth the distribution of anisotropies at low energies has no distinctive bunching, as observed in the single-turn labyrinth. This means that in important cells, there is an even distribution of very anisotropic, slightly anisotropic, and isotropic cells.

While the violin plots of Figure 4.19 are useful in seeing the overall distribution of metrics for the whole problem, it is also possible to plot them similarly to the flux maps shown previously. Figure 4.20 shows the M_4 distribution for the single and multiple turn labyrinth problems. Recall that this metric is the ratio of the contributon anisotropy to the standard

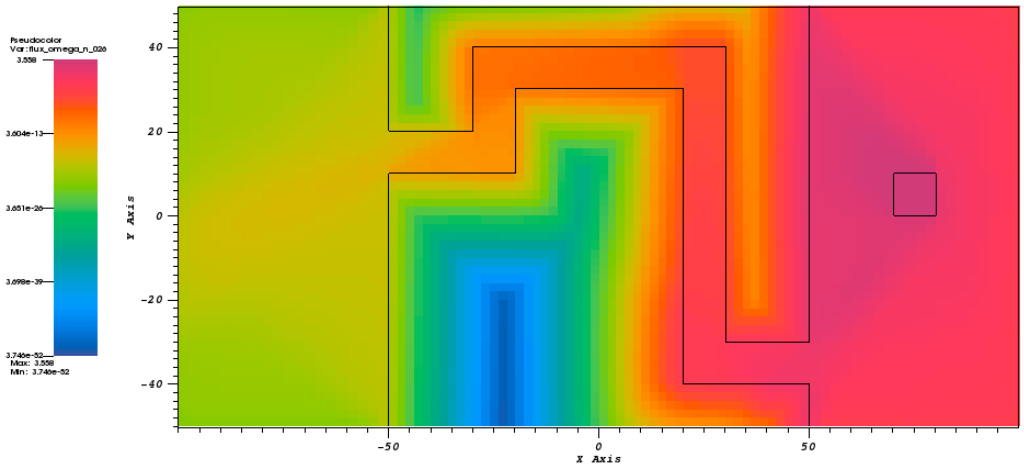

(b) Ω-flux flux map for lowest energy group, multiple turn labyrinth.

Figure 4.18: Flux map slice of multiple turn turn labyrinth. Flux maps have scales normalized to maximum and minimum values for each slice; between plots the scales are not consistent. These plots show the lowest energy group, group 026, for each cell in the problem midplane.

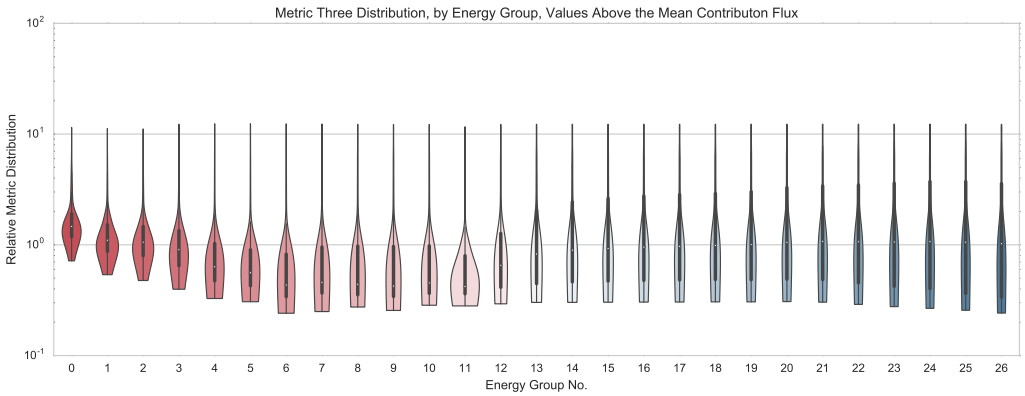

(a) M_3 distribution for single turn labyrinth

adjoint anisotropy. Cells that have blue coloring are those where the contributon max to average flux is lower than the adjoint. As a result, the forward and adjoint fluxes to not synergitically combine in angle. This generally means this is a region of lower importance. Values of unity mean that the contributon anisotropy is comparable to the adjoint anisotropy.

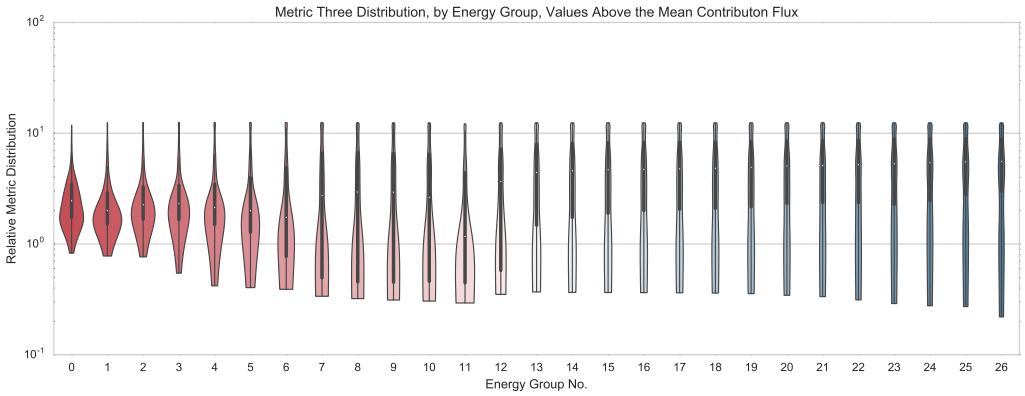

(b) M_3 distribution for multi-turn labyrinth

Figure 4.19: Violin plots of M_3 distribution using values above the mean contributon flux for labyrinth problems. Low energy group numbers correspond to high energies or fast particles, and are marked in red.

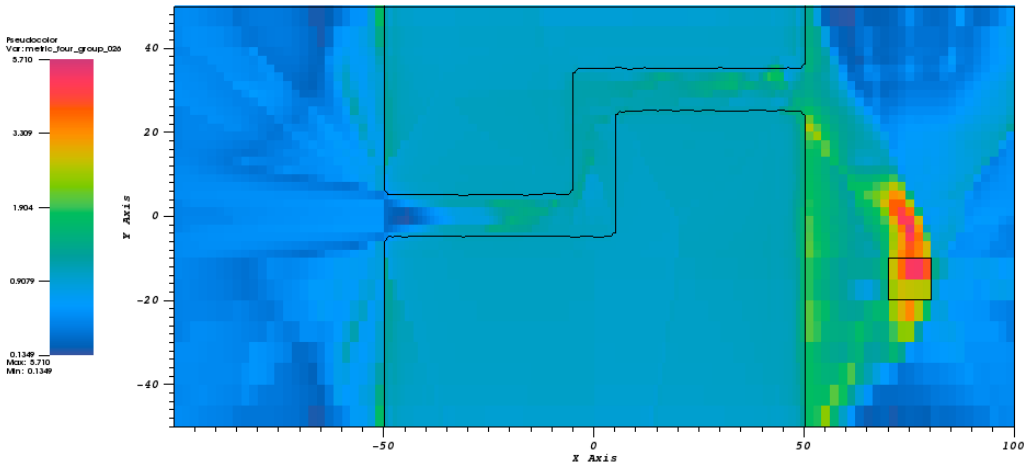

(a) M_4 lowest energy group, single turn labyrinth.

In figure 4.20a, it is clear that the concrete body of the maze is a region where the anisotropies are similar.

Figure 4.20a shows that the region where the anisotropy of the contributon flux differs the most from the adjoint flux is in the air region near the detector, and also in the air regions of the maze. Specifically, the anisotropy of the contributon flux is greater in the

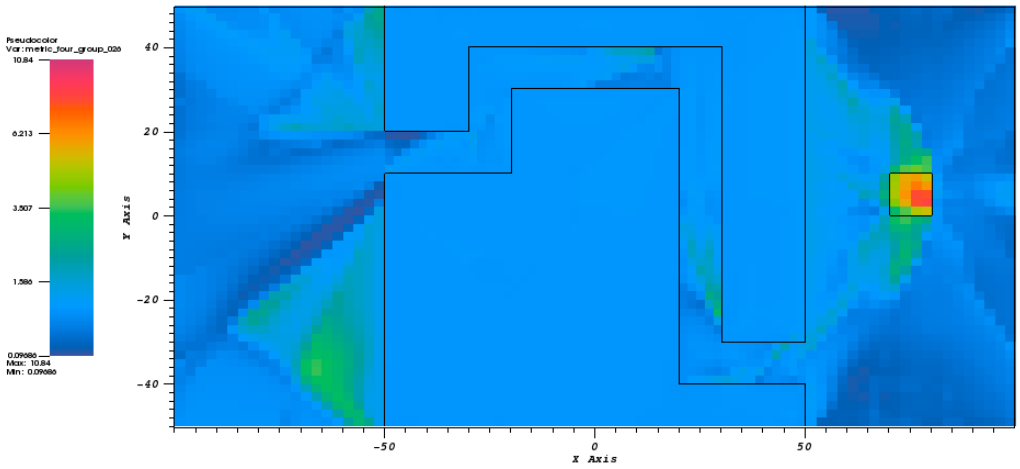

(b) M_4 for lowest energy group, multiple turn labyrinth

Figure 4.20: M_4 distributions at problem midplane for labyrinth problems.

air region between the detector and the maze, and the anisotropy of the contributon flux is lower in regions behind the detector. Conceptually, we expect this anisotropy behavior in the region just past the detector, as the contributon flux will combine positively if the forward and adjoint fluxes are travelling in opposite directions, and will combine negatively if they are travelling in the same direction. As a result, the anisotropy of the contributon flux behind the detector will be minimized when compared to the original adjoint angular flux.

Figure 4.20b shows, like Figure 4.20a, the M_4 distribution at the problem midplane for the lowest energy group for the multiple turn labyrinth. In this problem we similarly see the strongest anisotropy in the flux near the NaI detector. However, the range of values is different. The concrete region of the maze still shows similar anisotropies between the contributon and adjoint angular fluxes. The maze edge next to the NaI detector also has some fairly anisotropic regions, but overall the anisotropies are less different in this problem than in the single turn labyrinth. As a result, CADIS-Ω does not have as much angular information to capture, and its importance map is less effective. This was also illustrated in the flux map comparison of Figure 4.18.

Both figures have interesting secondary features in the anisotropy in the air regions. These regions look similar to ray effects, but are not always reflected in the flux maps themselves. The author is not sure how to explain these effects, but they are worth future study.

It must be noted that while the trends in these violins are interesting, we must also be

wary of using comparing the violins directly. The filtering algorithm used to pull values out is dependent only on the contributon flux solution for that problem, so the average contributon flux cutoff for the single-turn labyrinth and multiple-turn labyrinth are different. Using a raw value from the violin plot in Figure 4.19b and directly comparing it to one from Figure 4.19a may be misleading. Instead, this analysis will focus on the general behavior of the metrics in each problem, not specific metric values.

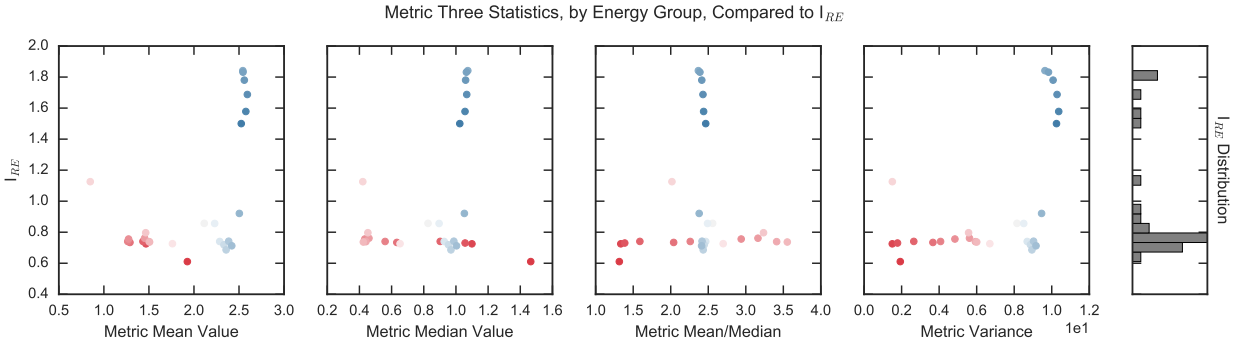

(a) RE improvement factor as a function of M_3 statistics for single turn labyrinth

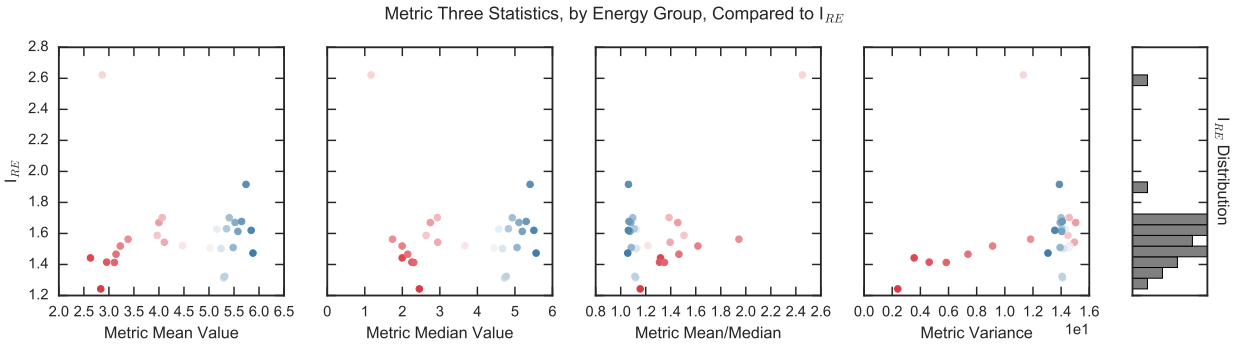

(b) RE improvement factor as a function of M_3 statistics for multi-turn labyrinth

Figure 4.21: Relative error improvement factor as a function of M_3 distribution statistics. Metric distribution statistics are calculated using values of M_3 in cells with contributon flux values above the mean. Colors of datapoints correspond to the energy group to which they belong.

Figure 4.21 shows the improvement factors of the relative errors between CADIS-Ω and CADIS for the labyrinth problems. The x-axes of the plots in Figures 4.21a and 4.21b use the distribution statistics from the violins in Figures 4.19a and 4.19b, respectively. Recall that because I_{RE} is the ratio of the relative error between CADIS-Ω and CADIS–and we seek a low relative error–that values of I_{RE} below 1.0 indicate method improvement for CADIS-Ω.

Looking at the differences between Figures 4.21a and 4.21b, some interesting effects can be observed. Recall from the relative error distribution plots for each problem (Figures 4.17

and 4.13) that CADIS-Ω had higher relative errors in all energy bins than CADIS for the multi-turn labyrinth, and a higher relative error in thermal energy groups in the single-turn labyrinth. Figure 4.21a shows the isolated grouping of poorer results for low energy bins in the single turn labyrinth. The rest of the values in this figure all show improvement in the relative error, while the low-energy group show better performance for CADIS. There is no distinct grouping in Figure 4.21b because all of the CADIS-Ω relative errors are higher than CADIS, so a distinct turnover in I_{RE} does not occur.

There does not seem to be a tight trend observable for any measurement of the M_3 distribution and I_{RE} in Figure 4.21a, but the higher values of I_{RE} generally occur in high mean values of M_3 and higer variances of M_3. Figure 4.21b also shows this trend in the metric mean and variance subplots, with a single outlier in an intermediate energy group. It also appears that the spread of I_{RE} values does not change as a function of any of the metric values.

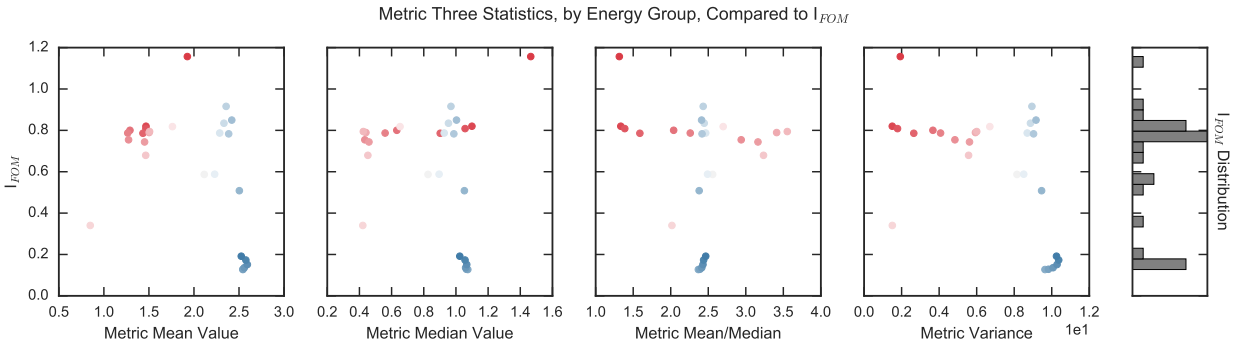

(a) FOM improvement factor as a function of M_3 statistics for single turn labyrinth

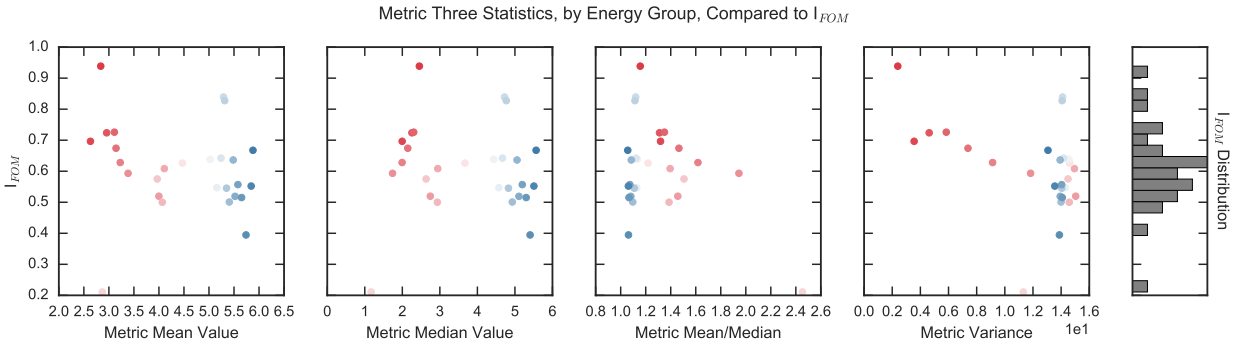

(b) FOM improvement factor as a function of M_3 statistics for multi-turn labyrinth

Figure 4.22: Figure of Merit improvement factor as a function of M_3 distribution statistics. Metric distribution statistics are calculated using values of M_3 in cells with contributon flux values above the mean. Colors of datapoints correspond to the energy group to which they belong.

Figure 4.22 builds off of what we've already observed in Figure 4.21. In this series of figures, I_{FOM} is plotted rather than I_{RE}. If CADIS-Ω has better FOM performance than CADIS, the resulting value of I_{FOM} will be above 1.0.

Many features from Figure 4.21 continue in Figure 4.22. The distinct grouping of low-energy results for the single turn labyrinth are also observable in 4.22a. The intermediate energy outlier for the multiple turn labyrinth is located at the bottom of all of the subplots in Figure 4.22b. By adjusting our results to include timing, even less of a trend with metric distribution measurements is seen in the improvement metric for the single turn labyrinth. However, for the multiple turn labyrinth it does appear that as the metric mean value increases, I_{FOM} decreases.

4.2.4 Steel Beam

The steel beam embedded in concrete FOM and timing results are summarized in Tables 4.9 and 4.10. Figures 4.23 and 4.24 show the results obtained by the track length tally in CADIS, CADIS-Ω and the nonbiased analog Monte Carlo.

	CADIS		CADIS-Ω		analog
	MC	MC_{hybrid}	MC	MC_{hybrid}	MC
tally avg	668	659	3e+03	2.96e+03	1.39
max RE	3.74	3.69	6.79	6.71	0.0448
min RE	1.43e+03	1.41e+03	1.33e+03	1.31e+03	–
time (mins)	414	420	2.09e+03	2.11e+03	22.3

Table 4.9: Figure of Merit comparison for steel bar embedded in concrete.

		CADIS	CADIS-Ω	analog
		time (minutes)		
MCNP time	total	414.45	2086.60	22.33
deterministic time	advantg_time	0.18	0.18	–
	denovo_time	5.69	25.64	–
	dispose_time	0.00	0.16	–
	omega_time	0.00	0.66	–
	total	5.87	26.49	–
wall time		420.32	2113.09	22.33

Table 4.10: Detailed timing results for steel bar embedded in concrete.

Tables 4.9 and 4.10 show that this problem is very difficult for analog Monte Carlo and that CADIS-Ω generally performs better than CADIS. In fact, CADIS-Ω has the best performance in this problem of all of the characterization problems.

For both CADIS and CADIS-Ω, this problem has a huge disparity in the FOMs calculated with the maximum and minimum relative error. As a result, depending on the convergence requirements that a user might require, the time to achieve a desired solution could vary significantly in applications. However, both CADIS and CADIS-Ω improve on the unbiased analog Monte Carlo's FOM by a factor of 10^2 or more.

CADIS-Ω outperforms CADIS for the FOMS calculated with the tally average relative error and the tally maxmimum relative error. This indicates that giving a limiting relative error to which all energy bins must converge, CADIS-Ω will achieve it in 1/3rd the time that CADIS will. Further, CADIS-Ω has a better FOM than CADIS when the deterministic runtimes are added. As shown in the timing table, the time to run and generate the variance reduction parameters for CADIS-Ω will always be longer than CADIS due to the addition of the forward transport run. The addition of deterministic runtimes has the potential to lower the FOM of CADIS-Ω more than that of CADIS, so CADIS-Ω's achievement of a FOM higher FOM with much longer runtimes in both Monte Carlo and ADVANTG illustrates just how much lower the relative error it achieves is. CADIS-Ω is very well-suited to a problem with these conditions.

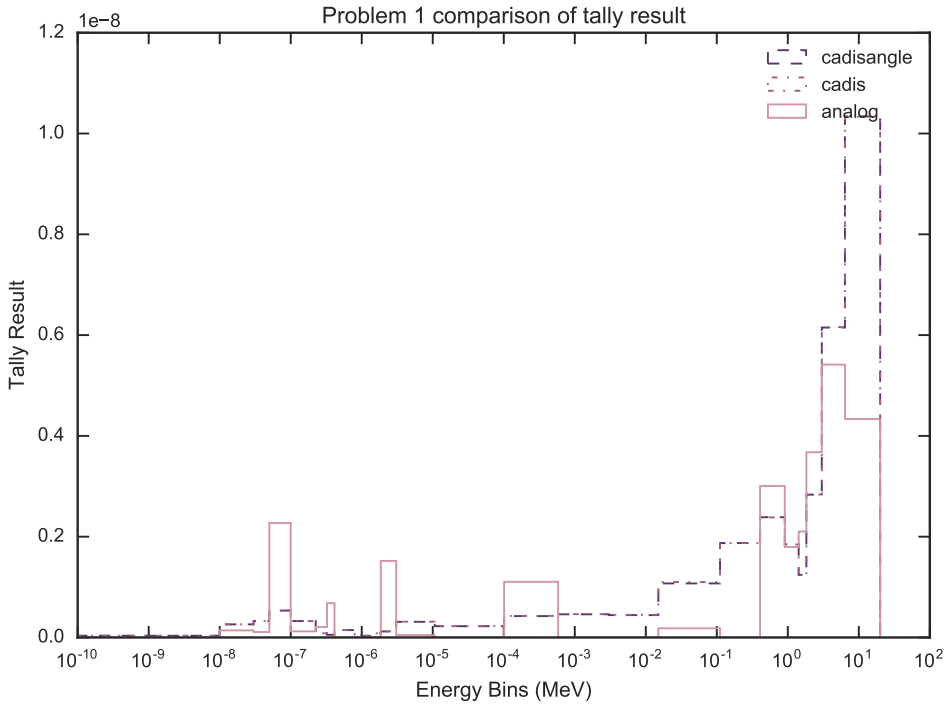

Figure 4.23: Tally results comparison between methods for steel bar embedded in concrete.

Figure 4.23 shows that CADIS and CADIS-Ω are in agreement for the tally results in all energy bins. The nonbiased Monte Carlo calculation differs from both of the hybrid methods. This supports what was observed in the nonbiased analog FOM values of Table

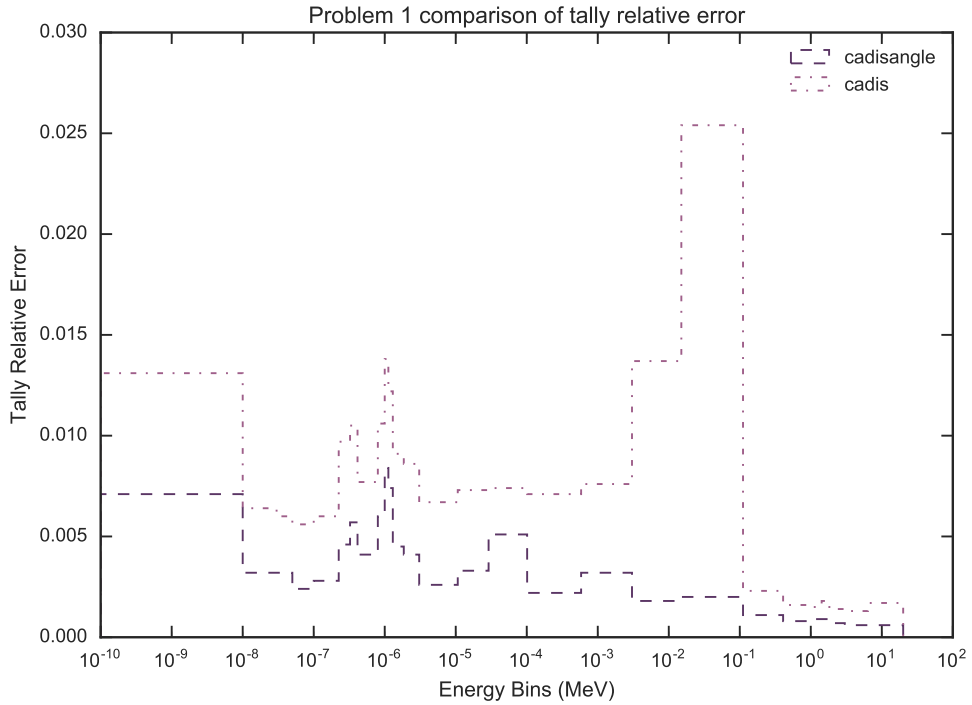

Figure 4.24: Tally relative error comparison between methods for steel bar embedded in concrete.

4.9. Figure 4.24 shows that CADIS-Ω achieves a consistently lower relative error than CADIS for all energy bins. For most energy bins, CADIS-Ω's relative errors are shifted a consistent fraction below CADIS'. In the energy regions between 10^{-4} and 10^{-1} MeV, this is not the case. For these energy regions CADIS' relative errors spike while CADIS-Ω's do not.

From the FOM results presented in Table 4.9 and the tally results and error in Figures 4.23 and 4.24, we can conclude that CADIS-Ω's source biasing parameters consistently move more particles in all tally energy bins more effectively than CADIS. The importance map generated by CADIS-Ω better reflects the problem physics and more efficiently transports particles to the desired tally location.

4.2.4.1 Air Channel Variant

The characterization problems have been designed to induce anisotropy in the flux. Most of these problems do so, in some part, by using air to induce particle streaming. The steel beam in concrete problem requires that particles interact with a high density material (either steel or concrete) before reaching the detector to induce a response. These next two variant problems explore whether the material choice of steel strongly affects the Ω-method's ability to generate variance reduction parameters. This first variant keeps the

geometric configuration of the steel beam problem the same, but the steel is replaced with air. If the Ω-methods are more sensitive to air, then this change in the materials composition should affect the results.

	cadis MC	MC_adjusted	cadisangle MC	MC_adjusted	analog MC
tally avg	432	390	396	364	5.63
max RE	1.17	1.05	0.247	0.227	0.0467
min RE	273	247	296	272	–
time (mins)	47.3	52.3	247	268	21.4

Table 4.11: Figure of Merit comparison for air variant of the steel beam problem geometry. In this variant problem, the steel bar volume region is replaced with air to exacerbate the suggested splitting issues encountered in other hybrid problems.

		cadis time (minutes)	cadisangle time (minutes)	analog time (minutes)
MCNP time	total	47.29	246.83	21.42
deterministic time	advantg_time	0.16	0.15	–
	denovo_time	4.90	20.50	–
	dispose_time	0.00	0.15	–
	omega_time	0.00	0.65	–
	total	5.05	21.30	–
wall time		52.34	268.13	21.42

Table 4.12: Detailed timing results for steel beam geometry air variant.

Tables 4.11 and 4.12 summarize the FOM and timing results for the air variant of the steel beam problem. Comparing the FOMs for this variant and for the steel variant (Table 4.9), it is clear that CADIS-Ω performs more poorly than CADIS with air. Interestingly, CADIS-Ω's minimum relative error FOM is better than CADIS', which is opposite to the results for the standard steel problem. For the maximum relative error, CADIS-Ω's FOM is 1/5th that of CADIS'. However, for this problem CADIS-Ω's runtime is almost five times that of CADIS. Considering this time difference, it appears that CADIS-Ω requires far more sampling with its importance map than CADIS. These sampling requirements also exist with the original steel problem, but the importance map reduces the tally variance enough to offset the time addition. This is not the case for the air variant. From this, we can conclude that the addition of air into this problem geometry reduces the sampling interaction points enough to negatively affect the Ω-method. Further, it lowers the FOMs achieved by both CADIS and

CADIS-Ω substantially that their improvement over the nonbiased analog reduces almost an order of magnitude.

The runtimes in Table 4.12 are also worth comparing with the original steel variant. In particular, the deterministic runtime in both of the promblems is on the same order of magnitude. However, the Monte Carlo runtime is far longer in the original steel version. The runtimes in the air variant are generally much shorter for CADIS and CADIS-Ω, but comparable for the nonbiased analog. In this problem, the fraction of time spent in the deterministic solve is much higher than in the steel version.

4.2.4.2 Concrete Channel Variant

In addition to the air variant of the steel beam geometry, we can see if having non-preferential flowpaths might affect the Ω-method's performance. Recall that the Ω-methods have been designed to incorporate angular information into the importance map. If no preferential flowpaths exist through the problem geometry, then the Ω-importance map may have less of an impact on improving the tally convergence. However, because the entire shield is composed of concrete, then the distance to smapling location should still be quite small as with the original steel version of the problem. As a result, there should be some positive effects on the Ω-methods due to sampling interaction frequency. Tables 4.13 and 4.14 show the FOM and timing results for this material variant of the steel beam geometry.

	cadis		cadisangle		analog
	MC	MC_adjusted	MC	MC_adjusted	MC
tally avg	2.6e+03	2.55e+03	3.16e+03	3.13e+03	1.54
max RE	14.5	14.2	9.48	9.39	0.0457
min RE	1.54e+03	1.51e+03	1.4e+03	1.39e+03	–
time (mins)	385	393	1.98e+03	2e+03	21.9

Table 4.13: Figure of Merit comparison for concrete variant of steel bar geometry. In this variant problem, the steel bar volume region is replaced with concrete to eliminate the preferential particle travel through the beam region.

Tables 4.13 and 4.14 show the results of the concrete variant of the steel beam problem. As with the original steel and air versions described previously, the runtimes for CADIS-Ω are quite long when compared to CADIS. In each variant, the runtimes are about five times longer than those observed for CADIS. Similarly to the steel variant, in this version CADIS-Ω achieves a superior FOM for the tally average FOM. However, CADIS-Ω's FOMS for the maximum and minimum relative error FOMs are both lower than CADIS'. Both CADIS and CADIS-Ω far outperform the nonbiased analog Monte Carlo.

To compare the performance of each of the variants of this problem, let us first compare the differences in the flux distributions for the Ω and CADIS versions of the problem. Figure 4.25 shows the adjoint and Ω fluxes for the steel beam in concrete version of this geometry.

		cadis time (minutes)	cadisangle time (minutes)	analog time (minutes)
MCNP time	total	385.11	1978.46	21.88
deterministic time	advantg_time	0.23	0.15	–
	denovo_time	7.42	19.58	–
	dispose_time	0.00	0.09	–
	omega_time	0.00	0.56	–
	total	7.65	20.29	–
wall time		392.76	1998.75	21.88

Table 4.14: Detailed timing results for concrete variant of steel bar.

It is clear from both of these two figures that there is a preferential flowpath through the steel beam for both the standard adjoint and for the Ω-fluxes.

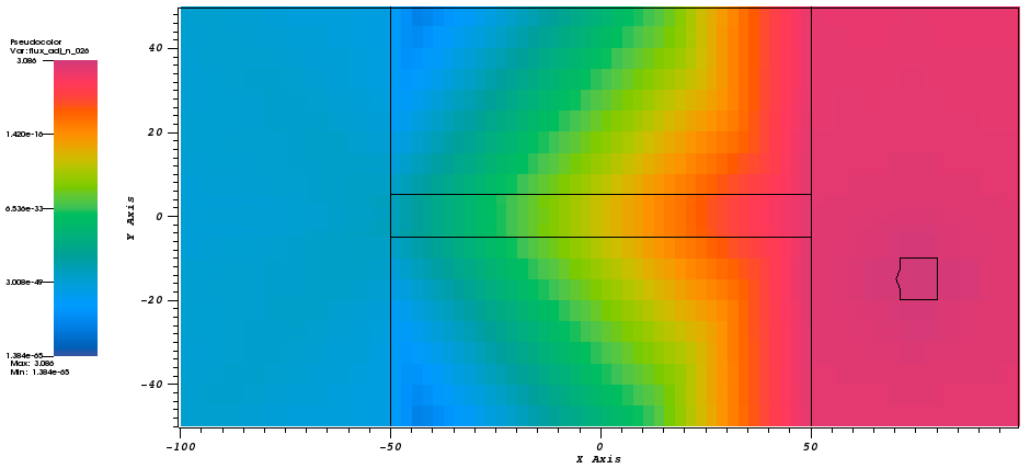

(a) Adjoint flux distribution, lowest energy group

As with the multiple-turn labyrinth, the flux maps are very similar between the adjoint and Ω-flux plots in this figure. Recall that M_2 is the ratio of the scalar Ω-flux to the scalar adjoint flux in each cell. Figure 4.26 shows the M_2 distributions for each of the material variants of the steel beam problem. Figure 4.26a contains the distribution of M_2 for the original steel variant, Figure 4.26b is of the variant with air replacing the steel, and Figure 4.26c. Note that Figure 4.26b has the colormap scaled to a log scale, while the other two

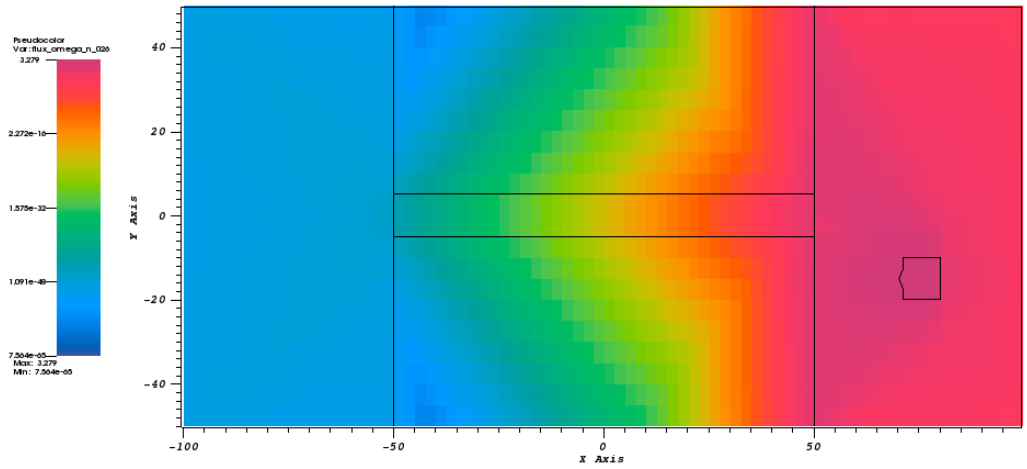

(b) Ω-flux distribution, lowest energy group

Figure 4.25: Flux maps for steel beam in concrete. Fluxes shown are at problem midplane, and energy group 026. The colormap for each has been scaled to the data in the plane.

figures do not. This is because the range is much larger in this figure, and a linear scale obscures the data.

By comparing the ratio of the Ω- to adjoint-fluxes in each of the figures in 4.26, the effect that material choice has on changing the Ω-flux becomes more apparent. First, all three plots show a constant value of M_2 within the concrete shield itself. As a result, we can conclude that materials in which the particles have a small mean free path of travel, the flux isotropy is fairly constant and does not differ between the Ω- and adjoint fluxes. Next, having a preferential flowpath through the shield does change the resultant Ω-flux. Depending on material, the flux may be very different (as with the air in Figure 4.26b) or fairly similar (as with the flux ratio in the steel in Figure 4.26a). All three problems show a very different distribution of fluxes near the adjoint source. This is the case with both of the labyrinth variants previously discussed.

The subfigures of Figure 4.27 complement those presented in Figure 4.26. As with Figure 4.26, the subfigures here are normalized by the adjoint problem. Rather than comparing the adjoint scalar fluxes, here the contributon anisotropy in each cell is compared to the adjoint. Similar features can be observed between the subfigures in 4.27 and their counterparts in 4.26. For exmaple, the anisotropies in the cells in the shield are the same as the adjoint. As a result, we see little- to no- difference between the Ω-method aniosotropy or the standard adjoint anisotropy. Figure 4.27b shows some interesting streaming effects on the anisotropy

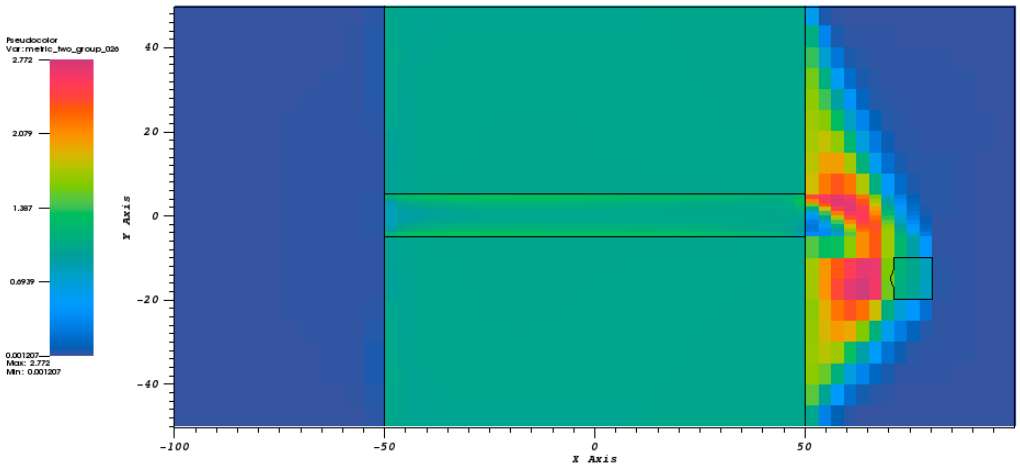

(a) M_2 distribution for steel beam in concrete.

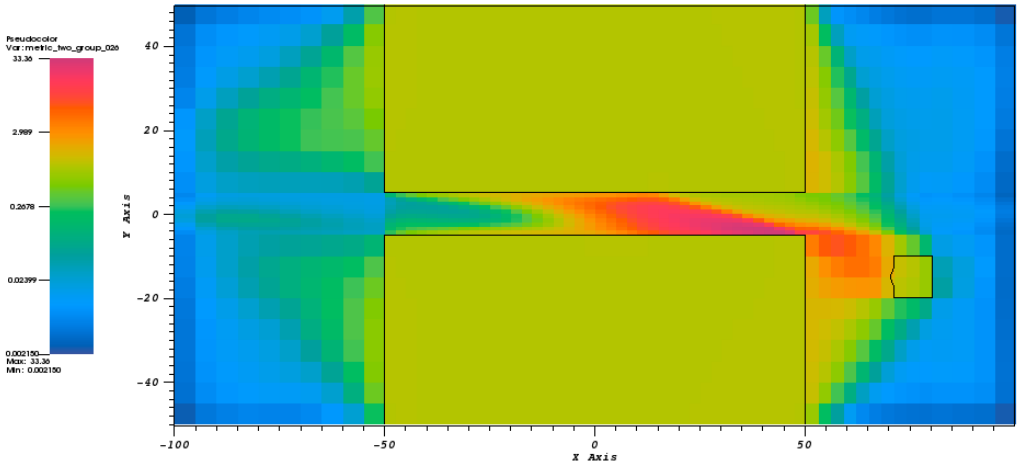

(b) M_2 distribution for steel beam in concrete, air variant.

in the air channel within the shield. In particular, the contributon anisotropy is larger for the majority of the air channel than the adjoint anisotropy. There is an exception to this observation at the M_4 values marked with dark blue in the air channel.

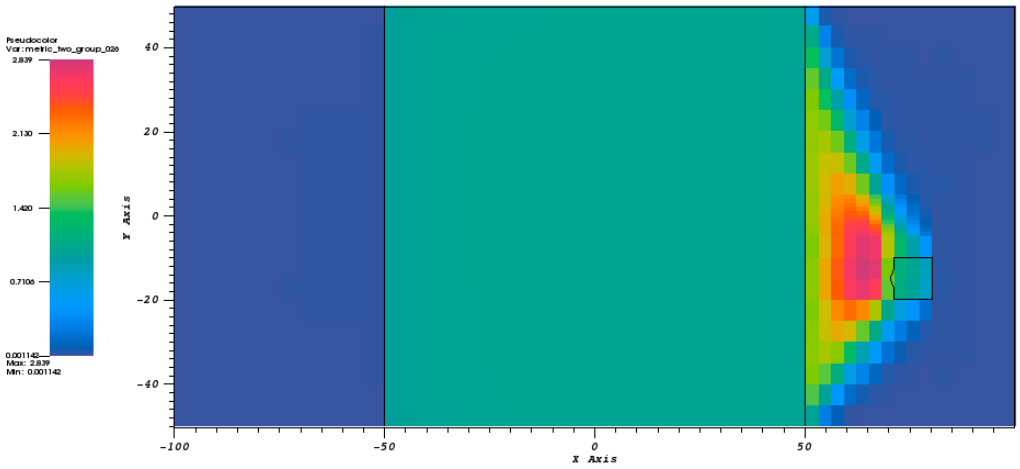

(c) M_2 distribution for steel beam in concrete, concrete variant.

Figure 4.26: M_2 distribution plots for material variants of steel beam in concrete. Distribution shown is for lowest energy group. Scales adjusted to match dataset of each figure.

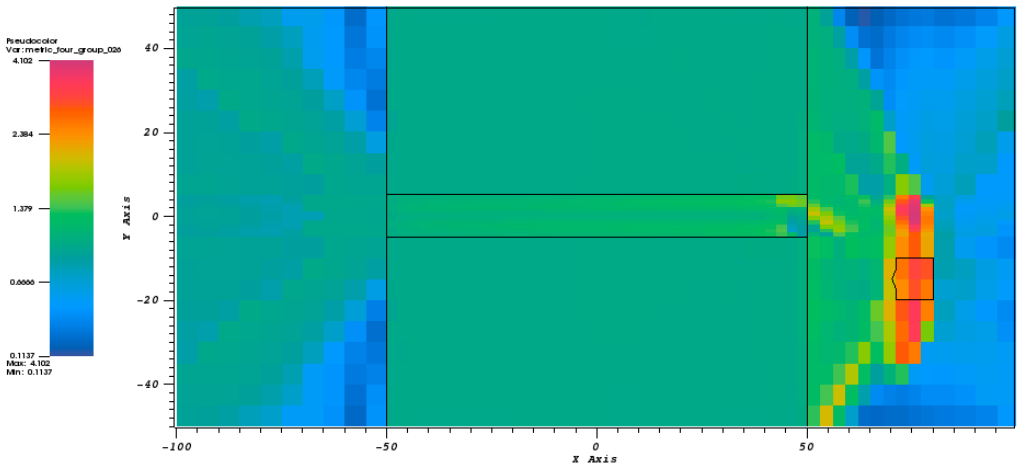

(a) M_4 distribution for steel beam in concrete.

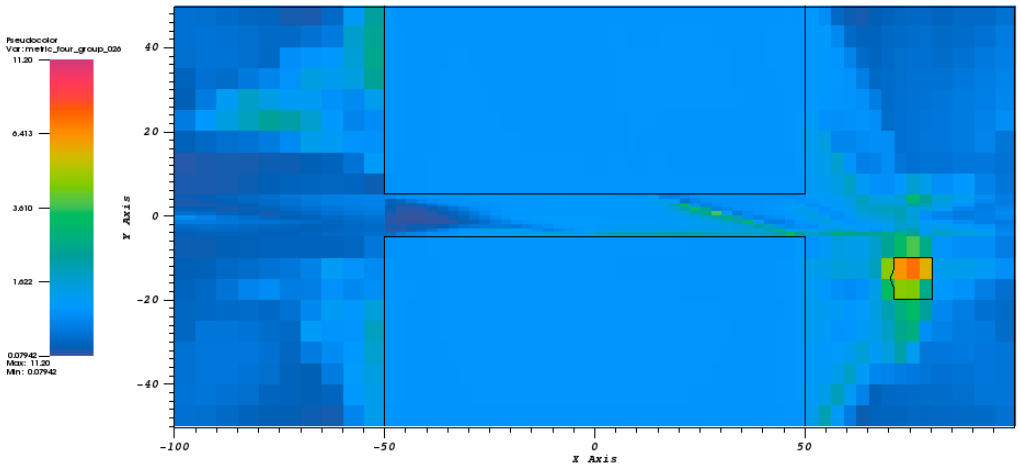

(b) M_4 distribution for steel beam in concrete, air variant.

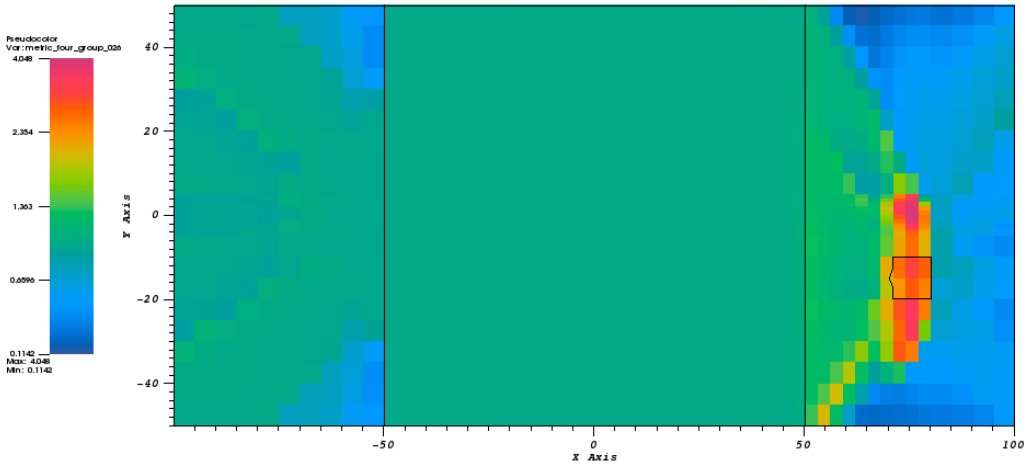

(c) M_4 distribution for steel beam in concrete, concrete variant.

Figure 4.27: M_4 distribution plots for material variants of steel beam in concrete. Distribution shown is for lowest energy group. Scales adjusted to match dataset of each figure.

All three subfigures in 4.27 show that there exist differences in the anisotropy near the adjoint source and near the forward source in all material variants of this problem. Unlike the subfigures of 4.26, the anisotropies extend all the way to the problem boundaries in the air regions of the problem. However, the anisotropy in the area of each problem near the detector is generally larger than the anisotropy in the area neaer the forward source.

With an intuition of how the Ω and adjoint-scalar fluxes differ both on the cell-scale, and how their anisotropies differ on the cell scale, we can now look at the effectiveness of each at predicting the Ω-method's success (or lack thereof). Recall that Figures 4.26 and 4.27 show the anisotropy distributions for the lowest energy group. On the next several figures, the data illustrated by these figures will correspond with the darkest blue violin and the darkest blue scatterplot data point, respectively. The next several figures attempt to collapse the substantial quantity of data available in Figures 4.26 and 4.27 to values with which we can correlate with Ω- relative error or FOM improvement.

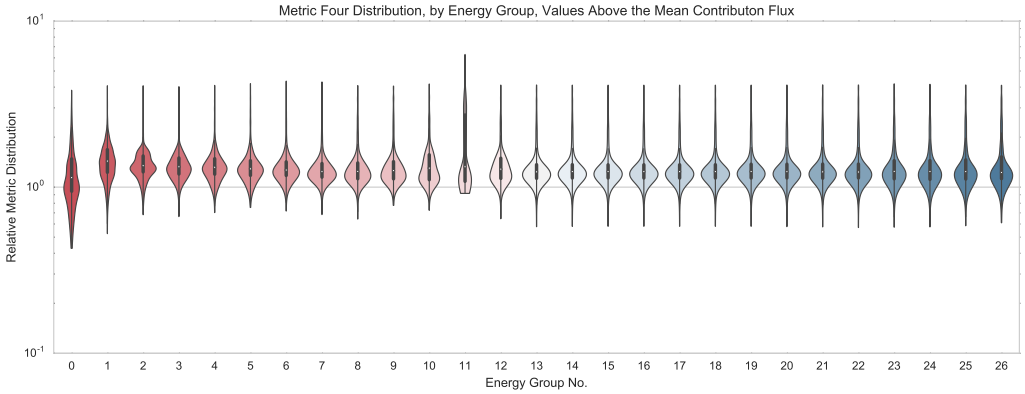

(a) M_4 distribution for steel beam geometry

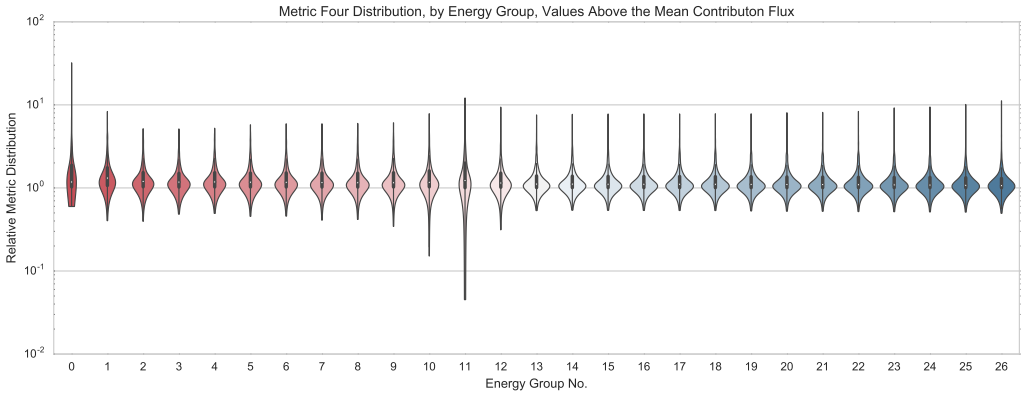

(b) M_4 distribution for air beam geometry

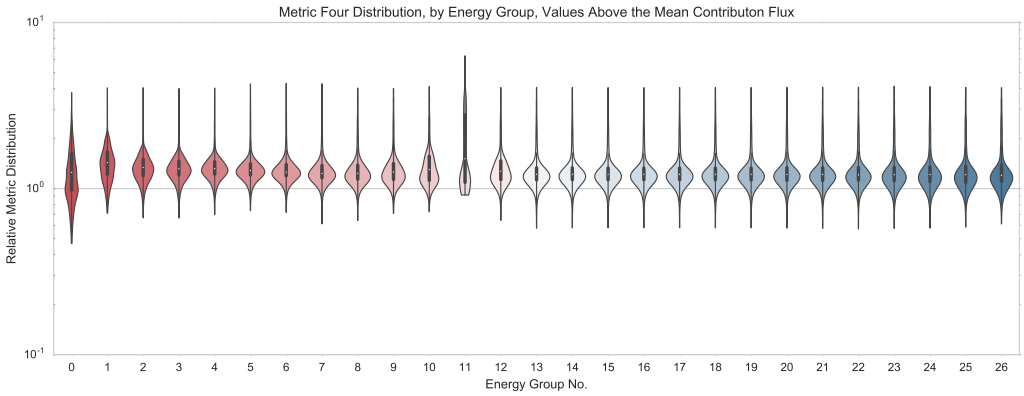

(c) M_4 distribution for concrete beam geometry

Figure 4.28: Distribution plots of M_4 for the steel beam problem geometry material variants. Distributions have been filtered from cells that are in bins above the contributon average flux in each problem. Coloring corresponds to energy group, red indicates a higher energy group and blue a lower energy group.

The beam problem material variants provide a very interesting opportunity to see the effect of material properties on I_{RE} and on the anisotropy metric distributions. Based on observations, the distributions for M_4 will be shown for these problem variants in 4.28 and 4.29. Figure 4.28a shows the M_4 distribution for each energy group as a violin plot for the original steel version of the problem. Figures 4.28b and 4.28c show the air and concrete variants of the problem, respectively. Note the similarity between the metric distributions for the steel and concrete variants of the problem (Figs. 4.28a and 4.28c). The metric distributions have similar ranges, similar distributions, and similar mean values. The only energy groups where there are noticeable differences are in the highest energy groups, where the local minimum values differ, and in energy group three, where the distribution between the two problems differs.

Compare what was observed in the concrete and steel variations of the problem to Figure 4.28b, which contains the M_4 distributions for air. The range in values for each of these violins is much larger than either 4.28a or 4.28c. Energy group 11 does not bottom out as it does in the previous two problems. The fastest energy group is strongly peaked upwards, as are many low energy groups. While the distribution of each of the metrics for this problem are much broader, the main body of the distributions are centered around lower values than either 4.28a and 4.28c.

The differences in the violin plots are purely due to differences in the sampling physics of the problem. Despite different materials in the concrete and steel variants of the problem, 4.28c and 4.28a have similar violin distributions. This tells us that while the overall energy spectrum of the problem may be different, the distribution of anisotropy within the problem may be more dependent on how likely particles are to collide. That is, because both steel

and concrete have higher interaction probabilities than air, their anisotropy distributions will be closer to each other than air.

Because the problem geometries and mesh sizes are identical between each of these problems, it is likely that the selection of values is at similar locations in each of the problems. However, because the filter matrix described in Section 4.1.3 is based on the contributon flux, which is problem specific, these will still differ between problems. Further, the number of cells selected from each energy group will differ between problems.

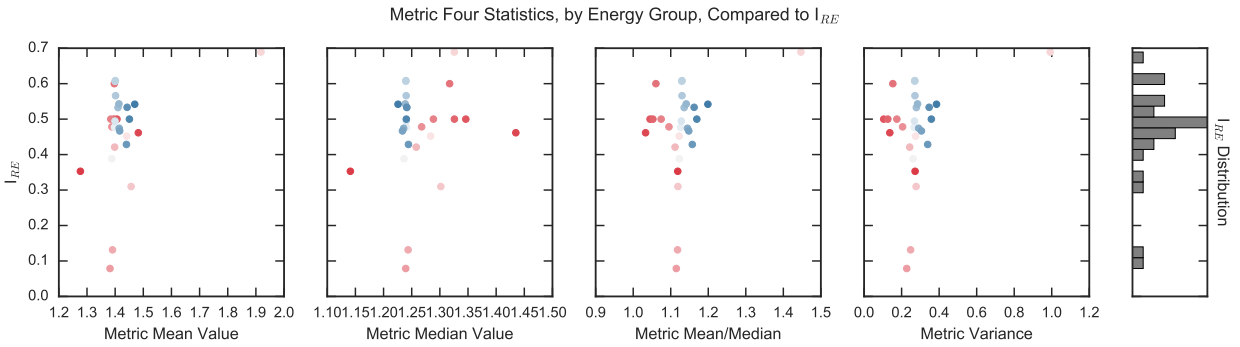

(a) I_{RE} for M_4 for steel beam geometry

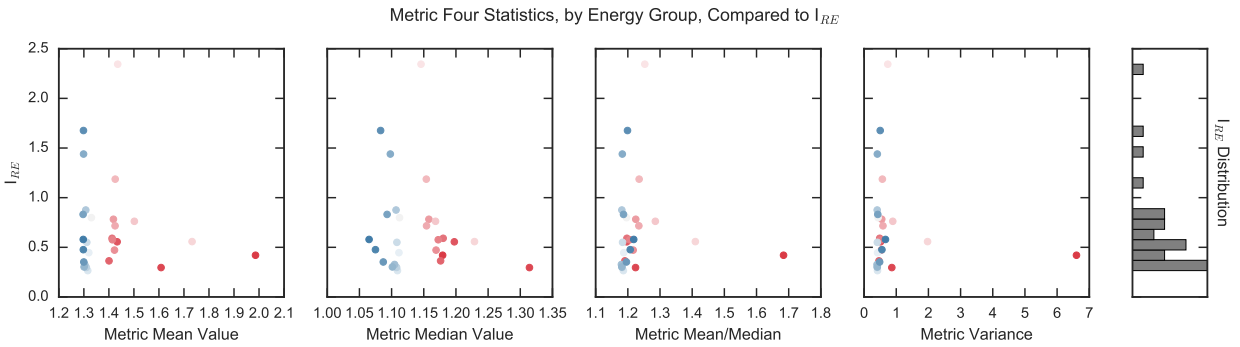

(b) I_{RE} for M_4 for air beam geometry

Based on the violin plots in 4.28, it was observed that the M_4 distribution was far different in the air variant of this problem geometry than the steel or concrete variants. This is also observable in Figure 4.29, which plots the relative error improvement metric, I_{RE} with different metric distribution values. Recall that a low I_{RE} means that the Ω method achieved a superior relative error to standard CADIS.

Figures 4.29a through 4.29c shows the relative error improvement factors for each of the steel beam material variants described in 4.28. For both the steel and concrete problems, CADIS-Ω has favorable values for I_{RE} in most energy bins. In Figures 4.29a and 4.29c there appears to be a trend in I_{RE} with both the metric variance and the metric skew–the ratio of the mean to the median values–which indicates that the metric distribution rather than

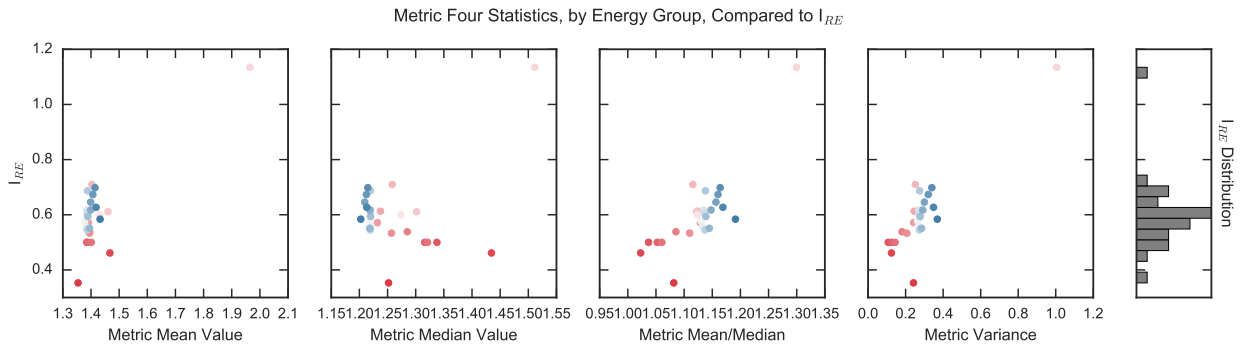

(c) I_{RE} for M_4 for concrete beam geometry

Figure 4.29: Scatterplots of values describing M_4 distribution against I_{RE} for steel beam problem geometry material variants. As with the distributions in 4.28, M_4 is based on values filtered out in cells located above the contributon flux average value. The values on the x-axes of the figures are evaluated based on the subset of M_4 values. Coloring of datapoints correspond to the energy groups.

the metric average are more likely to be related to the improvement in the relative error for these problems. This trend is not observable for the air variant in Figure 4.29b. In fact, the metric mean and median values are better indicators for I_{RE} than the distribution values.

Looking at the distributions of I_{RE} it is clear that despite the similar metric distribution values, the concrete and steel variants of this problem do have different performances. Disregarding energy group 11, which is an outlier in all three problem figures, the two problems have similar ranges of I_{RE}. However, the highest energy groups have the lowest I_{RE} for the concrete problem, while the lowest values in the steel problem occur in in intermediate energy groups.

4.2.5 U-Shaped Corridor

The U-shaped air corridor embedded in concrete FOM and timing results are summarized in Tables 4.15 and 4.16. Figures 4.30 and 4.31 show the results obtained by the track length tally in CADIS, CADIS-Ω and the nonbiased analog Monte Carlo.

Much like the single- and multiple-turn labyrinths, the U-shaped air corridor has a pathway of preferential movement for particles in a concrete shield. In this problem, the particles travel down the legs of the u-bend to a detector on the other side of the corridor. The particles should have preferential flowpaths through the air ducts, but it is possible for low energy particles to traverse the concrete barrier between the source and detector. The high energy particles tallied in the detector are more likely to have traveled through the air ducts and the low energy particles may be supplied from the shield or from scattering down the air duct.

The FOM table for the u-shaped corridor shows that this is a fairly difficult problem

	CADIS		CADIS-Ω		analog
	MC	MC_{hybrid}	MC	MC_{hybrid}	MC
tally avg	64.1	51.9	60.2	38.3	0.378
max RE	0.0183	0.0148	0.0144	0.00913	0.0644
min RE	14.9	12	13.4	8.54	–
time (mins)	54.6	67.5	188	296	15.5

Table 4.15: Figure of Merit comparison between methods for U-shaped air corridor in concrete.

		CADIS	CADIS-Ω	analog
		time (minutes)		
MCNP time	total	54.61	187.92	15.54
deterministic time	advantg_time	0.19	0.21	–
	denovo_time	12.68	105.90	–
	dispose_time	0.01	0.35	–
	omega_time	0.00	1.49	–
	total	12.87	107.60	–
wall time		67.48	295.52	15.54

Table 4.16: Detailed timing results for U-shaped air corridor in concrete.

for CADIS, CADIS-Ω, and the analog. For the tally average FOM, CADIS and CADIS-Ω achieve a FOM two orders of magnitude higher than the nonbiased analog. Both methods have comparable FOMs. In fact, CADIS and CADIS-Ω are in relative agreement for all FOMs calculated with the Monte Carlo runtime. Interestingly, the nonbiased analog Monte Carlo has a higher maximum relative error FOM than either method. However, this analog tally for this problem has many nontallied bins (as can be gathered from the major discrepancy in results in Figures 4.30 and 4.31). For the few bins that were tallied, the analog has a high FOM.

The tally results for the u-shaped corridor in Figure 4.30 show general agreement between CADIS and CADIS-Ω. The nonbiased analog has no agreement with either method. Comparing their relative errors in Figure 4.31, we can gather that this is a difficult problem for both methods. At high energies both CADIS and CADIS-Ω have very high relative errors, indicating untrustworthy results. To get the relative error in these regions for CADIS-Ω to below 0.10–a fairly standard threshold for Monte Carlo–it would have to run nearly 40x longer, or 900 hours. However, CADIS-Ω achieves a uniformly lower relative error than CADIS for all energy bins. Because the time to run CADIS-Ω is so much longer, the FOM is impacted and appears worse than CADIS. Therefore, should CADIS-Ω use the same runtime as CADIS, CADIS will achieve superior relative errors. Conversely, if CADIS-Ω uses

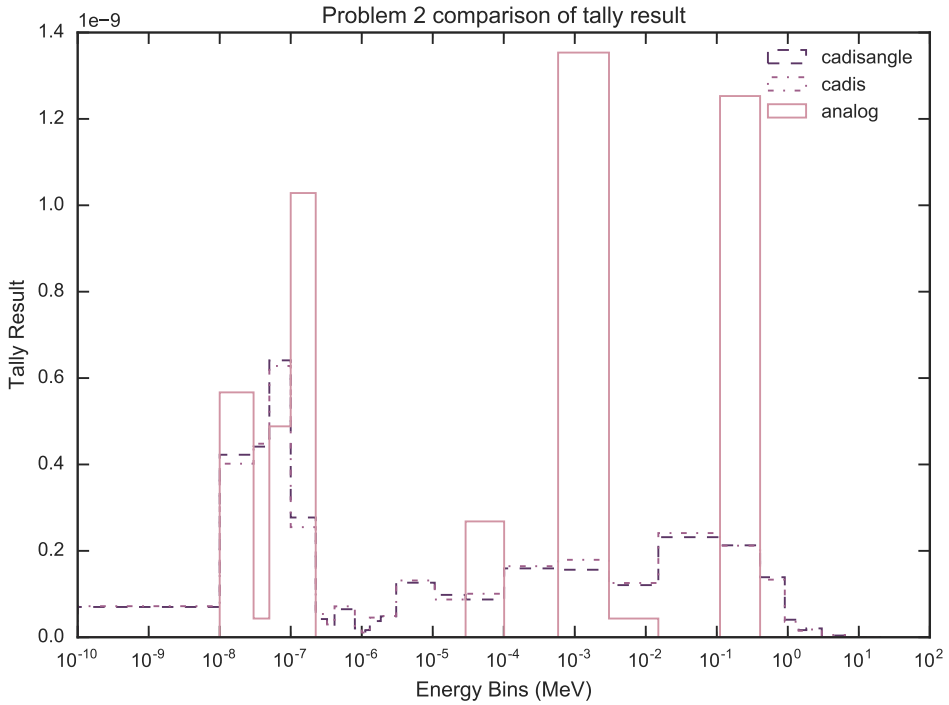

Figure 4.30: Tally results comparison between methods for U-shaped air corridor in concrete.

the same particle count as CADIS, CADIS-Ω will achieve superior relative errors.

While the u-shaped bend problem does not have FOMs for CADIS-Ω that significantly improve upon CADIS', CADIS-Ω still achieved lower relative errors than CADIS. Figure 4.32 shows the flux distributions in the U-bend located at the midplane containing the NaI detector. Figure 4.32a shows the adjoint scalar flux, Figure 4.32b shows the angle-integrated contributon scalar flux, and Figure 4.32c shows the Ω-flux, all at the same problem midplane.

As with the single-turn labyrinth, the adjoint scalar flux in Figure 4.32a shows substantial ray effects in the air regions near the adjoint source. As expected, the ray effects are mitigated once the particles interact with concrete. The difference in flux value between the orange region and the yellow regions of the plot is on the order of two- to three- orders of magnitude. The two ray effect fingers are separated by a distance of 10-20cm, meaning that a particle traversing air in this region may experience fairly large differences in importance between scattering events.

In this problem the forward source is offset in the z-plane from the detector by 100cm. The effects of this on the flux are visualized well by the contributon flux in Figure 4.32b. In the left-leg of the u-bend, the contributon flux decreases near the bottom. This is because particles are more biased in a deeper z-plane, towards the forward source. It is also clear from this figure that in the high energy region, the contributon flux streams particles through the concrete shield.

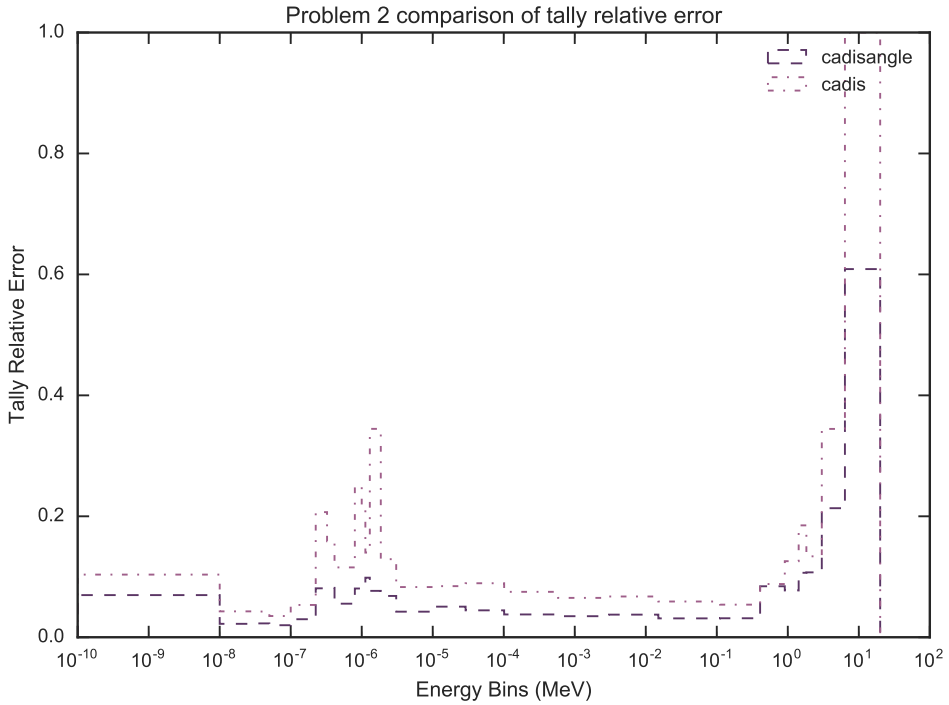

Figure 4.31: Tally relative error comparison between methods for U-shaped air corridor in concrete.

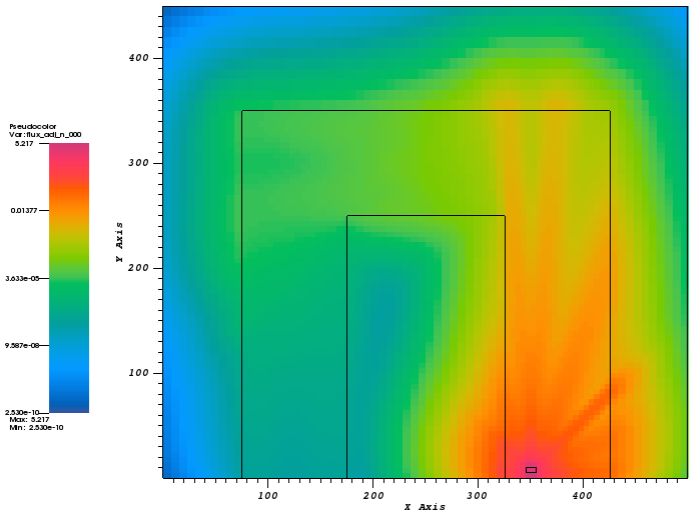

(a) Adjoint flux distribution, highest energy group

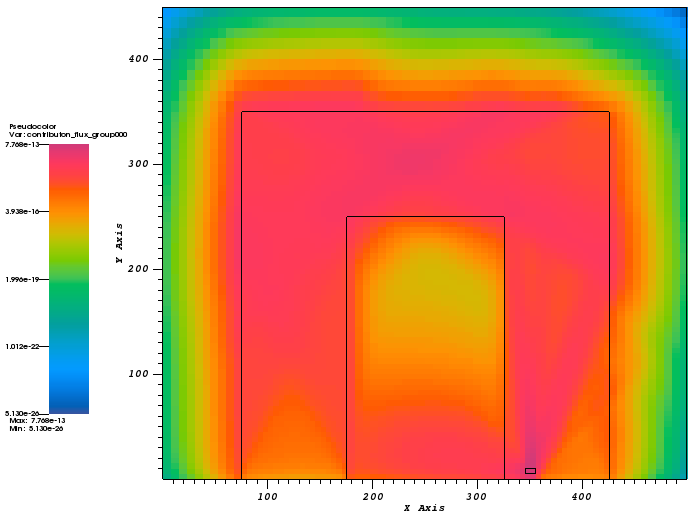

(b) Contributon flux distribution, highest energy group

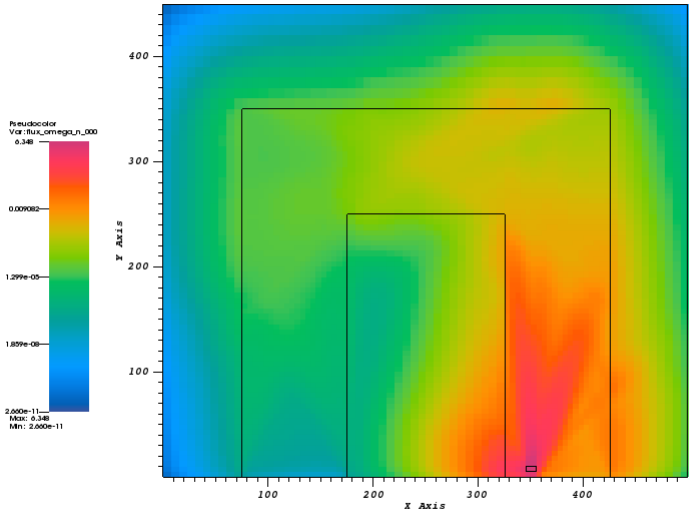

(c) Ω flux distribution, highest energy group

Figure 4.32: Flux distributions at problem midplane for U-shaped corridor. Distributions shown are for the highest energy group. In this problem the forward source and detector region are located in different z-plane locations.

The Ω-flux shown in Figure 4.32c does not attempt to force particles through the shield like the contributon flux, nor does it have as substantial of ray effects as the adjoint scalar

flux distribution. However, the ray effects in this variant are not completely mitigated. There appears to be a cone of particles extending into the u-bend that are of greater importance than the other regions near the detector. This is a clear effect of the forward flux distribution. However, the region just to the right of the detector location is of possible consequence. Between the detector and directly to the right, the flux decreases in magnitude more than two orders of magnitude. It is possible that the large gradient in importnace could be adversely affecting the time achieved by the Ω methods for this problem.

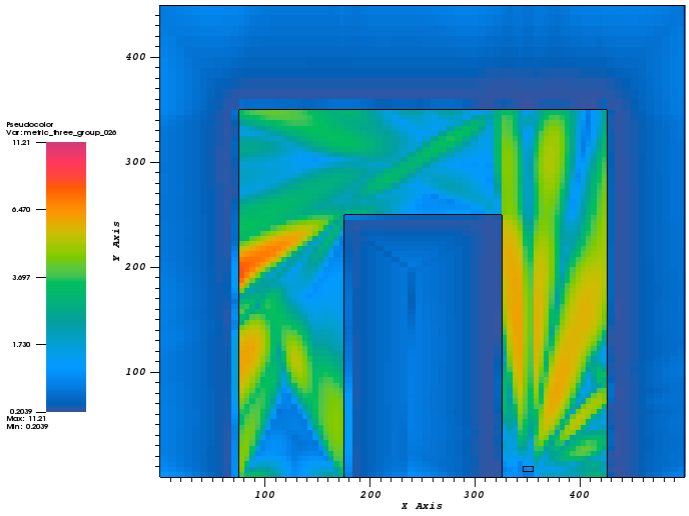

(a) M_3 distribution, visualized in plane containing detector

Figures 4.33a and 4.33b show the anisotropy metrics for the u-shaped bend. Figure 4.33a shows the M_3 distribution, which as one may recall is the ratio of the contributon maximum angular flux to the contributon average angular flux in the cell. M_4, which is visualized in Figure 4.33b, divides M_3 by the ratio of the maximum to average adjoint angular fluxes.

Comparing these two figures we can identify the effect of this normalization on the anisotropy metrics. Beginning with the M_3 distribution plot in Figure 4.33a, it is clear that we still observe the secondary ray effects in the flux anisotropies that were observed in the labyrinth problems. On the right side of the u-bend, we observe ray effects in the aniostropy that are likely from the adjoint flux distribution. On the left side of the bend we observe oblong circular distributions of anisotropy. These are more likely to be from particles emanating forward source distribution. The contributon flux anisotropies are much stronger in the air channels than in the concrete shield, as we would expect. In the shield immediately bounding the air, we observe a fairly isotropic flux distribution, but as particles reach closer to the edges the anisotropy increases slightly.

The M_4 distributions shown in 4.33b show how certain features of the anisotropy are removed when using the control adjoint angular flux. In particular, the shield region becomes

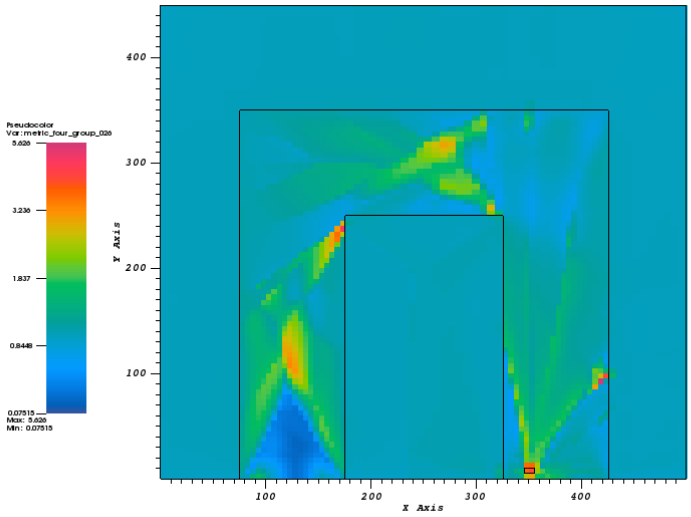

(b) M_4 distribution, visualized in plane containing detector

Figure 4.33: Anisotropy metrics plotted at problem midplane ($z = 55$) for U-shaped corridor. Energy group shown is for lowest energy.

completely normalized, meaning that the isotropy in the contributon flux matches that of the adjoint flux. The air regions are where real and substantial differences occur. In particular, we see peaks in the anisotropy where the forward and adjoint fluxes meet. At the top of the bend, the adjoint and forward fluxes have scattered relatively few times and thus generate a high aniosotropy in the contributon flux.

These anisotropy plots illustrate how in certain regions the flux anisotropy may be very high. Further, they show regions where the fluxes strongly interact with one another. In addition to helping to quantify the effectiveness of the method, they reveal interesting features of the solution that may not be obvious using standard flux figures.

4.2.6 Shielding with Rebar

The problem with rebar embedded both in the x- and y- directions in concrete has results summarized in Tables 4.17 and 4.18. Figures 4.34a and 4.34b show the results obtained by the track length tally in CADIS, CADIS-Ω and the nonbiased analog Monte Carlo.

The FOM results for the rebar-embedded concrete show that this is a very poor problem for CADIS-Ω, in general. CADIS-Ω has lower FOMs than CADIS in all measures. CADIS-Ω spends fractionally over five–both deterministically and in Monte Carlo–the transport time that CADIS does. Further, CADIS-Ω has poorer FOMs in both the tally average and maximum relative error than the nonbiased analog. This is due to CADIS-Ω requiring nearly 30x longer to run Monte Carlo than the nonbiased analog.

	CADIS		CADIS-Ω		analog
	MC	MC_{hybrid}	MC	MC_{hybrid}	MC
tally avg	1.15	1.09	0.0136	0.0127	0.948
max RE	0.0345	0.0327	0.00117	0.00109	0.0186
min RE	235	223	199	186	–
time (mins)	328	346	1.55e+03	1.66e+03	53.8

Table 4.17: Figure of Merit comparison between methods for rebar-embedded concrete.

		CADIS	CADIS-Ω	analog
		time (minutes)		
MCNP time	total	327.81	1550.54	53.82
deterministic time	advantg_time	0.28	0.29	–
	denovo_time	17.70	105.09	–
	dispose_time	0.03	0.41	–
	omega_time	0.00	2.05	–
	total	17.98	107.43	–
wall time		345.79	1657.97	53.82

Table 4.18: Detailed timing results for rebar-embedded concrete.

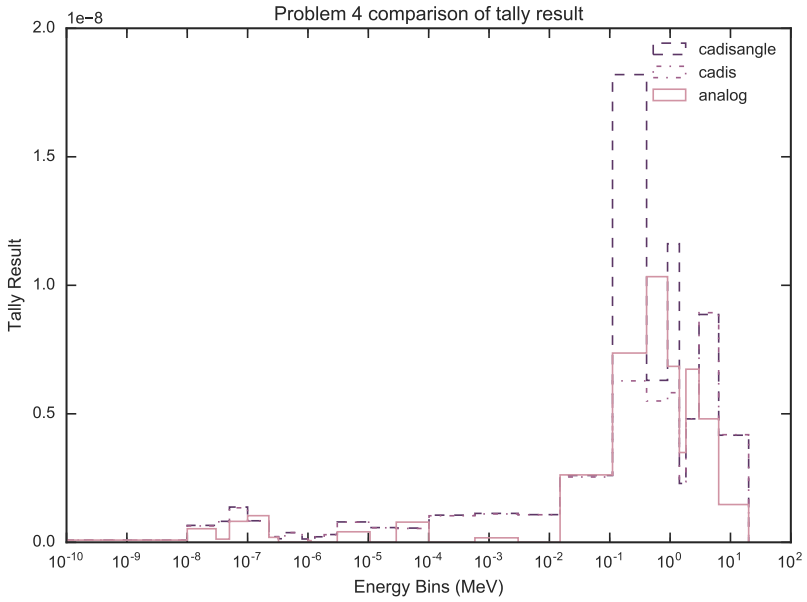

(a) Tally results comparison.

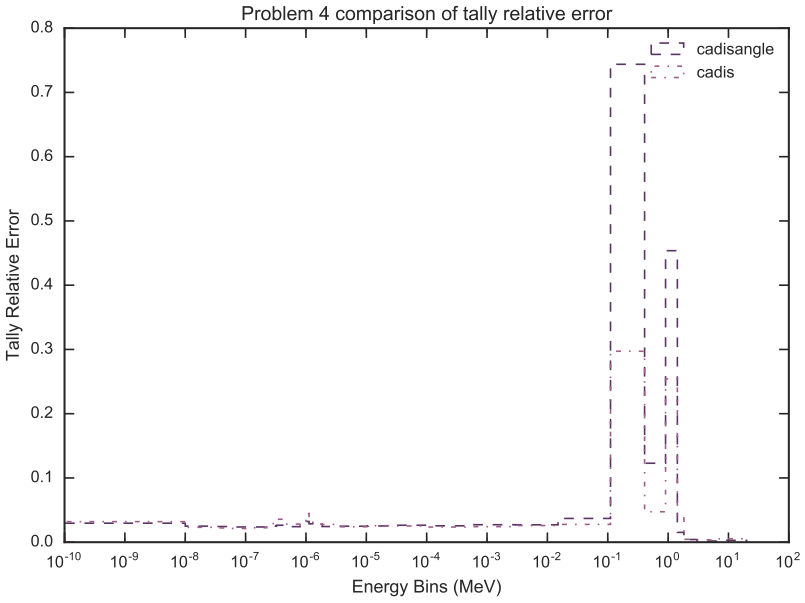

(b) Tally relative error comparison.

Figure 4.34: Tally result and error for rebar-embedded concrete, monodirectional Monte Carlo source

Figure 4.34a shows that the tally results for the rebar-embedded concrete do not generally agree between any method. CADIS and CADIS-Ω have better agreement with each other than with the nonbiased analog, but at high energies their results differ significantly. However, in comparing their relative errors in Figure 4.34b, the large discrepancy in their results is explained by the very high relative errors in this region. As with the U-shaped air corridor, neither method achieves satisfactory relative errors below 0.10 in high energy bins. However, both methods achieve comparatively good relative error results in energy bins below 10^{-1} MeV.

It is interesting that this problem appears to perform far more poorly than the steel beam in concrete. At this point, we must ask ourselves why a similar, but slightly more complex problem would have such substantively different results in the FOMs. This problem is undoubtedly difficult for both CADIS and FW-CADIS, but why does CADIS-Ω have such a poor performance in high energy bins which are usually more anisotropic than lower energy bins.

Section 4.1.2 described that flux anisotropy can be induced by the problem materials, geometry, or the source definition. Three of the characterization problem have monodirectional sources: the steel beam in concrete, the rebar-embedded concrete, and the nuclear medicine therapy room. At this point in the work it was discovered that ADVANTG does not support monodirectional sources, though it has in the past. As a result, the importance

maps generated by ADVANTG/Denovo automatically use an isotropic source distribution. However, the Monte Carlo input is not edited to reflect an isotropic source. As a result, the importance map does not match the physics in the problem.

This difference in the source definition did not affect the steel bar in concrete problem (Section 4.2.4) because the source comprises the entire wall at $x = 0$. However, both the rebar and the medical therapy room will have importance maps that do not match the physics of the defined Monte Carlo input. The results presented in Tables 4.17 and 4.18, as well as Figures 4.34a and 4.34b reflect a Monte Carlo simulation with a monodirectional source and a deterministic solver providing an importance map with an isotropic source. This, though unexpected, issue provides an opportunity for us to investigate the Ω-method's sensitivity to incorrect importance maps.

Tables 4.19 and 4.20 show the FOM and timing results for a Monte Carlo simulation with an isotropic source defined. Note that the deterministic times in Table 4.20 match those in Table 4.18. This is because the lack of support for monodirectional sources results in a deterministic solution that is agnostic to the defined Monte Carlo source. Figures 4.35a and 4.35b show the tally results and relative error for the case where the Monte Carlo and deterministic sources are consistent.

	cadis		cadisangle		analog
	MC	MC_adjusted	MC	MC_adjusted	MC
tally avg	80.5	45.6	260	132	0.257
max RE	1.52	0.862	1.31	0.662	0.109
min RE	221	125	214	109	–
time (mins)	23.5	41.4	111	218	9.15

Table 4.19: Figure of Merit comparison between methods for rebar-embedded concrete, isotropic Monte Carlo source.

The results in Table 4.19 are quite different than those in Table 4.17. The time for both CADIS and CADIS-Ω is reduced by more than an order of mangitude. In the original run of this problem, CADIS-Ω took 1,500 minutes to converge. Here that time is reduced to 111 minutes. Further, the tally average and tally maximum RE FOMs change between the tables by several orders of magnitude. This means that in addition to the shortened time reducing the FOMs, the relative errors also improved between the monodirectional and isotropic point source variants.

The tally results between Figs. 4.35a and 4.34a, show that having a consistently defined source between deterministic and Monte Carlo transport results in a closer tally result between CADIS and CADIS-Ω. This is also confirmed in Figs. 4.35b and 4.34b. In the origianl version of ths problem CADIS-Ω's relative errors at energy bins $> 10^{-1}$ were more than twice that of the REs achieved by CADIS. Interestingly, we see the opposite occur in the isotropic source definition. In figure 4.35b, CADIS has some energy bins with relative errors almost

		cadis time (minutes)	cadisangle time (minutes)	analog time (minutes)
MCNP time	total	23.47	110.67	9.15
deterministic time	advantg_time	0.28	0.29	–
	denovo_time	17.70	105.09	–
	dispose_time	0.03	0.41	–
	omega_time	0.00	2.05	–
	total	17.98	107.43	–
wall time		41.45	218.10	9.15

Table 4.20: Detailed timing results for rebar-embedded concrete, isotropic Monte Carlo source.

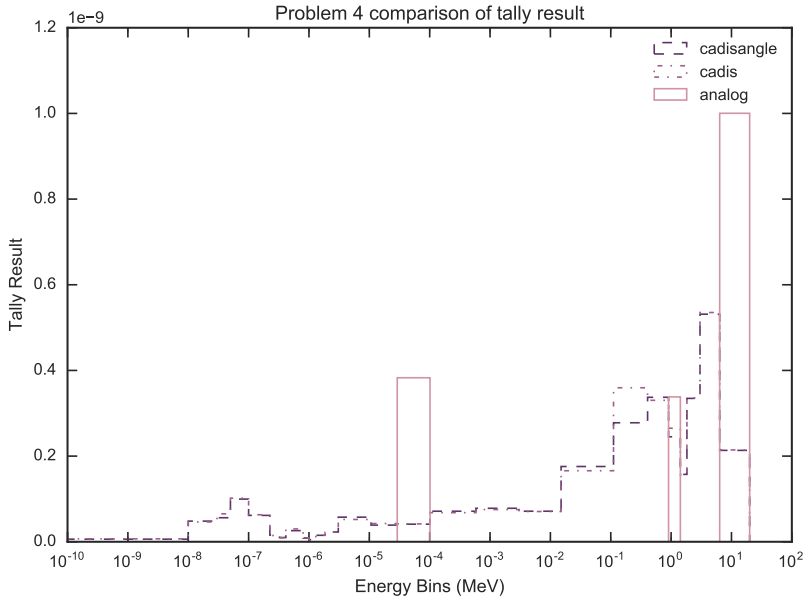

(a) Tally results comparison.

9x thos of CADIS-Ω in the same bin. However, it is worth noting that the scales between these two problems is very different. The highest RE achieved by CADIS in Figure 4.35b is lower than either CADIS or CADIS-Ω's RE in the monodirectional problem.

The plots in Figure 4.36 show the highest energy flux for the foward problem in Fig. 4.36a and the lowest energy Ω-flux distribution for the Ω-method in Figure 4.36b. Figure 4.36a clearly shows that the plate source on the left side of the problem is isotropically emitting particles. The Ω-flux in Figure 4.36b shows the preferential flowpaths for particles through the steel at low energies. Recall that the deterministic flux distributions will not change between the isotropic and monodirectional source definitions in Monte Carlo, so these

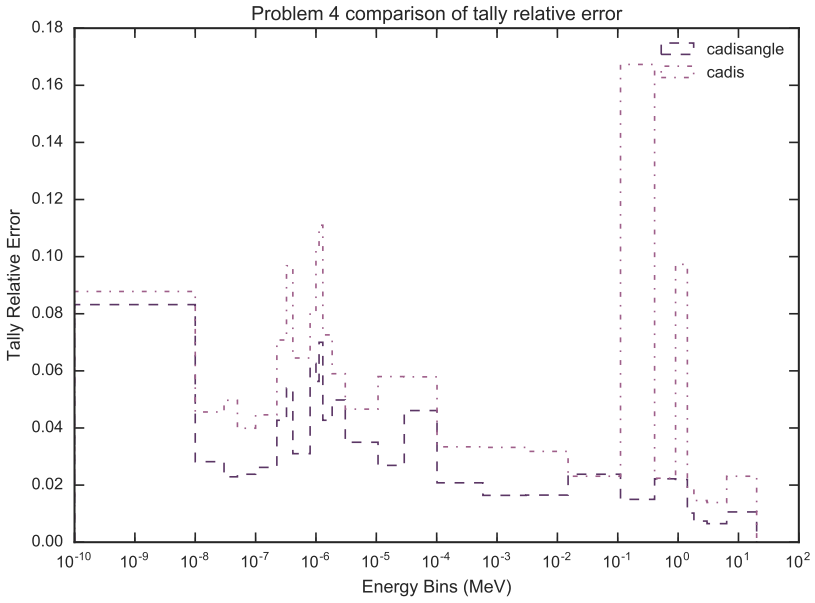

(b) Tally relative error comparison.

Figure 4.35: Tally result and error for rebar-embedded concrete, isotropic Monte Carlo source

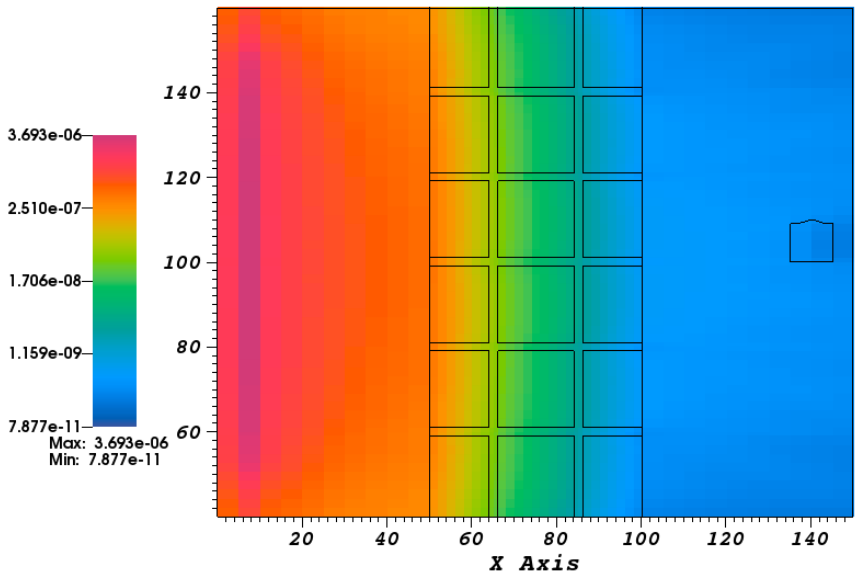

(a) Forward flux distribution, highest energy group

figures and any map of the metric distributions in the problem are the same regardless of the Monte Carlo source definition.

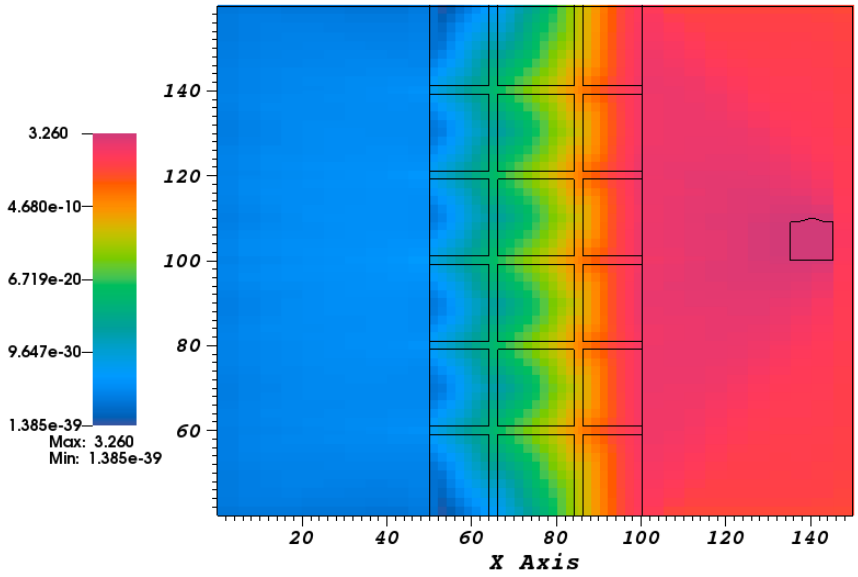

(b) Ω flux distribution, lowest energy group

Figure 4.36: Forward and Ω-flux distributions, rebar embedded in concrete. Slice is located at $y = 100$ centimeters

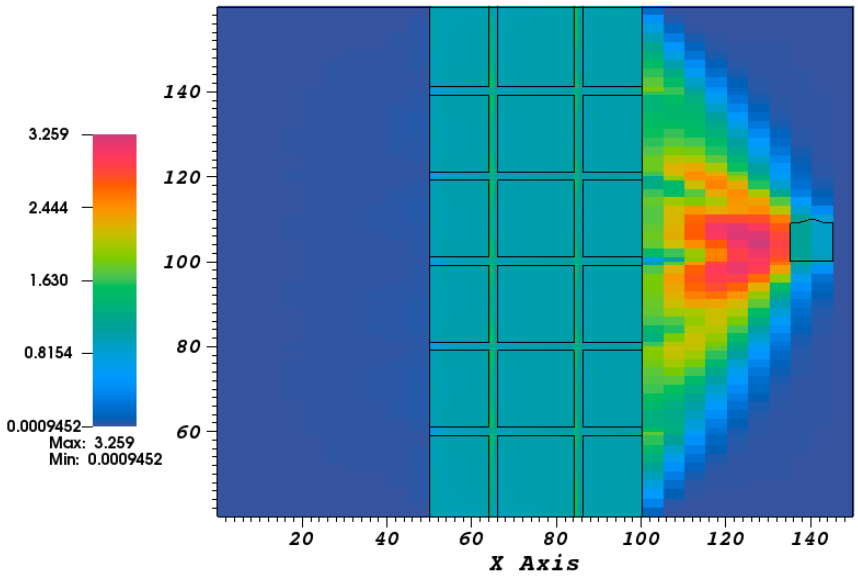

(a) M_2 distribution, lowest energy group.

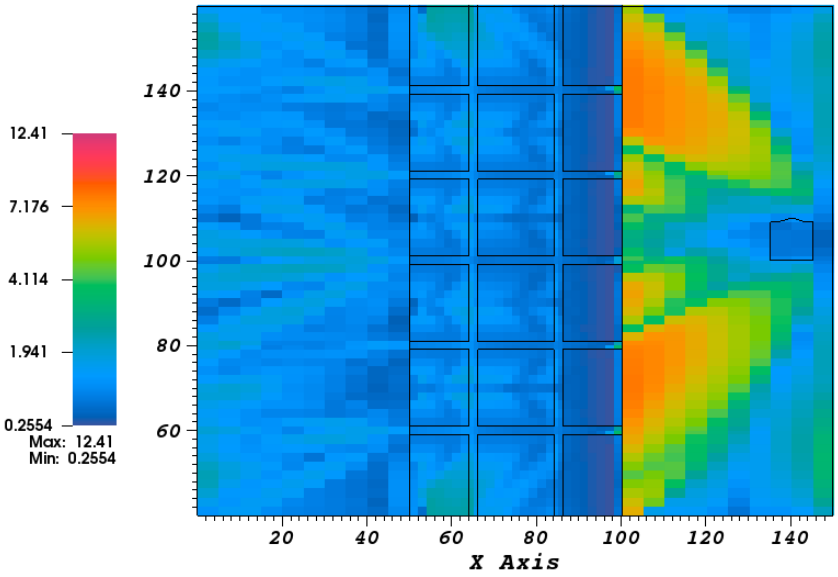

(b) M_3 distribution, lowest energy group.

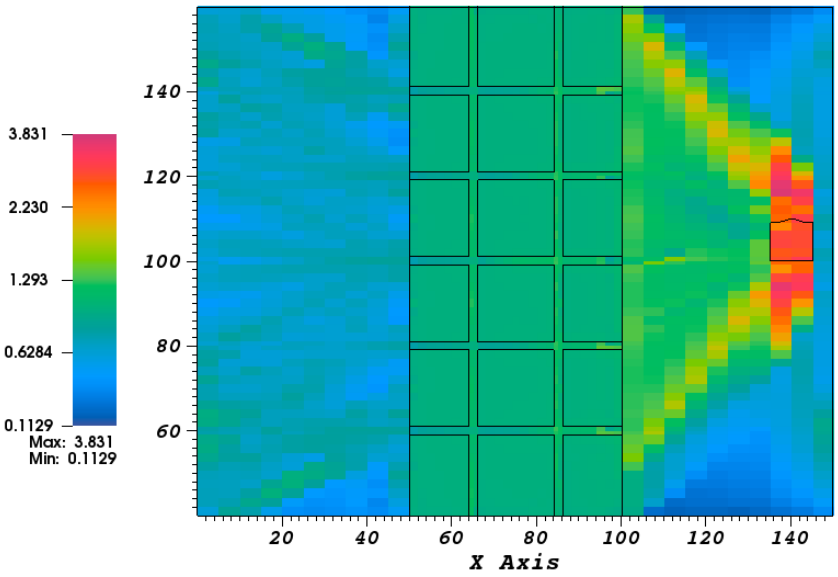

(c) M_4 distribution, lowest energy group.

Figure 4.37: Metric distributions for rebar-embedded concrete. Slice at $y = 100$ centimeters. Lowest energy group distributions shown.

The subfigures of 4.37 show the M_2, M_3, and M_4 distributions for the lowest energy group for the rebar problem. Recall that the M_2 distribution directly compares the Ω and adjoint scalar fluxes. Figure 4.37a shows that the biggest deviations of the Ω-flux from the adjoint are near the adjoint source. This was similarly observed in the steel beam problem variants. The regions of concrete are the same between CADIS and CADIS-Ω, but the rebar support structure shows that the Ω flux has a slightly higher importance for these regions. Glancing back towards the adjoint source region, the flux importances can be seen separating into fingers that line up with the concrete blocks in the problem.

The M_3 distribution of 4.37b shows the anisotropy of the contributon flux for this problem, and the M_4 distribution in Figure 4.37c shows the result of normalizing this anisotropy by the adjoint anisotropy. In the concrete blocks of Figure 4.37b some interesting anisotropy distributions occur closer to the forward source. As with Figure 4.37a, we can see the anisotropies separate into fingers that line up with the concrete blocks. On the adjoint source side of the shield, the anisotropies are the highest right next to the concrete blocks. On the forward source side of the shield, the areas next to the blocks are the least aniosotropic. When the metric is normalized by the adjoint in Figure 4.37c, some of the anisotropy effects are mitigated, meaning that the adjoint angular flux is the driving force behind the features that we observed in Figure 4.37b. However, on the forward source side of the shield there are strong anisotropies that line up with each of the metal rebar strucutres.

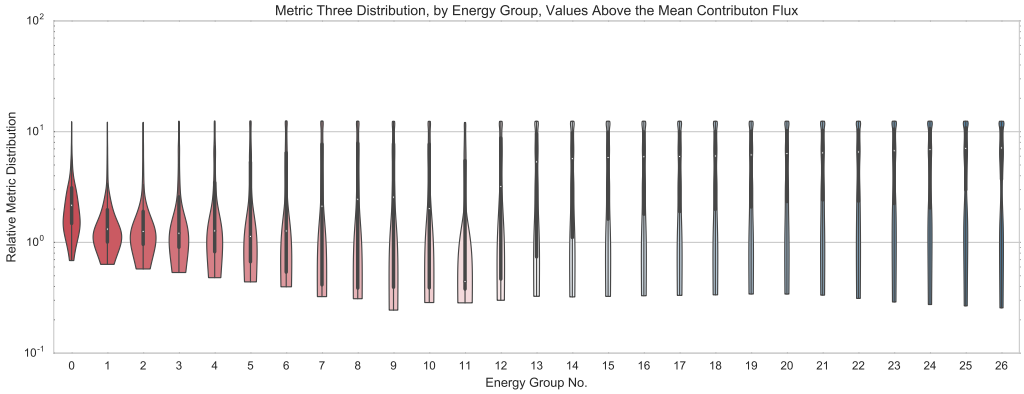

(a) M_3 distributions rebar embedded in concrete, filtered above the mean contributon flux.

While the metric distributions and the flux maps do not differ between the Monte Carlo source types, the scatterplots of I_{RE} and I_{FOM} will. Figure 4.38a shows a violin plot of the M_3 distributions for this problem. Figure 4.38b shows I_{RE} for the problem with a monodirectional Monte Carlo source trended against several metric values for M_3 values using the mean contributon flux filtering algorithm. Figure 4.38c shows these trends for the problem with an isotropic Monte Carlo source using the mean contributon flux filtering algorithm.

After inspecting the metric distributions against I_{RE} and I_{FOM}, no distinct trends were observable with any metric and either improvement factor. Because M_3 had the best trends,

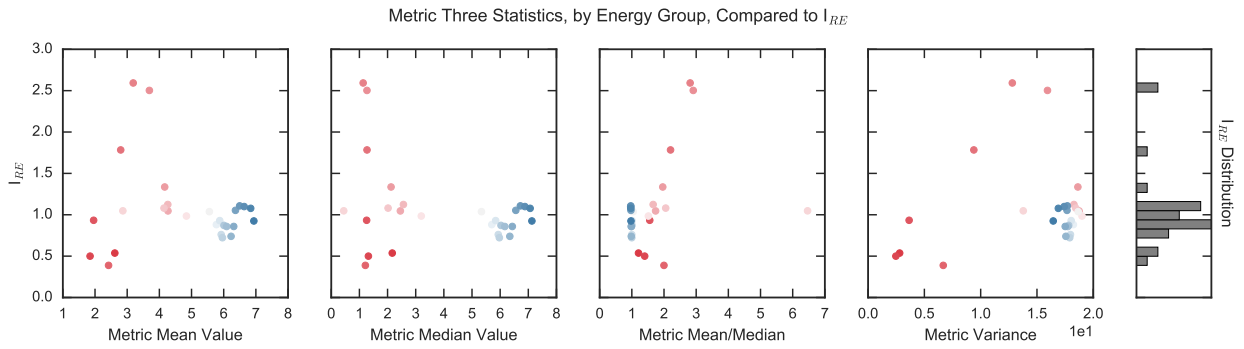

(b) I_{RE} for M_3 for rebar embedded in concrete, monodirectional Monte Carlo source.

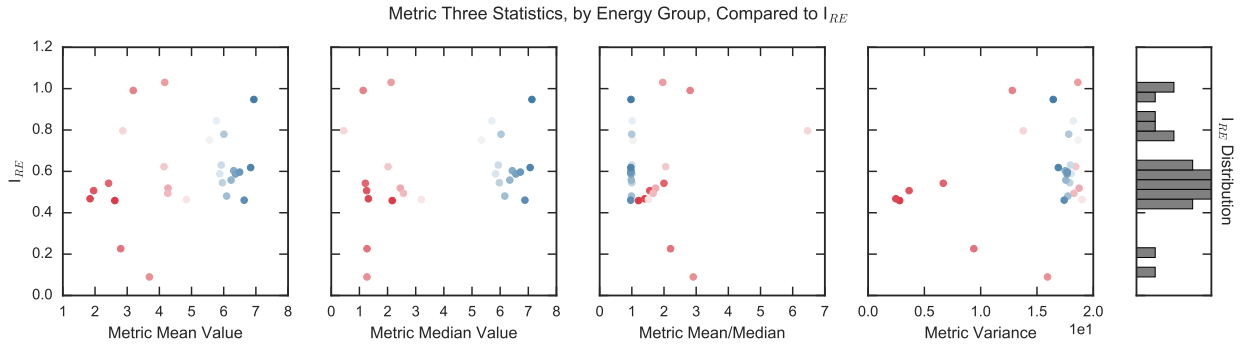

(c) I_{RE} for M_3 for rebar embedded in concrete, isotropic Monte Carlo source.

Figure 4.38: M_3 distribution and I_{RE} scatterplot for rebar-embedded in concrete. Values of M_3 have been filtered to be from cells that are above the contributon mean value.

it is included in the plots of Figure 4.38.

Figure 4.38a shows that low energy cells have a large spread but no centering value. There exist some very anisotropic cells at low energy groups, but there exist also exist some very isotropic cells. Conversely, in high energy groups the metric distribution has a very clumped distribution of values where the contributon max angular flux is higher than the average contributon angular flux in the cell.

Using values that can be computed from the distributions shown in Figure 4.38a, the relative error improvement between CADIS-Ω and CADIS can be plotted as shown in Figs. 4.38b and 4.38c. The x-values between each of these figures will be the same, but the y-ordinate values will differ as a result of their differing Monte Carlo source distributions.

In general Figure 4.38b shows there exist many energy bins where CADIS-Ω achieves a poorer relative error than CADIS. The bins where the comparative error is the worst is in intermediate energy regions. At low energy regions the relative errors are comparable, but as shown in the timing table, the FOM will be much lower for CADIS-Ω. There does appear to be a slight trend in I_{RE} with the ratio of the metric mean to the metric median

and with the metric variance. As with the steel beam problem, this shows that the metric distribution is a better predictor of the improvement in the relative error than the metric average or median value. However, these trends are not strong, and it would be difficult to predict the performance of a similar problem based on metric distributions. Comparing the results of Figure 4.38c to Figure 4.38b, some of these observations change with the isotropic source definition. First, CADIS-Ω performs better than CADIS uniformly in all energy bins. Next, there exists no trend in the metric distribution and I_{RE}. We cannot conclude that any version of the M_3 distribution can predict whether the Ω method will improve convergence for this problem.

It is possible that the filter matrix is not fine enough for this particular problem to pull out metric values of high importance, but even values filtered out above the mean contributon flux did not have strong correlations. However, with the cutoffs appearing in the distributions of 4.38a, choosing too high of a filter value may also remove much of the metric distribution.

Both CADIS and CADIS-Ω improve in the relative errors that they achieve as a resulf of having a source distribution that matches between the Monte Carlo and deterministic runs. As a result, the comparison between isotropic and monodirectional sources in this problem shows that having an importance map that does not match the problem will slow down convergence. Further, we can conclude that CADIS-Ω is more sensitive to having an importance map that doesn't match the Monte Carlo. This may be because the larger gradients in importance exacerbate splitting and rouletting from an unexpected source.

4.2.7 Therapy Room

The problem with a simplified representation of a nuclear medicine therapy room has FOM summarized in Table 4.21. Figures 4.39a and 4.39b show the results obtained by the track length tally in CADIS, CADIS-Ω and the nonbiased analog Monte Carlo. Note that the results for this problem had issues with reported times for the deterministic run, so the adjusted Monte Carlo (FOM_{hybrid}) is not reported and the timing table is not reported.

	cadis MC	MC_adjusted	cadisangle MC	MC_adjusted	analog MC
tally avg	5.81	5.71	106	8.34	2.81
max RE	0.463	0.455	0.822	0.0649	0.0136
min RE	37.6	37	32.9	2.6	0.793
time (mins)	44.7	45.4	39.9	506	248

Table 4.21: Tally relative error comparison between methods for simplified medical therapy room, Monte Carlo monodirectional source.

The therapy room with a monodirectional Monte Carlo source is a problem where CADIS-Ω performs fairly well when compared to CADIS and the nonbiased analog Monte Carlo.

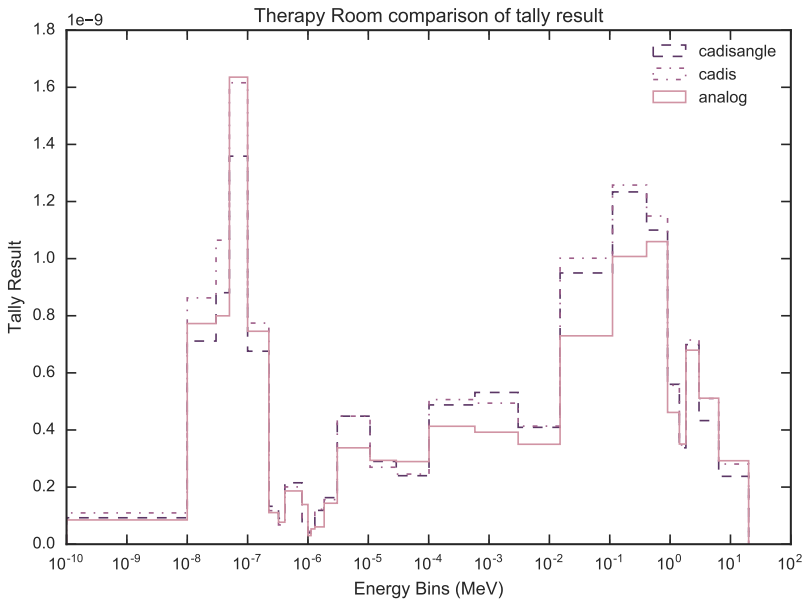

(a) Tally results comparison.

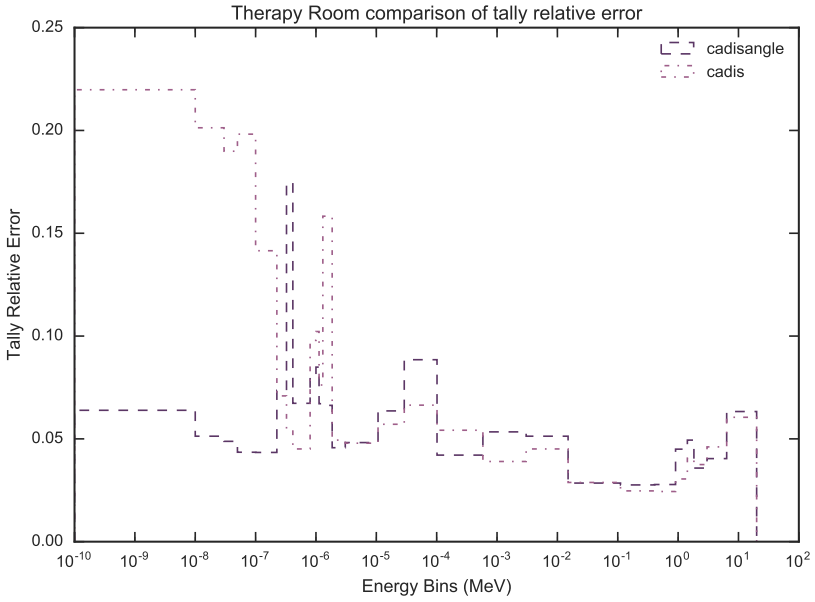

(b) Tally relative error comparison.

Figure 4.39: Tally result and error for simplified medical therapy room, monodirectional Monte Carlo source.

For the Monte Carlo runtime-exclusive FOMs, CADIS-Ω achieves better FOMs than CADIS and the nonbiased analog in both the tally average relative error and the tally maximum relative error. This is likely due to a softening of the importance map as a result of the concrete walls surrounding the therapy room. As a result, reflecting forward and adjoint particles decrease the strong gradient that exists in other problems, like the exit of the single turn labyrinth.

For this problem, CADIS-Ω achieved similar relative errors to CADIS for intermediate- and fast- energy bins. However, for low energy bins CADIS performed poorly and CADIS-Ω achieved satisfactory relative errors. These low energy bins are the only ones where CADIS-Ω really substantially outperformed CADIS. In a similar problem it would be advantageous to use CADIS-Ω as a method, but with deterministic runtime incorporated it may still be worthwhile to run with CADIS instead. If a user desires a tally with low energy bins exclusively, CADIS-Ω will be the advantageous method.

	cadis		cadisangle		analog
	MC	MC_adjusted	MC	MC_adjusted	MC
tally avg	29.8	11.4	192	72.4	52.3
max RE	0.829	0.316	3.51	1.32	0.292
min RE	387	148	423	159	10.7
time (mins)	287	753	281	747	91

Table 4.22: Tally relative error comparison between methods for simplified medical therapy room, Monte Carlo isotropic source.

As discussed in Section 4.2.6, the monodirectional source distribution in Monte Carlo is not actually reflected in the importance map generated by ADVANTG. As a result, the results for the isotropic source are shown in Table 4.22 and Figure 4.40.

Comparing the results from Tables 4.22 and 4.21, the isotropic source definition does improve the FOMS achieved by CADIS, CADIS-Ω, and the analog Monte Carlo. The minimum relative error FOMs see a factor of 10 improvement for both CADIS and CADIS-Ω. The time to run the biased problems is quite a bit longer, which is likely due to the placement of the source in the problem. Because the monodirectional source forced particles into the water phantom, they were sent into a region with relatively little variation in the flux. The Ω-method, in particular, avoids a region with very strong preferential flow. Avoiding splitting and rouletting as a result of crossing paths with large variations in the flux would allow the problem to run faster.

Despite the longer runtimes, CADIS and CADIS-Ω both achieve better FOMS in every measure by changing the source definition. Again, the effects of using the wrong importance map are reflected in longer runtimes for both problems.

Figure 4.40 shows the tally result and relative error for the isotropic source defined in Monte Carlo. Comparing the tally results of the isotropic source in Figure 4.40a to the

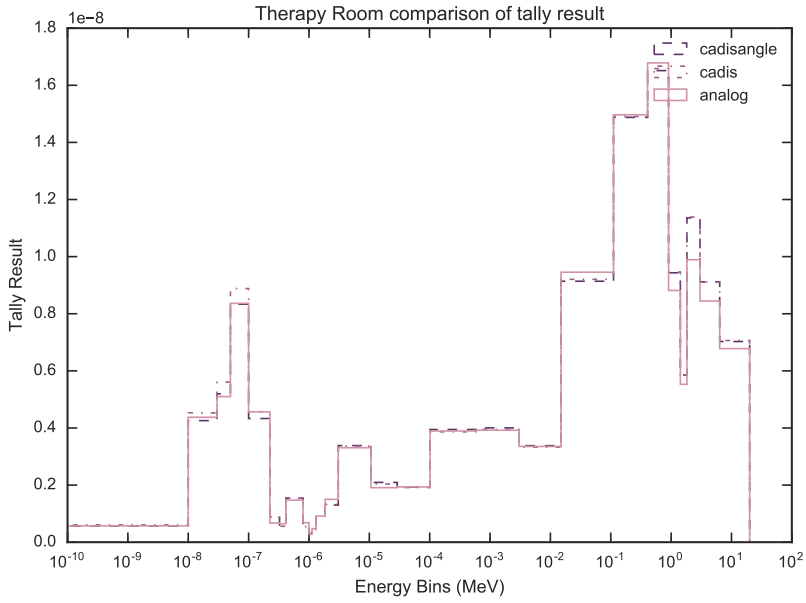

(a) Tally results comparison.

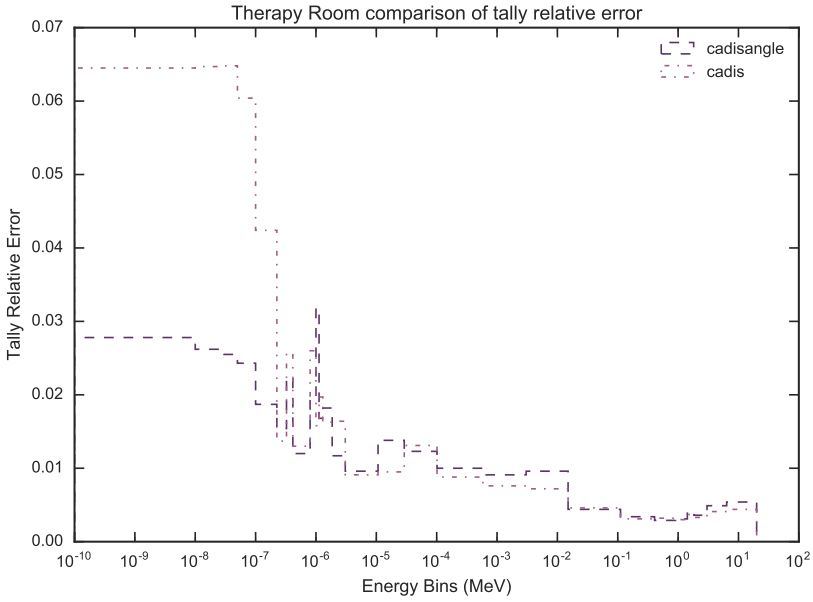

(b) Tally relative error comparison.

Figure 4.40: Tally result and error for simplified medical therapy room, isotropic Monte Carlo source.

monodirectional in Figure 4.39a, we can see that the results between all three methods agree better for the isotropic source distribution. The shapes of the relative error compare similarly between Figs. 4.40b and 4.39b, however the relative errors achieved by CADIS and CADIS-Ω are far smaller in the isotropic case. In both source definitions, CADIS struggles transporting low energy particles more than intermediate- or high-energy particles. CADIS-Ω handles these energies better, but it struggles in the lower-energy resonance regions slightly more than CADIS. As a result, there is some tradeoff with effectiveness for each method.

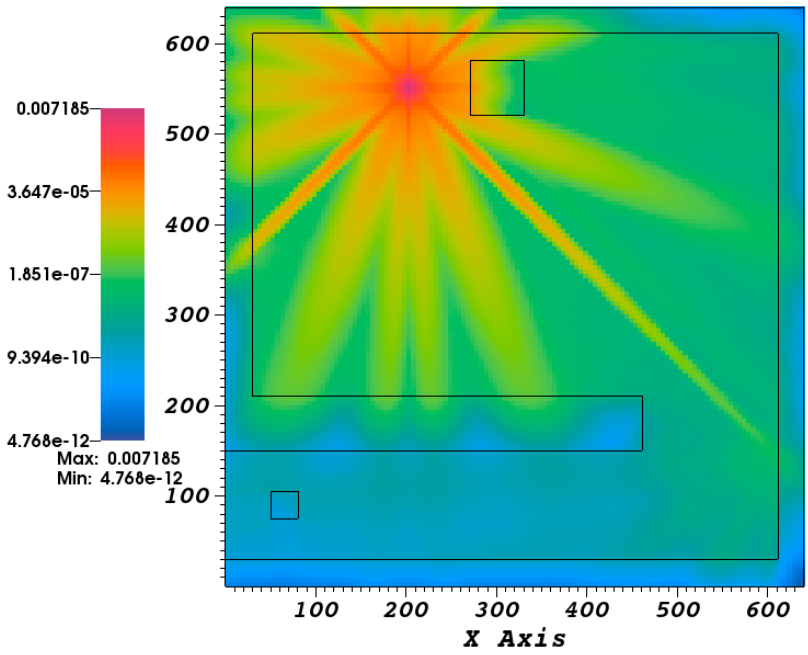

(a) Forward flux distribution, highest energy group

The flux maps for the therapy room are shown in Figure 4.41. Figure 4.41a shows the forward flux for the highest energy group. This figure has very strong ray effects that dominate the flux behavior near the water cell and near the forward source. Over just a few centimeters, the forward flux varies two- to three- orders of magnitude. The wall to the bottom right of the figure shows some secondary ray effects that occur after scattering. This is much more subtle than near the forward source, but there are three groupings of flux direction after this scatter, which may be magnified in the Ω-flux by the adjoint.

Figures 4.41b and 4.41c show the adjoint and Ω-fluxes for the therapy room problem. Unlike the labyrinth variants, where the Ω methods softened ray effects, there exist much stronger ray effects in the Ω-flux map for the therapy room. This is because the ray effects are primarily from the forward flux, which does not affect the standard adjoint flux whatsoever. However, the integration of the forward and adjoint in the Ω calculation causes some of the forward ray effects to be carried over into the adjusted adjoint. A compounding factor to this

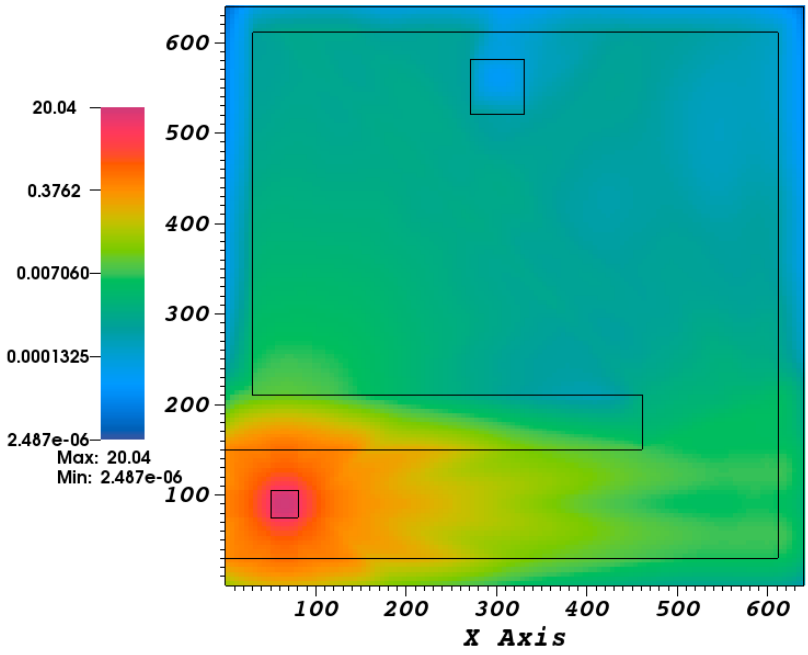

(b) Adjoint flux distribution, highest energy group

is that the adjoint particles travel in exactly the opposite direction to the forward particles at the region where the hallway meets with the room. It was discussed previously that the contributon flux will be magnified if forward and adjoint particles are travelling in opposite directions. Not only is this the case in the therapy room, but they are travelling in oppoiste directions down a ray effect. This magnifies the ray effect in the problem, so there is a tight band of particle travel diagonally across the Ω problem.

Figure 4.42 shows the M_4 distribution and the trends of I_{RE} for different values of the M_4 distribution for both the isotropic and monodirectional variants of the therapy room. These figures do not use a filtering algorithm. This is because this particular problem was run on a slightly earlier version of ADVANTG that did not output the angle-integrated contributon fluxes. As a result, the values used for the filter matrix are not accessible, and filtering cannot be used in this analysis. Future studies of this particular problem should compare the effects of the filtering algorithms of the distributions of Figs. 4.42b and 4.42b.

Figure 4.42a shows the full violin plots by energy group for the therapy room. Here we see that the lower energy groups have values clustered around a value slightly above 1. Violins in intermediate to high-intermediate energy groups have a lower mean value than the low energy violins, but their distribution tends to broaden. The broadening of the distribution is particualrly evident for energy group violins valued ≤ 8.

Figures 4.42b and 4.42c show the effect that this distribution has on I_{RE} for both the monodirectional and isotropic variants of the problem. Again, non of the anisotropy metrics

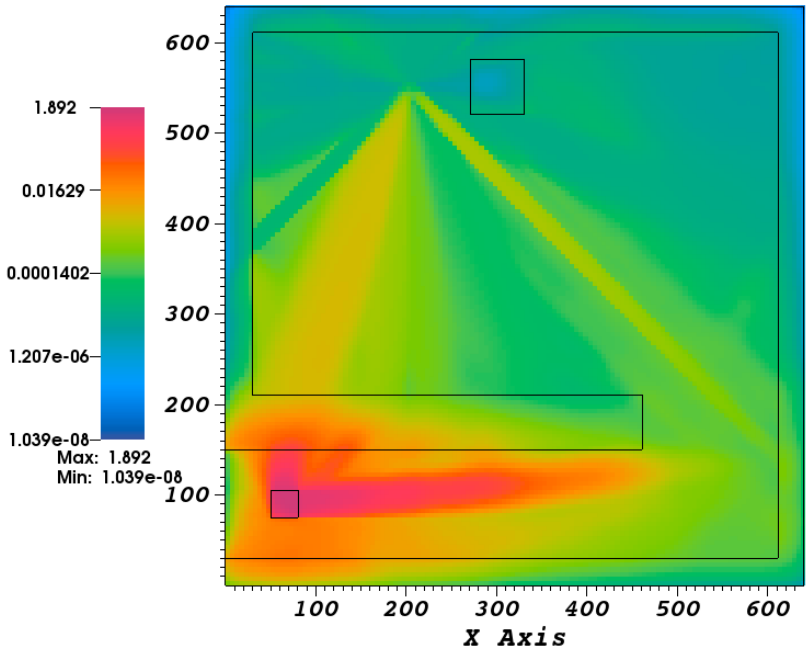

(c) Ω-flux distribution, highest energy group

Figure 4.41: Flux distributions at $z = 150$ centimeters for radiation therapy room.

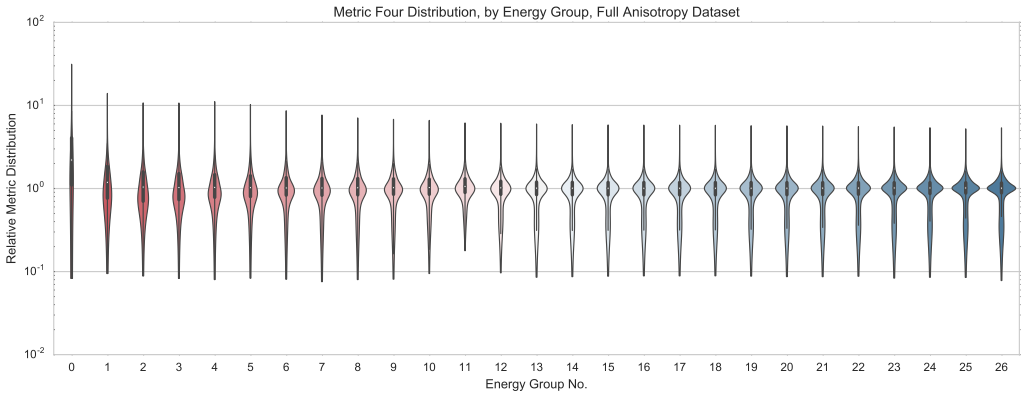

(a) Unfiltered M_4 distributions medical therapy room.

showed a strong trend for I_{RE} or I_{FOM} with any distribution, so the best figure was included here. Recall that a value below unity for these figures indicates that CADIS-Ω achieved a lower relative error in that bin. In both figures CADIS-Ω has roughly half of its values above unity and half below. There are some very low energy bins in which CADIS-Ω far outperforms CADIS, but then there are intermediate energy groups that CADIS-Ω's performance falters.

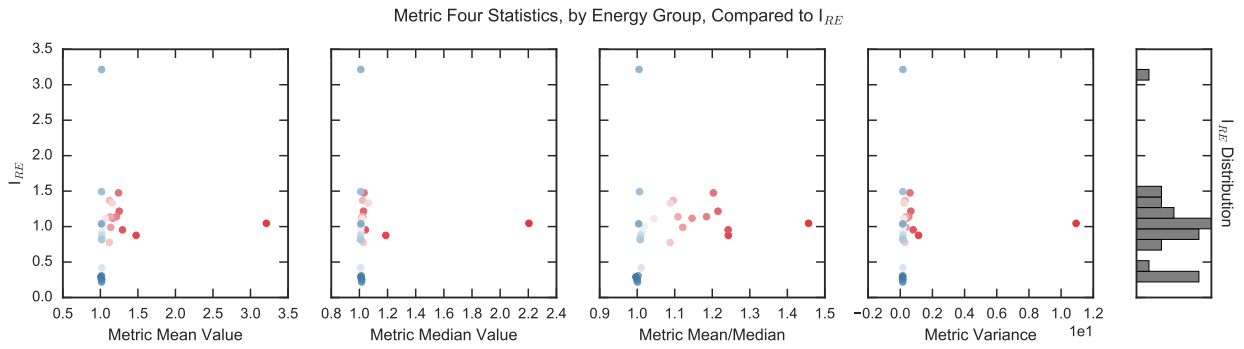

(b) I_{RE} for M_4 for therapy room, monodirectional Monte Carlo source.

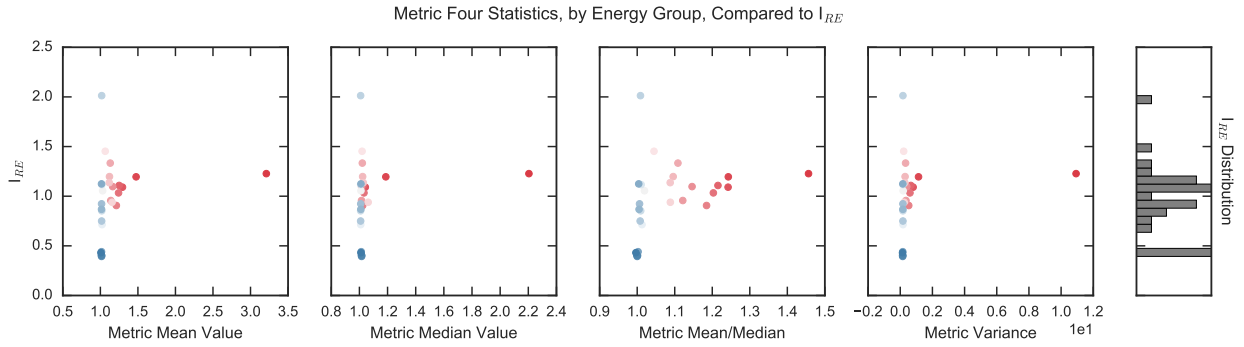

(c) I_{RE} for M_4 for therapy room, isotropic Monte Carlo source.

Figure 4.42: M_4 distribution and I_{RE} scatterplot for medical therapy room.. Values of M_4 have not been filtered with a filtering algorithm.

Neither figure shows a particular trend, but the metric skew does appear to be the subplot most closely resembling a trend.

In comparing Figure 4.42 to 4.38, this problem does not show as significant of a change in I_{RE} with respect to changing source definitions. This means that the ratio of relative errors between CADIS and CADIS-Ω remains the same, despite both achieving far lower relative errors overall in the isotropic case. That means, for this problem, CADIS and CADIS-Ω are both equally sensitive to a mismatch in importance map. This could be a result of the large fraction of air in the problem, which dominates the behavior of both methods. Conversely, the rebar problem required both CADIS and CADIS-Ω to sample frequently in the center of the problem, so the effects of mismatching maps was more isolated from other effects.

4.3 Sensitivity to Deterministic Parameter Choice

At this point in the Ω-method characterization, it has been shown how the Ω-methods behave in problems with differing geometries and materials. However, each of the problems presented

in Section 4.2 was run with the same deterministic calculation parameters. While the angular flux may have differed in these problems due to differences in the way the problems were constructed, it did not vary due to deterministic solver choices. Some deterministic solver choices will change the angular fluxes used to calculate the Ω-flux. Consequently, this may affect the behavior of the Ω-methods. This section will explore the effects of deterministic solver choices on the Ω-method's performance.

Section 4.2 showed that the Ω-methods have a strong weakness to "thin" materials, as CADIS and FW-CADIS do. Recall that a "thin" material is characterized by a low density, and thus a low macroscopic cross section, or interaction probability. In a pure streaming problem, the particle flux will decrease by a factor of r^2 from the source and never interact. In a thin material, a particle may stream several centimeters before interacting. As a result, the importance of a particle, which is related to the adjoint- or omega-flux, may vary several orders of magnitude over a mean free path of travel distance. At a collision, the particle then requires several orders of magnitude of sampling events.

The Ω-method's weakness to "thin" materials was confirmed by running the steel beam problem with air and concrete in the geometric location of the steel beam. In the "thin" material air version, CADIS-Ω performed poorer than CADIS. This was a strong contrast to the same geometric configuration with a steel beam, where CADIS-Ω outperformed CADIS. The success of CADIS-Ω in this problem also showed that the incorporation of the Ω-flux into a problem with materials with very different moderating properties but both with high probabilities of interaction, improves the performance of the Ω-methods beyond CADIS or the nonbiased analog.

Due to CADIS-Ω's superior performance to CADIS in the problem with a steel beam in concrete, this is the problem that will be used to characterize CADIS-Ω's sensitivity to deterministic parameter choice. In this section, the effect of deterministic solver choices on the performance of the Ω methods will be investigated. In particular, we are interested in how parameters that influence the angular flux will affect the performance of the Ω-methods. By using the same problem with differing solver options, the effect of solver options can be isolated from the material and geometric effects. By doing so, we seek to determine how resilient the Ω-methods may be to using low-fidelity solver options, how different the sensitivity of the Ω-methods are to solution quality when compared to CADIS, and how varying angular parameters may speed up or slow down the time to a desired solution. By quantifying these effects, we can determine the best parameter selection for the Ω-methods for this type of problem.

4.3.1 Parametric Study Description

The angle sensitivity parametric study will cover the subset of computational parameters that are most likely to influence the Ω method's solution. Because the Ω-flux is calculated from an angular integration of the forward and adjoint flux, calculation parameters that are most likely to influence the angular flux solution are the variables that will be perturbed. The two parameters that will be studied are the quadrature order and the P_N order.

The quadrature used in a deterministic solver is used do discretize the problem in angle. Quadrature options are split into two separate selections: the quadrature set or type, and the quadrature order. Because the Ω-methods require rotational symmetry, only quadrature sets that have rotational symmetry (generally these are triangular quadrature sets) can be used with the Ω-methods. In ADVANTG/Denovo, the triangular quadrature sets are: linear-discontinuous finite element, level-symmetric, and quadruple range. As discussed previously, quadruple range is selected as the ADVANTG default because it has good properties and guarantees positivity in the flux. Different quadrature sets have separate properties and are a realm of study unto their own. Thus, we will vary only quadrature order and not quadrature type in this sensitivity study.

Quadrature orders specify how fine of a resolution the quadrature set will be. As quadrature order increases, the angular discretization becomes finer, and the size of the angular flux matrices increases. The Ω methods use angular flux values that are written to a file after a Denovo transport solve, which are then read into memory to compute the Ω-flux. We expect to observe much slower deterministic recorded times in T_{det}–and, by extension, T_{hybrid}–for high quadrature orders because of the I/O demand to read and write the angular flux values. This I/O demand will not be as extreme for standard CADIS, as the angular flux values are not written in that case. Recall that the ADVANTG default quadrature order is 10. The quadrature orders used for the sensitivity study aimed to choose orders surrounding this value. This resulted in quadrature orders 5, 7, 10, 12, 15, 17, and 20 being chosen for variations in this parameter.

The P_N order determines the fidelity of the scattering expansion. The availability of P_N orders is dependent on the cross section dataset that is being used. For the 27G19N cross section library, the P_N order extends to 5. As a result, P_N orders of 1, 3, and 5 are chosen for variations in this parameter.

While the P_N order does affect angular information in the problem, it will not change the size of the angular flux matrices. As a result, deterministic runtimes between differing P_N orders may vary, but not as significantly as they will in differing quadrature orders due to the lack of change in I/O requirements as P_N order changes.

Other deterministic parameters may influence the variance reduction parameters calculated by the Ω methods. The spatial discretization, while not a primary factor influencing the angular flux, still may affect the Ω-methods' performance. A finer energy group structure may also influence the Ω-method solution. Finer energy groups will more effectively reflect resonance regions in scattering and absorption. Scattering effects in certain energy regions will have angular dependence and, thus, may have a stronger effect on the angular flux than a coarser energy discretization. Because these particular solution effects do not directly influence the angular flux and angular effects will be difficult to isolate, they will not be included in the angular sensitivity parametric study.

Several factors in the deterministic calculation should not have a strong effect on the angular flux distribution. These include the spatial solver, the convergence criteria for the solvers, and the within group solver types. Because these factors should not influence the angular flux any more than any other part of the solution, they will also not be included in

this parametric study.

4.3.2 Quadrature Order

The results that will be presented in the next two subsections will be similar to those presented in Section 4.2. However, our goal is to see how changing deterministic parameter type affects the results in the tally region. With this in mind, the presentation of the results may be adjusted to more effectively show the effect each parameter has on influencing the Monte Carlo transport.

Table 4.23 contains the FOM results for each of the quadrature orders run in the parametric study. The results are grouped by FOMs calculated with the same relative error. The first three sections of the table pertain to different FOM values, and the last section of the table shows timing results for the standard Monte Carlo (T_{MC}) and the total walltime (T_{hybrid}) for the calculation.

In the tally average relative error subsection of Table 4.23, two strong dips in the FOM appear in the CADIS results at S_N orders 5 and 10, and a dip in the CADIS-Ω FOMs occur at S_N order 12. These dips are much larger relatively than in the maximum or minimum relative error subsections of the table. This indicates that for these particular quadrature orders, fewer particles contribute to the detector response across all groups. We can also see in the CADIS-Ω results that quadrature orders 10, 15 and 17 all have a similar FOM for the tally average relative error using the Monte Carlo runtime. However, the FOMs for the same quadratures do not decrease more significantly when using T_{hybrid} to calculate the FOM, as suggested in Section 4.3.1. This suggests that the increased deterministic runtime for I/O is offset consistently by the change in the FOM between quadrature orders for CADIS-Ω.

In this subsection of the table it is also notable that the oscillations between maximum and minimum FOM values is much larger for CADIS-Ω than for CADIS. For low quadrature orders, CADIS-Ω shows substantial improvement in the FOM, while CADIS remains somewhat constant (this is omitting the major dips in FOM values noted in the previous paragraph). At higher quadrature orders, however, CADIS-Ω's performance is inverted and decreases with increasing quadrature order. CADIS, however, remains fairly constant in FOM for S_N orders 12 and above. Both methods far outperform the nonbiased analog Monte Carlo run.

The maximum relative error portion of the table also has several notable datapoints. For CADIS, the dips in FOM are still visible for S_N orders 5 and 10, but quadrature order 7 does not achieve the same high FOM as quadrature orders 12 and above as it does in the tally average subsection of the table. If the maximum relative error convergence is the limiting factor for the user, it appears that using any quadrature order above 10 is a good choice for CADIS. CADIS-Ω, conversely, has more varied results. No observable trend exists in the FOM with increasing quadrature order for CADIS-Ω. A dip in the FOM occurs at quadrature order 12, as it did in the tally average subsection of the table. This dip, like CADIS' dips, is not as significant as the dip in the tally average FOMs. Generally, CADIS has higher FOMs when using the maximum relative error as a success metric. In fact, the

only quadrature order where CADIS-Ω's FOM is larger than CADIS' is at quadrature order 10.

		CADIS		CADIS-Ω		analog
	S_N order	MC	MC_{hybrid}	MC	MC_{hybrid}	MC
tally avg	S_N 5	683	677	1.81e+03	1.79e+03	1.39
	S_N 7	2.55e+03	2.53e+03	2.46e+03	2.45e+03	
	S_N 10	669	659	2.96e+03	2.93e+03	
	S_N 12	2.46e+03	2.41e+03	187	183	
	S_N 15	2.48e+03	2.42e+03	2.98e+03	2.92e+03	
	S_N 17	2.47e+03	2.39e+03	2.96e+03	2.88e+03	
	S_N 20	2.46e+03	2.35e+03	1.89e+03	1.81e+03	
max RE	S_N 5	4.89	4.85	2.86	2.84	0.0448
	S_N 7	7.71	7.64	4.35	4.32	
	S_N 10	3.74	3.69	6.71	6.64	
	S_N 12	14.3	14.1	0.764	0.748	
	S_N 15	14.7	14.3	3.87	3.79	
	S_N 17	14.8	14.4	7.98	7.78	
	S_N 20	14.1	13.5	6.09	5.85	
min RE	S_N 5	1.14e+03	1.13e+03	1.09e+03	1.09e+03	–
	S_N 7	1.37e+03	1.36e+03	1.26e+03	1.25e+03	–
	S_N 10	1.43e+03	1.41e+03	1.32e+03	1.3e+03	–
	S_N 12	1.46e+03	1.43e+03	1.33e+03	1.3e+03	–
	S_N 15	1.47e+03	1.43e+03	1.32e+03	1.3e+03	–
	S_N 17	1.46e+03	1.42e+03	1.31e+03	1.28e+03	–
	S_N 20	1.46e+03	1.39e+03	1.31e+03	1.26e+03	–
Time (mins)	S_N 5	302	305	1.13e+03	1.14e+03	22.3
	S_N 7	324	327	1.62e+03	1.63e+03	
	S_N 10	414	420	2.11e+03	2.14e+03	
	S_N 12	406	414	2.09e+03	2.14e+03	
	S_N 15	404	413	2.1e+03	2.14e+03	
	S_N 17	405	418	2.11e+03	2.17e+03	
	S_N 20	406	425	2.12e+03	2.21e+03	

Table 4.23: Figure of Merit results for steel beam embedded in concrete, with variations in quadrature order. Subdivisions of the table indicate calculations of the FOM using different relative errors. The analog case has a single value for each relative error as it is not dependent on changes in deterministic calculation parameters.

In the minimum relative error subsection of Table 4.23 the CADIS and CADIS-Ω FOM

behavior is much more well-behaved than it is for the preceding two subsections of the table. There are no dips in the FOM value for either method, so the lowest relative error will consistently get better with increasing quadrature order. A slight shift to a $< 1\%$ lower FOM occurs for quadrature orders 17 and 20, which indicates that increasing quadrature fidelity does not help improve the FOM past S_N order 15. Similar behavior is observable for CADIS-Ω in the minimum relative error subsection of the table. CADIS-Ω has a consistently lower-valued FOM between 5%-10% for all quadrature orders when compared to CADIS. A turnover occurs in the CADIS-Ω FOMs at a lower quadrature order, meaning that CADIS-Ω does not benefit from increasing S_N order as much as CADIS using this FOM as a metric. However, beyond quadrature order 15 neither method sees a benefit in the FOM by increasing the quadrature order.

The timing results in the last section of the table show how much longer it takes CADIS-Ω to transport the standard Monte Carlo than CADIS. This was also noted in Section 4.2.4. In the introduction to this section, it was predicted that the I/O demands for CADIS-Ω would impact the MC_{hybrid} FOMs as quadrature order increases. However, because the CADIS-Ω Monte Carlo times are already so much longer than CADIS', this impact is not as significant as expected. Further, the increase in deterministic runtime seems to change similarly to the increase in Monte Carlo runtime as the importance map changes. This explains why the FOMs were not impacted so negatively in the previous sections of the table.

Let us use an illustrative example to compare the FOMs between CADIS and CADIS-Ω. Returning again to Table 4.23, at S_N order 5 the non-MC runtime is three minutes for CADIS, while it is around ten minutes for CADIS-Ω. At S_N order 20, the CADIS non-MC runtime is 19 minutes; the CADIS-Ω time is 100 minutes. For each of these cases, the non-MC runtime is about 4% that of the Monte Carlo runtime. Because this fractional time is fairly consistent between CADIS and CADIS-Ω, we do not see a strong impact on FOM_{hybrid} from the significantly longer non-MC runtimes in CADIS-Ω.

Table 4.23 shows that for the FOM using the tally average relative error, CADIS-Ω outperforms CADIS for most quadrature orders (with excpetions being S_N orders 7 and 12). For the majority of the quadrature orders, CADIS-Ω gets more particles to the tally region than CADIS in the same amount of time. By increasing quadrature order, CADIS-Ω generally increases the number of particles to the tally as a whole, while CADIS remains fairly constant. The table also shows that by using either the maximum or minimum relative error to calculate the FOM, CADIS generally outperforms CADIS-Ω. However, while both the maximum and minimum RE FOMs increase with increasing quadrature order in CADIS, this is not the case for the tally average FOM. This could be interpreted as that as the quadrature order increases, more particles reach the extreme tally bins, but fewer particles end up in the tally overall. For CADIS-Ω, this behavior is not quite the same. Instead, a peak occurs in the tally average FOMs at intermediate quadrature orders, and the minimum RE FOM decreases with increasing quadrature order.

In the Subsection 4.2, it was discussed that while the FOM shows how quickly a tally may approach a desired value, it does not show how effectively each method transported particles to the tally location. Because the same particle count was used in each variation

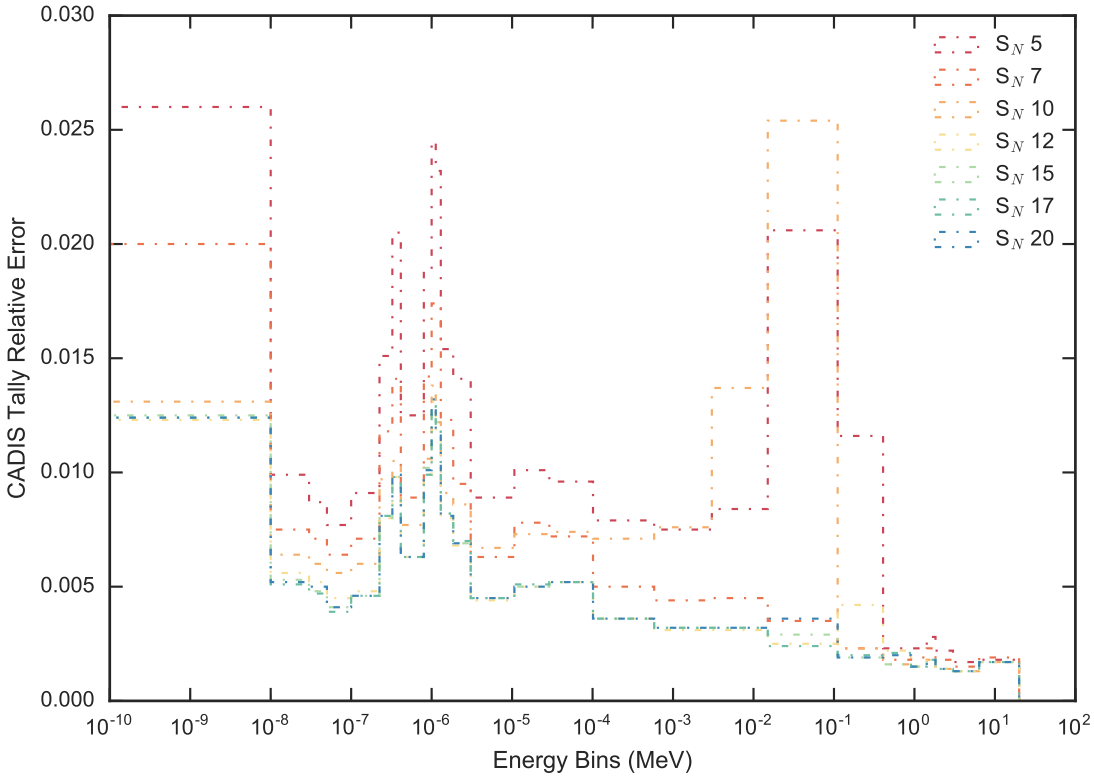

(a) Relative errors of CADIS results for differing S_N orders.

of the steel beam problem in the angle sensitivity study, the relative error results achieved by each method can reveal how well each method transported the same number of starting particles. The next several plots will present this information.

Figures 4.43a and 4.43b show the relative errors for all tally bins for each quadrature order run of the problem with the steel beam in concrete for CADIS and CADIS-Ω, respectively. Unlike Table 4.23, these plots show the overall behavior of the tally results as a function of changing quadrature order, so the behavior of non-extreme tally bins can also be observed. As noted in the discussion accompanying Table 4.23, these intermediate are important in evaluating the tally average relative error.

Figure 4.43a plots the tally relative error results for each of the CADIS runs, binned by energy. The warmer colored red and orange lines show the low quadrature order results, while the cooler colored lines correspond to higher quadrature results. For all of the energy bins below 10^{-4} MeV, a reduction in the relative error with increasing quadrature order can be observed. For quadrature orders S_N 12 and above, the relative error does not show as much of an improvement in the relative error. Between 10^{-4} and 10^{0} MeV, large spikes in the relative error for quadrature orders 5 and 10 exist, explaining the poor behavior of the tally average RE FOM and tally maximum RE FOM for CADIS. Quadrature order 7 has

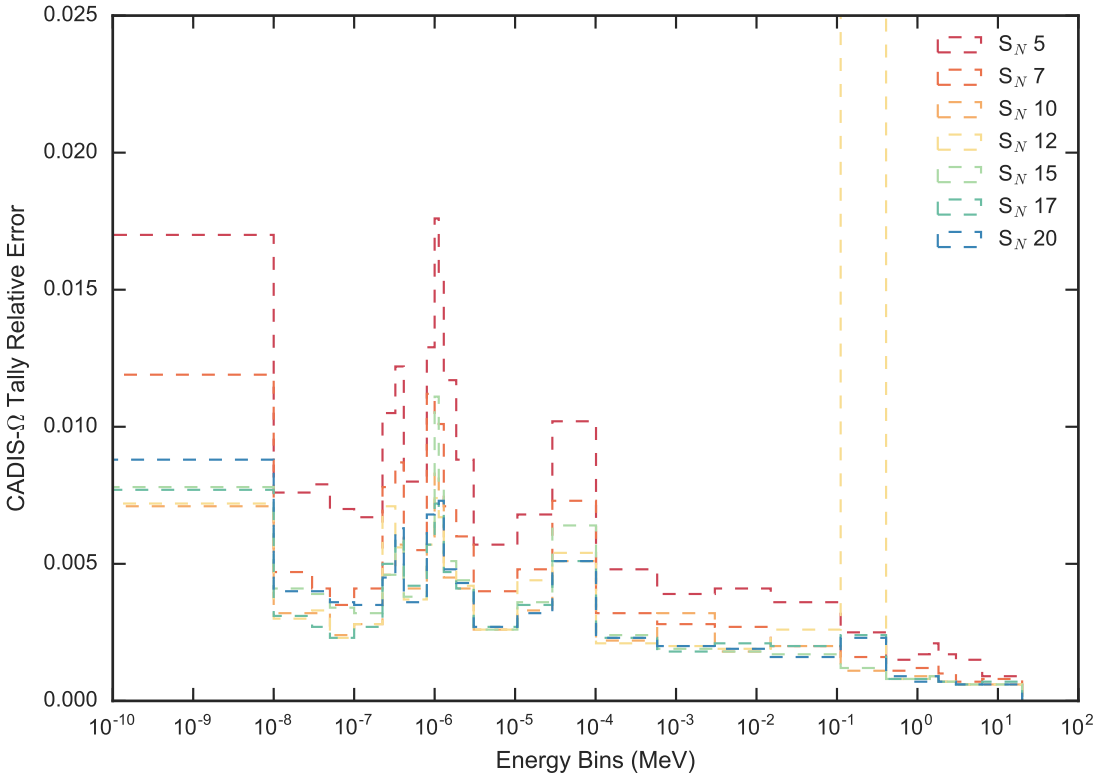

(b) Relative errors of CADIS-Ω results for differing S_N orders.

Figure 4.43: Relative error results for CADIS (Figure 4.43a) and CADIS-Ω (Figure 4.43b) for different quadrature orders for the problem with a steel beam in concrete.

relative errors much closer to quadrature orders 12 and above. Because these relative error spikes span so many bins, they affect the overall tally convergence, and, by extension, the tally average FOM. At very high energies ($> 10^0$ MeV), there is very little improvement in the relative error with increasing quadrature order.

Figure 4.43b shows the relative error results for CADIS-Ω. A number of interesting features exist in this figure that are not reflected in Figure 4.43a. For example, in the lowest energy region a decrease in the relative error is seen up to S_N 10, but then the relative error increases for higher S_N orders. In the wider energy bins between 10^{-6} and 10^{-1} MeV, quadrature orders 10 and above all achieve a similar relative error. This is not true in narrow energy bins, where higher quadrature orders do tend to have a lower relative error. Moving to higher energies, we can observe a significant spike in the relative error between 10^{-1} to 10^0 MeV for S_N order 12. Although this spike does not span several energy bins like those seen in Figure 4.43a, it is very high when compared to the other relative error bins. As a result, this single tally bin throws off the tally average FOM results in addition to the

tally maximum RE FOM, as observed in Table 4.23. In energy bins above this spike, most quadrature orders produce similar FOMs. The lowest valued energy bin is located in this high energy region.

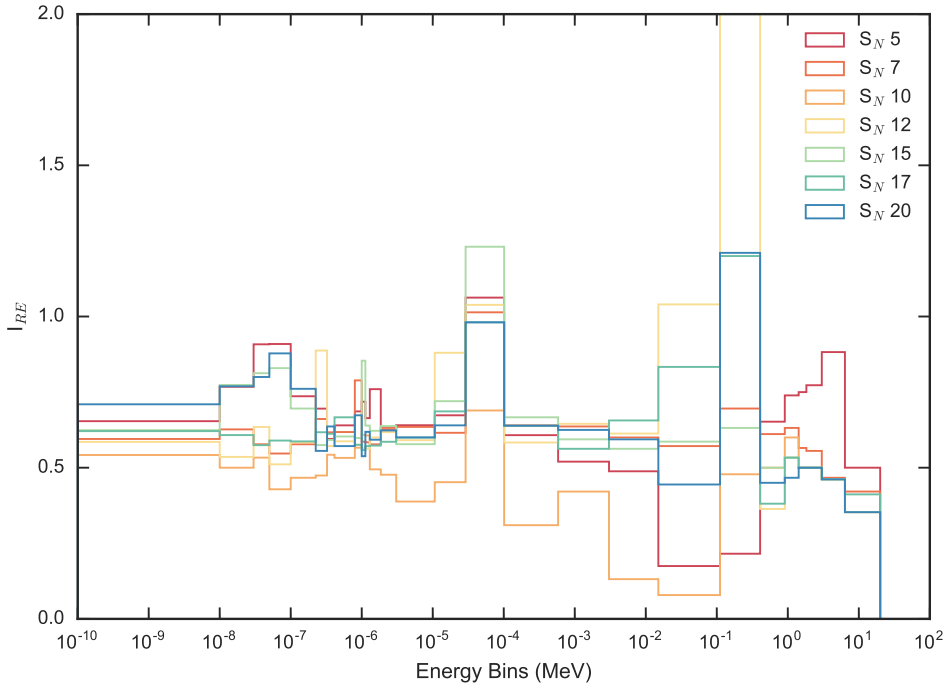

Figure 4.44: Relative error ratio (Eq. (4.1)) between CADIS-Ω and CADIS as a function of quadrature order for the problem with a steel beam embedded in concrete.

While Figure 4.43 shows the how the relative errors of the tally change with different quadrature orders, we have no indication of how CADIS and CADIS-Ω change in comparison to one another. Figure 4.44 shows the relative error improvement factor for each quadrature order. A value below unity indicates that CADIS-Ω achieved a better relative error than CADIS for that bin and quadrature order. In this figure we can clearly see the effect that the problematic energy bins in each method have on the improvement factor. In CADIS we observed that bins in the 10^{-3} to 10^{-1} were problematic for quadrature order 10; this is reflected in the very low value of I_{RE} for that energy range and quadrature order, as shown in by the orange line reaching the lowest values of $I_R E$. Conversely, we observed that CADIS-Ω had a very problematic energy bin between 10^{-1} and 10^{0} at quadrature order 12. The value of this I_{RE} is far above the y-limit of Figure 4.43, illustrated with the yellow line.

Figure 4.43 also shows that quadrature order 10 is generally the order in which CADIS-Ω outperforms CADIS the most. For this quadrature error, CADIS-Ω achieves the lowest error when compared to CADIS. The reasons for this are twofold: first, it is one of the best performing quadrature sets for CADIS-Ω, which achieves its lowest relative errors in almost

every energy bin in this quadrature order; second, it is a very poorly performing quadrature set for CADIS. This synergistic combination results in the best overall quadrature order for CADIS-Ω.

A region where quadrature order 10 is not the best quadrature order is in energy regions above 10^{-1} MeV, whre the higher quadrature orders–like 15, 17 and 20–outperform CADIS more. In the low ($< 10^{-5}$ MeV) and high ($> 10^{0}$ MeV) energy regions, CADIS-Ω obtains lower relative errors than CADIS for all quadrature orders. In intermediate energy regions, some spikes occur in regions that indicate a lower relative error is achieved by CADIS. However, generally CADIS-Ω achieves lower relative errors than CADIS for most energy bin and most quadrature orders. Returning again to the relative error figures of 4.43, the spike in I_{RE} between 10^{-5} and 10^{-4} MeV is explained by a relatively low relative error achieved by CADIS, where in CADIS-Ω a large spike in the relative error occurs. This is reflected in the ratio for $I_R E$.

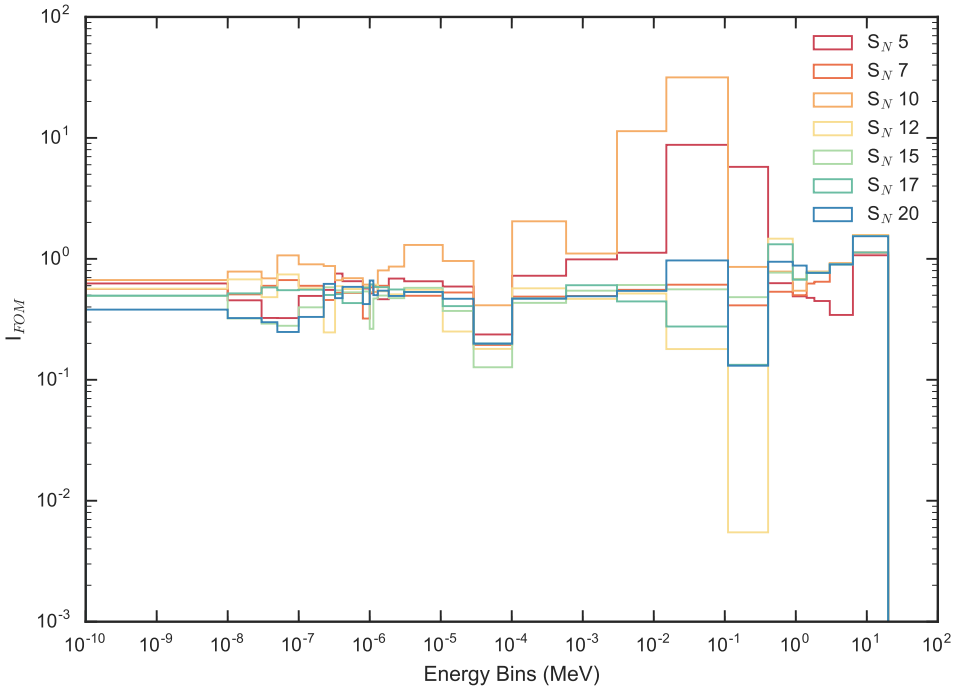

Figure 4.45: Figure of merit improvement factor (Eq. (4.2)) between CADIS-Ω and CADIS with changes in quadrature order for the problem with a steel beam embedded in concrete.

Figure 4.45 complements the results to Figure 4.44. Here the FOM improvement factor is plotted rather than the relative error improvement factor. Because a higher valued FOM is a better result, values above 10^{0} indicate that CADIS-Ω outperformed CADIS. On this plot it is quite clear that for higher energies, CADIS-Ω consistently outperforms CADIS more in higher quadrature orders, as observed with I_{RE}.

Let us return again to the high and low-energy regions of the plot, as explored with Figure 4.44. In this region it can be observed that for low energies, generally I_{FOM} decreases with increasing S_N order. This behavior reverses at high energies, where the ratio increases with increasing quadrature order. This may be an effect of anisotropy in each energy group, as the highest energy has the most anisotropy in the flux. Recall from Section 4.2.4 that the anisotropy metric was much higher at high energies than it was at low energies. It is possible that for this more anisotropic energy group, increasing the quadrature order improves the importance map in the Ω methods more, resulting in a better relative error, and, consequently, a better FOM. This would also explain the complementary behavior at low energies. Low energies generally have more isotropic behavior, and increasing the quadrature order would not help to improve anisotropy information in the importance map. As a result, increasing quadrature order would not help the FOM at low energies.

Despite a higher relative FOM at high energies, in higher quadrature orders CADIS-Ω's performance does not generally exceed CADIS'. For quadrature order 20, CADIS-Ω's FOM is almost always lower than CADIS. On Figure 4.45, the cooler toned lines which correspond to higher quadrature orders have lower values than the warmer toned lines. For quadrature order 5, the relative errors on Figure 4.44 were bookended by higher order quadratures at middle and low energies. This behavior is not the same in Figure 4.45, where the lowest quadrature order has a higher relative FOM than any of the quadrature orders above 10. This means that the time required to solve higher quadrature orders affects the FOM more negatively than the quadrature order decreases the relative error (and positively affects the FOM). It could also mean that the relative error improvement changes more for CADIS than CADIS-Ω with increasing quadrature order. As a result, the improvement factor at lower quadrature orders is better for CADIS-Ω than at higher quadrature orders.

4.3.3 Scattering (P_N) Order

Table 4.24 is much like that of Table 4.23, but with differing P_N orders than quadrature orders. The table is split into four regions, the first three corresponding to FOMs calculated with different relative errors and the last corresponding to Monte Carlo and hybrid runtimes for the problem. Each of the three first subsections of the table have different trends with P_N order, which will be described in the next several paragraphs.

In the tally average relative error subsection of the table one can see that CADIS has a dip in the FOM for P_N order 3; both P_N orders 1 and 5 are higher overall. This effect is not seen in CADIS-Ω, where a decrease in the FOM is observed with increasing P_N order. As a result, for CADIS-Ω, lower P_N orders are sufficient for generating biasing parameters, but for standard CADIS the highest P_N order achieves the best tally average FOM. Further, for every P_N order, the tally average FOM is higher for CADIS-Ω than CADIS.

As with Table 4.23, a dip in CADIS' FOMs is also observable in the maximum relative error subsection of the table. However, the dip observable at P_N order 3 also exists in the CADIS-Ω FOMs. If a user desires to have all tally bins to be below a particular relative

error, P_N order 3 is the worst option for both methods in this problem. For P_N order 1 CADIS-Ω is the better choice, and for P_N order 5, CADIS is the better choice.

		CADIS		CADIS-Ω		analog
	P_N order	MC	MC_{hybrid}	MC	MC_{hybrid}	MC
tally avg	P_N 1	1.76e+03	1.74e+03	2.99e+03	2.96e+03	1.39
	P_N 3	671	661	2.97e+03	2.94e+03	
	P_N 5	2.21e+03	2.16e+03	2.45e+03	2.42e+03	
max RE	P_N 1	7.19	7.09	8.06	7.98	0.0448
	P_N 3	3.75	3.7	6.74	6.66	
	P_N 5	14.8	14.5	8.24	8.12	
min RE	P_N 1	1.5e+03	1.48e+03	1.33e+03	1.31e+03	–
	P_N 3	1.43e+03	1.41e+03	1.32e+03	1.31e+03	–
	P_N 5	1.24e+03	1.22e+03	1.57e+03	1.55e+03	–
time (mins)	P_N 1	394	399	2.09e+03	2.11e+03	22.3
	P_N 3	413	419	2.1e+03	2.13e+03	
	P_N 5	559	571	2.55e+03	2.59e+03	

Table 4.24: Figure of Merit results for steel beam embedded in concrete, with variations in P_N order. Subdivisions of the table indicate calculations of the FOM using different relative errors. The analog case has a single value for each relative error as it is not dependent on changes in deterministic calculation parameters.

Comparing the FOMs for CADIS and CADIS-Ω using the minimum relative errors, some interesting trends are visible. In Table 4.23 we observed that as quadrature order increased, the minimum relative error FOM generally increased or stayed the same for both CADIS and CADIS-Ω. This is not the case in Table 4.24. As P_N order increases, the minimum relative error FOM for CADIS decreases, but for CADIS-Ω it increases. This means that increasing P_N order does not move more particles (and reduce the relative error) in the energy bin with the lowest relative error in CADIS, but it does in CADIS-Ω. Unlike the maximum relative error subsection of the table, at low P_N order CADIS outperforms CADIS-Ω, and at high P_N orders CADIS-Ω outperforms CADIS.

As with Table 4.23, Table 4.24 shows that the behavior of the FOMs do not follow the same trends between different relative error measurements. Depending on the user requirements for the method, one may be a better option than the other. For example, in comparing the FOMs using the maximum relative error, CADIS is better with higher P_N order. With the FOMs using the minimum relative error, CADIS-Ω is better with higher P_N orders.

Looking at the timing results in the last section of the table, we can see that CADIS-Ω takes at least five times longer than CADIS to perform a hybrid run. This is similar to

what was observed for the quadrature order results. However, increasing P_N order increased CADIS Monte Carlo runtimes roughly 40% between P_N orders 1 and 5, and increased CADIS-Ω runtimes about 22% for the same quadrature orders. While the total amount of time added to CADIS-Ω runtimes is longer, it is relatively less than the amount that was added to CADIS.

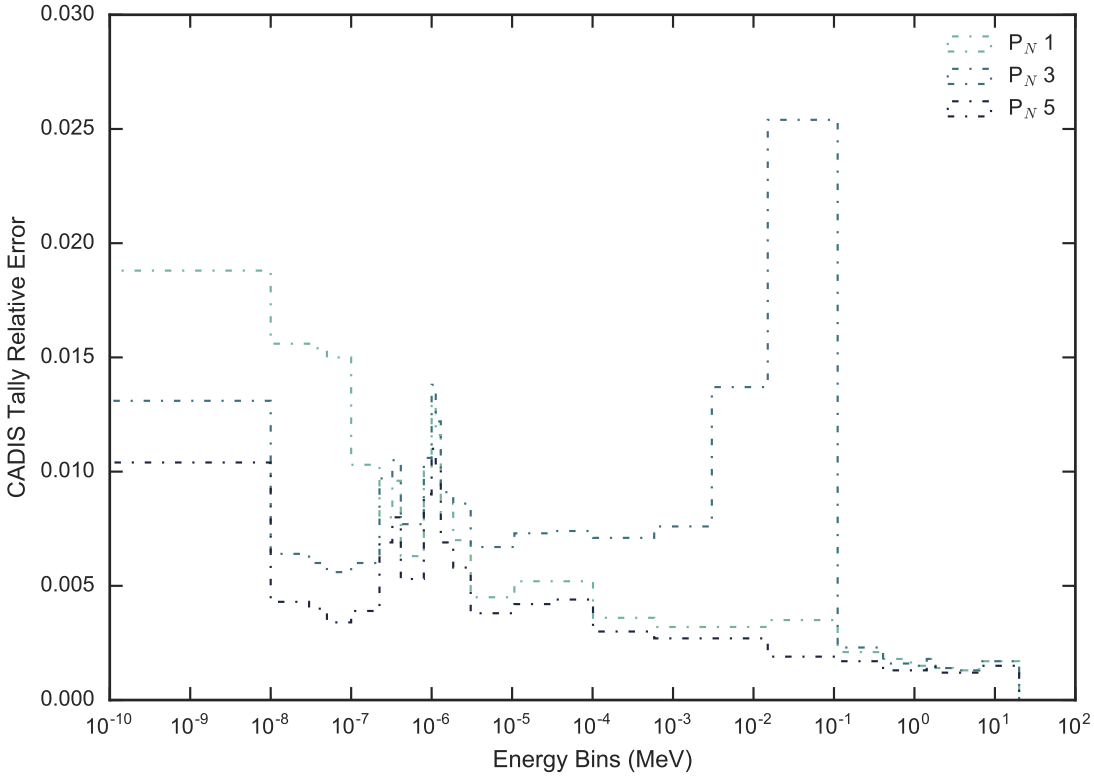

(a) Relative errors of CADIS results for differing P_N orders.

Figures 4.46a and 4.46b provide additional information on interpreting Table 4.24. Figure 4.46a shows the tally relative error results for each of the P_N order CADIS runs, and Figure 4.46b shows the relative error results for CADIS-Ω. In Figure 4.46a the highest relative error for CADIS' P_N order 1 is the most thermal energy bin, for P_N order 3 is the tally bin between 10^{-2}, and for P_N order 5 is the resonance region around 10^{-6}. The lowest relative error bin, however, is the same for all P_N orders. This bin is located just below the highest energy bin. The shifting location of the highest valued relative error energy bin helps to explain the strange trend of the FOMS in the second region of Table 4.24. Because the relative error bins become larger in epithermal energy groups at P_N order 3, and this shift spans several energy bins, it also helps to explain the tally average FOM shift to a lower value at P_N order 3.

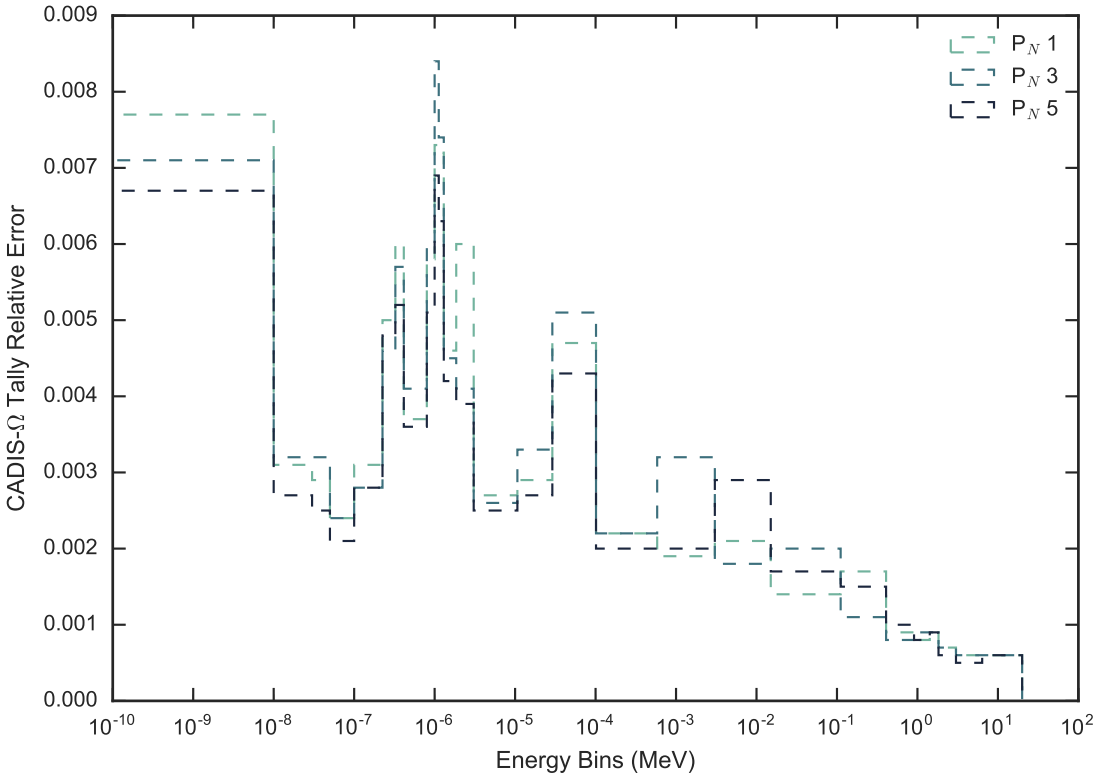

(b) Relative errors of CADIS-Ω results for differing P_N orders.

Figure 4.46: Relative error results for CADIS and CADIS-Ω with changes in P_N order for the problem with a steel beam in concrete.

In Figure 4.46b, no significant shift in the relative error happens at P_N order 3. However, we can observe a shifting location of the highest valued relative error. At P_N order 1 the highest valued relative error for CADIS-Ω is the lowest energy bin. At P_N order 3 the highest relative error bin is the resonance region located near 10^6 MeV, and at P_N order 5 these two bins appear to have a similar relative error. The highest overall observed relative error occurs in P_N order 3, which is why we see the shift to a lower FOM at P_N order 3 for the maximum relative error subsection of Table 4.24. This shift is not as significant as the several-bin spanning shift in CADIS, so it does not affect the tally average FOM in CADIS-Ω.

From Figures 4.46b and 4.46a, we can conclude that shifts in the relative error that dramatically change between P_N orders can affect the overall tally convergence. This shift is not predictable, and may not be observed if combined with a different set of deterministic parameters, such as quadrature order 15, where both CADIS and CADIS-Ω have no spikes in their relative errors.

Figure 4.47 shows the relative error improvement factor by different P_N orders. This plot

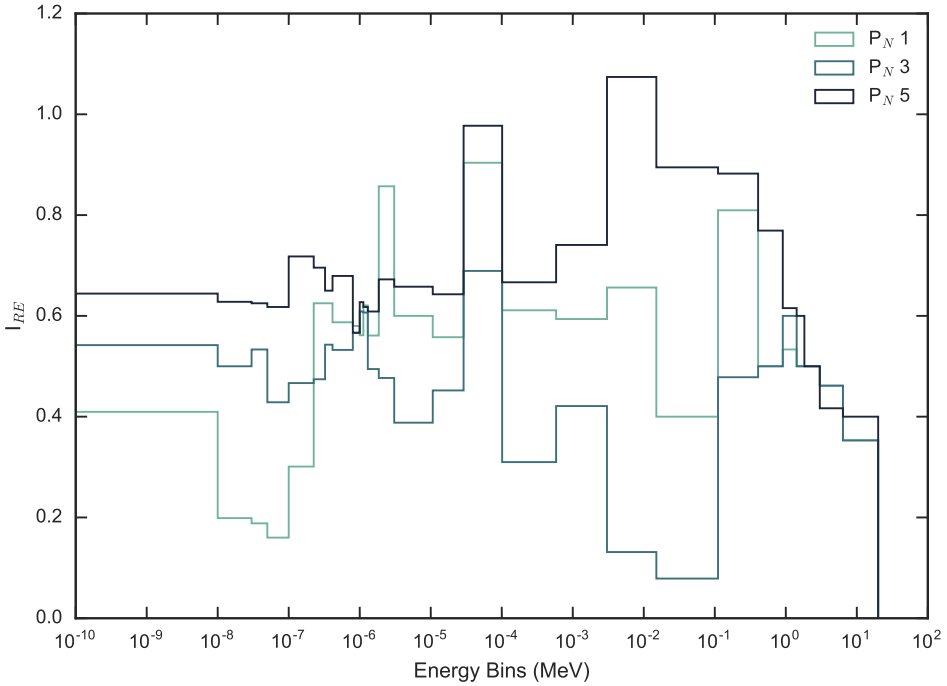

Figure 4.47: Relative error improvement factor (Eq. (4.1)) between CADIS-Ω and CADIS with changes in P_N order for the problem with a steel beam embedded in concrete.

complements what was observed in Figure 4.44. Recall that a value below unity indicates that CADIS-Ω achieved a better relative error than CADIS for a given energy bin and quadrature order. First, with the exception of a few energy bins in P_N order 5, CADIS-Ω has better relative errors than CADIS for the majority of P_N orders and energy bins. In general, P_N order 3 has the most energy bins that obtain low values of $I_R E$, and P_N order 5 has the fewest.

Another interesting feature illustrated in this plot is that different P_N orders perform the best in distinct energy regions. At low energies P_N order 1 achieves the best relative errors, at intermediate energies P_N order 3 achieves the best relative errors, and at high energies all three perform similarly.

For all three P_N orders, the energy bin located near 10^{-4} MeV is problematic. Returning again to the relative error plots of Figures 4.46a and 4.46b, this particular energy bin had a spike for CADIS-Ω, but remained relatively small for CADIS. The consistency in each method's performance across all P_N orders is reflected in this problematic energy bin.

Figure 4.48 shows the FOM improvement factor with increasing P_N order. As with the quadrature orders, the runtimes of CADIS-Ω impact the FOMs that it achieves such that many more energy bins are more in CADIS' favor than in the relative error plot. However, many more energy bins are above 10^0 I_{FOM} in P_N order than for quadrature order. As

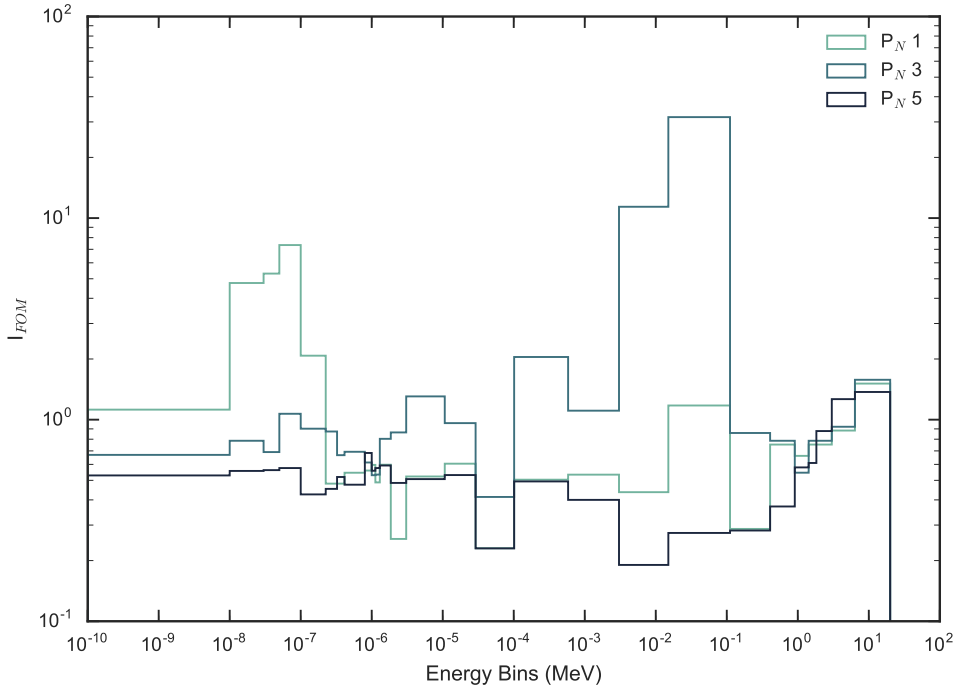

Figure 4.48: Figure of merit improvement factor (Eq. (4.2)) between CADIS-Ω and CADIS as a function of P_N order for the problem with a steel beam embedded in concrete.

with I_{RE}, the shift in performance in different energy groups changes with P_N order. At low energies, P_N order 1 achieves the best FOMs for CADIS-Ω, at intermediate energies P_N order 3, and at high energies all three P_N orders have superior performance with CADIS-Ω.

It should be noted that there is no P_N order for which CADIS-Ω obtains better FOMs than CADIS in all energy bins. Contrast this to the relative error plot, where CADIS-Ω had almost universally better relative errors than CADIS. Again this undescores the negative impact that time has on CADIS-Ω's FOM.

4.3.4 General Observations

At this point we are interested in which deterministic parameter value affects CADIS-Ω and CADIS' performance more significantly. We have looked at how varying each metric changes the relative error, I_{RE}, and I_{FOM}, and from that we have observed trends associated with varying each parameter. However, we have not compared each metric against the other. Figures 4.49 and 4.50 aid in this comparison. As with P_N order and S_N order, these plots show either the relative error or Figure of Merit results for the angle sensitivity study. Unlike the plots with I_{RE} and I_{FOM}, these figures show how the FOM and relative error change for a single method. That is, how much does the relative error or the Figure of Merit

change between the lowest- and highest- valued parameters run for CADIS or CADIS-Ω. These figures are useful to show how sensitive CADIS and CADIS-Ω are to P_N order and quadrature order, respectively.

In Figure 4.49, the ratio of the relative error in each tally bin is taken between the lowest and highest-valued parameter run of the parametric study. For P_N order (the purple lines in the figure) this is calculated with RE_{P_N1}/RE_{P_N5} and for quadrature order (the green lines in the figure) it is calculated with RE_{S_N5}/RE_{S_N20}. A ratio above unity means that the relative error obtained by the higher-valued parameter (P_N order 5 or S_N order 20) is lower than that of the lower-valued parameter.

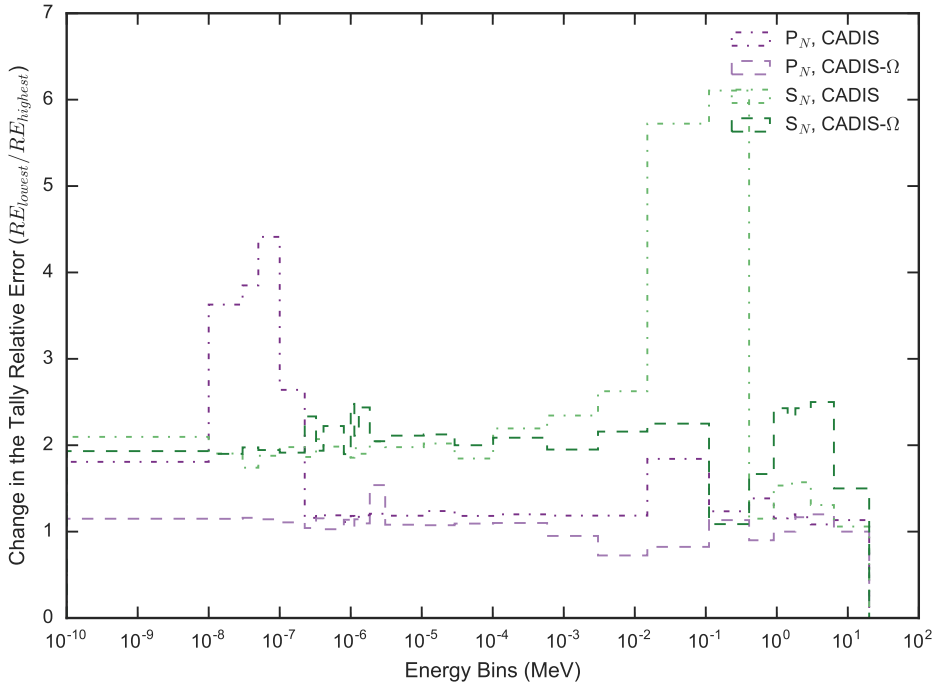

Figure 4.49: Ratio in the relative errors between the lowest and highest variable in the angle sensitivity study for CADIS and CADIS-Ω.

Figure 4.49 shows that a greater change in the relative error occurs for both CADIS and CADIS-Ω from S_N order 5 to 20 than it does for P_N orders. A notable exception to this is for CADIS in the energy range from 10^{-8} to 10^{-7} MeV, where the relative error improvement for P_N order exceeds any quadrature order line. Returning to the relative error results for just CADIS, as shown in Figure 4.46a, this energy range has a very high relative error for P_N order 1, especially when compared to the other energy regions nearby. In this energy range, the relative error drops from 0.015 to .005 from P_N order 1 to 3, but the energy bin immediately adjacent only drops about .005 total. The greater change in the relative error for this region accounts for the spike we see in Figure 4.49.

The data in this figure also shows us that increasing P_N order for CADIS-Ω does not reduce the relative error in the energy range from 10^{-3} to 10^{0} MeV. CADIS-Ω's purple line on this figure is located below unity in that energy region. Generally this line for CADIS-Ω does not see a huge improvement with increasing P_N order. For a problem like this, a low P_N order may be a good enough choice.

CADIS' results in the same energy region show improvement in the relative error. However, in many centrally-located energy bins, this improvement is very small. If a tally existed for a similar problem in these energy ranges, it may be sufficient to use CADIS with a low P_N order as well.

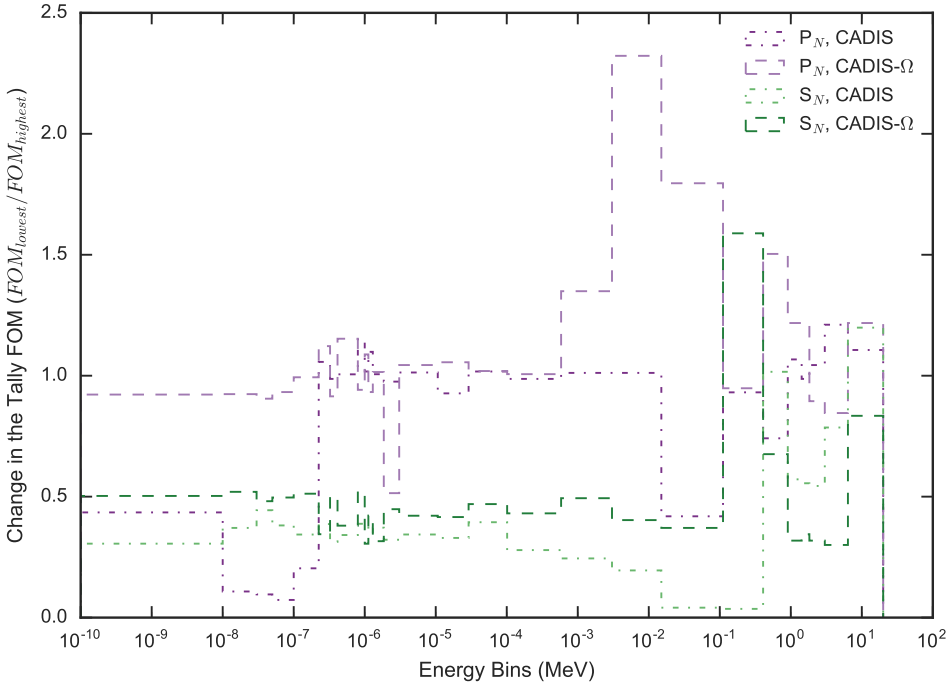

Figure 4.50: Ratio in the figure of merits between the lowest and highest variable in the angle sensitivity study for CADIS and CADIS-Ω.

In Figure 4.50, the linestyles and colors match those in Figure 4.49. The y-axis of this figure shows the ratio of the FOMs for the lowest- and highest-valued parameters. The purple lines are calculated by the ratio of FOM_{P_N1}/FOM_{P_N5}; the green lines show the ratio of FOM_{S_N5}/FOM_{S_N20}; the linestyles indicate the method type. In this plot, a low-valued ratio reflects a higher valued FOM obtained by the finer P_N or S_N order.

Some features from 4.49 are continued in Figure 4.50. For example, the energy bins between 10^{-8} and 10^{-7} MeV still show a large change for P_N order in CADIS. However, the addition of time to calculate the FOMs affects both methods. In Figure 4.49, we observed that for both methods, increasing P_N order or quadrature order generally decreased the

relative error. In Figure 4.50, this is not the case. At low energies, all methods have higher FOMs with increasing parameter resolution. At intermediate energies, only S_N order strongly changes the FOM. At high energies, energy bins for both S_N and P_N order wildly oscillate between improved and not improved.

The CADIS lines in Figure 4.50 generally lie at lower values than CADIS-Ω. Consequently, larger changes in the FOM are observable with increasing either P_N or S_N order. This is the case for most energy bins, but not above 10^0 MeV. In this region, CADIS-Ω and CADIS shift between energy bins in which method sees a larger change with parameter value selection.

By inspecting both Figure 4.49 and 4.50, a few common themes appear. First, CADIS has a larger change in the tally relative error and FOM than CADIS-Ω for most energy bins. Second, this general observation does not hold for energy bins greater than 10^{-1}. At these energy regions, CADIS-Ω achieves a better relative error with increasing S_N order, but not P_N order. Neither CADIS-Ω or CADIS have a dominant trend in FOM values in this region. Another observation is that generally S_N order has a greater effect on the relative errors and FOMS for both methods. This is not the case in the high energy region for FOM values, where both methods are comparable.

4.4 Method Recommendations

The performance of CADIS-Ω has been characterized and compared against CADIS and a standard, nonbiased analog Monte Carlo run for a series of problems. Section 4.2 showed how varying geometric configuration and material composition of various problems with anisotropy affected the performance of the Ω methods. Subsections 4.3.3 and 4.3.2 showed how varying P_N order and quadrature order changed the tally results and tally convergences for the steel beam problem embedded in concrete. In doing this characterization, we sought to determine in which problems and with which solver options the Ω methods were best suited. A secondary objective was to determine the sensitivity of the Ω-methods to changes in the solver options. With these objectives in mind, we can evaluate the Ω methods' performance based on the study performed in the preceding subsections.

4.4.1 Problem Selection

Section 4.2 revealed that CADIS-Ω does not outperform CADIS for all problems containing anisotropy in the flux. Depending on how and where the flux anisotropy was induced in the problem, CADIS-Ω had the potential to significantly increase the FOM in Monte Carlo. These results were not consistent, and are not entirely predictable.

In comparing the single turn and multiple turn labyrinths, it was observed that more scattering effects decrease the effectiveness of CADIS-Ω. Because more scattering is required to penetrate the multiple turn labyrinth, the performance of CADIS-Ω was poorer. In the

single turn labyrinth energy bins that had more isotropy in the flux induced by scattering also were poorer performing for CADIS-Ω.

To add to this complexity, problems with little- to no- scattering were also difficult for CADIS-Ω to handle. These problems were also problematic for CADIS, as they were generally comprised of "thin" materials to induce streaming effects. As a result, sampling events occurred over several centimeters, which also was over several orders of magnitude in flux change. This resulted in very high relative errors, as observed in the beam facility problem. This was not as problematic in the therapy room example because the problem was bounded by 10cm of concrete, which allowed for particle scattering rather than leakage.

Several material variants of the steel beam in concrete problem were run. The results of this small study confirmed that both CADIS and CADIS-Ω obtain poorer FOMs with air than with steel or concrete. In the case of the air variant, the FOMs obtained by CADIS-Ω were generally lower than CADIS, but the relative errors were also better. For all material variants of the steel beam problem, CADIS and CADIS-Ω achieved superior FOMs to the nonbiased analog, but these were an order of magnitude lower for the air variant.

The rebar-embedded concrete problem showed that for problems with geometric complexity, CADIS-Ω can also struggle. Because the rebar in this problem was not always directed in line with the detector tally, particles could more freely move perpendicular to the tally path, crossing out of importance with a preferential flowpath. As a result, in high energy bins the tally relative error was very high for both CADIS and CADIS-Ω. However, CADIS-Ω's performance was poorer. The FOMs obtained by CADIS-Ω in this problem were one to two orders of magnitude smaller than CADIS or the nonbiased analog.

CADIS-Ω achieved lower relative errors than CADIS for many problems, but often this was offset by a very long runtime. The long runtime impacted the FOM. As a result, even though CADIS-Ω achieves a lower relative error for the same particle count, it may be more advantageous to simply run standard CADIS for longer. In a few instances, the runtime for CADIS-Ω is comparable to CADIS. This occurs in the beam and therapy room problems, for example. Although these problems are not the best for either CADIS or CADIS-Ω, there is no caveat to using CADIS-Ω if choosing a hybrid method.

The characterization problems' variations in material and geometric configuration showed that there is no distinct behavior for which CADIS-Ω is universally better. However, in problem geometries where preferential flowpaths are directed towards the tally detector, and where materials provide short mean free paths to interaction or resampling sites, CADIS-Ω is a well-suited method.

4.4.2 Deterministic Solver Choice

The angle-based parametric study provided a number of interesting obervations on the performance of the Ω methods. First, the effect of T_{det} does not change the FOM with CADIS-Ω more than CADIS. In Section 4.3.2 the hypothesis that I/O requirements would severely impact the FOM for CADIS-Ω was shown to not be as impactful as hypothesized. The FOM

change between FOM_{MC} and FOM_{hybrid} was roughly the same for CADIS as CADIS-Ω because the CADIS-Ω runtimes are so much longer than CADIS.

Next, the only consistent region in which CADIS-Ω outperforms CADIS is in high energies. For almost all P_N orders and all quadrature orders, CADIS-Ω achieved lower relative errors and higher FOMs than CADIS. In high energy bins, increasing quadrature order showed a decrease in $I_R E$, increasing P_N order did not show a large change in $I_R E$. In the same bins, I_{FOM} values above unity were observed for both P_N and S_N order, but no trends with changing parameter value were observed.

By including the runtime to calculate the FOM, the comparative performance of CADIS-Ω dropped when compared to using the relative error. Several energy bins in CADIS-Ω–for quadrature orders and P_N orders–achieved better FOMs than CADIS. However no P_N order consistently outperformed the other, while low S_N orders generally achieved better FOMS for CADIS-Ω than CADIS. However, despite the lack of consistent performance for a single P_N order, the raw values obtained with P_N order are promising. With P_N order there were more energy bins that had high I_{FOM} values than with quadrature order.

Another observation that can be extended from Section 4.2 is that CADIS-Ω consistently biases particles better than CADIS. For the same number of source particles, CADIS-Ω achieves lower relative error than CADIS for most energy bins with both P_N order and quadrature order. This means that while sampling may be slow, the importance map generated with the Ω flux is generally better at moving particles to the tally region than CADIS.

Based on the results in Section 4.3, a number of recommendations can be made based on deterministic solver choice. First, the best P_N order choice is dependent on the energy range in which one is tallying. For low energy regions, P_N order 1 will give the best FOMs relative to CADIS, for intermediate energies P_N 3 is a better choice, and for high energies any P_N order is satisfactory. In general, because lower P_N orders have lower runtimes, these will get the best results for CADIS-Ω the fastest, and have comparatively the best relative errors and FOMs against CADIS. Next, the best S_N order choice is

If one has to choose between varying P_N order and S_N order to improve the importance map for their method, varying S_N order will have a greater impact. This is the case for using either CADIS or CADIS-Ω. However, both methods have a turnarount point at which increasing S_N order does not improve the relative error enough to offset the time increase of the method. For CADIS-Ω, this occurs in bins above S_N 15, and for CADIS it occurs in bins aboe S_N 12. For this type of problem, and using all energy bins in the tally, CADIS-Ω will obtain the best results with a lower P_N order and intermediate S_N orders.

4.4.3 Lessons Learned

The characterization problems that were run were heavily biased towards low-density streaming to induce anisotropy in the flux. This subset of problems, though highly anisotropic, are not the best for a method so dependent on weight-window type biasing, because particle streaming allowed for particles to cross several orders of magnitude in the flux before resampling. This meant that in a high-importance region a particle may split many thousands

of times in a new splitting event. Unfortunately, the Ω-methods are not immune to this issue and so suffered the same effects as CADIS, even with positive effects like the reduction of ray effects. Further, with the strong dependence on angle, the Ω-fluxes may have exacerbated this streaming-sampling effect in regions with strong angular dependence around the detector. In a problem like the single turn labyrinth, where the Ω-flux generated a strong line of importance between the exit of the labyrinth and the detector and drastically dropped the importance behind the detector, a particle has much more opportunity to cross several orders of magnitude of importance than it does in CADIS. This is likely what caused CADIS-Ω to take longer in Monte Carlo transport than CADIS in many of the characterization problems.

It should also be noted that while the angle-dependent parametric study revealed how P_N order and quadrature order may affect a problem's results, the best parameter choices for this problem are by no means a prescriptive solution for other problems. Section 4.2 showed how different the characterization problems' results were, depending on the source definition, the material composition of the problem, and the geometric configuration of the problem. Using the deterministic parameter choices that appear the best for the steel beam in concrete may not be the best for, say, a multi-turn labyrinth. From this study we have a good starting point from which to further characterize the method for other application problems.

Chapter 5

Conclusions

Hybrid methods are and will be a realm of continued importance in radiation transport methods development. The application space and demand for hybrid methods continues to grow. With this growth, accurately and efficiently modeling the physics of increasingly complex problems is paramount for safety and security. In this dissertation, a new set of hybrid methods were proposed, implemented, and characterized. From this work, several pathways have revealed themselves for future hybrid methods work.

5.1 Assessment of the Ω-methods

The results in Chapter 4 showed that CADIS-Ω has varied performance when compared to CADIS over the problem space investigated. Depending on the geometric configuration, the material composition, and the solver options used, the method can outperform or underperform CADIS by an order of magnitude. This underscores the difficulty of developing a method that is broadly applicable to a large subset of application space. Further, it illustrates the necessity for further methods development.

Several characterization problems were formulated that contained anisotropy in the flux. The mechanisms for inducing anisotropy in the flux anisotropy were either from the source, or from physical interactions with the problem materials and geometry. The success of the Ω-methods was not directly correlated with any single physical mechanism, but both CADIS and CADIS-Ω struggled in problems primarily comprised of air.

In the single turn labyrinth, CADIS-Ω achieved lower relative errors in epithermal and fast energy groups. These groups were shown to have flux anisotropies with anisotropy distributions that were clumped around a particular anisotropy value. For the multiple turn labyrinth, CADIS achieved uniformly lower relative errors than CADIS-Ω. For both the steel beam in concrete and the u-shaped bend, CADIS-Ω achieved lower relative errors than CADIS but had runtimes 3-7x longer than those of CADIS. For the geometrically complex rebar-embedded concrete, CADIS-Ω had higher relative errors than CADIS. In high energy regions, the convergence for energy bins would take days of computational runtime to get

to a relative error of less than 10%. For two heavily air-centered problems, CADIS-Ω and CADIS both had comparable relative error achievements.

In addition to checking the limitations of the Ω-methods with respect to geometry and material composition, the sensitivity of the methods to deterministic parameter selection was also studied. In particular, the effect of quadrature order and P_N order on method performance were studied. For both CADIS and CADIS-Ω, the change in quadrature order had a stronger effect on the change in the relative error and the FOM. CADIS showed stronger sensitivity to changes in both P_N order and quadrature order over CADIS-Ω. CADIS also proved to have more and higher magnitude oscillations in the relative error between different P_N and quadrature orders. Spikes in the relative error occurred in both methods, but more frequently in CADIS. Both methods showed improvement in the FOM and relative error with increasing quadrature order and P_N order. In high energies, CADIS-Ω achieved superior FOMS to CADIS for all P_N orders and quadrature orders.

Chapter 4 showed a few examples of the anisotropy metrics when they showed promising trends with I_{RE} or I_{FOM}. These metrics did provide information on the relative distribution of anisotropy in the problem, and they also showed some trends with the improvement factors. However, most problems did not have significant trends, so more work must be done to fully characterize hybrid methods using this novel analysis technique.

The Ω-methods have been characterized with their sensitivity to geometric and material configuration, as well as their sensitivity to deterministic calculation parameter choice. It is clear from the results in Sections 4.2 and 4.3 that the Ω-methods are not always the best choice for reducing the variance in problems with anisotropy. This is from a combination of many effects, but primarily the varied range of runtimes when compared to CADIS. In many problems, CADIS-Ω was able to obtain lower relative errors for tally bins than CADIS, but the runtimes were significantly longer. The generally longer runtime for CADIS-Ω negatively impacts the FOMs that it is able to achieve, thus negating its more effective transport of particles.

5.2 Suggested Future Work

While this dissertation covered the characterization of CADIS-Ω over a fairly broad spectrum of anisotropy-containing problems, there are a number of fruitful pathways by which the method could be improved or characterization expanded. Broadly, these fall into three categories: improvements to the software implementation and algorithmic design, expansion of the characterization space, and application to larger, real-life problems. The next few subsections addresses each one of these categories individually.

5.2.1 Software Improvement

This subsection addresses the improvements that could be made to the software and analysis methods to enhance understanding of the omega methods. A discussion on how improving

software performance aids in future work will start this section. An explanation of how extending the breadth of analysis helps to understand the Ω-methods further will finish the section.

To calculate the Ω flux, a rotation of either the adjoint or forward flux matrix is required to ensure that the directional variable Ω is consistent between the forward and adjoint, or that $\Omega_{adjoint} = \Omega_{forward}$. Because quadrature sets are not always straightforward to interpolate, a rotationally symmetric quadrature set is currently required for computing the Ω-fluxes in order to perform this rotation. Should a method be developed that does have interpolatable quadrature points, it would be a good candidate to calculate Ω-fluxes for solutions that are not rotationally symmetric.

The anisotropy metrics described in Section 3.2.1 at this point have not shown significant trends with either the relative error or figure of merit improvement metrics (I_{RE} and I_{FOM}). To filter out values of each metric to regions more important to the problem solution, two filtering algorithms were proposed: one that only uses values of metrics from cells with contributon fluxes above the mean contributon flux, and the other that uses values from cells that have a flux above the median contributon flux. Using these filtering algorithms did show interesting features in the anisotropy metric distributions as well as shifts in I_{RE} and I_{FOM}. However, trends were not apparent for the majority of the metrics. A useful modification to the filtering algorithm would be to select certain percentages of high-valued contributon flux locations. For example, perhaps selecting out the cell locations containing the top 10% of contributon fluxes would reveal a trend in the improvement metrics. It is possible that too many values are being selected from the entire problem even with the existing filters, so an even stricter filtering algorithm may help.

To filter the anisotropy metrics, the contributon flux distribution was chosen as the filter base. This is an intuitively good choice because it will use values near both the forward- and adjoint- sources, and also the values between them where particles are most likely to flow. Further, the contributon flux is something that is method agnostic. That is, it can be used as a filtering algorithm for non-Ω methods and it will still reveal problem information. However, an argument could also be made to use the omega flux distribution as a filtering base, as that is the method in which we are interested. Modifying the filtering algorithms to use the Ω-flux distribution may provide trends in the method improvement metrics that are not apparent using the contributon flux.

The Ω-methods, as currently implemented in both Exnihilo and ADVANTG, are entirely serial. That is, there is no parallelization in any part of the Ω-flux calculation, or supporting code to that effect. In the results presented in Chapter 4, T_{hybrid} was calculated to remove parallelization effects so that CADIS and CADIS-Ω were comparable. While the results were adjusted accordingly, this is not the best implementation for production software or more difficult use cases. As mentioned previously, the ADVANTG software is entirely serial, so parallelization is not required for VR parameter generation. However, Exnihilo/Denovo is parallelized. The parallelization of the Ω-flux calculation in this code would significantly improve its usability. Parallelization would reduce the actual time to calculate the Ω-fluxes and anisotropy metrics.

Another algorithmic improvement to the Ω-methods is to reduce the memory requirements for both the computation of the Ω-fluxes and the anisotropy metrics. Much of this could be accomplished with parallelization. However, even the serial version of the Ω-methods could be adjusted to read in the angular flux data in "chunks" so as to not read in datasets larger than the memory available on the system. As a first order approach, the angular fluxes could be read in serially by energy group. Depending on the energy group structure, this has the potential to reduce the memory load at a particular time by 20x or 200x. At present, the Ω-methods are limited by memory requirements. Without a large computing cluster, there is no feasible way to calculate the Ω-fluxes for a problem of reasonable complexity.

Another alternative modification to the Ω-methods is to bypass writing the angular flux matrices entirely. This would reduce the I/O requirements for the method, and also not demand as much disk space. However, this is a non-trivial task, as the forward and angular fluxes for a cell must both be in memory to compute the Ω-method for that cell. To store the complete angular flux matrices in memory will present the same memory limitations that the Ω-methods currently face, so some algorithmic challenges exist should this be a path of future work.

The Ω-methods are currently implemented on a localized development version of both Exnihilo and ADVANTG. If a larger audience wishes to use or access them, they would require support beyond that of a standard software release. Depending on the continued characterization of the Ω-methods, integrating this software into future releases of Exnihilo and ADVANTG may be useful.

Each of the areas proposed in the previous paragraphs are areas in which the Ω-methods can be improved upon or areas that may improve our understanding of the Ω-methods' behavior. Expanding the filtering algorithm for the anisotropy metrics may also help us to understand more broadly how anisotropy is distributed in different problems. Expanding our understanding of the Ω-methods' strengths and deficiencies can also improve future hybrid methods.

5.2.2 Characterization Problem Extension

Broadening the scope of the characterization problem study is another fruitful avenue for exploration. In this vein, there exits a two-pronged approach: first extending the types of problems (more diverse materials, less air in problems, more diverse geometries) will enhance knowledge of the methods. Next, extending the scope of the parametric studies will help to inform how resilient the Ω-methods might be to changes in the solutions space that indirectly impacts angle. In this realm, the deterministic calculation specifics, like quadrature type will be addressed.

The characterization problems studied covered a broad range of anisotropy-inducing physics. The geometries chosen were fairly simple, with very few materials. The majority of the problems used air in some portion of their geometry to have streaming-induced anisotropy of the flux. Depending on their geometries, this caused sampling issues and

slowdown of the CADIS-Ω method. For example, the problem variants of the steel beam embedded in concrete geometry illustrated the CADIS-Ω method's susceptibility to air. In the air-filled beam variant of the problem, the Ω-method had the lowest improvement margin when compared to CADIS of the three matierial variants. A beneficial extension of the characterization problem study would be to replace the air in this geometry with a high atomic mass material that maintains scattering anisotropy but includes more sampling interaction points. Using problems with greater material diversity and more problems with preferential flowpaths (that are not air), would be an interesting extension to the characterization problem materials.

While the characterization problems are fairly simple geometrically, it may be advantageous to investigate simpler problem geometries with even less geometric complexity. In comparing the single- and multiple-turn labyrinths, we observed that with too little anisotropy in the problem, the Ω method's performance suffers. However, a simpler geometry of the labyrinth (perhaps an elbow bend), or a hallway in concrete with no air rooms, can show if there is a turnover in labyrinth anisotropy in which the Ω methods perform the best.

The results presented in Section 4.3 showed that CADIS-Ω is generally more resilient than CADIS to changes in quadrature and P_N discretization. As a result, CADIS-Ω can use a coarser problem discretization to obtain variance reduction parameters, saving computational cost in terms of both runtime and memory. The results in Section 4.3 also showed that CADIS-Ω was less susceptible to large fluctuations in the relative errors in intermediate energy energy bins.

Beyond sensitivity to quadrature order and P_N order, it may be worth investigating the sensitivity of each method to other deterministic calculation parameters. If, like quadrature order and P_N order, CADIS-Ω generates better importance maps with lower-fidelity solutions in other deterministic parameters, then even more computational time could be saved. For something like mesh refinement, the number of mesh cells can significantly alter the speed at which the deterministic solution converges.

Investigating the impact of quadrature type may also be an area of future work. In Section 4.3, it was observed that both CADIS and CADIS-Ω showed greater sensitivity to changes in quadrature order than P_N order. CADIS showed a greater sensitivity to changes in quadrature order than CADIS-Ω. We expect that the behavior of other quadrature sets will be similar, but this may be worth verifying in future use cases. It is possible that the different properties of different quadrature sets may more strongly affect the Ω-methods' performance.

In addition to characterizing the performance of CADIS-Ω, it will be important to characterize FW-CADIS-Ω. In Chapter 3, the Ω-method theory for both CADIS and FW-CADIS were presented. Indeed, FW-CADIS-Ω has also been implemented in Exnihilo and ADVANTG. The scope of this project did not extend to the characterization of FW-CADIS-Ω, though it could prove useful to characterize for large, global calculations. A similar set of characterization problems can be designed for FW-CADIS-Ω, but with global mesh tallies rather than small detectors.

It would also be beneficial to perform a thorough investigation into the Ω-methods'

mitigation or multiplication of ray effects. Both the forward and the adjoint angular fluxes will have ray effects in problems with long mean free paths. As discussed in Section 4.2, the ray effects may also be multiplied depending on the geometric configuration of the problem. The degree to which the Ω-flux exacerbates or minimizes ray effects as a function of these locations would be an interesting study and may help in further specifying to which problems the Ω-methods is suited. Further, the difference in the construction of the adjoint between CADIS and FW-CADIS means that CADIS-Ω and FW-CADIS-Ω will have different sensitivities to ray effects.

Further characterization of the Ω methods' performance with different problem geometry and material configurations will deepen our understanding for which applications the methods may be best suited. For large scale, high-impact, high-complexity problems, issues observed in the characterization problem studies may be exacerbated. Before applying this method to application problems, it will be important to have confidence that the methods will achieve better results than other methods.

5.2.3 Application Problems

Based on the data presented in Sections 4.2 and 4.3 we believe that the CADIS-Ω-method has the potential to be applied to a number of application problems. These problems include, but are not limited to: detectors near dry cask nuclear waste storage, dry cask storage beds, nuclear containment buildings, and nuclear spent fuel cooling pools.

The dry casks are a promising use case for the CADIS-Ω-method because they have small air channels for ventilation, but their body is primarily metal tubes containing nuclear fuel surrounded by concrete. These rods are pointed towards the ventilation ducts, and so the results from the steel bar embedded in concrete suggest that this may be a more complex application of the physics it represents.

Further, a bed of dry cask storage containers will have several spaces through which particles may travel. A use case of this may be to calculate the dose rate standing at the boundary of such a facility, or to consider if the cask loading matches the owner-provided loading list. Because this problem has so much air, it may be more difficult for the Ω-methods. However, with the thick soil boundary in the $z-$plane the Ω-methods may still perform well.

Nuclear spent cooling pools have used fuel rods clustered in assemblies arranged in rows submerged in water. These rods emit a range of highly energetic particles. Spent fuel cooling pools will be an interesting extension of the steel beam in concrete, as water is a highly moderating material not dissimilar to the concrete from the characterization problem. The fuel rods act as both a source and a preferential flowpath, so the differing source distribution in this problem may yield interesting results.

Each of these application problems uses the physics modeled in the characterization problems but applies them to a more geometrically and materially complex problem. In extending the Ω-methods to these problems and comparing them to CADIS and FW-CADIS, we can also understand how sensitive the Ω-methods are to more difficult problems. If, as noted in

the characterization problems subsection, the Ω-methods are more resilient to deterministic problem solution fidelity in larger more complex problems, these problems will benefit significantly from the decreased deterministic solution time and the lower computational burden demanded by the Ω-methods.

5.3 Concluding Remarks

In this dissertation, a new group of hybrid methods called the Ω-methods were proposed. The Ω-methods are built on the foundational work of CADIS and FW-CADIS to generate angle-informed variance reduction parameters. The two new methods proposed were CADIS-Ω and FW-CADIS-Ω. Both methods use the Ω-flux, a form of the adjoint scalar flux calculated by weighting the adjoint angular flux with the forward angular flux, to generate source biasing and weight window values. By using the forward angular flux normalization, the importance map generated for the Ω-methods is adjusted to include the directionality of the forward and the adjoint particles without explicitly including angle in the source biasing or weight window values.

The Ω-methods were implemented in two software packages developed at Oak Ridge National Laboratory: Exnihilo and ADVANTG. The functionality to generate the Ω-fluxes were implemented in Exnihilo, which contains the deterministic transport solver Denovo. The infrastructure to generate variance reduction parameters consistent with CADIS and FW-CADIS was implemented in ADVANTG. The development of these methods now allows for any user to use the Ω-methods, should they have access to the software.

In addition to the Ω-methods method proposal and implementation, CADIS-Ω has been characterized on a wide variety of problems with flux anisotropies. The problems were designed to understand the method's limitations and in what parameter space the method can and should be used. To more fully understand the method's' behavior and how flux anisotropy affected its ability to perform, a number of anisotropy metrics were proposed. These metrics were then used to investigate if performance improvement could be correlated with anisotropy in any way.

The anisotropy metrics did not show significant trends with the FOM or the solution relative error, but their distributions did help reveal more about the distribution of anisotropy in the problems. In particular, it was easily observable how the distribution of anisotropy changed between energy groups for a particular problem. Future use of these metrics may also aid us in more fully understanding other hybrid methods' performance.

CADIS-Ω is a promising hybrid method. If used with a well-suited problem, it has the potential to improve the FOM over traditional methods by an order of magnitude. This offers significant time and energy savings. However, the Ω-methods are not without their drawbacks. If used in a poorly-suited problem they can take substantially more time to transport particles in Monte Carlo. The Ω-methods' characterization and performance study presented in this dissertation have contributed a broader understanding of these types

of hybrid methods, and have created ample pathways forward for future hybrid methods analysis.

Bibliography

[1] John C. Wagner and Alireza Haghighat. "Automatic Variance Reduction for Monte Carlo Shielding Calculations with the Discrete Ordinates Adjoint Function". In: *Proceedings of the Joint International Conference Mathematical Methods and Supercomputing in Nuclear Applications* 1 (1997), p. 67. URL: http://www.ornl.gov/sci/nsed/rnsd/staff/Publications/WagnerPubs/wagner_ssprings97_auto.pdf (visited on 08/28/2015).

[2] Alireza Haghighat and John C. Wagner. "Monte Carlo variance reduction with deterministic importance functions". In: *Progress in Nuclear Energy* 42.1 (2003), pp. 25–53. URL: http://www.sciencedirect.com/science/article/pii/S0149197002000021 (visited on 08/28/2015).

[3] John C. Wagner and Alireza Haghighat. "Automated variance reduction of Monte Carlo shielding calculations using the discrete ordinates adjoint function". In: *Nuclear Science and Engineering* 128.2 (1998), pp. 186–208. URL: http://www.ans.org/pubs/journals/nse/a_1951 (visited on 08/28/2015).

[4] John C. Wagner. "An automated deterministic variance reduction generator for Monte Carlo shielding applications". In: *Proceedings of the American Nuclear Society 12th Biennial RPSD Topical Meeting*. 2002, pp. 14–18. URL: http://wp.ornl.gov/sci/nsed/rnsd/staff/Publications/WagnerPubs/wagner_rpsd_apr2002_advantg.pdf (visited on 09/07/2015).

[5] John C. Wagner, Edward D. Blakeman, and Douglas E. Peplow. "Forward-Weighted CADIS method for global variance reduction". In: *Transactions of the American Nuclear Society* 97 (2007), p. 630. URL: http://wp.ornl.gov/sci/nsed/rnsd/staff/Publications/WagnerPubs/Wagner_FW-CADIS_Nov2007_ANS-Trans.pdf (visited on 08/28/2015).

[6] John C. Wagner, Edward D. Blakeman, and Douglas E. Peplow. "Forward-weighted CADIS method for variance reduction of Monte Carlo calculations of distributions and multiple localized quantities". In: *Proceedings of the 2009 Int. Conference on Advances in Mathematics, Computational Methods, and Reactor Physics, Saratoga Springs, NY*. 2009. URL: http://www.ornl.gov/~5pe/p038.pdf (visited on 08/28/2015).

[7] Elmer Eugene Lewis and Warren F. Miller. *Computational methods of neutron transport*. United States: John Wiley and Sons, Inc.,New York, NY, 1984.

[8] X-5 Monte Carlo Team. *MCNP - A General N-Particle Transport Code, Version 5, Volume I: Overview and Theory*. User Manual LA-UR-03-1987. Los Alamos National Laboratory, Apr. 2003.

[9] Forrest B. Brown et al. "MCNP version 5". In: *Transactions of the American Nuclear Society* 87.273 (2002), pp. 02–3935.

[10] J. S. Hendricks and T. E. Booth. "MCNP variance reduction overview". In: *Monte-Carlo Methods and Applications in Neutronics, Photonics and Statistical Physics*. Springer, 1985, pp. 83–92. URL: http://link.springer.com/chapter/10.1007/BFb0049037 (visited on 08/28/2015).

[11] X-5 Monte Carlo Team. *MCNP - A General N-Particle Transport Code, Version 5, Volume II: Users Guide*. User Manual LA-CP-03-0245. Los Alamos National Laboratory, Apr. 2003.

[12] T. E. Booth. "Automatic importance estimation in forward Monte Carlo calculations". In: *Transactions of the American Nuclear Society* 41 (1982), pp. 308–309. URL: http://inis.iaea.org/search/search.aspx?orig_q=RN:14757371 (visited on 12/10/2014).

[13] J. S. Hendricks. "A code-generated Monte Carlo importance function". In: *Trans. Am. Nucl. Soc* 41 (1982), pp. 307–308. URL: http://inis.iaea.org/search/search.aspx?orig_q=RN:14753414 (visited on 12/10/2014).

[14] T. E. Booth and J. S. Hendricks. "Deep Penetration by Monte Carlo". In: *Trans. Am. Nucl. Soc.;(United States)* 43.CONF-821103- (1982), p. 609. URL: http://www.osti.gov/scitech/biblio/6041526 (visited on 10/19/2015).

[15] Thomas E. Booth and John S. Hendricks. "Importance Estimation in Forward Monte Carlo Calculations". In: *Fusion Science and Technology* 5.1 (Jan. 1984), pp. 90–100. URL: http://epubs.ans.org/?a=23082 (visited on 05/29/2017).

[16] T. M. Evans and J. S. Hendricks. "An Enhanced Geometry-Independent Mesh Weight Window Generator for Mcnp". English. In: vol. 1. Nashville, TN: Los Alamos National Lab., NM (United States), Apr. 1998, p. 165. URL: https://www.osti.gov/scitech/biblio/663177 (visited on 06/05/2017).

[17] K. A. Van Riper and Alamos National Laboratory Los. *Generation of a Monte Carlo Variance Reduction Map from a Deterministic Transport Calculation*. Tech. rep. LA-UR-95-0747. Los Alamos National Lab., NM (USA), 1995.

[18] Thomas E. Booth. "Common misconceptions in Monte Carlo particle transport". In: *Applied Radiation and Isotopes*. Proceedings of the 8th International Topical Meeting on Industrial Radiation and Radioisotope Measurement Applications (IRRMA-8) 70.7 (July 2012), pp. 1042–1051. ISSN: 0969-8043. DOI: 10.1016/j.apradiso.2011.11.037. URL: http://www.sciencedirect.com/science/article/pii/S0969804311005914.

[19] Jeffery Lewins. "Importance, the Adjoint Function: The Physical Basis of Variational and Perturbation Theory in Transport and Diffusion Problems". In: (1965). URL: http://www.osti.gov/scitech/biblio/4752764 (visited on 09/07/2015).

[20] EHUD Greenspan. "Developments in perturbation theory". In: *Advances in Nuclear Science and Technology* 9 (1976), pp. 181–268.

[21] Jeffery Lewins. "Developments in perturbation theory". In: *Advances in Nuclear Science and Technology* 4 (1968), pp. 309–332.

[22] I. Lux and L. Koblinger. *Monte Carlo Particle Transport Methods: Neutron and Photon Calculations.* CRC Press, 1991.

[23] Gerald Goertzel and Malvin H. Kalos. "Monte Carlo methods in transport problems". In: *Progress in Nuclear Energy* 2 (1958), pp. 315–369.

[24] M. H. Kalos. "Importance Sampling in Monte Carlo Shielding Calculations: I. Neutron Penetration Through Thick Hydrogen Slabs". In: *Nuclear Science and Engineering* 16.2 (1963), pp. 227–234. URL: http://www.ans.org/pubs/journals/nse/a_26504 (visited on 09/07/2015).

[25] Roger R. Coveyou, V. R. Cain, and K. J. Yost. "Adjoint and importance in Monte Carlo application". In: *Nuclear Science and Engineering* 27.2 (1967), pp. 219–234. URL: http://www.ans.org/pubs/journals/nse/a_18262 (visited on 08/28/2015).

[26] J. S. Tang and T. J. Hoffman. "Monte Carlo shielding analyses using an automated biasing procedure". In: *Nuclear Science and Engineering* 99.4 (1988), pp. 329–342. URL: http://www.ans.org/pubs/journals/nse/a_23562 (visited on 08/28/2015).

[27] *SCALE: A Comprehensive Modeling and Simulation Suite for Nuclear Safety Analysis and Design*. Tech. rep. ORNL/TM-2005/39, Version 6.1. Oak Ridge National Laboratory, 2011.

[28] M. L. Williams. "Generalized contributon response theory". In: *Nuclear Science and Engineering* 108.4 (1991), pp. 355–383. URL: http://www.ans.org/pubs/journals/nse/a_23835 (visited on 08/28/2015).

[29] Mark L. Williams and Harish Manohara. "Contributron Slowing-Down Theory". In: *Nuclear Science and Engineering* 111.4 (1992), pp. 345–367. URL: http://www.ans.org/pubs/journals/nse/a_15483 (visited on 08/28/2015).

[30] M. L. Williams. *A Fundamental Study of Contributon Transport Theory and Channel Theory Applications*. Tech. rep. DOE/ER/12899–T1. Louisiana State University, 1994.

[31] T. L. Becker. "Hybrid Monte Carlo/Deterministic Methods for Deep-Penetration Problems". PhD thesis. Doctoral Dissertation, University of Michigan, 2009.

[32] M. L. Williams and W. W. Engle. *The Concept of Spatial Channel Theory Applied to Reactor Shielding Analysis*. Tech. rep. ORNL/TM-5467. Oak Ridge National Laboratory, 1976.

[33] M. L. Williams. "The Relations Between Various Contributon Variables Used in Spatial Channel Theory". In: *Nuclear Science and Engineering* 63.2 (June 1977), p. 220. URL: http://epubs.ans.org/?a=27033 (visited on 01/11/2016).

[34] Marat Seydaliev and D. L. Henderson. "Contributon Theory for Shielding Analysis". In: *Madison, WI: Fusion Technology Institute (University of Wisconsin)* (2008). URL: http://icf4.neep.wisc.edu/pdf/fdm1338.pdf (visited on 08/28/2015).

[35] John C. Wagner et al. "Review of hybrid (deterministic/Monte Carlo) radiation transport methods, codes, and applications at Oak Ridge National Laboratory". In: *Progress in Nuclear Science and Technology* 2 (2011), pp. 808–814. URL: http://www.aesj.or.jp/publication/pnst002/data/808-814.pdf (visited on 08/28/2015).

[36] Marc A. Cooper and Edward W. Larsen. "Automated weight windows for global Monte Carlo particle transport calculations". In: *Nuclear science and engineering* 137.1 (2001), pp. 1–13. URL: http://www.ans.org/pubs/journals/nse/a_2171 (visited on 08/28/2015).

[37] M. M. Miften and Edward W. Larsen. "The quasi-diffusion method for solving transport problems in planar and spherical geometries". In: *Transport Theory and Statistical Physics* 22.2-3 (1993), pp. 165–186. URL: http://www.tandfonline.com/doi/abs/10.1080/00411459308203811 (visited on 12/10/2014).

[38] V. Ya Gol'Din. "A quasi-diffusion method of solving the kinetic equation". In: *USSR Computational Mathematics and Mathematical Physics* 4.6 (1964), pp. 136–149. URL: http://www.sciencedirect.com/science/article/pii/0041555364900850 (visited on 10/08/2014).

[39] Troy L. Becker, Allan B. Wollaber, and Edward W. Larsen. "A hybrid monte carlo-deterministic method for global particle transport calculations". In: *Nuclear science and engineering* 155.2 (2007), pp. 155–167. URL: http://www.ans.org/pubs/journals/nse/a_2653 (visited on 08/28/2015).

[40] Douglas E. Peplow, Edward D. Blakeman, and John C. Wagner. "Advanced Variance Reduction Strategies for Optimizing Mesh Tallies in MAVRIC". In: *TRANSACTIONS-AMERICAN NUCLEAR SOCIETY* 97 (2007), p. 595. URL: http://www.researchgate.net/profile/John_Wagner10/publication/237784020_Advanced_Variance_Reduction_Strategies_for_Optimizing_Mesh_Tallies_in_MAVRIC/links/54cd206d0cf24601c08cce96.pdf (visited on 10/19/2015).

[41] John C. Wagner and Scott W. Mosher. "Forward-Weighted CADIS Method for Variance Reduction of Monte Carlo Reactor Analyses". In: *Transactions of the American Nuclear Society* 103 (2010), pp. 342–345. URL: http://aprs.ornl.gov/nsed/rnsd/staff/Publications/WagnerPubs/Wagner-FW-CADIS-ANS-2010W_final.pdf (visited on 08/28/2015).

[42] Randal S. Baker and Edward W. Larsen. "A local exponential transform method for global variance reduction in Monte Carlo transport problems". In: Karlsruhe, Germany: Los Alamos National Lab., NM (United States), Apr. 1993. URL: http://www.osti.gov/scitech/biblio/10167411.

[43] Andrew Davis and Andrew Turner. "Comparison of global variance reduction techniques for Monte Carlo radiation transport simulations of ITER". In: *Fusion Engineering and Design*. Proceedings of the 26th Symposium of Fusion Technology SOFT-26 86.9-11 (Oct. 2011), pp. 2698–2700. URL: http://www.sciencedirect.com/science/article/pii/S0920379611000718 (visited on 10/19/2015).

[44] A. J. Van Wijk, G. Van den Eynde, and J. E. Hoogenboom. "An easy to implement global variance reduction procedure for MCNP". In: *Annals of Nuclear Energy* 38.11 (Nov. 2011), pp. 2496–2503. URL: http://www.sciencedirect.com/science/article/pii/S0306454911003203 (visited on 10/19/2015).

[45] Douglas E. Peplow. "Comparison of hybrid methods for global variance reduction in shielding calculations". In: *Transactions of the American Nuclear Society* 107 (2012), p. 512. URL: http://www.ornl.gov/~5pe/p069.pdf (visited on 10/19/2015).

[46] Kenneth A. Van Riper, Todd J. Urbatsch, and Patrick D. Soran. *AVATAR Automatic variance reduction in Monte Carlo calculations*. Tech. rep. Los Alamos National Lab., NM (United States), 1997. URL: http://www.osti.gov/scitech/biblio/527548 (visited on 10/08/2014).

[47] Edwin T. Jaynes. "Information theory and statistical mechanics". In: *Physical review* 106.4 (1957), p. 620. URL: http://journals.aps.org/pr/abstract/10.1103/PhysRev.106.620 (visited on 08/28/2015).

[48] Edwin T. Jaynes. "Information theory and statistical mechanics. II". In: *Physical review* 108.2 (1957), p. 171. URL: http://journals.aps.org/pr/abstract/10.1103/PhysRev.108.171 (visited on 08/28/2015).

[49] O. B. Moskalev. "The reconstruction of a positive function from its finite fourier series". In: *Transport Theory and Statistical Physics* 22.2-3 (1993), pp. 347–358. URL: http://www.tandfonline.com/doi/pdf/10.1080/00411459308203818 (visited on 05/30/2017).

[50] Wallace F. Walters and Todd A. Wareing. "An accurate, strictly-positive, nonlinear characteristic scheme for the discrete-ordinate equations". In: *Transport Theory and Statistical Physics* 25.2 (1996), pp. 197–215. URL: http://www.tandfonline.com/doi/abs/10.1080/00411459608204836 (visited on 05/30/2017).

[51] "A Nonlinear Positive Method for Solving the Transport Equation on Course Meshes". In: Arlington, TX: Los Alamos National Laboratory, Apr. 1994. URL: http://www.iaea.org/inis/collection/NCLCollectionStore/_Public/25/048/25048476.pdf (visited on 05/30/2017).

[52] Douglas E. Peplow, Scott W. Mosher, and T. M. Evans. *Consistent Adjoint Driven Importance Sampling using Space, Energy, and Angle*. Tech. rep. ORNL/TM-2012/7. Oak Ridge National Laboratory, Aug. 2012.

[53] H. C. Gupta and S. R. Dwivedi. "Sampling of scattering angle in deep-penetration Monte Carlo". In: *Annals of Nuclear Energy* 12.4 (Jan. 1985), pp. 213–216. ISSN: 0306-4549. DOI: 10.1016/0306-4549(85)90047-7. URL: http://www.sciencedirect.com/science/article/pii/0306454985900477.

[54] S.R. Dwivedi. "A new importance biasing scheme for deep-penetration Monte Carlo". en. In: *Annals of Nuclear Energy* 9.7 (Jan. 1982), pp. 359–368. ISSN: 03064549. DOI: 10.1016/0306-4549(82)90038-X. URL: http://linkinghub.elsevier.com/retrieve/pii/030645498290038X.

[55] Taro Ueki and Edward W. Larsen. "A kinetic theory for nonanalog Monte Carlo particle transport algorithms: exponential transform with angular biasing in planar-geometry anisotropically scattering media". In: *Journal of Computational Physics* 145.1 (1998), pp. 406–431. URL: http://www.sciencedirect.com/science/article/pii/S0021999198960399.

[56] J. S. Hendricks and L. L. Carter. "Anisotropic angle biasing of photons". In: *Nuclear Science and Engineering* 89.2 (1985), pp. 118–130. URL: http://www.ans.org/pubs/journals/nse/a_18186 (visited on 10/19/2015).

[57] J. P. Both, J. C. Nimal, and T. Vergnaud. "Automated importance generation and biasing techniques for Monte Carlo shielding techniques by the TRIPOLI-3 code". In: *Progress in Nuclear Energy* 24.1 (1990), pp. 273–281. URL: http://www.sciencedirect.com/science/article/pii/0149197090900468 (visited on 08/28/2015).

[58] Scott A. Turner and Edward W. Larsen. "Automatic variance reduction for three-dimensional Monte Carlo simulations by the local importance function transform-I: Analysis". In: *Nuclear Science and Engineering* 127.1 (1997), pp. 22–35. URL: http://cat.inist.fr/?aModele=afficheN&cpsidt=2833140 (visited on 12/09/2014).

[59] Scott A. Turner and Edward W. Larsen. "Automatic variance reduction for three-dimensional Monte Carlo simulations by the local importance function transform-II: Numerical results". In: *Nuclear Science and Engineering* 127.1 (1997), pp. 36–53. URL: http://cat.inist.fr/?aModele=afficheN&cpsidt=2833141 (visited on 12/09/2014).

[60] Kendra P. Keady and Edward W. Larsen. "A Modified Monte Carlo Local Importance Function Transform Method". In: *Nuclear Engineering and Design* 295 (2015), pp. 625–631. URL: http://www.sciencedirect.com/science/article/pii/S0029549315002915 (visited on 02/10/2016).

[61] Scott W. Mosher et al. "Automated weight-window generation for threat detection applications using ADVANTG". In: Saratoga Springs, New York: Oak Ridge National Laboratory (ORNL), May 2009. URL: http://www.northeastern.edu/sds/RadiationsensorData.pdf.

[62] Thomas M. Evans et al. "Denovo: A new three-dimensional parallel discrete ordinates code in SCALE". In: *Nuclear Technology* 171.2 (2010), pp. 171–200. URL: http://www.ans.org/pubs/journals/nt/a_10782 (visited on 08/28/2015).

[63] E. Somasundaram and T. S. Palmer. *Implementation of hybrid variance reduction methods in a multi group Monte Carlo code for deep shielding problems*. Tech. rep. American Nuclear Society, 555 North Kensington Avenue, La Grange Park, IL 60526 (United States), 2013. URL: http://www.osti.gov/scitech/biblio/22212710 (visited on 08/28/2015).

[64] D. S. Lucas et al. "Applications of the 3-D Deterministic Transport Attila for Core Safety Analysis". In: *Americas Nuclear Energy Symposium 2004*. 2004. URL: https://www.researchgate.net/profile/Hans_Gougar/publication/237614641_Applications_Of_The_3-D_Deterministic_Transport_Attila_For_Core_Safety_Analysis/links/02e7e5267dd5feb36c000000.pdf.

[65] Jeremy Sweezy et al. "Automated variance reduction for MCNP using deterministic methods". In: *Radiation protection dosimetry* 116.1-4 (2005), pp. 508–512. URL: http://rpd.oxfordjournals.org/content/116/1-4/508.short (visited on 08/28/2015).

[66] R. E. Alcouffe et al. *PARTISN manual*. Tech. rep. LA-UR-02-5633, Los Alamos National Laboratory, 2002.

[67] Georgeta Radulescu et al. "Dose Rate Analysis of As-Loaded Spent Nuclear Fuel Casks". In: (2013). URL: http://www.ornl.gov/~5pe/p087.pdf (visited on 10/08/2014).

[68] Y. F. Chen et al. "Surface Dose Rate Calculations of a Spent-Fuel Storage Cask by Using MAVRIC and Its Comparison with SAS4 and MCNP". In: *Nuclear Technology* 175.1 (2011), pp. 343–350. URL: http://www.ans.org/pubs/journals/nt/a_12306 (visited on 08/28/2015).

[69] R. J. Sheu et al. "Dose Evaluation for an Independent Spent-Fuel Storage Installation Using MAVRIC". In: *Nuclear Technology* 175.1 (2011), pp. 335–342. URL: http://www.ans.org/pubs/journals/nt/a_12305 (visited on 08/28/2015).

[70] Scott W. Mosher. *A New Version of the ADVANTG Variance Reduction Generator*. Tech. rep. Oak Ridge National Laboratory (ORNL), 2010. URL: http://www.osti.gov/scitech/biblio/978283 (visited on 08/31/2015).

[71] Aaron M. Bevill and Scott W. Mosher. *A New Source Biasing Approach in ADVANTG*. Tech. rep. Oak Ridge National Laboratory (ORNL), 2012. URL: http://www.osti.gov/scitech/biblio/1044655 (visited on 08/28/2015).

[72] The HDF Group. *Hierarchical Data Format, version 5*. /HDF5/. 1997-2017.

[73] Douglas E. Peplow, Scott W. Mosher, and Thomas M. Evans. *Consistent Adjoint Driven Importance Sampling using Space, Energy, and Angle*. Tech. rep. Oak Ridge National Lab., TN (United States), 2012.

[74] Ahmad M. Ibrahim et al. "The Multi-Step CADIS Method for Shutdown Dose Rate Calculations and Uncertainty Propagation". In: *American Nuclear Society Radiation Protection and Shielding Division 2014 Topical Meeting*. 2014, pp. 14–18. URL: `http://www.ornl.gov/~5pe/p089.pdf` (visited on 08/28/2015).

[75] T. M. Evans and T. A. Wareing. "The Solution of Well Logging Problems Using Hybrid Transport Methods on Unstructured Meshes". In: *Proceedings of the Mathematics and Computation, Reactor Physics and Environmental Analysis in Nuclear Applications* (1999), p. 1393.

[76] Christoph Borgers and Edward W. Larsen. "Asymptotic derivation of the Fermi pencil-beam approximation". In: *Nuclear science and engineering* 123.3 (1996), pp. 343–357. URL: `http://www.ans.org/pubs/journals/nse/a_24198` (visited on 08/28/2015).

[77] Ahmad M. Ibrahim et al. "Analysis of Shutdown Dose Rate in Fusion Energy Systems Using Hybrid Monte Carlo/Deterministic Techniques". In: *American Nuclear Society Radiation Protection and Shielding Division 2014 Topical Meeting*. 2014, pp. 14–18. URL: `http://www.ornl.gov/~5pe/p088.pdf` (visited on 08/28/2015).

[78] R. J. Hagler and A. H. Fero. "ISFSI site boundary radiation dose rate analyses". In: *Radiation protection dosimetry* 116.1-4 (2005), pp. 411–416. URL: `http://rpd.oxfordjournals.org/content/116/1-4/411.short` (visited on 08/28/2015).

[79] K. W. Burn. "A new weight-dependent direct statistical approach model". In: *Nuclear science and engineering* 125.2 (1997), pp. 128–170. URL: `http://www.ans.org/pubs/journals/nse/a_24262` (visited on 08/28/2015).

[80] John C. Wagner et al. "Hybrid and parallel domain-decomposition methods development to enable monte carlo for reactor analyses". In: *Progress in Nuclear Science and Technology* 2 (2011), pp. 815–820. URL: `http://www.ornl.gov/~5pe/p055.pdf` (visited on 08/28/2015).

[81] *SCALE Code System*. Tech. rep. ORNL/TM-2005/39, Version 6.1. Oak Ridge National Laboratory, June 2016. URL: `https://rsicc.ornl.gov/codes/ccc/ccc8/ccc-834.html`.

[82] B. Rearden et al. "Modernization Enhancements in SCALE 6.2". In: *PHYSOR 2014 - The Role of Reactor Physics Toward a Sustainable Future*. Kyoto, Japan, Sept. 2014.

Appendix A

Software for this Project

The majority of the software for this method is available in open source repositories. This includes the characterization problem inputs, the scripts used to postprocess the HDF5 and SILO files, and the datasets that were used to generate these results. The next few subsections of this appendix contain the URLs and descriptions of how to access these publicly-available resources. However, some of the software–namely the code added to ADVANTG and the Exnihilo code suite–are export controlled and is not freely available. The code used for that will be included here, and what is easily separable is committed separately in a different repository.

The version of Exnihilo used to run this work was:
branchname: angular_hybrid_method
commit hash: 81fd08b8cc62b00ee72a2305c5f4493691acb059

The version of ADVANTG used to run this work was:
branchname: MMM
commit hash: 03321f9fb084e3b9219c07c454e0c6d265a565f1

A.1 Omega Flux Calculation

The majority of the software for this method are available in open source repositories. The snippet in this subsection is contained in Exnihilo, which is not publicly available. As such, snippets will be included here for transparency.

```
##############################################################################
# File   : omnibus/postprocess/integrator.py
# Author: Madicken
# Date   : Tue Mar 17 16:41:55 2015
#
#<+ This file holds all of the tools necessary for doing the post-processing
# of a .txt output file, integrating the adjoint and forward angular fluxes,
```

```
# and returning
# the adjoint scalar flux in a .silo file readable by Advantg. +>
##############################################################################
from __future__ import (division, absolute_import, print_function, )
#-----------------------------------------------------------------------------#
import numpy as np
import os
import re
import h5py
from nemesis import (const_View_Field_Dbl)
from nemesis import (Silo_Mesh_Writer as SiloMeshFile)

##############################################################################

class h5reader(object):
    def __init__(self, filename, adjoint=False):
        # declare all variables that this object will contain; filename is a
        # required user input and adjoint mode is False by default. A
        # True will result in a matrix rotation to ensure the omega
        # coordinates in forard and adjoint are consistent.
        self.filename = str(filename)
        self.adjoint = adjoint
        self.mesh_g = []
        self.mesh_x = []
        self.mesh_y = []
        self.mesh_z = []
        self.quadrature_weights = []
        self.angular_flux = []
        self.angles = []
        self.group_bounds = []
        pass

    def __call__(self):
        pass

    def filereader(self):
        h5file = h5py.File(self.filename,'r')

        # Read in the data from h5file
        self.angles = h5file['/denovo/angles'][:]
        angular_flux = h5file['/denovo/angular_flux'][:]
        self.mesh_g = h5file['/denovo/mesh_g'][:]
        self.mesh_x = h5file['/denovo/mesh_x'][:]
        self.mesh_y = h5file['/denovo/mesh_y'][:]
        self.mesh_z = h5file['/denovo/mesh_z'][:]
        self.group_bounds_n = h5file['/denovo/group_bounds_n'][:]
        self.quadrature_weights = h5file['/denovo/quadrature_weights'][:]

        # Set variables for the expected size of the data
        z_len = len(self.mesh_z)-1
```

```
        y_len = len(self.mesh_y)-1
        x_len = len(self.mesh_x)-1
        g_len = len(self.mesh_g)
        m_len = len(self.quadrature_weights)

        # consider putting an assertion to check the variables rather than
        # trimming it.

        # Remove padding from the angular flux matrix
        self.angular_flux = angular_flux[:g_len,:z_len,:y_len,:x_len,:m_len]

                # Resort the angular fluxes to match -omega for the
        # adjoint calculation
        if self.adjoint == True:
            angle_locs = h5reader.location_generator(self,self.angles)
            new_flux = h5reader.sort_by_reverse_angles(self,self.angular_flux,
                    self.angles, angle_locs)
            self.angular_flux = new_flux


    def location_generator(self,data):
        location_dict = {}
        for d in range(len(data)):
            location_dict[str(data[d])] = d
        return location_dict

    def sort_by_reverse_angles(self,data,angles,angle_dict):
        reverse_data = np.zeros(np.shape(data))
        for angle in angles:
            reverse_data[:,:,:,:,angle_dict[str(angle)]] = \
                    data[:,:,:,:,angle_dict[str(-angle)]]
        return reverse_data


class Integrator(object):
    def __init__(self, forwarddata, adjointdata):
        self.forwarddata = forwarddata
        self.adjointdata = adjointdata
        self.integrated_numerator = []
        self.integrated_denominator = []
        self.integrated_fluxes = []
        self.mesh_g = adjointdata.mesh_g
        self.mesh_z = adjointdata.mesh_z
        self.mesh_y = adjointdata.mesh_y
        self.mesh_x = adjointdata.mesh_x
        self.group_bounds_n = adjointdata.group_bounds_n

        # anisotropy metric variables. Used in the case of anisotropy
        # quantification for omega-method analysis. See
        # quantify_anisotropy
```

```
        # function for descriptions of each metric.
        self.forward_anisotropy = np.array([])
        self.adjoint_anisotropy = np.array([])
        self.contributon_anisotropy = np.array([])
        self.metric_one = np.array([])
        self.metric_two = np.array([])
        self.metric_three = np.array([])
        self.metric_four = np.array([])
        self.metric_five = np.array([])
        self.metric_six = np.array([])
        self.metric_seven = np.array([])
        pass

    def calculate_weighted_fluxes(self):
                # First unpack the relevant data from object created in
        # filereader
        forward_flux = self.forwarddata.angular_flux
        adjoint_flux = self.adjointdata.angular_flux
        quadrature_weights = self.forwarddata.quadrature_weights

        # Create numerator and denominator arrays
        numerator = forward_flux[:,:,:,:]*\
                adjoint_flux[:,:,:,:]*quadrature_weights
        denominator = forward_flux[:,:,:,:]*quadrature_weights

        # Integrate the denominator and numerator separately,
        # then divide the
        # values to obtain a weighted adjoint scalar flux
        integrated_numerator = 4.*np.pi*np.sum(numerator, axis=4)
        integrated_denominator = np.sum(denominator, axis=4)
        try:
            weighted_scalar_flux = \
                    np.divide(integrated_numerator,\
                    integrated_denominator)
        except RuntimeWarning:
            pass
            print('You have a 0 division error, \
                    replacing first element with 0')
            weighted_scalar_flux[0,0,0,0] = 0.0


        self.integrated_fluxes = weighted_scalar_flux
        self.integrated_numerator = integrated_numerator
        self.integrated_denominator = integrated_denominator
        pass

    def quantify_anisotropy(self):
        # First unpack the relevant data from object
        # created in filereader
        forward_flux = self.forwarddata.angular_flux
```

```
adjoint_flux = self.adjointdata.angular_flux
omega_fluxes = self.integrated_fluxes
contributon_fluxes = self.integrated_numerator
fwd_quadrature_weights = self.forwarddata.quadrature_weights
adj_quadrature_weights = self.adjointdata.quadrature_weights

# Create forward info
forward_mat = forward_flux[:,:,:,:]*fwd_quadrature_weights
fwd_scalars = np.sum(forward_mat, axis=4)
fwd_max_val = forward_mat.max(axis=4)
fwd_min_val = forward_mat.min(axis=4)
fwd_quad_sum = np.sum(fwd_quadrature_weights)

# Create adjoint info
adjoint_mat = adjoint_flux[:,:,:,:]*adj_quadrature_weights
adj_scalars = np.sum(adjoint_mat, axis=4)
adj_max_val = adjoint_mat.max(axis=4)
adj_min_val = adjoint_mat.min(axis=4)
adj_quad_sum = np.sum(adj_quadrature_weights)

# Create contributon info
contributon_mat = 4.*np.pi*adjoint_flux[:,:,:,:]*\
        forward_flux[:,:,:,:]*fwd_quadrature_weights
cont_scalars = contributon_fluxes
# cont_scalars = np.sum(contributon_mat, axis=4)
cont_max_val = contributon_mat.max(axis=4)
cont_min_val = contributon_mat.min(axis=4)

# now quantify forward anisotropy
avg_flux = fwd_scalars/fwd_quad_sum
fwd_ratio = fwd_max_val/avg_flux

# now quantify adjoint anisotropy
avg_flux = adj_scalars/adj_quad_sum
adj_ratio = adj_max_val/avg_flux
adj_ratio_min = np.divide(adj_max_val,adj_min_val)

# calculate the contributon ratio (advantg does this already)
scalar_cont_product = adj_scalars*fwd_scalars

# quantify contributon ratio (Metric No. 1)
cont_ratio_one = scalar_cont_product/cont_scalars

# calculate the ratio between omega and adjoint
# fluxes (Metric No. 2)
cont_ratio_two = omega_fluxes/adj_scalars

# quantify max to avg contributon anisotropy
# (Metric No. 3)
avg_flux = cont_scalars/fwd_quad_sum
```

```
        cont_ratio_three = cont_max_val/avg_flux

        # quantify the ratio between omega and adjoint fluxes
        # (Metric No. 4)
        cont_ratio_four = cont_ratio_three/adj_ratio

        # quantify max to min contributon anisotropy
        # (Metric No. 5)
        cont_ratio_five = np.divide(cont_max_val,cont_min_val)

        # quantify the ratio between omega and adjoint fluxes
        # (Metric No. 6)
        cont_ratio_six = cont_ratio_five/adj_ratio_min

        # load the anisotropy ratios into object
        self.forward_anisotropy = fwd_ratio
        self.adjoint_anisotropy = adj_ratio
        self.metric_one = cont_ratio_one
        self.metric_two = cont_ratio_two
        self.metric_three = cont_ratio_three
        self.metric_four = cont_ratio_four
        self.metric_five = cont_ratio_five
        self.metric_six = cont_ratio_six

class SaveData(object):
    def __init__(self, data):
        self.data = data
        self.mesh_x = data.mesh_x
        self.mesh_y = data.mesh_y
        self.mesh_z = data.mesh_z
        self.mesh_g = data.mesh_g
        self.integrated_fluxes = data.integrated_fluxes
        self.forward_anisotropy = data.forward_anisotropy
        self.adjoint_anisotropy = data.adjoint_anisotropy
        self.contributon_flux = data.integrated_numerator
        self.contributon_anisotropy = data.contributon_anisotropy

        # convert the mesh vectors to cell-centerd values
        x = self.midpoint_finder(self.mesh_x)
        y = self.midpoint_finder(self.mesh_y)
        z = self.midpoint_finder(self.mesh_z)
        (self.Z,self.Y,self.X) = np.meshgrid(z,y,x, indexing='ij')
        pass

    def omega_by_group(self, filename):
        ''' This function saves the integrated angular fluxes
        into the silo file by
        group. '''
        # first delete the file if it already exists
        filename = str(filename)
```

```
        os.system('rm␣%s' %(filename))

        # write the data by group into a silo file with the
        # filename specified by
        # the user.
        with SiloMeshFile('%s' %filename) as f:
            f.write_mesh(*map(const_View_Field_Dbl.fromarray, (self.mesh_x,
                self.mesh_y, self.mesh_z)))
            f.write("x", self.X)
            f.write("y", self.Y)
            f.write("z", self.Z)
            for group in self.mesh_g:
                f.write("omega_flux_%03d" %(group), \
                        self.integrated_fluxes[group])

    def anisotropies_to_hdf5(self, filename):
        '''Saves quantified anisotropies to an hdf5 file for
        postprocessing.

        If all anisotropies are calculated, then the file
        will include metrics one through six (see
        Integrator.quantify_anisotropy for a description
        of each metric), the forward, adjoint, and contributon
        anisotropies, and the contributon scalar flux.'''
        filename = str(filename)
        os.system('rm␣%s' %(filename))

        metricnames = {"one": self.data.metric_one,
                "two": self.data.metric_two,
                "three": self.data.metric_three,
                "four": self.data.metric_four,
                "five": self.data.metric_five,
                "six": self.data.metric_six}
        for name, variable in metricnames.iteritems():
            assert variable.size, \
                    "metric␣"+str(name)+"␣contains␣no␣data"

        # write the data by group into a silo file with the
        # filename specified by
        # the user.
        with h5py.File('%s' %filename, 'w') as f:
            fname = f.create_group('forward_anisotropy')
            aname = f.create_group('adjoint_anisotropy')
            cname = f.create_group('contributon_flux')
            for name, variable in metricnames.iteritems():
                mname = f.create_group('metric_%s' %name)
                for group in self.mesh_g:
                    mname.create_dataset('group_%03d' %group,\
                            data=variable[group])
            for group in self.mesh_g:
```

```
            fname.create_dataset('group_%03d' %group,
                    data=self.forward_anisotropy[group])
            aname.create_dataset('group_%03d' %group,
                    data=self.adjoint_anisotropy[group])
            cname.create_dataset('group_%03d' %group,
                    data=self.contributon_flux[group])

    def anisotropies_to_silo(self, filename):
        ''' This function saves all of the anisotropies in
        the problem used for
        problem diagnostics by group to a silo file for
        visualization purposes.

        If all anisotropies are calculated, then the file
        will include metrics one through six (see
        Integrator.quantify_anisotropy for a description of
        each metric), the
        forward, adjoint, and contributon anisotropies,
        and the contributon
        scalar flux. '''
        filename = str(filename)
        os.system('rm_%s' %(filename))

        metricnames = {"one": self.data.metric_one,
                "two": self.data.metric_two,
                "three": self.data.metric_three,
                "four": self.data.metric_four,
                "five": self.data.metric_five,
                "six": self.data.metric_six}
        for name, variable in metricnames.iteritems():
            assert variable.size, \
                    "metric_"+str(name)+"_contains_no_data"

        # write the data by group into a silo file with the
        # filename specified by the user.
        with SiloMeshFile('%s' %filename) as f:
            f.write_mesh(*map(const_View_Field_Dbl.fromarray, \
                    (self.mesh_x,
                self.mesh_y, self.mesh_z)))
            f.write("x", self.X)
            f.write("y", self.Y)
            f.write("z", self.Z)
            for group in self.mesh_g:
                for name, variable in metricnames.iteritems():
                    f.write("metric_%s_group_%03d" %(name, group),
                            variable[group])

        # if the forward anisotropy has been quantified, also write
                # them to the file
                if self.forward_anisotropy.size:
```

```
                f.write("F_anis_group_%03d" %(group),
                        self.forward_anisotropy[group])

            # if the adjoint anisotropy has been quantified,
            # write it to file too
            if self.adjoint_anisotropy.size:
                f.write("A_anis_group_%03d" %(group),
                        self.adjoint_anisotropy[group])

            # if contributon anisotropy quantified,
            # write it to file too.
            if self.contributon_anisotropy.size:
                f.write("C_anis_group%03d" %(group),
                        self.contributon_anisotropy[group])

            # if contributon flux quantified, write
            # it to file.
            if self.contributon_flux.size:
                f.write("contributon_flux_group%03d" %(group),
                        self.contributon_flux[group])

    def midpoint_finder(self, mesh_vector):
        new_mesh = np.zeros(len(mesh_vector)-1)
        new_mesh = (mesh_vector[0:-1]+mesh_vector[1:])/2
        return new_mesh

#-----------------------------------------------------------------------#
if __name__ == '__main__':
    main()

##########################################################################
# end of Denovo/tools/integrator.py
##########################################################################
```

A.2 Anisotropy Quantification

See the function *quantify_anisotropy* in Appendix A.1 on how the anisotropies are calculated.

A.3 Inputs and Scripts

A.3.1 Parametric Study Problems

The characterization problem MCNP and ADVANTG inputs are all available at the public repository: https://github.com/munkm/caskmodels

The problems were executed from commit hash no.:

`0bc315bf2f49f83627a563f710bf4f586ec3e489`

Directions on how to run these problems are available in the repository as well.

A.3.2 Postprocessing Scripts

A suite of postprocessing tools were created to create the figures herein. The tools, the datasets, and directions on how to recreate the figures in this dissertation are available at: https://github.com/munkm/thesiscode

The figures in this dissertation were created with the suite of tools at commit hash no.:

`28329c86b939d30d2ac236bfccaf026d7e57556d`

This repository has three folders:

- notebooks
- scripts
- submission_scripts
- data

Submission scripts is the folder containing the .pbs runscripts used to run these problems on the remote ORNL machine remus. If one has access to a similar machine with the same queueing system, these will run them on the same number of cores as run in the studies of this dissertation. Alternatively, there are directions on how to run each problem on a local machine in that directory.

Scripts contains the scripting tools used to parse the datasets generated by ADVANTG and Denovo. This suite has plotting tools, MCNP postprocessing tools, statistical analysis tools to analyze anisotropy metrics, and HDF5 postprocessing tools. The plotting tools can be used to generate the tally result and relative error histograms, the categorical violin, strip, or boxplots for each metric, and the comparitive histograms from the angle-informed study. The scripts folder also has a tool for automatically setting up the parametric study, as outlined in Section 4.3. The tool includes an automatically generated submission script, for ease of use for future parametric studies. The flux maps for each problem were generated with VisIT, which is not an automated process. Future work will be to make these reproducible as well.

Notebooks contains a few Jupyter notebooks that provide examples on using the plotting tools used in this suite. An interested user can understand how the postprocessing tools work and categorize data to compare the adjoint, CADIS, and CADIS-Ω methods.

The **data** folder is mostly empty, but contains a makefile that a user can execute to automatically download the datasets from this project. This folder also has instructions on how to use the plotting tools to analyze the data just downloaded. One should be aware that the datasets from these few problems are still significant, at roughly 800Gb.

These tools are by no means comprehensive and cover all types of comparative hybrid methods figures. For example, they will likely not be the best tools with which to analyze the Forward-Weighted methods. The top level repository contains a README file with the future features added to the repository.

A.3.3 Supporting Repositories

The violin and scatterplots used throughout this thesis were made with a modified version of the seaborn frontend to matplotlib. That modification includes adjusting categorials to be over logrithmic scales. The URL for the modified repository is:
https://github.com/munkm/seaborn